SUPERSTRUCTURES AND CHARGE-DENSITY WAVES IN DISTORTED AND INTERCALATED LAYER MATERIALS

A thesis presented for the degree of

Doctor of Philosophy

in the University of London

by

Christopher Brian Scruby

Imperial College of

Science and Technology

May 1976

ἀφορῶντες εἰς Ἰησουν

Heb. 12 v 2.

ABSTRACT

Transmission electron and X-ray diffraction studies, and high resolution phase-contrast electron microscopy, have shown that, except for NbS_2, all the Group Va transition metal layer dichalcogenides are unstable with respect to periodic structural deformation in some temperature range. Incommensurate and commensurate distorted phases have been identified in 1T TaS_2, $4H_b$ TaS_2, 1T VSe_2 and 2H $TaSe_2$. The deformations remain incommensurate in 2H $NbSe_2$.

The three distorted phases of 1T TaS_2 make this compound unique; two are incommensurate. A detailed model of the deformation structure of $1T_2$ (room temperature phase) has been proposed from diffractometer data, in which groups of metal atoms form planar clusters. The distortion modes on the Ta sublattice are predominantly LA, and on the S sublattice $TA_\perp$, out of phase with the Ta by $2\pi/3$. There are thus periodic variations in layer thickness and rhombohedral stacking of deformations. There is a 30% increase in deformation amplitude at the $1T_1 \rightarrow 1T_2$ transition, and a further 15% from $1T_2$ to $1T_3$. $1T_1$ and $1T_3$ TaS_2 also show some degree of metal clustering. At the transition to the $\sqrt{13}a \times \sqrt{13}a$ superlattice ($1T_3$) there is a deformation stacking change to give a triclinic cell. The deformation structures of the other materials are related to 1T TaS_2, but mostly with reduced displacements.

The superstructures are interpreted in terms of lattice deformations which are coupled to charge-density waves in the conduction d-bands. This arises as a consequence of the condensation of phonons into modes softened by an enhanced Kohn Anomaly. The phase transitions occur at temperatures in agreement with electrical measurements, and the charge-density wave

model is used to try and explain the anomalous properties of these materials. The transformations are also discussed in terms of energy gaps which are opened up by the deformation potential at the Fermi level.

The distortion wave vector spans the Fermi Surface and the changes with temperature are discussed on this basis. Characteristic diffuse scattering observed in octahedral polytypes, is interpreted as a direct image of the Fermi Surface.

It becamesnecessary to develop scattering theory for a distorted structure, and incommensurate superstructures are discussed in some detail.

The intercalation complex of pyridine with 2H TaS_2 was also studied, and a model proposed for the structure. Most important is a stacking change of the host lattice:— AcA BcB → AcA|AbA, on intercalation. The possible relationship between this complex and charge-density waves is discussed.

TABLE OF CONTENTS

		Page
	LIST OF FIGURES	11
	LIST OF TABLES	22
1	INTRODUCTION	24
	1.1 General	24
	1.2 Structural Properties	27
	1.2.1 The Undistorted Materials	28
	1.2.2 Other Polytypes of the Undistorted Materials	31
	1.2.3 The Distorted Tellurides	32
	1.3 Electronic Properties	34
	1.3.1 Electronic Band Structure	34
	1.3.2 Electrical and Magnetic Measurements	37
	1.3.3 Superconductivity	43
	1.4 Intercalation	44
2	SCATTERING OF RADIATION BY SUPERSTRUCTURES	48
	2.1 Scattering by a Regular Lattice of Atoms	48
	2.2 Diffraction by a Layer Material	49
	2.2.1 Stacking of the Layers	49
	2.2.2 Effects of Intercalation	51
	2.3 Superstructures	52
	2.3.1 Indexing Commensurate Superstructures	53
	2.3.2 Indexing Incommensurate Superstructures	54
	2.4 Single Periodic Distortion of a Lattice	55
	2.4.1 Distorted Monatomic Lattice	56
	2.4.2 Redistribution of Scattered Intensity	58
	2.4.3 Equivalence of Commensurate and Incommensurate Analysis.	59
	2.4.4 Choice of Analysis Close to Limiting Case	63

2.5 Multiple Distortions in a Lattice 64

2.5.1 Phase Correlation 64

2.5.2 Matrix Cell Containing More than One Atom 66

2.5.3 Symmetry-Related Distortions 70

2.5.4 Symmetry-Related Distortions and Phase 74

2.5.5 Distortion Mode 75

2.6 Non-Sinusoidal Deformations 77

2.6.1 Fourier Components, $2\underline{Q}_1$, $2\underline{Q}_2$, $2\underline{Q}_3$ 80

2.6.2 Fourier Components, $\underline{P}_1$, $\underline{P}_2$, $\underline{P}_3$ 81

2.6.3 Special Non-Sinusoidal Functions 82

2.6.4 Diffraction from 1-D Commensurate Clusters 85

2.6.5 Diffraction from 1-D Incommensurate Clusters 86

2.6.6 Effect of Omitting Higher Fourier Components 88

3 THE KOHN ANOMALY AND CHARGE-DENSITY WAVES 89

3.1 Electronic Susceptibility and Screening 89

3.2 Phonons and the Kohn Anomaly 91

3.2.1 Free Electron Model - Spherical Fermi Surface 91

3.2.2 The Kohn Anomaly 94

3.2.3 Non-Spherical Fermi Surfaces 95

3.2.4 Radius of Curvature of the Fermi Surface 97

3.2.5 Phonon Image of Fermi Surface 98

3.3 Ordering and the $q = 2k_f$ Instability 101

3.4 Charge-Density Waves and Spin-Density Waves 102

3.5 Charge-Density Waves and Energy Gaps 106

3.6 Metal-Insulator Transitions 109

3.7 Superconductivity and Charge-Density Waves 111

4 EXPERIMENTAL PROCEDURES 114

4.1 Materials 114

4.2 Intercalation 115

4.3 Electron Diffraction Studies 115

4.4 High-Resolution Phase Contrast Electron Microscopy 116

4.5 X-ray Diffraction Studies 118

5 DIFFRACTION RESULTS AND INTERPRETATION: TANTALUM DISULPHIDE (PYRIDINE) 121

5.1 Introduction 121

5.2 Tantalum Disulphide Matrix Structure 121

5.2.1 Change in Cell Dimensions on Intercalation 121

5.2.2 Tantalum - Sulphur Layer Distance 123

5.2.3 Stacking of the Tantalum Disulphide Layers 126

5.3 Ordering of Pyridine Molecules 132

5.3.1 Pyridine Lattice 132

5.3.2 Orientation of Pyridine Molecules 142

5.4 Discussion of Structural Results 151

6 DIFFRACTION RESULTS AND INTERPRETATION: 1T TANTALUM DISULPHIDE 156

6.1 Introduction 156

6.2 Reciprocal Lattice Geometry: Matrix Reflexions 159

6.3 Reciprocal Lattice Geometry: Satellite Reflexions in $1T_1$ and $1T_2$ TaS_2 159

6.4 Reciprocal Lattice Geometry: Satellite Reflexions in $1T_3$ TaS_2 164

6.5 Evidence for a Deformation Superstructure 165

6.6 Determination of Deformation Wave Vector 169

6.7 Stacking of Deformation Waves in Adjacent Layers 173

7 DETAILED DEFORMATION STRUCTURE OF 1T TANTALUM DISULPHIDE 177

7.1 Introduction 177

7.2 Magnitude of In-Layer Displacements in 1T TaS_2 179

7.2.1 Structure Factors of $\underline{M}(h0.0)$ — Total Displacement 180

7.2.2 Structure Factors of $\underline{S}_{h0.0}(10.1)$ and $\underline{S}_{h0.0}(\bar{1}0.\bar{1})$ — Determination of U_Q Fundamental Distortion Amplitude 183

7.2.3 In-Layer Distortion of Sulphur Sublattice 186

7.2.4 Direction of $\underline{U}_Q$ and Mode of Deformation Waves 188

7.2.5 Higher Fourier Components 189
(a) Wave Vector a Multiple of Fundamental $\underline{Q}_i$

7.2.6 Higher Fourier Components 192
(b) Wave Vectors, $\underline{P}_i$

7.2.7 Phases of Deformation Waves 193

7.3 Calculations Based on Detailed Model for Distorted Layer 194

7.3.1 Summary of Initial Values for Parameters 194

7.3.2 Deformation Wave Combinations 194

7.3.3 Details of Structure Factor Calculation 197

7.3.4 Interpretation in Terms of Metal Atom Clusters 205

7.4 Displacements Perpendicular to the Layers in $1T_2$ TaS_2 209

7.5 Deformation Structure of $1T_1$ TaS_2 213

7.5.1 Introduction 213

7.5.2 Direction of Deformation Amplitude $\underline{U}_Q$ 213

7.5.3 Magnitude of the Displacements 215

7.5.4 Metal Atoms Clusters in $1T_1$ TaS_2 217

7.6 Diffuse Scattering in $1T_1$ TaS_2 218

7.7 Deformation Structure of $1T_3$ TaS_2 221

7.8 Coherence Length of the Deformation Waves 227

7.9 Distorted Layer Models for the Three Phases 231

8 DIFFRACTION RESULTS AND INTERPRETATION: OTHER OCTAHEDRAL MATERIALS 233

8.1 Introduction 233

8.2 $4H_b$ Tantalum Disulphide 233

8.3 1T Vanadium Diselenide 239

8.4 1T Tantalum Diselenide 242

9 DIFFRACTION RESULTS AND INTERPRETATION: TRIGONAL PRISMATIC MATERIALS 244

9.1 Introduction 244

9.2 2H Niobium Diselenide 244

9.3 Niobium Disulphide 250

9.4 2H Tantalum Diselenide 250

9.5 2H Tantalum Disulphide 254

10 PHASE-CONTRAST LATTICE IMAGES 255

10.1 Introduction 255

10.2 Molybdenum Disulphide 255

10.3 β - Molybdenum Telluride 257

10.4 1T Tantalum Disulphide 259

10.5 $4H_b$ Tantalum Disulphide 263

11 GENERAL DISCUSSION OF RESULTS 264

11.1 Summary of Structural Results 264

11.2 Electronic Origin of the Structural Deformations 270

11.3 Metal Atom Clusters and Localisation of Charge 271

11.4 Deformation Waves and the Kohn Anomaly 274

11.5 Fermi Surface Images in the Octahedral Materials 275

11.6 Fermi Surface Images in the Trigonal Prismatic Materials 280

11.7 Inelastic Neutron Scattering Results 282

11.8 Temperature Dependence of Charge-Density Wave Vector 286

11.9 Transitions to Commensurate Superstructures 287

11.9.1 Materials with Octahedral Co-ordination 290

11.9.2 Energy Gaps at the Fermi Level 291

11.9.3 Materials with Trigonal Prismatic Co-ordination 293

11.9.4 1T Tantalum Disulphide 294

11.10 Displacements of Anions and Stacking of Charge-Density Waves 297

11.11 Supporting Evidence from Doping and Intercalation Experiments 298

11.11.1 Doping Experiments 300

11.11.2 Intercalation Experiments 302

11.12 Pressure Measurements and Superconductivity 304

12 FINAL CONCLUSIONS AND FUTURE WORK 307

ACKNOWLEDGEMENTS 314

REFERENCES 315

APPENDIX 1 321

APPENDIX 2 325

APPENDIX 3 334

LIST OF FIGURES

		Page
1	The layer structure of the transition metal dichalcogenides of formula, MX_2.	28
2	Octahedral (a) and trigonal prismatic (b) co-ordination of the metal atom by the chalcogens.	28
3	Plan and section of the structure of a layer material with the stacking sequence AbC, space group $P\bar{3}m$.	29
4	Plan and section of the structure of a layer material with the stacking sequence AbA CbC, space group $P6_3/mmc$.	30
5	Plan and section of the structure of a layer material with the stacking sequence AbA BaB, space group $P6_3/mmc$.	31
6	Distortion of a hexagonal matrix of metal atoms to give an orthorhombic structure in WTe_2. Increased bond lengths are shown by broken lines.	32
7	Section showing the distorted layer structure of $TaTe_2$. The metal atoms occupy distorted octahedral sites.	33
8	Simplified band structure for the layer materials of Groups IVa, Va, VIa (from Yoffe, 1973).	35
9	Part of APW band structure calculations (from Mattheiss, 1973) showing conduction band and Fermi level for 1T and 2H TaS_2. The inset of the first Brillouin zone for a hexagonal lattice shows the points of high symmetry.	36
10	Magnetic susceptibility data for the tantalum dichalcogenides, compiled from several authors (see text).	38
11	Temperature dependence of resistivity for 1T TaS_2 (Thompson, Gamble, Revelli, 1971), showing the two transitions of interest: $1T_1 - 1T_2$, and $1T_2 - 1T_3$.	39
12	Resistivity data for the tantalum dichalcogenides, compiled from several authors (see text).	41

13	Magnetic susceptibility data for pure and intercalated 2H TaS_2 (Thompson, Gamble and Koehler, 1972).	46
14	Indices for typical hexagonal (trigonal) matrix reflexions; a* and b* are reciprocal axes.	55
15	Relationship of superstructure reciprocal axes to those of matrix structure.	55
16	Indices of a typical group of first order satellite reflexions from superstructure with hexagonal symmetry.	55
17	Pattern of satellite reflexions for parent matrix reflexions with different Bessel function argument (ordinate: geometrical part of structure factor).	57
18	Structure factors for row of reciprocal lattice of structure distorted by a single deformation wave parallel to $\underline{K}$.	58
19	Comparison of commensurate and incommensurate deformation of a 1-D lattice, showing the geometry also of the reciprocal lattice.	60
20	Variation of the signs of the first two contributions to scattering from 3 symmetry-related deformation waves, with the phase ϕ of each wave.	73
21	Pattern of structure factors expected from symmetry-related waves, when the mode is mostly LA.	77
22	Pattern of structure factors expected from symmetry-related waves, when the mode is mostly $TA_{\perp}$.	77
23	Variation of signs of first and second harmonic contributions to scattering, with the phases, ϕ_Q and ϕ_{2Q}.	81
24	Relationship of the wave vectors $\underline{P}_1$, $\underline{P}_2$, $\underline{P}_3$ to the fundamental $\underline{Q}_1$, $\underline{Q}_2$, $\underline{Q}_3$.	82
25	Deformation of 1-D lattice produced by various modulating function discussed in the text.	83
26	Structure factors calculated for a $6\underline{a}$ commensurate deformation in a 1-D lattice.	85

27	Structure factors calculated for an incommensurate deformation in a 1-D lattice of almost the same periodicity as in Figure 26, with which it may be compared.	86
28	Showing the effect of omitting higher Fourier components of the distortion for a group of matrix and satellite reflexions.	87
29	The effect of a perturbing potential δU on the Fermi distribution of electrons.	90
30	Variation of the screening parameter with wave vector $\underline{q}$, showing Kohn anomaly at $\underline{q} = 2\underline{k}_f$.	92
31	The Kohn Anomaly for a spherical Fermi Surface, as the perturbing wave vector $\underline{q}$ is increased through the critical value $2\underline{k}_f$	93
32	The Kohn Anomaly for Surfaces of different shape.	95
33	The form of the Kohn anomaly in the electronic susceptibility χ for a flat sheeted Surface.	98
34	The form of the Kohn anomaly for a Surface with radius of curvature of 15 k_f (Fehlner & Loly 1974)	98
35	The Kohn Anomaly in the phonon spectrum for three general types of Fermi Surface (Afanasev & Kagan).	99
36	Formation of a charge-density wave in response to a perturbing phonon in a 1-D lattice.	103
37	The form of the CDW for a sinusoidal (a) and a sawtooth (b) modulating deformation function.	103
38	Distortion of a lattice produces gaps in the electronic energy band structure.	107
39	An overall lowering of energy for the conduction electrons only occurs when the boundary introduced by the perturbation coincides with the Fermi level.	107
40	Distortion of spherical Fermi Surface in vicinity of energy gap.	108
41	The effect of an energy gap at the zone boundary in narrow and wide band metals (Adler & Brooks, 1967).	110
42	Oscillation X-ray diffraction photograph of TaS_2 (pyridine), showing part of the 10.ℓ row (with 10.9 and 10.22 marked), and part of the 00.ℓ row (with 00.24 and 00.34 marked).	122

43	Comparison of observed and calculated structure factors for the 00.ℓ reflexions (data from Table 5)	124
44	Comparison of observed and calculated structure factor data for the three possible stacking sequences for the 'empty' expanded TaS_2 lattice (data from Table 6).	130
45	Profiles of 01.ℓ reflexions from diffractometer measurements. A typical 00.ℓ reflexion is given for comparison.	131
46	Selected area electron diffraction pattern which shows the pyridine superlattice in one orientation. Reflexions R and S are discussed in the text.	133
47	Accompanying diagram for Figure 46 and 48; (a) and (b) show the pyridine superlattice in one and three symmetry-related orientations respectively. Q and Q' are discussed in the text.	134
48	Oscillation X-ray diffraction pattern showing the superlattice in three orientations (cf. Figure 47b) Reflexion R & S are the same as in Figure 46.	133
49	Centred rectangular cell ($\sqrt{3}a \times 2\frac{1}{2}a$) discussed in the text.	135
50	Coincidence cell for the TaS_2 lattice and the pyridine superlattice.	137
51	$2\sqrt{3}a \times 2\frac{1}{2}a$ pyridine supercell, corresponding to reflexions R and S in Figures 46 & 48.	138
52	Model (a) for parallel orientation of pyridine molecules.	144
53	Model (b) for perpendicular orientation of pyridine molecules.	144
54	Comparison of observed 00.ℓ intensity data with calculated values for the empty host lattice (I_c) and models (a) & (b). Data from Table 9.	147
55	Four simple models for the packing of the pyridine molecules in the interlamellar space (perpendicular orientation), and discussed in the text.	149
56	The stacking change which accompanies the expansion of the layer separation on intercalation with pyridine. The unit cells are also shown.	152

57 The 3 possible stacking sequences for the expanded TaS_2 lattice, showing (a) octahedral, (b) trigonal prismatic, (c) tetrahedral environments associated with an interlamellar site adjacent to a Ta atom in the lower layer. 152

58 Selected area diffraction patterns with incident electron beam parallel to $\underline{c}^*$: (i) $1T_1$ at 340 K, identifying the triangular grouping $\{\underline{S}_M(10.1)\}$ and indicating by arrow one $\underline{S}_M(11.0)$ reflexion near the origin; (ii) $1T_2$ at 290 K, the arrow indicating a $\underline{S}_M(11.0)$ reflexion, and the inset showing a triangular grouping $\{\underline{S}_M(10.1)\}$ when the beam is tilted slightly; (iii) $1T_3$ TaS_2 at 150 K. 157

59 Oscillation X-ray photographs with incident beam in similar orientation to Figure 58 for (i) $1T_1$ at 390 K, (ii) $1T_2$ at 290 K, (iii) $1T_3$ TaS_2 at 80 K. 158

60 Reciprocal cells for each distorted 1T TaS_2 phase, where $\underline{Q}_{i1}$, $\underline{Q}_{i2}$, $\underline{Q}_{i3}$ are distortion wave vectors. In (i) $1T_1$ and (ii) $1T_2$ the unit cell is that of the matrix, satellite reflexions lying both in the hk.0 plane (●) and at $\pm\frac{1}{3}\underline{c}^*$ (○). In $1T_3$ (iii) the commensurate distortions define a reduced reciprocal cell, shown here in projection. 158

61 Oscillation X-ray photographs with incident beam approximately perpendicular to $\underline{c}^*$, and showing part of the matrix 20.ℓ row for each phase, and satellites. This can be compared with patterns predicted by rhombohedral distortion cells in $1T_1$ and $1T_2$, and by twinned triclinic cells in $1T_3$ TaS_2 (see text). The patterns for $1T_1$ and $1T_2$ differ as a result of the change in the orientation of $\underline{Q}$. 160

62 The octahedron of first order satellite reflexions in $1T_1$ and $1T_2$ TaS_2, and its orientation relative to the matrix reciprocal axes. 161

63 Selected area electron diffraction pattern from $1T_2$ TaS_2, with incident beam tilted away from normal incidence. First order satellites are clearly visible. 162

64 Intensity predicted for (a) ordering and (b) distortion mechanisms for the satellite reflexions, for scattering vector $K \lesssim 1$. Also shown: ratio of satellite to parent matrix reflexion intensity. 166

65 Oscillation x-ray photograph of $1T_2$ TaS_2 with incident beam normal to $\underline{c}^*$ (cylindrical camera), and showing the relative increase in satellite intensity parallel to $\underline{a}$ (oscillation axis). Compare the intensities of the satellites indicated by arrow. 168

66 Temperature variation of the satellite reflexions in $1T_2$ TaS_2. 171

67 Hexant of matrix hk.0 plane of reciprocal lattice in $1T_2$ TaS_2. This diagram only showsmatrix and $\{\underline{S}_M(10.1)\}$ satellites for clarity. Radius of satellite is proportional to observed structure factor (Table 17). 178

68 Observed (a) and calculated structure factors for the $\underline{M}$(h0.0) reflexions: (b) for the undistorted TaS_2 matrix, and (c) for the distorted model of the matrix. Also shown is the Ta contribution to the structure factor alone. (Values from Table 11). 181

69 Observed structure factors for first order satellites of $\underline{M}$(h0.0) reflexions, at $\underline{M}+\underline{Q}_1$ and $\underline{M}-\underline{Q}_2$. 184

70 Average values of structure factors for pairs of satellite reflexions of $\underline{M}$(10.0) and $\underline{M}$(11.0) — from Table 13. 188

71 Showing the calculated directions of the deformation wave vectors relative to the distortion amplitudes. 189

72 Second order satellites chosen close to the origin of reciprocal space in order to estimate the second Fourier component of the distortion. 190

73 Observed structure factors for $\{\underline{S}_{h0.0}(11.0)\}$ satellites (radius proportional to structure factor). 191

74 $\{S_{00.0}(11.0)\}$ and $\{S_{10.0}(11.0)\}$ satellites chosen close to origin of reciprocal space in order to estimate magnitude and direction of $\underline{U}_p$. 192

75 Showing the choice of orthogonal reciprocal vectors $\hat{\underline{Q}}$ and $\hat{\underline{P}}$. 195

76 Summary of the computer programme written to calculate structure factors for the model of $1T_2$ TaS_2 with 9 deformation waves. 198

77 Comparison of observed and calculated structure factors for matrix and satellite reflexions (from Table 17). For each matrix reflexion there is a group of six $\{\underline{S}_M(10.1)\}$ reflexions (labelled 1 to 6) and a group of 6 $\{\underline{S}_M(11.0)\}$ reflexions (labelled 7 to 12). The twelve satellites correspond in order to those in Table 17 , and it must be remembered also that they are symmetrically disposed about each matrix reflexion. 202

78 Pattern of displacements in the $1T_2$ TaS_2 distortion cell from nine deformation waves of proposed model. 206

79 Distribution of average density of Ta atoms resulting from the deformation structure of $1T_2$ TaS_2. Broad regions where the density is slightly increased are separated by narrow regions of much decreased density ('gaps'). 206

80 Displacements of the sulphur atoms (positive or negative) in the two layers surrounding the tantalum layer. Note that displacements in both S layers are outward from the Ta layer at the centre of the metal atom cluster (cf Figure 79). 206

81 Comparison of observed and calculated structure factors for $\{\underline{M}(00.\ell)\}$ reflexions (from Table 20). 208

82 Comparison of observed and calculated structure factors for $\underline{S}_{00.\ell}(10.1)$ reflexions (Table 21). The Ta contribution to the s. factor is also given. 208

83 Enlargement from Figure 59 (i) showing $\{S_{20.0}(10.1)\}$ satellites in $1T_1$ TaS_2. 214

84 Stationary X-ray diffraction photograph (beam approximately parallel to $\underline{c}^*$) to show diffuse streaks in $1T_1$ TaS_2. 214

85 Pattern of diffuse scattering in first Brillouin zone of matrix reciprocal lattice. 219

86 (a) S.A.D.P. for $1T_1$ TaS_2 at 420 K, showing diffuse streaking which images the Fermi Surface. All six $\underline{S}_M(10.1)$ satellites are visible because of crystal buckling. (b) Plot of phonon wave vectors which satisfy $\underline{q} \triangleq 2\underline{k}_f$ for Fermi Surface of Figure 110, and are in $TA_\perp$ modes with $|\underline{k}.\underline{U}_q|^2$ large. 220

87 The diffuse streaking can either be described by $TA_\perp$ N-phonons, with wave vector $\underline{Q}$; or as LA U-phonons with wave vector $\underline{Q} + \underline{a}^*$, depending on which matrix reflexion is taken as origin. 220

88 The metal atoms are drawn together into clusters which lie on a $\sqrt{13}\,a \times \sqrt{13}\,a$ superlattice in $1T_3$ TaS_2. 223

89 Showing the indices of the matrix and satellite reflexions from $1T_3$ TaS_2 which are referred to in Table 23. 223

90 Comparison of calculated structure factors for $1T_3$ and $1T_2$ TaS_2. The commensurate and incommensurate models give good agreement at small scattering vector. Observed values for $1T_2$ are also given. 226

91 Microdensitometer traces for matrix and satellite reflexions from all three phases of 1T TaS_2. 228

92 Cluster deformation structures proposed for (i) $1T_1$, (ii) $1T_2$, (iii) $1T_3$ TaS_2, and based on calculations outlined in Chapter 7. Note that the clusters are identical only in $1T_3$ TaS_2. For clarity the structures are drawn with an exaggerated distortion amplitude of 10%. 229

93 Deformation structures based on purely sinusoidal distortion waves, with U_Q = 0.1 a. This should be compared with Figure 92. 230

94 Selected area diffraction patterns from $4H_b$ TaS_2 at (a) about 430 K, (b) about 415 K, and (c) 290 K. Plate (b) is from an area of crystal enclosing transformed and untransformed material. 234

95 Comparison of the form taken by the diffuse scattering in three octahedral materials, and based on electron diffraction data. 238

96 Selected area diffraction patterns from 1T VSe_2 at (a) 290 K, (b) 150 K and (c) about 40 K. 240

97 Selected area diffraction patterns from 2H $NbSe_2$ at (a) 150 K and (b) 16 K. 245

98 Microdensitometer trace along a central reciprocal lattice row, showing two satellite reflexions. 246

99 Normalised intensity (after subtraction of inelastic background) of satellites shown in Figure 98 as a function of reduced temperature. 246

100 Calculated matrix and satellite reflexion structure factors, based on model discussed in text. The variation with h is π out of phase for the satellites relative to the matrix. 248

101 Selected area diffraction patterns from 2H $TaSe_2$ at (a) 290 K, (b) 150 K and (c) about 40 K. (a) and (b) may be compared with Figure 97 (a) & (b). 251

102 Model for $3\underline{a}$ x $3\underline{a}$ distortion supercell in 2H $TaSe_2$ (10% distortion amplitude). In contrast to Figure 92 (iii) it can be seen that it is not possible to incorporate <u>all</u> the atoms in the marked unit cell into the clusters and maintain symmetry. 253

103 Phase-contrast lattice image showing the MoS_2 unit cell in projection (inset shows diffraction pattern and position of aperture). 256

104 Phase-contrast lattice images from β-$MoTe_2$. In (a) the electron beam is incident normal to the layers, while in (b) it is tilted slightly. The inset shows the position of the diffraction aperture for these images. 256

105 Diagram showing part of a single distorted β-$MoTe_2$ layer (from Brown, 1966). Also marked are axes of the monoclinic cell (x,y) and the pseudohexagonal cell (x',y'). The metal atoms, in chains, are drawn shaded, and all atoms are projected on to the plane of the paper. 258

106 The result of adding together the first two Fourier components of a 1-D lattice with phase 0 (A) & $\pi/2$(B). 258

107 Phase-contrast lattice images from $1T_2$ TaS_2 (inset again showing diffraction conditions). In (a) the electron beam is incident normal to the layers, while in (b) it is tilted sufficiently for the fundamental distortion periodicity to be visible. 260

108 Phase contrast lattice image from $4H_b$ TaS_2, with incident beam normal to layers. The inset shows the diffraction conditions. 262

109 Comparison of superlattice adopted by Group Va layer materials below T_d. 268

110 ΓKM section of 1T TaS_2 Fermi Surface as deduced from diffraction measurements (Chapter 7). The parts of the surface imaged in diffraction by $TA_{//}$ phonons (Figure 86) are drawn as solid lines. Parts drawn as broken lines recently confirmed by Yamada et al(1975). $\underline{q}_{i1}$ is the wave vector of the condensed mode in $1T_1$ TaS_2. Points (O) inferred from calculation (Mattheiss, 1973), and (X) from diffraction data (Chapter 6). 275

111 Showing how the Fermi Surface of Figure 110 is very well adapted for 'nesting' as a result of a perturbation of wave vector $\underline{q} = 2\underline{k}_f$. 275

112 ΓKM section of 1T VSe_2 Fermi Surface as deduced from electron diffraction (Chapter 8). The parts of the surface directly imaged are drawn solid. Points (X) are from the diffraction data for the condensed mode. 278

113 Hexant of Brillouin zone summarising the geometry of the Fermi Surfaces of the octahedral materials, as deduced from diffraction. Superlattice periodicities have also been marked. 278

114 ΓKM section of the upper and lower band Fermi Surfaces for 2H TaS_2, as deduced from band structure calculation (Figure 9, Mattheiss, 1973). 279

115 Comparing the Surfaces of octahedral and trigonal prismatic polytypes of TaS_2. Possible superlattice periodicities have been included. 281

116	Alternative construction for deformation wave vector in 2H $NbSe_2$ (from Rice & Scott, 1975).	281
117	Direct observation of the Kohn Anomaly in the phonon spectra from trigonal prismatic layer materials (Moncton et al, 1975).	283
118	Variation in magnitude of incommensurate deformation wave vectors in $1T_2$ TaS_2, 2H $TaSe_2$ and 2H $NbSe_2$. (b) and (c) are from Moncton et al.	285
119	(a) Charge-density distribution in deformation cell resulting from sinusoidal CDWs, and (b) resulting from metal atom clustering.	289
120	(a) In $1T_1$ TaS_2 only the fundamental wave vectors span the Fermi Surface; (b) in $1T_2$ and $1T_3$ apparently the higher harmonics of the distortion <u>also</u> span the Surface. This argues for the stability of the superstructures in these two phases.	289
121	Part of one segment of 1T TaS_2 Fermi Surface at 330 K (a). In (b) more detail is given of the variation of the deformation wave vector in the three distorted phases.	295
122	Variation of Fermi Surface-spanning wave vector with varying concentrations of substituent metal (Wilson et al 1975). Note that q only varies when the dopant is from another Group.	299
123	A possibility for the perturbation wave vector for the pyridine superlattice in intercalated 2H TaS_2, which would couple with CDWs in the host material conduction band.	303

LIST OF TABLES

		Page
1	The transition metals of Groups IVa, Va and VIa which form layer dichalcogenides.	27
2	Summary of structural types for the Group Va dichalcogenides (from Wilson & Yoffe, 1969).	33
3	Summary of structural data for the sulphides and selenides of Group Va transition metals (data from Wilson & Yoffe, 1969, and DiSalvo et al, 1973).	34
4	Transition temperatures, T_d, for the Group Va materials determined from electrical and magnetic measurements.	43
5	Comparison of observed and calculated structure factors for the 00.ℓ reflexions from TaS_2(pyridine).	126
6	Comparison of observed and calculated structure factors for 01.ℓ reflexions from TaS_2(pyridine).	129
7	Calculated structure factors for 00.ℓ reflexions based on model with pyridine molecules parallel to host TaS_2 layers.	145
8	Calculated structure factors for 00.ℓ reflexions based on model with pyridine molecules perpendicular to TaS_2 host layers.	146
9	Comparison of intensity data for selected 00.ℓ reflexions from TaS_2(pyridine) for models with different orientation of the pyridine.	148
10	Variation of deformation wave vector with temperature in 1T TaS_2.	173
11	Observed and calculated structure factors for h0.0 matrix reflexions from $1T_2$ TaS_2, assuming three symmetry-related distortions of amplitude 0.173 Å.	183
12	Determination of U_Q from observed structure factors of $S_{h0.0}(10.1)$ and $S_{h0.0}(\bar{1}0.\bar{1})$ reflexions from $1T_2$ TaS_2.	185
13	Observed structure factors for $\{S_{10.0}(10.1)\}$ and $\{S_{11.0}(11.0)\}$ reflexions from $1T_2$ TaS_2.	188
14	Observed and calculated structure factors for selected $S_{h0.0}(20.\bar{1})$ reflexions from $1T_2$ TaS_2.	190

15 Structure factors for selected $S_{h0.0}(11.0)$ reflexions from $1T_2$ TaS_2. 193

16 Summary of intitial values of the parameters for the deformation cell in $1T_2$ TaS_2. 194

17 Observed and calculated structure factors for $\underline{M}(h0.0)$ matrix reflexions and their satellites; values of parameters chosen to give best overall agreement. 199

18 Structure factors for matrix reflexions and satellites: values of parameters chosen to give best agreement for first order satellites. 200

19 Structure factors for matrix reflexions and satellites: values of parameters chosen to give best agreement for $\{\underline{S}_M(11.0)\}$ satellites. 201

20 Structure factors for $\underline{M}(00.\ell)$ reflexions. Calculated values for a model without TA distortions are also given. 210

21 Structure factors for $\underline{S}_{00.\ell}(10.1)$ satellites. 210

22 Comparison of satellite intensities in $1T_1$ and $1T_2$ TaS_2. 216

23 Calculated structure factors and intensities for hk.0 reflexions from a model for $1T_3$ TaS_2. 225

24 Observed h0.0 structure factors for β - $MoTe_2$ (from Brown, 1966). 257

25 Summary of structural deformation properties of the Group Va layer dichalcogenides. 267

26 Deformation wave vectors and cell basis vectors for hexagonal 2-D superlattices. 267

27 Average interlayer metal atom separations for Group Va layer dichalcogenides. 273

1 INTRODUCTION

1.1 General

The interdependence of the structural and electronic properties of materials is a well-established and important area of study in the field of solid state physics. As such it is very well documented, and both the effects of crystal structure on electronic properties, and the influence of electronic properties on crystal structure are discussed in some detail in standard works, such as those of Brillouin 1946, Mott and Jones 1936, Wilson 1953, Peierls 1969, Kittel 1971, and Ziman 1972.

The transition metal layer dichalcogenides — of general formula MX_2, where M represents a transition metal and X is sulphur, selenium or tellurium — have proved to be a particularly interesting group of materials, in which to study the relationship between crystal and electronic structures. This is partly because their layer structure is suited to strong coupling between the lattice and the electrons, in what may be considered as a two-dimensional system for many purposes. The conduction bands in the metallic materials are furthermore formed chiefly by the overlap of d-orbitals on the transition metal atoms, and are therefore rather marrow. The narrowness of the conduction bands is accentuated by the relatively large interatomic spacings for a metal, and consequently the conduction electron system is very sensitive to any perturbation which leads to a localisation of charge.

The strong bonding within the MX_2 layers, and the weak bonding between layers leads to highly anisotropic mechanical properties also. In particular the crystals readily undergo basal plane cleavage. This property makes them ideally suited

to examination in the electron microscope, and for study by techniques which require ultra-high vacuum cleavage of crystals, such as photoemission. The crystals normally grow as thin hexagonal platelets, and since thermodynamic considerations also make the growth of good, large, single crystals very difficult indeed, the layer dichalcogenides are less than ideal for study by single crystal X-ray and neutron diffraction. The general structural characteristics of the layer dichalcogenides formed by the transition metals of Groups IVa, Va and VIa are summarised in Section 1.2.

The fundamental anisotropy of these materials also manifests itself in their optical, electrical and magnetic properties as one would expect. In those members of the group which are metallic, for instance, the electrical conductivity parallel to the layers is on average an order of magnitude higher than that perpendicular. It is however the Group Va materials which have recently stimulated extra interest by the anomalies which occur in their electrical and magnetic properties, and which cannot be explained on the basis of a regular band scheme. Section 1.3 deals with their electronic properties while section 1.3.2 in particular summarises their anomalous electrical and magnetic behaviour. The review articles by Wilson and Yoffe (1969) and Yoffe (1973) very adequately cover most of the properties of the transition metal layer materials.

In this present study the Group Va layer dichalcogenides are examined over a wide range of temperature by electron and X-ray diffraction, in order to determine whether the electrical and magnetic anomalies have a structural counterpart, and whether the apparent transitions are linked to crystallographic changes. Electron diffraction enables a wide range of crystals to be examined rapidly, while X-ray diffraction is reserved chiefly for detailed study and quantitative measurements.

Preliminary electron diffraction patterns (Wilson and Yoffe, 1969) from 1T tantalum disulphide showed a complex superlattice formation, although X-ray powder diffractograms failed to confirm this, and these results are taken as the starting point for this investigation. The interpretation of the intricate diffraction patterns in terms of complex deformation superstructures requires the development of some further scattering theory, and this appears in Chapter 2. In order to identify the mechanism coupling the structural instabilities observed in diffraction with the anomalous electronic properties, the theory of the Kohn Anomaly (Kohn 1959) and of the formation of charge-density waves (Overhauser 1968) is outlined in Chapter 3.

The experimental work is centred on what proves to be the most remarkable of materials, 1T tantalum disulphide, and the results are presented in Chapters 6 and 7. Diffraction results obtained for other octahedral materials appear in the following Chapter (8), while those for the materials with trigonal prismatic coordination are presented in Chapter 9. Lattice resolution studies on some of the distorted compounds are reported in Chapter 10.

Another fascinating property of the layer materials is their ability to be intercalated by a variety of inorganic and organic species. Some of the earliest intercalation experiments were carried out using graphite as well as molybdenum and tunsten disulphides, when the intercalated species were alkali metals (Rüdorff, 1959). The transition metal dichalcogenides can be intercalated with pyridine and other related compounds (Gamble, DiSalvo, Klemm & Geballe, 1970), and Chapter 5 forms a study of the superstructure of the intercalation complex of pyridine and tantalum disulphide.

The superstructures of the distorted and intercalated Group Va layer materials are extremely interesting, both from a purely structural point of view, and because of their electronic origin; the latter is discussed in some detail in Chapter 11. Chapter 12 attempts to summarise some of the main conclusions and also discusses briefly possible future developments of the work.

1.2 Structural Properties

This study is chiefly concerned with the Group Va transition metal dichalcogenides. However, for the sake of completeness the structural properties of all the Groups IVa, Va and VIa compounds will be summarised. A much fuller account of their structure is to be found in the article of Wilson and Yoffe (1969), who also review their properties in the context of the structure of many other transition metal compounds.

Each MX_2 layer (where M is a transition metal listed in Table 1) consists of a'sandwich'as shown in Figure 1.

IVa	Va	VIa
$\underline{Ti}^{22}$	$\underline{V}^{23}$	(Cr^{24})
$3d^2$	$3d^3$	
$4s^2$	$4s^2$	
$\underline{Zr}^{40}$	$\underline{Nb}^{41}$	$\underline{Mo}^{42}$
$4d^2$	$4d^4$	$4d^5$
$5s^2$	$5s$	$5s$
$\underline{Hf}^{72}$	$\underline{Ta}^{73}$	$\underline{W}^{74}$
$4f^{14}$	$4f^{14}$	$4f^{14}$
$5d^2$	$5d^3$	$5d^4$
$6s^2$	$6s^2$	$6s^2$

Table 1 The Group IVa, Va, VIa transition metals which form layered dichalcogenides (Cr does not do so). The filling of the outer electron shells is also given.

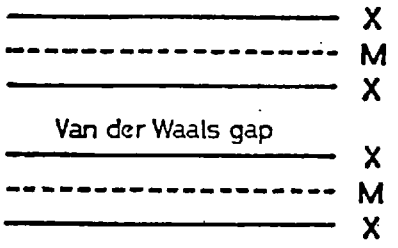


FIGURE 1

Covalent and ionic forces account for bonding within each layer, while van der Waals forces account for bonding between adjacent layers. This leads to strongly anisotropic properties, the most obvious of which being their easy cleavage parallel to the layers.

1.2.1 The Undistorted Materials

In the undistorted (sometimes known as regular) layer dichalcogenides, the metal and the two chalcogen atoms each lie on a hexagonal matrix of sites. The relative positions of the three layers is such that the coordination of the metal by the chalcogens is either octahedral or trigonal prismatic (Figure 2).

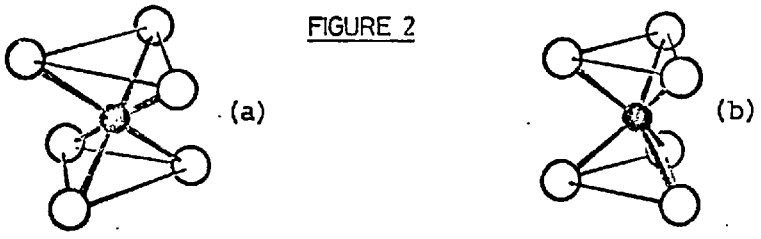


FIGURE 2

It is noteworthy that the high symmetry octahedral co-ordination occurs in a wide variety of compounds, while the lower symmetry trigonal prismatic co-ordination is relatively rare outside these materials. Part of the reason lies in the fact that octahedral co-ordination gives a close-packed structure, while trigonal prismatic gives a less favourable, lower density structure.

Both types of co-ordination imply nevertheless that all atoms lie on one of the three special sites in the 2-D hexagonal cell: (0,0), $(\frac{1}{3},\frac{2}{3})$ or $(\frac{2}{3},\frac{1}{3})$, which will be denoted by the letters A, B, C; a, b, c, as is conventional. Upper and lower case letters will be reserved for non-metals and metals respectively. Greek letters α, β, γ will be used to denote positions in a deformation cell when this becomes necessary. All the undistorted materials have centrosymmetric structures, and many of them belong to either or both of the following space groups at room temperature:

(1) $P\bar{3}m$ (D^3_{3d})

The regular materials with octahedral co-ordination belong to this trigonal group. The metal atoms are situated at the position (0,0,0) and the chalcogens at $\pm(\frac{2}{3},\frac{1}{3},z)$, where $z(\text{ideal}) = \frac{1}{4}$. There is one MX_2 sandwich per unit cell, and the structure type is often referred to as 1T, or as the cadmium iodide structure. The stacking sequence is therefore AbC. The reason that this structure has trigonal rather than hexagonal symmetry derives from the octahedral disposition of the chalcogens about the metal atoms.

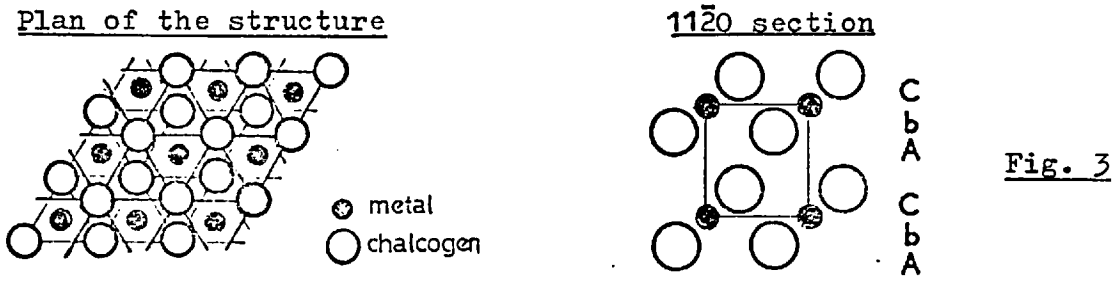


Fig. 3

All the Group IVa compounds and some of the Va compounds belong to this space group. For example:

1T HfS_2 (Greenaway and Nitsche, 1965) - Group IVa

1T VSe_2 (Røst and Gjertsen, 1964) - Group Va.

(2) $P6_3/mmc$ (D^4_{6h})

The regular materials with trigonal prismatic coordination

belong to this space group. There are two MX_2 layers per unit cell, and several stacking sequences consistent with the symmetry. The two sequences assumed by the pure materials are both called 2H; they are:

(a) AbA CbC Here the metal positions are $\pm(0,0,\frac{1}{4})$, and the chalcogen positions are $\pm(\frac{1}{3},\frac{2}{3},z)$ and $\pm(\frac{1}{3},\frac{2}{3},\frac{1}{2}-z)$, where z(ideal) = 0.113. The difference between this structure and that of the octahedral materials lies in the disposition of the chalcogen atoms. It is these which gives a different symmetry and a two-layer structure. The metal atoms in both cases lie on a primitive hexagonal sublattice.

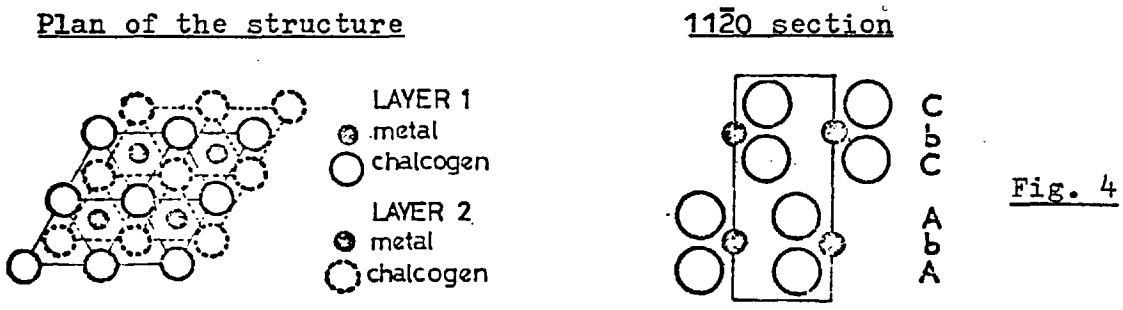


Fig. 4

All the examples of materials with this structure come from Group Va:

2H NbS_2 (Jellinek, Brauer and Muller, 1960),

2H $NbSe_2$ (Brown and Beerntsen, 1965),

2H TaS_2 (Jellinek, 1962),

2H $TaSe_2$ (Bjerkelund and Kjekshus, 1967).

(b) AbA BaB The metal positions are $\pm(\frac{1}{3},\frac{2}{3},\frac{1}{4})$, and the chalcogen positions $\pm(\frac{2}{3},\frac{1}{3},z)$ and $\pm(\frac{2}{3},\frac{1}{3},\frac{1}{2}-z)$, where again z(ideal) = 0.113. It is worth noting that this is the first of the stacking sequences so far considered in which the metal atom positions do not superimpose in successive layers.

This structure is adopted by Group VIa materials:

2H MoS_2 (Wildervanck and Jellinek, 1964)

2H $MoSe_2$ (James and Lavik, 1963)

2H WS_2 (Wildervanck and Jellinek, 1964)

2H WSe_2 (Hicks, 1964).

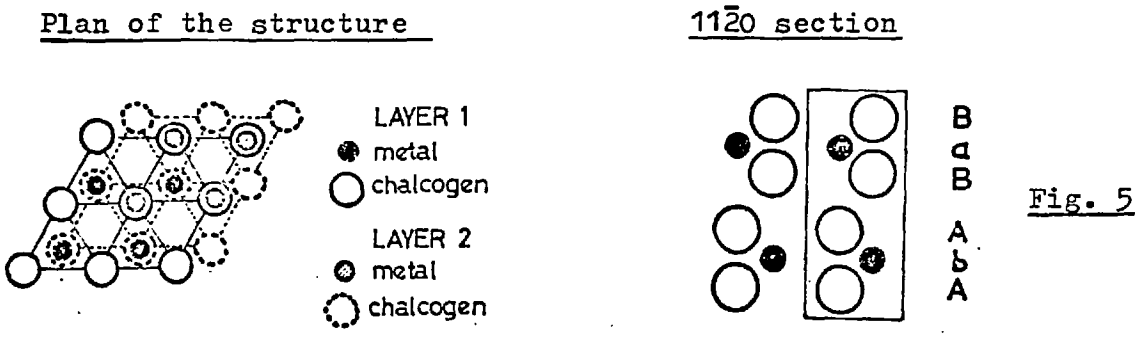


Fig. 5

1.2.2 Other Polytypes of the Undistorted Materials

Some of the materials have other stable polytypes, whose structures are different from those outlined in the previous section. The differences may involve stacking sequence and co-ordination.

There is an alternative stacking sequence, AbA BcB CaC, for the trigonal prismatic materials. This rhombohedral structure which has three MX_2 layers per unit cell, is usually designated 3R. It is a stable polytype at room temperature for the Group VIa dichalcogenides, such as 3R MoS_2 and 3R WS_2. In fact natural molybdenite occurs as a mixture of 2H MoS_2 and 3R MoS_2 .

In different temperature ranges, some of the Group Va materials have stable polytypes with either co-ordination. The 2H polytype is stable for TaS_2 and $TaSe_2$ at room temperature. At higher temperatures (above about 790 °C for the sulphide) the octahedral 1T polytype becomes the stable one. This polytype can also exist as a metastable phase at room temperature by rapid quenching from 800 + °C. This is the phase for which Wilson and Yoffe (1969) report a complex'superlattice' structure.

Depending on growth conditions, crystals with both types

of co-ordination can be obtained. Two common examples are the $4H_b$ and 6R polytypes with respectively the stacking sequences:

AbA CbA CbC AbC,

AbA BcA BcB CaB CaC AbC,

(DiSalvo, Bagley, Voorhoeve & Waszczak, 1973; Jellinek, 1962).

1.2.3 The Distorted Tellurides

Most of the transition metal layer tellurides have distorted structures at room temperature. Molybdenum telluride for example transforms at 850°C from the (undistorted) α-form which has the 2H structure, to the β-form. β-$MoTe_2$ has octahedral co-ordination, but without the CdI_2 structure since the molybdenum atoms in adjacent layers do not superimpose. Both this material & WTe_2 have distorted structures at room temperature. Within each layer, the Mo or W atoms are displaced from the centres of the octahedra so as to give zig-zag chains in which the metal-metal distances are reduced (Brown 1966). The planes of tellurium atoms buckle outwards from the layer where the metal atoms are drawn closer together, and inwards elsewhere. The effect of the distortion on the plane of tungsten atoms in WTe_2 is illustrated in Figure 6. β-$MoTe_2$ has a very similar structure except that the stacking of the layers is very slightly different so that the symmetry is lowered from orthorhombic to monoclinic.

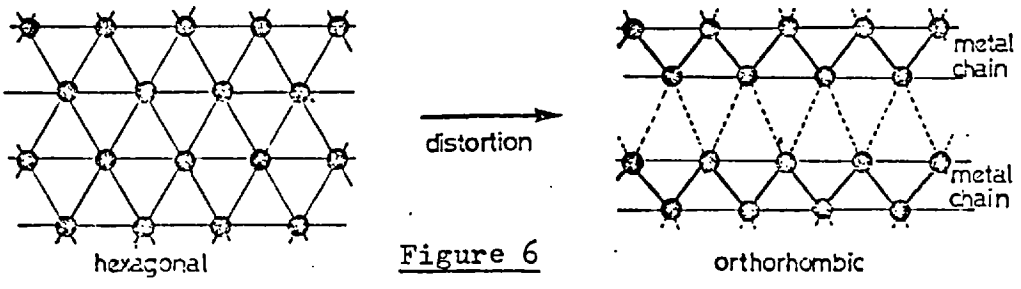


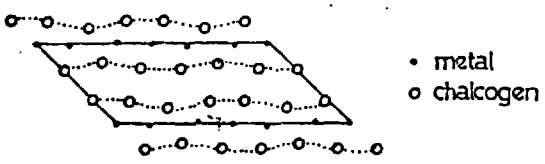
Figure 6

In Group Va, all the tellurides have distorted CdI_2 structures. The general effect of the displacements of the metal atoms in $NbTe_2$ and $TaTe_2$ is somewhat similar to WTe_2, except that the

periodicity of the distortion is 50 % greater so that double zig-zag chains of metal atoms results (Brown, 1966). In Figure 7 the stacking of the layers in $TaTe_2$ is shown. It must be noted that more recent electron diffraction studies, using crystals prepared by cooling pulse heated material, have shown a $\sqrt{19}\,a \times \sqrt{19}\,a$ superlattice structure for these two tellurides, Van Landuyt, Remaut and Amelinckx (1970).

Many of the structural properties of the Group Va layer dichalcogenides are summarised in Tables 2 and 3.

Figure 7



Section showing the distorted octahedral layer structure of $TaTe_2$ (unit cell marked)

Chalcogen / Metal	$-S_2$	$-Se_2$	$-Te_2$
V	Non-stoichiometric, $V_{1+x}S_2$	octahedral (1T)	distorted octahedral
Nb	trigonal prism (2H, 3R)	trigonal prism (2H, 3R)	distorted octahedral
Ta	trigonal prism (2H, 3R) octahedral(1T) mixed (4H, 6R)	trigonal prism (2H, 3R) octahedral(1T) mixed (4H, 6R)	distorted octahedral

Table 2 Summary of structural types for Group Va dichalcogenides, based on Wilson & Yoffe (1969), and not including the results of the present investigation.

Material	Polytype	Stacking	a (Å)	c (Å)
VSe_2	1T	AbC	3.35	6.10
NbS_2	2H	AbA CbC	3.31	2 x 5.945
NbS_2	3R	AbA BcB CaC	3.33	3 x 5.967
$NbSe_2$	2H	AbA CbC	3.449	2 x 6.27
$NbSe_2$	3R	AbA BcB CaC	3.45	3 x 6.29
TaS_2	1T	AbC	3.346	5.86
TaS_2	2H	AbA CbC	3.315	2 x 6.05
TaS_2	3R	AbA BcB CaC	3.32	3 x 5.937
TaS_2	$4H_b$	AbA CbA - CbC AbC	3.332	4 x 5.905
$TaSe_2$	1T	AbC	3.477	6.272
$TaSe_2$	2H	AbA CbC	3.434	2 x 6.348
$TaSe_2$	3R	AbA BcB CaC	3.435	3 x 6.392
$TaSe_2$	$4H_b$	AbA CbA - CbC AbC	3.46	4 x 6.29

Table 3 Summary of structural data for the sulphides and selenides of Group Va transition metals (from Wilson & Yoffe, 1969, where fuller details are given, and DiSalvo et al, 1973).

1.3 Electronic Properties

1.3.1 Electronic Band Structure

As with the metals themselves, the electronic properties of the transition metal layer materials are largely dependent on the characteristics of the narrow d-bands, which lie just above the valence band in the energy band scheme. Once this valence band is full, subsequent electrons must be accommodated in these non-bonding d-bands.

These are formed as a result of overlap between orbitals on neighbouring atoms, which are predominantly d in character. There is very little overlap between metals in different layers,

so that the d-bands are well approximated as 2-dimensional. The width and position of the bands is determined by a variety of factors: interatomic distances, crystal symmetry, ligand electronegativity, the electronic configuration of the atoms. Band character depends on hybridisation, and mixing of metal and chalcogen states.

Band structure calculations, such as those of Mattheiss (1973) which use an augmented plane wave treatment, show that the lower symmetry of the trigonal prismatic co-ordination separates off a separate band from the other d-bands which has d_{z^2} character. With the higher symmetry of octahedral coordination the d-bands all overlap. The difference between Groups IV, V and VI can be illustrated very simply by means of a band scheme (Figure 8, after Yoffe, 1973). No attempt has been made in Figure 8 to show mixing of states.

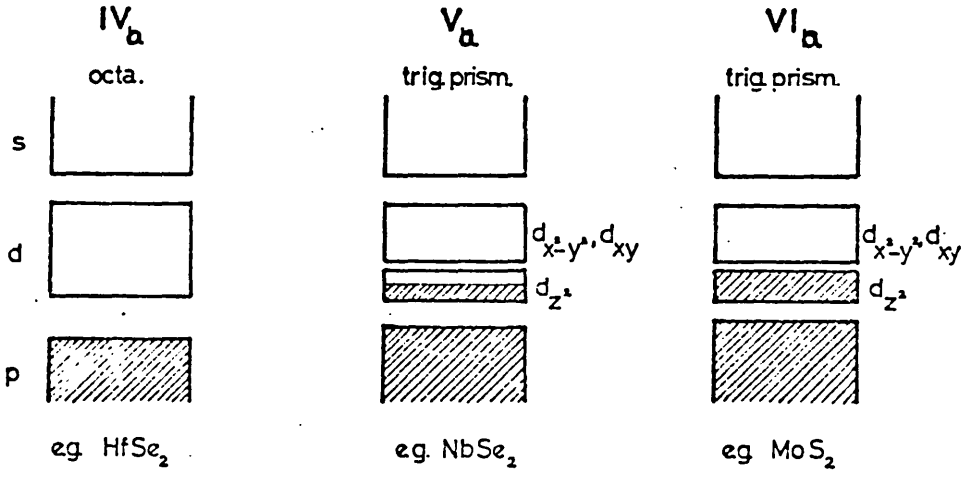


Figure 8

In Group IVa there are no electrons free to enter the conduction d-band; and as this simple model predicts, the sulphides and selenides of zirconium and hafnium are insulating. Apparent exceptions are the titanium compounds, which behave as metals, but this may be due to non-stoichiometry (excess of metal).

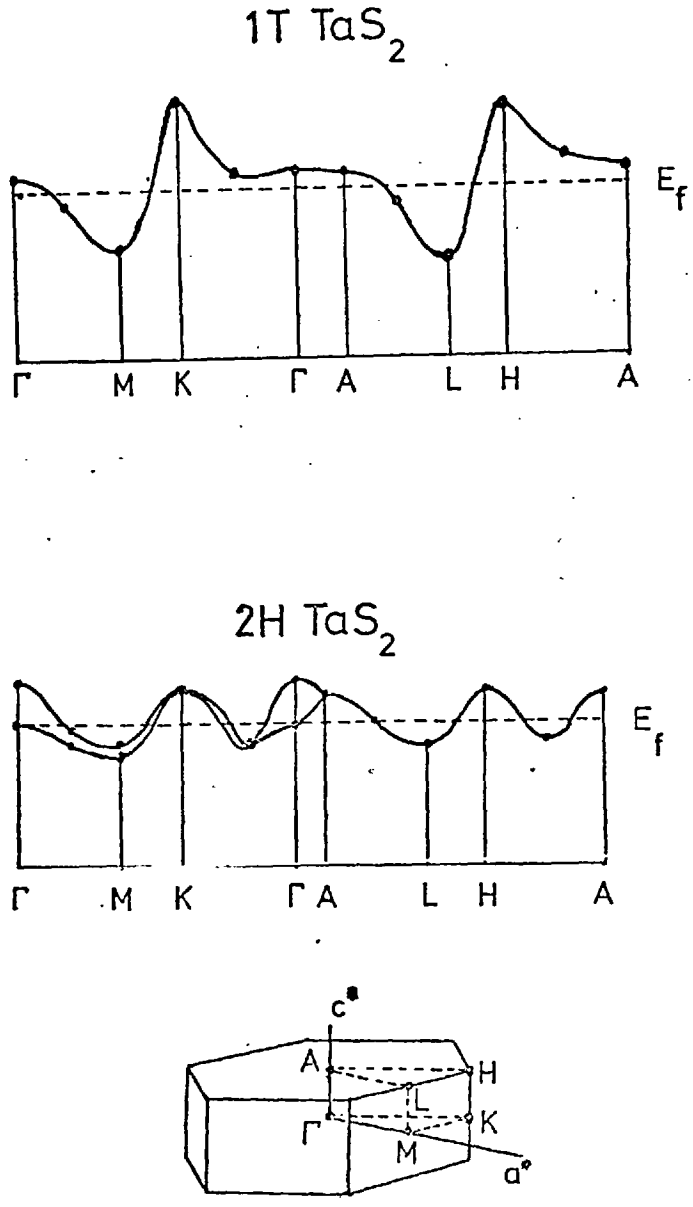


Figure 9 Part of APW band structure calculations (from Mattheiss, 1973) showing conduction band and Fermi level for 1T and 2H TaS_2. The inset of the first Brillouin zone for a hexagonal lattice shows the points of high symmetry.

The Group Va materials with trigonal prismatic coordination also conform well to the predictions of this model. Experiments confirm that these compounds are indeed metallic, with one electron per atom in the conduction band. 1T VSe_2 is a somewhat better metal (i.e. lower resistivity) than 2H $NbSe_2$ at room temperature. This bears out the fact that the single electron in the octahedral material occupies a wider band (cf. band scheme for Group IVa) because of the higher symmetry. The d_{z^2} band is extremely narrow and $NbSe_2$ is consequently a poorer conductor. The octahedral compounds of tantalum exhibit anomalous electrical properties, which make it impossible to fit them into this simple band scheme. At lower temperatures nearly all the Group Va materials (of both coordinations) show some anomalous behaviour, and this is considered in more detail in the next section. In Figure 9 part of the calculated band structure (Mattheiss, 1973) is reproduced for an octahedral (1T TaS_2) and for a trigonal prismatic (2H TaS_2) member of Group V, so as to show the conduction band.

The undistorted materials of Group VIa are semiconductors, and this bears out the model of Figure 8 which predicts just this, with a full 2-electron d_{z^2} band separated by a small energy gap from the rest of the d-bands.

1.3.2 Electrical & Magnetic Measurements

The layer dichalcogenides have been studied by a large number of workers in different laboratories, with the result that there is a wealth of electrical and magnetic data in the literature. Much of it is reviewed by Wilson & Yoffe (1969) and Yoffe (1973). In this section, only those measurements which are of specific interest to the present work will be included. The emphasis will therefore be on some of the anomalous results.

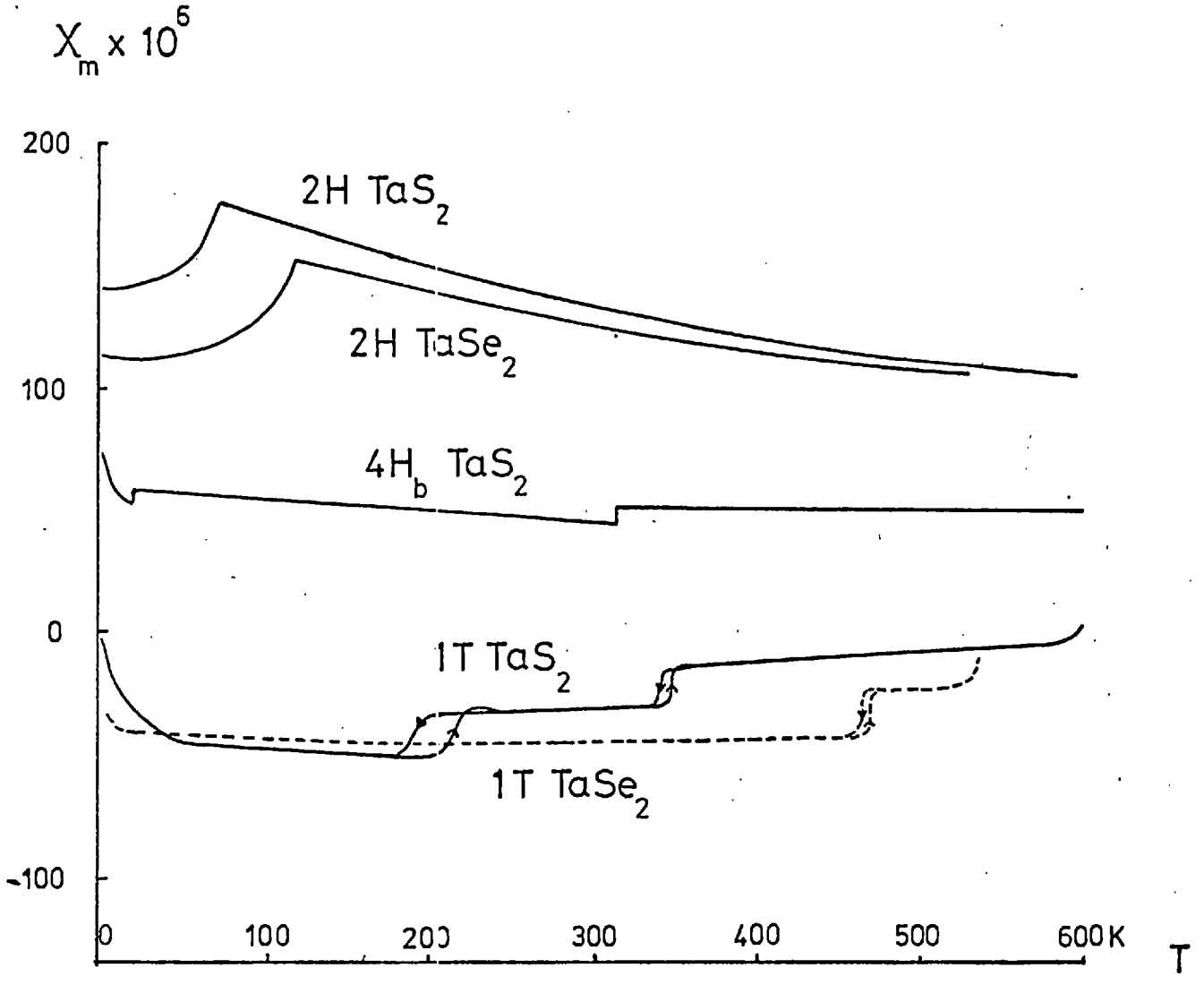


Figure 10 Magnetic susceptibility data for the tantalum dichalcogenides, compiled from several authors (see text).

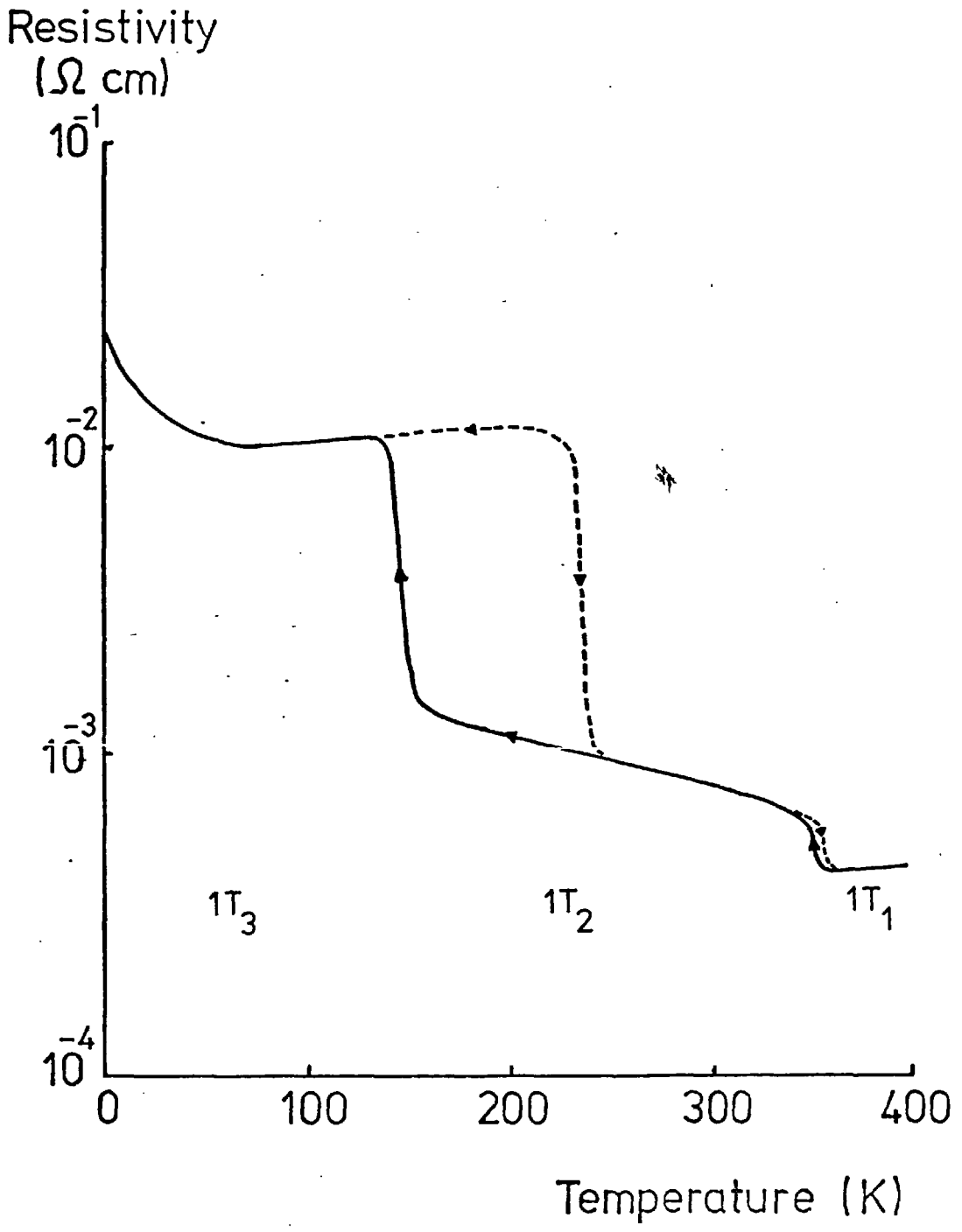


Figure 11 Temperature dependence of resistivity for 1T TaS_2 (Thompson, Gamble, Revelli, 1971), showing the two transitions of interest: $1T_1 - 1T_2$, and $1T_2 - 1T_3$.

Most of the data of interest is for the tantalum dichalcogenides, and Figure 10 summarises magnetic susceptibity data from several authors: DiSalvo, Bagley, Voorhoeve, Waszczak (1973); DiSalvo, Maines, Waszczak (1974); Thompson, Gamble, Koehler (1972). No correction for core diamagnetism has been made. The band models discussed in the previous section predict that the Group Va materials should have a high density-of-states at the Fermi level and be paramagnetic. The 2H compounds are fairly consistent with this, apart from anomalous behaviour at low temperatures, but the 1T and $4H_b$ polytypes show an anomalously low susceptibility, and both 1T polytypes are diamagnetic over the majority of the range of temperature studied. Thompson, Gamble and Revelli (1971) in fact report a paramagnetic → diamagnetic transition on cooling 1T TaS_2 through 315 K. Van Landuyt, Van Tendeloo & Amelinckx (1974) detected this during the course of their electron diffraction studies. There is evidence of phase transitions in all the materials, but of different character in the 2H materials from the 1T.

The transitions are even more striking in resistivity data. The most dramatic behaviour is observed in 1T TaS_2, which has two distinct transitions (Figure 11), Thompson, Gamble and Revelli (1971). Figure 12 combines this data with resistivity measurements for other tantalum dichalcogenides (DiSalvo, Maines, Waszczak, 1974; DiSalvo, Bagley, Voorhoeve, Waszczak, 1973; Thompson, Gamble, Koehler, 1972.

In both 1T TaS_2 and 1T $TaSe_2$ there are sharp first order transitions. The lower of the two transitions in the sulphide has irremovable hysteresis in both resistivity and susceptibility data. While the selenide apparently returns to metal-like behaviour at low temperatures (the criterion being the slope of the resistivity curve), 1T TaS_2 exhibits quite different

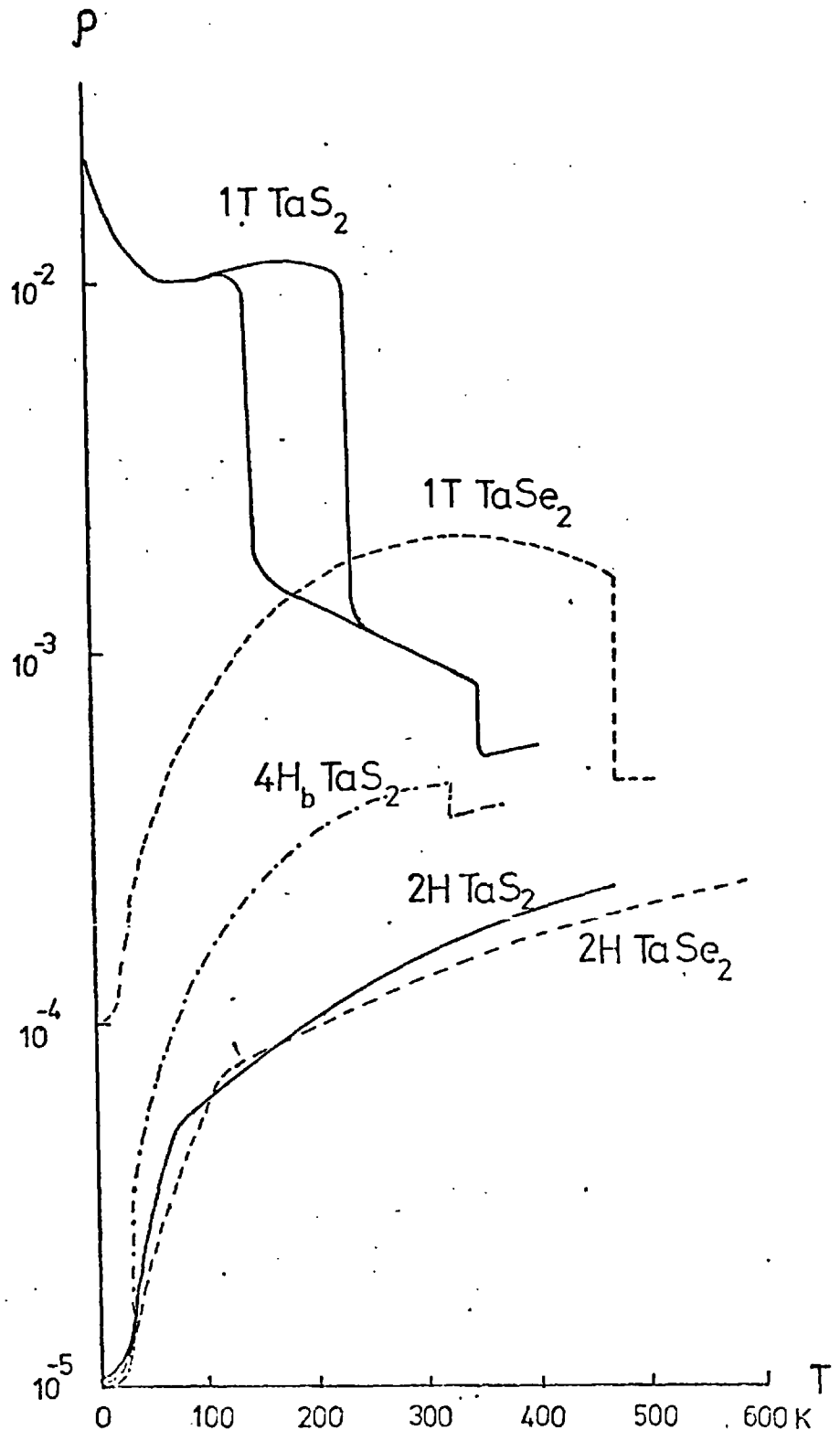


Figure 12 Resistivity data for the tantalum dichalcogenides, compiled from several authors (see text).

behaviour. Its resistivity increases as the temperature is lowered in $1T_2$ and $1T_3$ (notation as in Figure 11); behaviour more reminiscent of a semiconductor, as originally pointed out by the authors, Thompson, Gamble and Revelli (1971). It is however not possible to fit a simple Arrhenius plot to the results, and the conduction process must therefore be a complex one, with some form of enhanced carrier scattering, since the number of carriers is in fact relatively high (Thompson et al 1971). Indeed, infra-red reflectivity measurements (Benda, 1974) show that the normal Drude free-carrier scattering is absent in 1T TaS_2, and only appears on substantial doping with titanium.

While the conductivity immediately below the transitions decreases in the 1T polytypes, the conductivity by way of contrast improves in the 2H polytypes. There is also a difference in the form of the transitions: while they are first order in the 1T polytypes (low temperature one in the sulphide) they appear to be second order in the 2H. There is also a difference between the chalcogens which can be detected: the transition generally takes place at a higher temperature when sulphur is replaced by selenium.

As it might be expected for a polytype with alternate octahedral and trigonal prismatic layers, the susceptibility and resistivity of $4H_b$ TaS_2 are intermediate between those of 1T and 2H. The higher transition in the mixed polytype is similar in character to that in 1T $TaSe_2$ and therefore might be supposed to take place in the octahedrally coordinated layers. The data suggest in addition a weaker transition in the trigonal prismatic layers at low temperatures, by a similar reasoning.

Anomalous electrical behaviour is also found in 2H $NbSe_2$ (Lee, Garcia, McKinzie & Wold, 1970). There is a reversal in the sign of the Hall coefficient at about 26 K. Confirmatory evidence

for some form of structural transformation at this temperature comes from the anomaly in NMR data (Valic, Abdolall and Williams 1974) also detected in pure crystals of the compound.

1T VSe_2 shows evidence of a transformation at 105 K, from NMR Knight shift measurements (Silbernagel, 1974).

The temperatures (T_d) at which these various anomalies occur are summarised in Table 4:

Material	Coordination	T_d
1T VSe_2	octa.	105 K
2H $NbSe_2$	tr. prism.	26 K
1T TaS_2	octa.	350 K
		190 K
1T $TaSe_2$	octa.	473 K
2H TaS_2	tr. prism.	80 K
2H $TaSe_2$	tr. prism.	120 K
$4H_b$ TaS_2	octa.	315 K
	tr. prism.	20 K

Table 4 Summary of temperatures (T_d) at which anomalous transitions occur in electrical and magnetic data. References to the original work appear in the text.

1.3.3 Superconductivity

Many of the Group Va dichalcogenides are superconductors. The niobium compounds have the highest superconducting transition temperatures (T_c) in the Group: 2H $NbSe_2$ at 7.0 K and 2H NbS_2 at 6.3 K (Van Maaren and Schaeffer, 1966; Grant, Griffiths, Pitt & Yoffe, 1974). DiSalvo (1971) reports that 1T TaS_2 does not superconduct, although earlier measurements (Van Maaren and Schaeffer, 1966) had suggested that it does so, at 0.8 K. In 2H TaS_2, T_c varies considerably according to the quality of the crystals (DiSalvo, 1971), from 1.8 to 4.1 K. 2H $TaSe_2$

superconducts at 0.15 K (Van Maaren and Schaeffer, 1966).

In pressure measurements with the niobium dichalcogenides, Grant, Griffiths, Pitt & Yoffe (1974) have shown an interesting difference between the selenide and the sulphides (2H and 3R). Only 2H $NbSe_2$ shows an increase in T_c with increasing pressure. In the sulphides, T_c remains constant.

1.4 Intercalation

In common with other layer materials, many of the Group Va dichalcogenides can be intercalated with alkali and other metals, and with organic molecules. For a quite recent review of intercalation in these compounds, see Yoffe, (1973).

Intercalation by alkali metals is best understood in terms of charge transfer. When sodium, for instance, enters the interlamellar space, it donates electrons to the host lattice, which fill empty states in the conduction d-bands. The half-filled d_{z^2} band in a Group Va material with trigonal prismatic co-ordination fills up therefore, so that it begins to resemble a Group VI semiconductor. In intercalation complexes with Group VIa materials, electrons from the sodium must occupy the next band up in energy above the already full d_{z^2} band. Thus changes from semiconducting to metallic behaviour as well as the reverse can be obtained by intercalation (see Omloo and Jellinek, 1970; Acrivos, Liang, Wilson & Yoffe, 1971; Somoano, Hadek and Rembaum, 1973). Evidence for the ordering of the intercalated alkali metals on a superlattice has been obtained by Carter and Williams (1972).

The intercalation of layer compounds with organic nitrogen compounds can also be explained in terms of charge transfer. Gamble, Osiecki and DiSalvo (1971) report that 2H NbS_2 and 2H TaS_2 form analogous series of organic intercalation complexes.

They were however unable to prepare them for MoS_2 or WS_2. This is consistent with charge transfer only being able to take place from the nitrogen lone pair to a partially filled band. Alkali metals are not restricted as much in their intercalation complexes, presumably because their ionisation occurs with a greater release of energy.

In a series of experiments with a wide variety of intercalation complexes of Lewis bases and Group Va materials, Gamble, Osiecki, Cais, Pisharody, DiSalvo & Geballe (1971) showed that the interlayer separation increases only very slightly with aliphatic chain length, when the length is small. They interpreted this as indicating that the chains lie parallel to the layers. In this configuration, increasing the chain length reduces the number of amine groups per TaS_2 formula unit, and correlated with this, they discovered a progressive decrease in the superconducting transition temperature. For larger chain lengths in the alkyl amines, the increase in interlayer separation is approximately proportional to the length, indicating that the molecules are now oriented perpendicular to the layers. Under these conditions, the superconducting transition temperature remains constant. One explanation for this behaviour of T_c is that charge transfer (assumed proportional to the number of amine groups per TaS_2 formula unit) raises the Fermi level in the host material, with a consequent reduction in the density-of-states (assumed to be a maximum when the band is half filled).

Gamble, DiSalvo, Klemm and Geballe (1970) proposed that in its superconducting complex with 2H TaS_2, the pyridine molecules were oriented perpendicular to the layers of the host lattice. However, in a more recent paper, Gamble, Osiecki and DiSalvo (1971) suggested rather that the pyridine molecules were

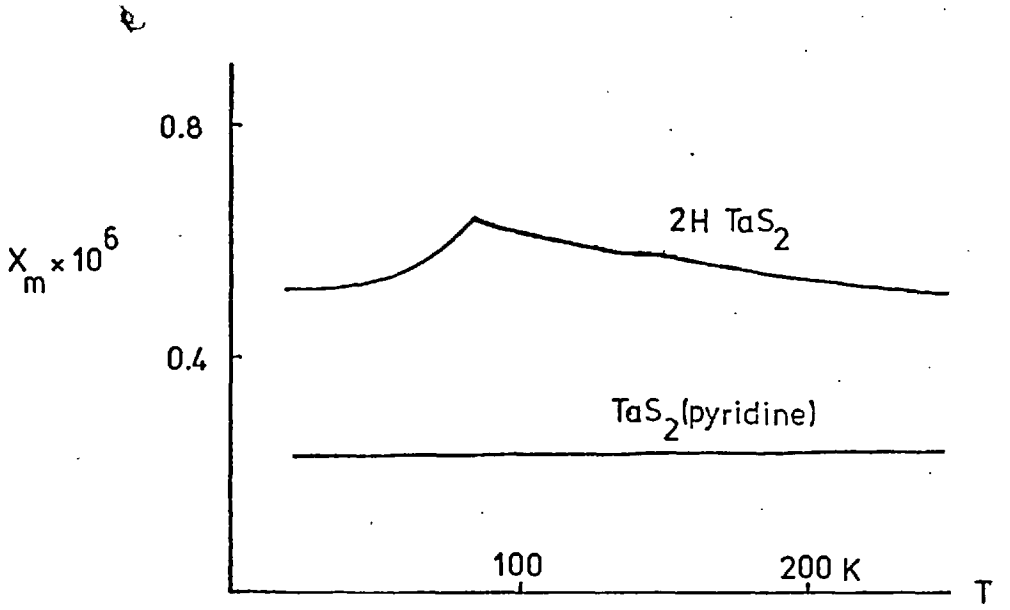


Figure 13 Magnetic susceptibility data for pure and intercalated 2H TaS_2 (Thompson, Gamble and Koehler, 1972).

oriented parallel to the layers. They based their conclusion chiefly on the results of a comprehensive series of intercalation experiments using pyridine molecules, which had a wide variety of substituent groups. All the substituted pyridine complexes (and some of the substituent groups were relatively bulky) produced approximately the same expansion of the van der Waals gap as pure pyridine. The authors noted however the presence of two phases in $TaS_2(pyridine)_{\frac{1}{2}}$ from their measurements of the c-axis expansion. Further experiments (Thompson, 1974) have confirmed that there are two possible phases resulting from this intercalation. The more stable and ordered phase, with $c = 2 \times 12.01$ Å, apparently is produced in the presence of excess sulphur. The other phase, with $c = 2 \times 11.85$ Å, is less stable and somewhat disordered: it is produced when there is a deficiency of sulphur, for instance by the reaction of the pyridine with sulphur from the host lattice.

Of particular interest to this investigation are the results of Thompson, Gamble and Koehler(1972) obtained with the same intercalation complex of pyridine with 2H TaS_2. They show that intercalation removes the magnetic susceptibility anomaly (Figure 13) and also the resistivity anomaly, which are present in pure 2H TaS_2.

Other evidence for a charge transfer mechanism in intercalation by organic nitrogen compounds, includes the change in electric field gradient at the niobium nucleus in NbS_2 when it is intercalated with pyridine (Ehrenfreund, Gossard and Gamble, 1972). There is also a change in free carrier absorption resulting from intercalation with organic species, measured by Beal and Liang (1973).

2a x 2a superlattices have been detected in the complexes of pyridine and aniline with $NbSe_2$ (Williams and Robinson, 1973) and of aniline with 2H $TaSe_2$ (Beal and Liang, 1973).

2 SCATTERING OF RADIATION BY SUPERSTRUCTURES

This Chapter deals mainly with the theory of scattering by superstructures. It is however convenient first to consider the general case of a regular lattice of atoms, and apply this to layer structures, before progressing to the various types of superstructure . The approach to scattering theory generally speaking follows that of Ziman (1972).

As far as possible upper case letters, e.g. $\underline{K}$, $\underline{Q}$, $\underline{M}$, $\underline{S}$, will be used for vectors in the reciprocal lattice whose basis is $\underline{a}^*$, $\underline{b}^*$, $\underline{c}^*$, where $\underline{a}^*$, etc, are defined in the conventional crystallographic way, i.e. $\underline{a}^* = \frac{\underline{b} \wedge \underline{c}}{\underline{a}.\underline{b} \wedge \underline{c}}$.

Lower case letters will be used according to the following definition: $\underline{k} = 2\pi\underline{K}$, $\underline{q} = 2\pi\underline{Q}$, etc..

2.1 Scattering by a Regular Lattice of Atoms

If the basis vectors of the lattice are $\underline{a}$. $\underline{b}$. $\underline{c}$. then any primitive lattice vector can be written

$$\underline{r} = \underline{\ell} = u\underline{a} + v\underline{b} + w\underline{c} \qquad \text{where u,v,w are integers.}$$

If the charge-density surrounding each atom is $V(\underline{r})$ and atoms are situated at lattice points, then the total charge-density scattering radiation is:

$$\rho(\underline{r}) = \sum_{\ell} V(\underline{r}).\delta(\underline{r} - \underline{\ell}) \qquad \delta(\underline{r}) \text{ is Dirac } \delta\text{-function}$$

Assuming that the Born Approximation holds (the situation is therefore one of kinematical scattering), then the pattern of diffracted radiation is given by the Fourier Transform of $\rho(\underline{r})$:

$$\rho(\underline{K}) = \int \rho(\underline{r}) \exp(2\pi i \underline{K}.\underline{r}) d\underline{r}$$

$$= \frac{1}{N} \sum_{\ell} V(\underline{K}) \exp(2\pi i \underline{K}.\underline{\ell}) \quad .....(1)$$

Here $\underline{K}$ is the scattering vector, N is the number of unit cells in the crystal, and $V(\underline{K})$ is the Fourier Transform of $V(\underline{r})$, also called the atomic scattering factor.

In the limit as $N \to \infty$, then

$$\rho(\underline{K}) \quad \to \quad V(\underline{K})\ \delta_{\underline{K},\underline{M}}$$

where $\underline{M} = h\underline{a}^* + k\underline{b}^* + \ell\underline{c}^*$ is a reciprocal lattice vector, and where

$$\underline{M}.\underline{\ell} \quad = \quad hu + kv + lw$$

If each unit cell of the crystal contains I atoms, at positions $\underline{x}_i = (x_i, y_i, z_i)$ within the unit cell, such that:

$$\underline{r}_i \quad = \quad \underline{\ell} + \underline{x}_i \ , \quad i = 1,2,.....I,$$

Then
$$\rho(\underline{K}) \quad = \quad \sum_i V_i(\underline{K})\ \exp(2\pi i \underline{K}.\underline{x}_i)\ \ \delta_{\underline{K},\underline{M}}$$

and $V_i(\underline{K}) = f_i$ is the scattering factor of the atom at position $\underline{x}_i$.

This can alternatively be written as the structure factor of the reflexion $hk\ell$:

$$F(hk\ell) \quad = \quad \sum_i f_i\ \exp(2\pi i(hx_i + ky_i + \ell z_i)) \quad .... \ (2)$$

2.2 Diffraction by a Layer Material

2.2.1 Stacking of the Layers

When considering a layer material it is often very convenient to take a single layer and the scattering from it, and then to work out the effect of stacking identical layers to give the complete structure.

The lattice vectors $\underline{a}$ and $\underline{b}$ are assumed to lie within the layer so that $\underline{c}^*$ is perpendicular to it. In the regular layer dichalcogenides, which have hexagonal symmetry, $\underline{c}$ is also perpendicular to the layers. Then for a single layer (i.e. one MX_2 'sandwich' of a layer dichalcogenide):

$$\rho(\underline{K}) \quad = \quad \sum_i V_i(K)\ e^{2\pi i \underline{K}_{//}.\underline{x}_{i//}}\ \delta_{\underline{K},\underline{M}_{//}}\ e^{2\pi i \underline{K}_{\perp}.\underline{x}_{i\perp}} \ ... \ (3)$$

The vectors have been resolved into components parallel and perpendicular to the layers, e.g.

$$\underline{M} \quad = \quad \underline{M}_{//} + \underline{M}_{\perp}$$
$$\quad = \quad (h\underline{a}^* + k\underline{b}^*) + \ell\underline{c}^*$$

The expression (3) for single layer scattering shows that the reciprocal lattice is an array of rods parallel to $\underline{c}^*$. The last

factor in the expression modulates the rods in the direction of $\underline{c}^*$, and is unity if all the atoms in the unit cell have $\underline{x}_i = 0$.

Suppose that the layers stack so as to give a n-layer stacking sequence. Then the expression (3) for $\rho(\underline{K})$ must be multiplied by the following factor:

$$\{1 + \exp(2\pi i \underline{K}.\underline{R}) + \ldots + \exp(2\pi i n \underline{K}.\underline{R})\}\ \delta_{\underline{K},\underline{M}_\perp} \quad \ldots\ (4)$$

Here $\underline{R}$ is the stacking vector, and $\underline{M}_\perp = \ell\underline{c}^* = \ell/(n \times \text{interlayer sep}^{n})$ This factor (4) modulates the rods in a direction parallel to $\underline{c}^*$ to give now discrete reflexions.

A convenient example to take is that of the 3R stacking sequence , AbA BcB CaC, adopted by some polytypes of NbS_2 and MoS_2. The three layer stacking vector $\underline{R}$ may be written in terms of the unit cell coordinates, i.e. $\underline{R} = (-\frac{1}{3}, \frac{1}{3}, \frac{1}{3})$. Expression (4) becomes in this case

$$\{1 + \exp(2\pi i/3(-h+k+\ell)) + \exp(4\pi i/3(-h+k+\ell)\}\ \delta_{\underline{K},\underline{M}_\perp}$$

This is zero unless $-h+k+\ell = 3m$, where m is an integer. This condition is the standard one for systematic absences from this lattice.

The situation for the 2H polytypes is rather more complex because the metal atoms and the chalcogen atoms have different stacking vectors.

Another useful separation of variables can be made from equation (2):

$$F(hk\ell) = \sum_i f_i \exp(2\pi i(hx_i + ky_i) \times \exp(2\pi i \ell z_i)$$

i.e. the coordinates of the atoms parallel to and perpendicular to the layers have been separated.

In particular, if $\ell = 0$,

$$F(hk0) = \sum_i f_i \exp(2\pi i(hx_i + ky_i)$$

and the reflexions in the hk0 section of the reciprocal lattice therefore give information about the projection of the unit cell.

2.2.2 Effects of Intercalation

(i) As a result of intercalation and the presence of matter in the interlamellar space, there is a change in the separation of the MX_2 layers, and this is usually although not always an increase. There are generally only very small changes in the interatomic distances within the layers.

If the layer separation increases by a factor α, then in reciprocal space $\underline{c}^*$ is reduced by a factor $1/\alpha$. Thus the proportions of the unit cell and the reciprocal lattice change, while the space group of the host lattice remains unchanged.

(ii) Intercalation may be accompanied by a stacking change of the host lattice, i.e. a change in stacking vector $\underline{R}$. The change may mean that a new space group is adopted by the host lattice, e,g. in the change from a 2H to a 3R stacking sequence. Some space groups however permit more than one possible stacking sequence consistent with the symmetry.

(iii) Even without taking into account any scattering from the intercalated material itself, there are changes in the ihtensities of the matrix lattice reflexions due to effects (i) and (ii).

(iv) Scattering by the intercalated material can have two effects in the diffraction pattern. First, the atoms in the interlamellar space may scatter radiation into the matrix reflexions. The consequent change in intensity could be expected to be most marked for the 00.ℓ reflexions from a hexagonal layer material, since the intercalated material is constrained to lie within the interlamellar spaces which have the same separation as the host MX_2 layers.

(v) Secondly, intercalated material may scatter radiation so as to give reflexions which cannot be indexed on the matrix unit cell, and defining a superstructure for the intercalated material.

2.3 Superstructures

The term superstructure will be used when periodicities and spacings exist in a lattice which are greater than those of the matrix lattice unit cell. The new periodicities arise in general from one of the following:

(i) Periodic fluctuations in density or ordering. This may be of two or more species of atom in the matrix structure, for instance of two components in a binary alloy. It may involve one species of atom in the ordering of vacancies or interstitials in a crystal lattice. A further example is the ordering of intercalated molecules in the interlamellar space in layer materials. There may be short range order giving rise to diffuse scattering of incident radiation, or long range order giving rise to discrete satellite reflexions.

(ii) Periodic fluctuations of atomic positions, i.e. displacements from regular lattice sites. This type of superstructure is of major interest to the current investigation. The displacements may be caused by incoherent phonons in the lattice, when thermal diffuse scattering of radiation results, or by coherent periodic structural distortions which give rise to scattering at discrete points in reciprocal space, i.e. satellite reflexions.

How the two basic types of superstructure are distinguishable in diffraction is considered in detail in sections 6.5 and 7.6. Each however may give superstructures whose periodicities do or do not coincide with a matrix lattice vector. If there is coincidence, thenthe superstructure is said to be commensurate with the matrix structure. The term superlattice will be reserved for this case. What would have been the matrix unit cell in the absence of the superlattice must now be referred to as a sub-cell. Therefore, if ($\underline{A}$,$\underline{B}$,$\underline{C}$,) and ($\underline{a}$,$\underline{b}$,$\underline{c}$) are superlattice and matrix sub-lattice basis vectors respectively, the condition for

commensurateness may be written:

$$\begin{cases} \underline{A} = n_{11}\underline{a} + n_{12}\underline{b} + n_{13}\underline{c} \\ \underline{B} = n_{21}\underline{a} + n_{22}\underline{b} + n_{23}\underline{c} \\ \underline{C} = n_{31}\underline{a} + n_{32}\underline{b} + n_{33}\underline{c} \end{cases} \quad \ldots\ldots (5)$$

where the n_{ij} are integers. Equivalent relationships which can be derived from these, exist between the reciprocal lattice vectors.

In the case of intercalation, there may be both a matrix sub-cell and an intercalate sub-cell. Here the supercell is defined as the smallest coincidence cell between the two structures.

An incommensurate superstructure is one for which finite integers, n_{ij}, cannot be found to satisfy the equations (5). This condition, that the superstructure periodicities never coincide with a matrix periodicity, is very difficult to satisfy in practice. Clearly a commensurate superlattice with a very large coincidence cell, and an incommensurate superstructure are barely distinguishable. In general it is only possible to say that a superstructure is incommensurate within a certain range, depending on the accuracy of experimental observation.

Electrostatic and geometrical considerations usually ensure that an ordered superlattice is commensurate and has a relatively small coincidence cell. The energy balance between commensurate and incommensurate deformation structures is more delicate, and both kinds may be favoured under the appropriate circumstances.

2.3.1 Indexing Commensurate Superstructures

The satellite and matrix reflexions can together be indexed using the supercell which they define. However it is often convenient to be able to distinguish reflexions corresponding to the matrix sub-cell, especiialy since these are often noticeably different in character in the diffraction pattern. The matrix reflexions are defined by a relationship between the indices,

and for example for the 2-D $\sqrt{13}a \times \sqrt{13}a$ superlattice (chapters 6 and 7) this is that $4h + k = 13n$, where n is an integer. Reflexions for which this relationship fails to hold are referred to as superlattice reflexions.

In the case of an intercalated structure it is often more convenient to index the host matrix and the intercalate lattice reflexions separately than to use the coincidence cell. The notation $\underline{M}(hk\ell)$ and $\underline{In}(hk\ell)$ will be used for matrix and intercalate when a distinction needs to be drawn.

2.3.2 Indexing Incommensurate Superstructures

In a structure subjected to incommensurate periodic deformation, a distinction always has to be made between the matrix and deformation cells. $\underline{M}(hk\ell)$ and $\underline{S}_M(hk\ell)$ will therefore be used to distinguish the indices of the matrix and satellite reflexions. This notation readily enables any satellite reflexion to be identified. Furthermore, $\underline{M}$ and $\underline{S}_M$ are also interpreted as reciprocal lattice vectors, $\underline{M}$ being the vector from the origin to the matrix reflexion, and $\underline{S}_M$ from the matrix reflexion to the satellite. Thus the scattering vector for the satellite reflexion $\underline{S}_M$ is:

$$\underline{K} = \underline{M} + \underline{S}_M$$

This notation allows the indices of the matrix reflexion to be included, i.e. $\underline{S}_{hk\ell}(h'k'\ell')$ is the satellite associated with the parent matrix reflexion $\underline{M}(hk\ell)$ and indexed $h'k'\ell'$ on the deformation cell.

The materials under consideration have hexagonal or trigonal matrix cells and deformation cell mostly, and it is convenient here to apply this notation to such systems in more detail. In Fig. 14, which shows one choice for the orientation of the hexagonal reciprocal axes, some typical matrix reflexions have

been indexed:

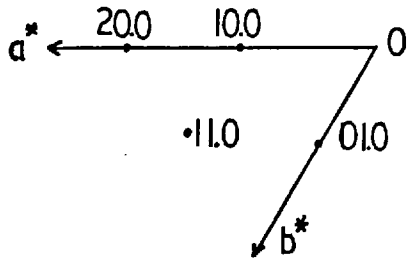


Fig.14

The reciprocal axes will generally be chosen as shown in Fig. 15 (i.e. $\underline{a}^{*\prime}$, $\underline{b}^{*\prime}$), although their precise orientation relative to the matrix reciprocal axes ($\underline{a}^*$, $\underline{b}^*$) depends on the material under study:

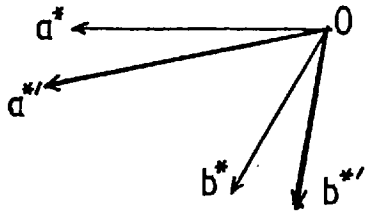


Fig.15

Thus a typical cluster of reflexions $\underline{S}_M$ may be indexed as in the following Figure:

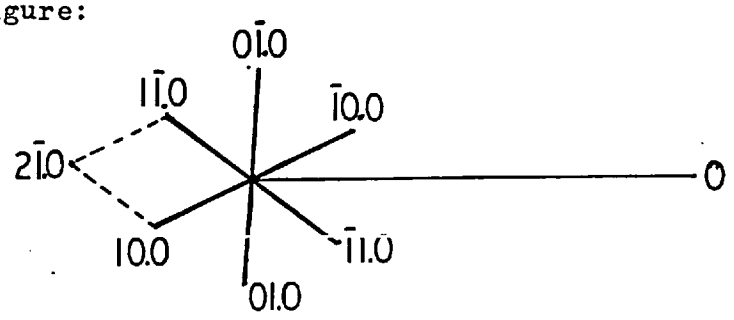


Fig.16

2.4 Single Periodic Distortion of a Lattice

Because of its importance to the present investigation, the theory of the diffraction effects of a distorted structure will be discussed in some detail. The theory will develop from the simplest case of a monatomic lattice deformed by a single periodic distortion as discussed by other authors (e.g. James 1948, Overhauser 1971, Ziman 1972, Korekawa 1967), to the relatively complex situation which obtains in the transition metal dichalcogenides. In these materials the unit cell contains more than one species of atom, there is whole series of symmetry related distortion waves (see section 2.5), and the deformation profile is no longer sinusoidal (2.6).

The theory will not include time dependent terms, largely because X-ray and electron diffraction are not sensitive to this

dependence. However, the question of phase coherence will be considered (section 2.5.1) and this is related to whether a deformation wave is static or in motion (i.e. a phonon). Initially phase coherence will be assumed to exist between the deformation waves, and at this stage the words 'distortion', 'deformation wave' etc. will be used to include static and dynamic situations. The diffraction consequences of an incommensurate distortion wave becoming commensurate with the matrix lattice will also be considered.

2.4.1 Distorted Monatomic Lattice

Suppose that a monatomic lattice is deformed by a periodic disturbance of wave vector $\underline{Q}$ and vector amplitude $\underline{U}_Q$. ($Q = 1/\Lambda$, where Λ is the wavelength of the deformation wave.)

Then the displacement $\delta\underline{r}$ of an atom at the point $\underline{\ell}$ on a lattice defined by the basis $(\underline{a},\underline{b},\underline{c})$ is given by:

$$\delta\underline{r}(\underline{\ell}) = \underline{U}_Q \sin(2\pi i\underline{Q}.\underline{\ell} + \phi_Q) \qquad \ldots (6)$$

where $\underline{\ell} = u\underline{a} + v\underline{b} + w\underline{c}$

The displacement is thus a sinusoidal function of the original position of the atom rather than of the new position. In (6) ϕ_Q is the phase of the distortion in the sense that for a static wave when $\underline{\ell} = 0$, $\delta\underline{r} = 0$ for $\phi_Q = 0$ and $\delta\underline{r} = 0$ for $\phi_Q = \pi/2$. However for an incommensurate situation, only relative phases and changes in phase are important. The choice of ϕ_Q is arbitrary in the case of a single incommensurate wave, but it will remain in the equations to aid later theory.

In order to obtain the scattering at $\underline{K}$, we substitute $\underline{\ell} + \delta\underline{r}$ for $\underline{\ell}$ in equation (1). Thus we have:

$$\rho(\underline{K}) = \left[\frac{1}{N}\sum_{\ell} V(\underline{K}).e^{2\pi i\underline{K}.\underline{\ell}}\right].e^{2\pi i\underline{K}.\underline{U}_Q}\sin(2\pi\underline{Q}.\underline{\ell} + \phi_Q) \qquad \ldots. (7)$$

$$= [\rho(\underline{K})]_o \cdot \sum_{n=-\infty}^{\infty} J_n(2\pi\underline{K}.\underline{U}_Q)\, e^{2\pi i\underline{Q}.\underline{\ell}}\, e^{in\phi_Q}$$

In (7) $[\rho(\underline{K})]_o$ is the pattern of scattered radiation for the undistorted structure, and the following identity has been used to expand the second exponential function:

$$e^{ix\sin\theta} \equiv \sum_{-\infty}^{\infty} J_n(x)\, e^{in\theta}$$

After simplification the expression for $\rho(\underline{K})$ becomes:

$$\rho(\underline{K}) = \sum_n \left\{\frac{1}{N}\sum_{\underline{\ell}} V(\underline{K}).e^{2\pi i(\underline{K}+n\underline{Q}).\underline{\ell}}\right\}\left\{J_n(2\pi\underline{K}.\underline{U}_Q)\, e^{in\phi_Q}\right\}$$

$$= \sum_{n=-\infty}^{+\infty}\left\{V(\underline{K}).\delta_{\underline{K}+n\underline{Q},\underline{M}}\right\}\left\{J_n(2\pi\underline{K}.\underline{U}_Q)\, e^{in\phi_Q}\right\} \quad \ldots (8)$$

in the limit as $N \to \infty$.

This defines a diffraction pattern in which each matrix reflexion at $\underline{M} = h\underline{a}^* + k\underline{b}^* + \ell\underline{c}^*$ is accompanied by an infinite series of satellites at $\underline{M} \pm n\underline{Q}$.

The structure factor of the matrix reflexion (n = 0) is given by:

$$F(\underline{M}) = V(\underline{M}).J_o(2\pi\underline{M}.\underline{U}_Q)$$

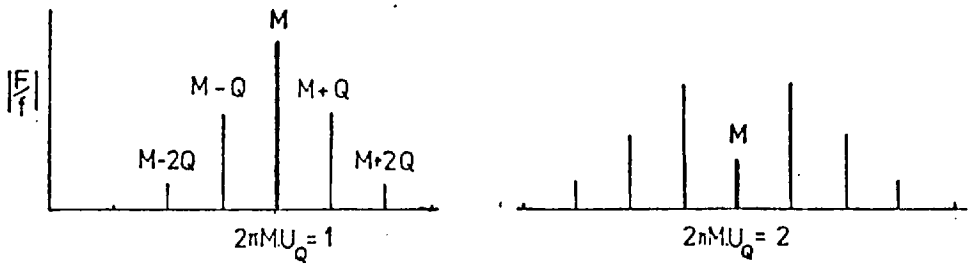
i.e. compared with the undistorted structure it is reduced by a factor $J_o(2\pi\underline{M}.\underline{U}_Q)$ which becomes significant for $2\pi\underline{M}.\underline{U}_Q > 1$.

The structure factor for a satellite reflexion of order n is given by:

$$F(\underline{M} \pm n\underline{Q}) = V(\underline{M} \pm n\underline{Q}).J_{\mp n}(2\pi(\underline{M} \pm n\underline{Q}).\underline{U}_Q)\, e^{\mp in\phi_Q}$$

Since for a given argument, the magnitude of the Bessel Function rapidly decreases with order n, it can be seen that the higher order satellites must be extremely weak. The pattern of satellite reflexions for values of 1 and 2 for the Bessel Function argument are shown in Fig. 17.

Figure 17



Thus the deformation reciprocal lattice is convoluted with the matrix reciprocal lattice, and this is a consequence of the fact that in direct space the deformation periodicty modulates the crystal lattice.

Figure 18 shows a simple example of the diffraction pattern, or rather one row of the reflexions, obtained when $\underline{Q}$ and $\underline{U}_Q$ are both parallel to $\underline{a}^*$, one matrix reciprocal basis vector. In the example $\underline{Q} \triangleq 0.22\underline{a}^*$ and $\underline{U}_Q \triangleq 0.08\underline{a}^*$.

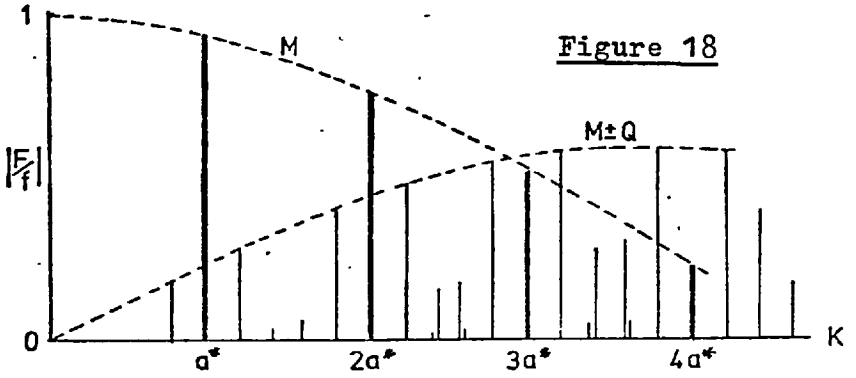


Figure 18

It can be immediately seen that there is considerable overlapping of the clusters of satellites about neighbouring matrix reflexions. The increase in satellite structure factor with K to a maximum close to $K = 4a^*$ is also apparent.

The first order satellite reflexion becomes equal in magnitude to the matrix reflexion when

$$J_o(2\pi\underline{K}.\underline{U}_Q) = J_1(2\pi\underline{K}.\underline{U}_Q)$$

i.e. when $2\pi\underline{K}.\underline{U}_Q = 1.44$

This occurs for $\underline{K} \triangleq 3\underline{a}^*$ for Fig. 18.

2.4.2 Redistribution of Scattered Intensity

For the undistorted lattice the reciprocal lattice intensities are proportional to the square of the atomic scattering factor, f^2, where other factors have been ignored. When the lattice is distorted the matrix intensities are reduced by a factor $[J_o(2\pi\underline{M}.\underline{U}_Q)]^2$. The difference in intensity has been redistributed into the satellite reflexions.

Thus the expression

$$f^2\{1 - [J_o(2\pi \underline{M}.\underline{U}_Q)]^2\}$$

is a measure of the total intensity scattered into all the satellites of a given matrix reflexion $\underline{M}$.

Conservation of energy is assured since from the previous section, equation (7),

$$\rho(\underline{K})^2 = |\rho(\underline{K})|_o^2 \cdot |\exp(2\pi i \underline{K}.\underline{U}_Q \sin(2\pi \underline{Q}.\underline{\ell} + \phi_Q))|^2$$
$$= |\rho(\underline{K})|_o^2$$

2.4.3 Equivalence of Commensurate & Incommensurate Analyses

The analysis given for an incommensurate distortion superstructure in 2.4.1 is quite different from the analysis for the commensurate case where atom positions within a supercell are defined in the conventional way. As it has already been pointed out, it is difficult to distinguish in practice whether a deformation superstructure with very large periodicities is commensurate or not with the lattice. The two analyses, although ostensibly different, should therefore give the same results in the limit as the initially incommensurate distortion wave "locks" on to the lattice. In this limit the Bessel function expressions (see for instance equation (8)) should simplify into the conventional trigonometric functions of structure analysis.

The need to verify that this is indeed so is particularly important as regards the present study, since most of the Group Va layer dichalcogenides undergo incommensurate - commensurate transitions in their distorted phases.

The equivalence of the two approaches will be proved for the simplest distortion model, i.e. a 1-D monatomic crystal (Fig.19).

(a) Commensurate Distortion

If the pericdicity of the distortion is 2a and the atomic displacements are $\pm U$ from their regular sites, then the

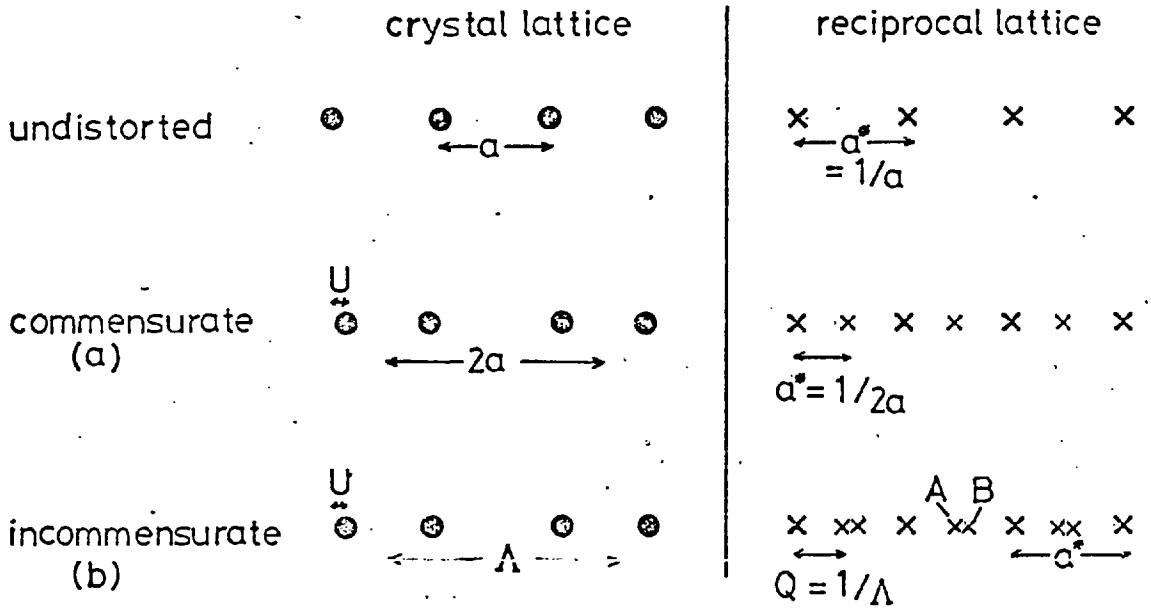


Figure 19 Comparison of commensurate and incommensurate deformation of a 1-D lattice, showing the geometry also of the reciprocal lattice.

fractional coordinates of the atoms in the distorted material are $\pm(\frac{1}{4} - U/2a)$.

Assuming one atom per unit cell, the structure factor of the hth reflexion is

$$F(h) = f\cos(h\pi/2 - h\pi U/a)$$
$$= f\cos(h\pi/2 - 2\pi KU) \qquad \text{since } K = h/2a$$

Therefore:

for h even, i.e.'matrix' reflexions

$$|F(h)| = f\cos(2\pi KU)$$

for h odd, i.e.'superlattice' reflexions

$$|F(h)| = f\sin(2\pi KU).$$

(b) Incommensurate Distortion

The periodicity Λ of the distortion is taken to be very slightly greater than 2a, so that $Q < a^*/2$. The deformation wave can be written:

$$\delta r = U\sin(2\pi \underline{Q}.\underline{\ell})$$

Consider the almost coincident first order satellites A and B of the matrix reflexions M(h) and M(h + 1) respectively (see Fig. 19). The structure factors for A and B are given by:

A: $F(ha^* + Q) = f.e^{\pi ih} J_{-1}(2\pi(ha^* + Q).U)$

B: $F(ha^*+a^*-Q) = f.e^{\pi i(h+1)} J_1(2\pi(ha^*+a^*-Q).U)$

There is in fact an infinite series of satellites in the vicinity of $(h + \frac{1}{2})a^*$. These are of progressively higher order and from parent matrix reflexions further away. For example there is a satellite from the matrix reflexion, $(h - r)a^*$, at

$$K = (h - r)a^* + (2r + 1)Q$$

This has its structure factor given by:

$$F(K) = f.e^{\pi i(h - r)}.J_{-(2r + 1)}[2\pi((h-r)a^* + (2r+1)Q).U] \quad \ldots (9)$$

These are all at least of order 1, and reflexions A and B predominate.

We can add all the structure factors in the vicinity of $(h+\frac{1}{2})a^*$ by summing F(K) , equation (9), over all values of r from $-\infty$ to $+\infty$. We are thereby adding satellite contributions from every matrix reflexion . Now let us consider the limit as $Q \rightarrow \frac{1}{2}a^*$. The scattering vector,K, for every satellite included in expression (9), is given by

$$K \rightarrow (h+\tfrac{1}{2})a^*$$

Thus all the satellites superimpose in this limit. A change in Q such as this, leading to commensurateness, is in fact observed experimentally in for instance $1T_2$ TaS_2 (see section 6.6).

$$\sum_{r=-\infty}^{\infty} F(K) \rightarrow (-1)^h f\left\{\sum_r (-1)^r J_{-(2r+1)}(2\pi K.U)\right\}$$

$$= (-1)^{h+1}.f.\sin(2\pi KU) \quad \text{see Note below}$$

i.e. $$\underline{|F| = f.\sin(2\pi KU)}$$

for the commensurate satellite reflexion

Secondly we consider what happens to the original matrix reflexions. A somewhat similar analysis is followed, there being this time second and higher order satellites of other matrix reflexions in the vicinity of ha^*. For example, from the matrix reflexion at $(h-r)a^*$, there is a satellite at

$$K = (h-r)a^* + 2rQ$$

with structure factor F(K) given by:

$$F(K) = f.e^{\pi i(h-r)}.J_{-2r}[2\pi((h-r)a^* + 2rQ)U]$$

In this case, in the limit as $Q \rightarrow \frac{1}{2}a^*$,

$$K \rightarrow ha^*$$

$$\sum_r F(K) = (-1)^h f\left\{\sum_r e^{-\pi ir} J_{-2r}(2\pi KU)\right\}$$

$$= (-1)^h f\cos(2\pi KU) \quad \text{see Note below}$$

i.e. $$\underline{|F| = f.\cos(2\pi KU)}$$ for the matrix

In the limit as the deformation locks on to the lattice, the analytical expressions become identical with those from the conventional analysis (a).

When the analysis is extended to a 3-D structure with symmetry related deformation waves, in the limit of commensurateness the 3-D clusters of satellites merge together into single superlattice reflexions.

Note: The summations of even and odd order Bessel function series to give cosine and sine functions can readily be obtained from the identity:

$$e^{iz\sin\theta} = \sum_{n=-\infty}^{\infty} J_n(z)\, e^{in\theta}$$

by putting $\theta = \pi/2$ and taking real and imaginary parts.

2.4.4 Choice of Analysis close to Limiting Case

If a deformation wave is truly incommensurate with the matrix lattice, but is sufficiently close to being commensurate that the clusters of satellites referred to at the end of the previous Section (2.4.3) cannot be resolved by the equipment into individual reflexions, then the intensity data obtained by integrating over the whole cluster can be used to refine the positions of the atoms in a conventional superlattice structure. When the satellites are individually resolved, then a Bessel function analysis should be used. Both analyses must lead to similar values for atomic displacements, although the former will have made an approximation to a supercell. Although the fit with experimental data must deteriorate rapidly for $2\pi KU_Q > 1$, the simpler conventional analysis is possibly preferable, provided that the superstructure is sufficiently close to a commensurate superlattice, and that the deformation amplitude is sufficiently small for the approximation to be valid over an appreciable volume of reciprocal space.

For small deformation amplitude and small scattering vector, the first order satellite in each cluster of reflexions will predominate, and only a slightly inferior approximation

results just from measuring the intensity of this.

The alternative problem is also worth consideration, whereby the Bessel Function analysis is used for a long-period ($Q \ll a^*$) commensurate superlattice (cf. Böhm 1975). The same criterion applies, notably that the approximation is valid for $2\pi KU_Q < 1$. This approximation is equivalent to the following:

$$\cos(2\pi KU) \triangleq J_o(2\pi KU)$$

$$\sin(2\pi KU) \triangleq 2J_1(2\pi KU)$$

In this regime, the incommensurate approach gives the amplitudes and directions of the deformation waves more readily, while the commensurate approach is better suited to giving atom positions within a supercell. For a direct comparison of how well both types of analysis can fit a set of experimental data see section 7.1 and Figure 92 in particular.

2.5 Multiple Distortions in a Lattice

In section 2.4 the treatment only allowed for one deformation wave in the lattice. It is necessary in order to interpret the the experimental data obtained for the layer dichalcogenides to develop a somewhat more complex model, involving a whole series of deformation waves with different wave vectors, etc.. In this section therefore the following situations will be studied in detail:

(a) Deformation waves in a polyatomic crystal (2.5.2)

(b) Symmetry related deformation waves (2.5.3)

(c) Deformation waves with different mode (2.5.5)

(d) Higher harmonics of the fundamental distortion (2.6.1, 2.6.2)

(e) Non-sinusoidal deformation waves (2.6.3)

2.5.1 Phase Correlation

First however it is necessary to examine the question of phase.

Whilst the phase factor ϕ_Q introduced in 2.4.1 can be arbitrarily set to zero for a single incommensurate distortion wave, the same is not true for two or more deformation waves. When a number of distortions are together modulating a lattice of atoms their combined effect as observed by diffraction depends very much on the phase factor, since this controls how the scattering contributions add together. Deformation waves whose wave vectors are incommensurate both with one another and with the matrix lattice scatter radiation independently, and will not be considered further here. The distortion waves in the layer materials have wave vectors which are not independent, and which are related by equations of the general form:

$$\sum_{i=1}^{r} n_i \underline{Q}_i = 0$$

where the summation is for all r deformation waves. $\underline{Q}_i$ is the wave vector of the ith deformation, and the n_i are integers.

So if we wish to determine the scattering at $\underline{K} = \underline{M} + \underline{Q}$, we must include scattering both from individual periodic distortions and from all possible combinations such that the sum of the wave vectors is $\underline{Q}$. We therefore consider all possible j combinations which satisfy the following equation:

$$\sum_{i=1}^{r} m_{ij} \underline{Q}_i = \underline{Q} \qquad \text{where the } m_{ij} \text{ are integers.}$$

Details of possible combinations in a hexagonal layer material are dealt with in sections 2.5.3, 2.6.2, 7.3.2.

How these combinations contribute to the scattering depends first on whether there is coherence between the deformation waves, that is whether there is a fixed relationship between the ϕ_Q. Complete incoherence means random phase differences. Here the dynamic and static situations become distinct, for with phonons propagating through the lattice, $\phi_Q = \phi_Q(\underline{r},t)$ for each phonon, and scattering is in general incoherent. With static deformations good phase coherence is expected.

When the scattering from the different deformation waves is incoherent it is the intensities which must be added together. For coherent scattering the amplitudes of the contributions must be added, and due account taken of their phases. In the former case the intensity of radiation scattered by the distortions tends to be distributed evenly over reciprocal space, while in the latter case interference between contributions produces marked variations in satellite intensities.

Most of the treatment which follows assumes that the deformation waves are static, since this is the situation which is observed for the layer dichalcogenides, and that there is coherence, except where stated otherwise. Incoherent scattering of radiation by phonons will be discussed in sections 7.6, 8.2, 8.3, when the diffuse scattering observed in the materials with octahedral co-ordination is interpreted.

2.5.2 Matrix Cell Containing More than One Atom

Suppse that the unit cell contains I atoms, with the ith atom at position $\underline{x}_i$ in the cell. The atoms may be similar or of different species. Then if the deformation of wave vector $\underline{Q}$ displaces the ith atom by a distance $\delta\underline{r}_i$, so that the amplitude and phase of the distortion on the sub-lattice corresponding to the ith atom are U_Q^i and ϕ_Q^i, equation (6) becomes:

$$\delta\underline{r}_i = \underline{U}_Q^i \sin(2\pi\underline{Q}.(\underline{\ell} + \underline{x}_i) + \phi_Q^i)$$

Assuming coherent scattering of radiation from the different atomic species, the total scattering is found by summing equation (8) over all I atoms in the cell, i.e.

$$\rho(\underline{K}) = \sum_{i=1}^{I}\sum_{n=-\infty}^{\infty}[V_i(\underline{K}).e^{2\pi\underline{K}.\underline{x}_i}.\delta_{\underline{K}+n\underline{Q},\underline{M}}].[J_n(2\pi\underline{K}.\underline{U}_Q^i).e^{2\pi in\underline{Q}.\underline{x}_i}\ e^{in\phi_Q^i}]$$

The structure factor of the reflexion at $\underline{K} = \underline{M} \pm n\underline{Q}$ becomes:

$$F(\underline{M} \pm n\underline{Q}) = \sum_{i=1}^{I}[V_i(\underline{M} \pm n\underline{Q})\ e^{2\pi i\underline{M}.\underline{x}_i}]\ [\ J_{\mp n}(2\pi(\underline{M}\pm n\underline{Q}).\underline{U}_Q^i).e^{\mp in\phi_Q^i}] \quad \ldots \quad (10)$$

The term in the first pair of square brackets is the expression for the scattering from the undistorted lattice (cf equation 7). The diffraction pattern is therefore the convolution of the deformation reciprocal lattice with the matrix reciprocal lattice, as for the simpler case of section 2.4.1.

It can be seen in equation (10) that the Bessel Function, $J_n(2\pi\underline{K}.\underline{U}_Q)$ plays a similar role to the atomic scattering factor, $V_i(\underline{K})$, and that the deformation phase factor, $e^{in\phi_Q}$ is equivalent to the geometrical part of the structure factor, $e^{2\pi i\underline{M}.\underline{x}_i}$. While $[V_i(\underline{K}).e^{2\pi i\underline{M}.\underline{x}_i}]$ gives the amplitude of scattering by atoms at positions $\underline{x}_i$ in the matrix unit cell, $[J_n(2\pi\underline{K}.\underline{U}).e^{in\phi_Q}]$ gives the amplitude of scattering by distortions with phase ϕ_Q in the deformation cell.

It is important to note that the factor $\exp(2\pi i\underline{M}.\underline{x}_i)$ occurs in the structure factor of the satellites as well as in the matrix reflexions. The interference between scattering from different atoms in the unit cell should therefore also be observed for the satellite reflexions. The factor, $\exp(in\phi_Q)$, which is additional, means that there may be a phase shift in the interference. If this is applied for the specific case of a transition metal dichalcogenide, whose cell contains a metal atom at the origin, 0, and chalcogen atoms at $\pm\underline{x}$, then the structure factors for the undistorted material are given by:

$$F(\underline{M}) = f_M + 2f_X \cos(2\pi\underline{M}.\underline{x})$$

where the subscripts M and X for the atomic scattering factor, f, refer to metal and chalcogen atoms respecitively.

When this material is deformed by a periodic distortion of wave vector $\underline{Q}$, and amplitudes $\underline{U}_M$, $\underline{U}_X$, and phases ϕ_M, ϕ_X, on the two species of atom, then the structure factor at $\underline{K} = \underline{M} - n\underline{Q}$, is given by:

$$F(\underline{M} - n\underline{Q}) = f_M J_n(2\pi\underline{K}.\underline{U}_M) e^{in\phi_M} + f_X J_n(2\pi\underline{K}.\underline{U}_X) \{e^{2\pi i\underline{M}.\underline{x} + in\phi_{X1}} + e^{-2\pi i\underline{M}.\underline{x}+in\phi_{X2}}\}$$

In this equation ϕ_{X1} and ϕ_{X2} represent the phases for each of the two chalcogen layers. If however the deformation waves are disposed so that there is a centre of symmetry in the deformation cell, the phases may be written:

$$\phi_M = 0, \quad \phi_{X1} = -\phi_{X2} = \phi .$$

Then the above equation simplifies to the following:

$$F(\underline{M} - n\underline{Q}) = f_M J_n(2\pi\underline{K}.\underline{U}_M) + 2f_X J_n(2\pi\underline{K}.\underline{U}_X) \cos(2\pi\underline{M}.\underline{x} + n\phi) \quad \ldots (11)$$

This shows that there is a phase shift of ϕ introduced into the cosine factor. While the chalcogen contribution to the structure factor of the matrix reflexions is proportional to $\cos(2\pi\underline{M}.\underline{x})$, the contribution to the first order satellites is proportional to $\cos(2\pi\underline{M}.\underline{x} + \phi)$.

It is sometimes more useful to re-write this factor as

$$\cos(2\pi\underline{K}.\underline{x} + \phi')$$

where $\phi' = \phi + 2\pi\underline{Q}.\underline{x}$, i.e. the phase of the deformation wave relative to an origin at the chalcogen atom site. This shift in phase of the chalcogen part of the structure factor will be discussed further and applied to specific materials in sections 7.4, 9.2, 11.10.

Clearly either if the scattering factor of the chalcogen is much less than that of the metal, or if the deformation amplitude on the chalcogen sublattice is much smaller than on the metal sublattice, the chalcogen contribution to the satellite reflexions will hardly be observed. The effect of the phase shift in the cosine term is only marked when the chalcogen contribution is large (cf. 7.2.3).

Finally in this section the stacking of the deformation waves in successive MX_2 layers will briefly be studied. A first and

important point to note is that the stacking sequence of the distortions is not necessarily the same as that of the matrix layers. The diffraction pattern from the deformations in a single layer is a series of rods in reciprocal space which are parallel to $\underline{c}^*$. The stacking of the deformations in a sequence of layers modulates the rods to give discrete reflexions. In the absence of phase correlation between deformations in neighbouring layers, the rods remain unmodulated.

It is supposed that the deformation waves form a regular N-layer stack and that the stacking vector is $\underline{R}$. Then, by comparison with equation (4), the structure factor for the rod must be multiplied by A, where:

$$A = \{1 + e^{2\pi i \underline{S}.\underline{R}} + \ldots + e^{2(N-1)\pi i \underline{S}.\underline{R}}\}$$

Here $\underline{S}$ is the reciprocal vector from the parent matrix reflexion to the discrete satellite reflexion lying on the rod. The series for A can be summed as a geometrical progression, thus:

$$A = \frac{1 - \exp(2N\pi i \underline{S}.\underline{R})}{1 - \exp(2\pi i \underline{S}.\underline{R})} \quad \ldots\ (12)$$

The scalar product $\underline{S}.\underline{R}$ can be determined by separating the vectors into components parallel and perpendicular to the layers cf. section 2.2.1).

$$\text{i.e.} \quad \underline{S}.\underline{R} = S_{//} R_{//} + S_{\perp} R_{\perp}$$

$S_{//} R_{//}$ is the phase shift within the layer and must be equal to 1/N or 2/N etc. for a regular stacking sequence.

$S_{\perp} R_{\perp}$ is the phase shift normal to the layers. Since $R_{\perp} = c$, and $S_{\perp} = \ell c^*/N$; therefore

$$\underline{S}.\underline{R} = (1 + \ell)/N$$

where ℓ is indexed on the N-layer deformation cell. Thus the expression (12) becomes for this case:

$$A = \frac{1 - \exp(2\pi i(1 + \ell))}{1 - \exp(2\pi i(1 + \ell)/N)}$$

A is zero unless $1 + \ell \equiv 0 \pmod{N}$.

Therefore, for a N = 3 layered stack of deformations the only permissible values of ℓ are -1, 2, 5,..... and the satellite reflexions occur at $\pm\frac{1}{3}c^*$, $\pm\frac{2}{3}c^*$, etc.

2.5.3 Symmetry Related Distortions

Although one atom per unit cell will be assumed for simplicity in the following treatment, an extension to the case of more than one atom can readily be made in the manner outlined in section 2.5.2.

When a crystal with high symmetry is deformed, either a single distortion wave in one (usually high symmetry) direction results or else several distortion waves in directions related by the symmetry of the crystal. In the former case a domain structure must result, with the directions of the distortions in each domain related by the symmetry of the undistorted crystal. The latter case is however of more direct importance, although domain structures do occur in some of the distorted phases. For instance a crystal with trigonal symmetry (e.g. an octahedrally co-ordinated layer dichalcogenide) would be distorted by three waves at angles of 0, 120°, 240°. For such a deformation structure, equation (6) is replaced by:

$$\delta\underline{r} = \underline{U}_1\sin(2\pi\underline{Q}_1\cdot\underline{\ell} + \phi_1) + \underline{U}_2\sin(2\pi\underline{Q}_2\cdot\underline{\ell} + \phi_2) + \underline{U}_3\sin(2\pi\underline{Q}_3\cdot\underline{\ell} + \phi_3)$$

where the subscripts 1, 2, 3 refer to each of the three symmetry direction. Then, following the analysis of section 2.4.1, we obtain the equivalent of equation (7), only with an exponential term corresponding to each of the three waves. Expanding each exponential as a Bessel function series as before gives:

$$\rho(\underline{K}) = \sum_{n_1}\sum_{n_2}\sum_{n_3} V(\underline{K})\cdot\delta_{\underline{K}+n_i\underline{Q}_i,\underline{M}}\cdot J_{n_1}(2\pi\underline{K}.\underline{U}_1).J_{n_2}(2\pi\underline{K}.\underline{U}_2).J_{n_3}(2\pi\underline{K}.\underline{U}_3)\times \exp(i\textstyle\sum_i n_i\phi_i) \quad \ldots (13)$$

Although this equation is more complex than (8), it is

essentially of the same form. For each additional deformation wave there is a convolution of its reciprocal lattice with $[\rho(\underline{K})]_o$. The expression for the scattered radiation is therefore multiplied by another Bessel function and phase factor. Equation (13) can readily be extended to any number of deformation waves by continuing the convolution process.

As soon as more waves than one are allowed, each matrix reflexion becomes surrounded by a complete 3-D deformation reciprocal lattice. For the case of trigonal symmetry the deformation reciprocal lattice has basis vectors $\underline{Q}_1$, $\underline{Q}_2$, $\underline{Q}_3$.

From (13) the structure factor for scattering at $\underline{K} = \underline{M} + \underline{Q}$ can be found:

$$F(\underline{M}+\underline{Q}) = V(\underline{K}) \prod_i \sum_{n_i} J_{n_i}(2\pi \underline{K}.\underline{U}_i)\, e^{in_i\phi_i} \quad \ldots (14)$$

where the triple summation is over all values of n_1, n_2, n_3 which satisfy the condition that:

$$-\underline{Q} = n_1\underline{Q}_1 + n_2\underline{Q}_2 + n_3\underline{Q}_3$$

We also have the following relationships linking the parameters, deduced from symmetry:

$$\underline{Q}_1 + \underline{Q}_2 + \underline{Q}_3 = 0$$
$$|\underline{Q}_1| = |\underline{Q}_2| = |\underline{Q}_3| = Q$$
$$\underline{U}_1 + \underline{U}_2 + \underline{U}_3 = 0$$
$$|\underline{U}_1| = |\underline{U}_2| = |\underline{U}_3| = U$$
$$\phi_1 = \phi_2 = \phi_3 = \Phi$$

There is clearly an infinite number of terms in the triple summation of (14), but the terms rapidly become very small for increasing n_i. For a given range of scattering vector $\underline{K}$, a fixed number of terms only need be included.

Contributions to the Matrix Reflexion

The main term in the scattering at the matrix reflexion at $\underline{M}$ is that involving zero order Bessel Functions. Other terms do however also contribute, but they are in general very small.

The values of the n_i which satisfy the conditions for scattering at the matrix reflexion can be found from the relationships:

$$\left.\begin{aligned} \sum_i n_i \underline{Q}_i &= 0 \\ \sum_i \underline{Q}_i &= 0 \end{aligned}\right\}$$

The only values which satisfy these two equations are:

$$n_1 = n_2 = n_3 = n \qquad \text{where n is any integer.}$$

The contributions with n odd, cancel in pairs for $n > 0$ and $n < 0$, since:

$$(J_n(z))^3 = -(J_{-n}(z))^3 \qquad \text{for n odd}$$

and

$$(J_n(z))^3 = (J_{-n}(z))^3 \qquad \text{for n even}$$

Bessel functions being even or odd with n, their order:

$$\therefore \quad J_{-n}(z) = (-1)^n J_n(z)$$

Thus the expression for the structure factor of the matrix reflexion becomes:

$$\begin{aligned} F(\underline{M}) = V(\underline{M})\{ & J_o(2\pi \underline{M}.\underline{U}_1).J_o(2\pi \underline{M}.\underline{U}_2).J_o(2\pi \underline{M}.\underline{U}_3) + \\ & 2J_2(2\pi \underline{M}.\underline{U}_1).J_2(2\pi \underline{M}.\underline{U}_2).J_2(2\pi \underline{M}.\underline{U}_3)e^{6i\phi} \\ & + \text{higher order terms}\} \quad \ldots (15) \end{aligned}$$

Even the second term is very small, and it is unlikely that higher order terms need ever be considered under normal conditions.

Contributions to the First Order Satellites

Each of the three deformation waves gives pairs of satellites, i.e. at $\underline{K} = \underline{M} \pm n\underline{Q}_i$. The six first order satellites can be indexed (see 2.3.2) as $\{\underline{S}_M(10.\ell)\}$.

Contributions to the scattering at for instance $\underline{M} + \underline{Q}_1$ may be found by solving the following equations:

$$\begin{aligned} \sum_i n_i \underline{Q}_i &= -\underline{Q}_1 \\ \sum_i \underline{Q}_i &= 0 \end{aligned}$$

This leads to the relationships for the n_i:

$$\begin{aligned} n_2 &= n_3 = n \\ n_1 &= n - 1 \end{aligned}$$

The expression for the structure factor for this satellite reflexion becomes:

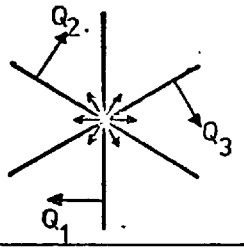
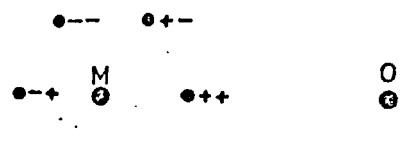
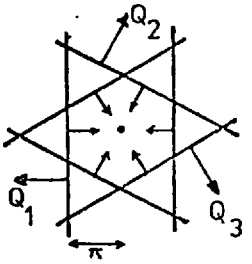
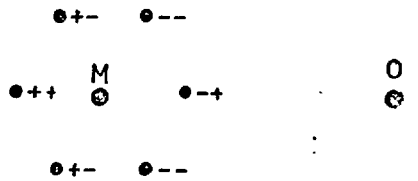
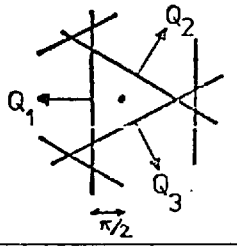
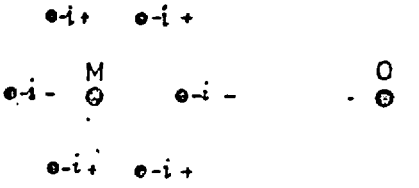
ϕ	direct space	reciprocal space
0		
π		
$\pi/2$		

Figure 20 Variation of the signs of the first two contributions to scattering from 3 symmetry-related deformation waves, with the phase ϕ of each wave.

$$F(\underline{M}+\underline{Q}_1) = V(\underline{K})\{J_{-1}(2\pi\underline{K}.\underline{U}_1)J_o(2\pi\underline{K}.\underline{U}_2)J_o(2\pi\underline{K}.\underline{U}_3)e^{-i\phi} + J_o(2\pi\underline{K}.\underline{U}_1)J_1(2\pi\underline{K}.\underline{U}_2)J_1(2\pi\underline{K}.\underline{U}_3)e^{2i\phi} + \text{higher order terms}\} \quad \ldots (16)$$

The terms decrease rapidly in magnitude, although not so sharply as the contributions to the matrix reflexion. However, except for $2\pi\underline{K}.\underline{U} > 1$ only the first two terms, as shown above need be taken into consideration. The second term clearly arises as a result of the following combination of deformation wave vectors:

$$\underline{Q}_2 + \underline{Q}_3 = -\underline{Q}_1$$

For three symmetry-related deformation waves the number of significant terms in the structure factors,(15) and (16), is relatively small. With a larger number of deformation waves the number of significant terms rapidly increases (see in particular section 7.3.1).

2.5.4 Symmetry-Related Distortions and Phase

The value of the phase must be specified now that the model comprises more than one deformation wave, since it determines how the terms in equations (15) and (16) add together by virtue of the factors, $\exp(in\phi)$. The sign of each term is also determined by the angle between $\underline{K}$ and $\underline{U}_Q$. The question of distortion mode will be taken up in section 2.5.5, while in this section it will be assumed that $\underline{U}_Q$ and $\underline{Q}$ are parallel (i.e. a longitudinal mode).

In Fig.21 the phases of the first two contributions to the six first order satellites are shown, following equation (16). Three values only, 0, 180° and 90°, for the phase angle are shown. Only one of the two nodal lines has been shown for each deformation wave, i.e. where the directions of the atomic displacements are away from the nodes (shown by arrows). From Fig.20 it can be seen that:

(a) If $\phi = 0$ or π, all the contributions are real, and either add or subtract from one another to maximum effect for the paired

satellites $\underline{M} \pm \underline{Q}$.

(b) If $\phi = \pi/2$ (or indeed $3\pi/2$) there are contributions in both the real and imaginary parts of the structure factor. Consequently the pairs of satellites at $\underline{M} \pm \underline{Q}$ no longer alternate in intensity but rather are approximately equal.

(c) The difference in direct space between $\phi = 0$ and $\phi = \pi$, is in exchanging displacements away from the origin for displacements towards the origin, while in reciprocal space it is to exchange the addition and subtraction of contributions from $\underline{M} - \underline{Q}$ to $\underline{M} + \underline{Q}$ and vice versa.

Clearly, when the phase angle takes some general value, the effect in diffraction will be intermediate between the cases outlined above. In particular there will be a partial shift in intensity towards one satellite in the $\underline{M} \pm \underline{Q}$ pair.

2.5.5 Distortion Mode

In general the displacement $\underline{U}_Q$ will be in a direction different from that of the wave vector $\underline{Q}$. Except in Fig. 20, so far in this Chapter the distortion mode has not been specified. It is very convenient, for a layer material, to resolve $\underline{U}_Q$ into three mutually perpendicular components:

$$\underline{U}_Q = \underline{U}_L + \underline{U}_T + \underline{U}_N$$

These components are readily identified with the three modes as conventionally defined for the propagation of phonons in a solid:

$\underline{U}_L$ is parallel to $\underline{Q}$ and therefore represents the longitudinal acoustic (LA) component of the wave.

$\underline{U}_T$ is perpendicular to $\underline{Q}$, but lies within the layer and therefore represents the parallel transverse acoustic ($TA_{//}$) mode.

$\underline{U}_N$ is perpendicular both to $\underline{Q}$ and to the layers and therefore represents the perpendicular transverse ($TA_{\perp}$) mode.

These definitions have assumed implicitly that $\underline{Q}$ lies within the layer. This assumption can be justified on physical grounds since the coupling between the layers is at least an order of magnitude weaker than the coupling between atoms within each layer. Where layer-layer interactions mean that there is a component of the distortion periodicity parallel to $\underline{c}^*$ (e.g. as a result of the packing of static deformations) the vector $\underline{Q}$ will be reserved for the in-layer component, and the perpendicular component will be treated separately. For a 3-layer stack of deformation waves, the reciprocal lattice vector joining a satellite reflexion to its parent is therefore

$$\underline{S}_M = \underline{Q} + \tfrac{1}{3}\underline{c}^* \ .$$

It is also sometimes convenient to combine the two components $\underline{U}_L$ and $\underline{U}_T$ of the displacement amplitude into an in-layer component $\underline{U}_{//}$, while leaving separate $\underline{U}_N$ the perpendicular component. This combination is readily executed only if $\underline{U}_L$ and $\underline{U}_T$ differ in phase by 0° or 180°. In general the in-layer displacement is given by

$$\delta\underline{r}_{//} = \underline{U}_L \sin(2\pi\underline{Q}.\underline{\ell} + \phi_L) + \underline{U}_T \sin(2\pi\underline{Q}.\underline{\ell} + \phi_T)$$

This can only be simplified as follows if $\phi_L = \phi_T = \phi$:

$$\underline{r} = (\underline{U}_L \pm \underline{U}_T)\sin(2\pi\underline{Q}.\underline{\ell} + \phi)$$

In all other cases the scattering by $\underline{U}_L$ and $\underline{U}_T$ must be considered separately, the situation being equivalent to having two sets of deformation waves. Thus, for a single deformation wave with components $\underline{U}_L$ and $\underline{U}_T$ and phases ϕ_L and ϕ_T, the scattering at $\underline{K} = \underline{M} - n\underline{Q}$ is given by:

$$F(\underline{M} - n\underline{Q}) = \sum_{r=-\infty}^{\infty} V(\underline{K}) J_r(2\pi\underline{K}.\underline{U}_L) J_{n-r}(2\pi\underline{K}.\underline{U}_T) e^{ir\phi_L + i(n-r)\phi_T} \qquad \ldots (17)$$

For $2\pi\underline{K}.\underline{U} < 1$, the expression for the structure factor can be approximated by including only the first two terms in the summation:

$$F(\underline{M} - n\underline{Q}) = V(\underline{K})\{J_1(2\pi\underline{K}.\underline{U}_L)\, J_o(2\pi\underline{K}.\underline{U}_T)\, e^{i\phi_L} + J_o(2\pi\underline{K}.\underline{U}_L)\, J_1(2\pi\underline{K}.\underline{U}_T)\, e^{i\phi_T}\}$$

For $\phi_L = 0$ and $\phi_T = \pi/2$ it can be seen that the longitudinal contribution is in the real part of the structure factor while the transverse is in the imaginary part.

The structure factor expression for combining the in-layer ($\underline{U}_{//}$) and perpendicular ($\underline{U}_N$) components is similar to (17). Extensive calculation would result from applying equation (17) in the general case, especially for large values of the Bessel function arguments. It is therefore convenient in practice to restrict study to the following two regimes:

(a) where terms in ($2\pi\underline{K}.\underline{U}_{//}$) predominate, i.e. close to the reciprocal plane containing the matrix hk.0 relfexions.

(b) where terms in ($2\pi\underline{K}.\underline{U}_N$) predominate, i.e. close to the matrix $\underline{c}^*$ axis.

Finally in this section Figs 21, 22 demonstrate how a change from an LA to a $TA_{//}$ mode within the layer affects the magnitude of the structure factors of the six first order satellites.

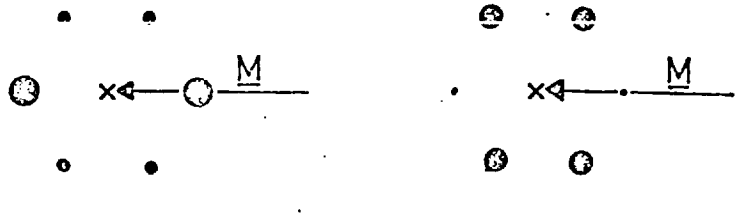


Fig 21 $U_L \gg U_T$ Fig 22 $U_L \ll U_T$

2.6 Non-Sinusoidal Deformations

The extension of the preceding to the study of non-sinusoidal deformation waves is unfortunately not simple when the distortion periodicities are incommensurate with the matrix lattice. Different types of modulating function are far more readily incorporated into the theory of commensurate deformations (see Böhm 1975). In the incommensurate situation, however, analytical solutions are impossible to obtain without extensive approximation. The need for this further development will be fully justified

when the experimental results for 1T TaS_2 are studied in detail in chapter 7.

With the complex interactions within a real material, the inability of the lattice to sustain a static sinusoidal distortion comes as no surprise, especially when displacements of up to 5% of the interatomic spacings are involved. Indeed the mechanism stabilising the distortions in the Group Va layer dichalcogenides appears to favour a non-sinusoidal modulating function, as to be discussed in chapter 11.

If the primary deformation is one within the metal atom layers in the MX_2 sandwich, then as $\underline{U}_Q$ increases the following might also be expected to occur:

(a) displacements of the chalcogens with the layers;

(b) displacements of the metal atoms perpendicular to the layers;

(c) displacements of the chalcogen atoms perpendicular to the layers.

These possibilities have already been considered in general terms in sections 2.5.2 and 2.5.5. Although these associated deformation waves may differ in phase from the primary deformation, they necessarily have the same wave vector, $\underline{Q}$.

In addition to (a), (b), (c), further periodic relaxations of the lattice with different wave vector may take place. The fundamental deformation waves (with wave vectors $\underline{Q}_1$, $\underline{Q}_2$, $\underline{Q}_3$) induce higher harmonics of the deformation cell with, for example, the wave vectors: $2\underline{Q}_1$, $3\underline{Q}_1$, $2\underline{Q}_2$, $\underline{Q}_1 - \underline{Q}_2$, $2\underline{Q}_3 - \underline{Q}_2$.
Each member of what may turn out to be an infinite series of higher harmonics, will in general have a different amplitude and phase. The presence of these higher order Fourier components indicates in fact a more complex modulating function, rather in

the same way that higher order reflexions from a crystal lattice define more precisely the atomic structure within the unit cell. This direct comparison follows from the fact that diffraction patterns give the Fourier Transform of the charge density.

Let $P(\underline{\ell})$ be a general periodic modulation function with fundamental periodicities along the three symmetry directions defined by wave vectors $\underline{Q}_1$, $\underline{Q}_2$, $\underline{Q}_3$.

i.e. $\underline{r} = \underline{\ell} + P(\underline{\ell})$.

This may be compared with the expression used in 2.5.3 for three symmetry related sinusoidal functions:

$$\delta\underline{r} = \underline{\ell} + \sum_{i=1}^{3} \underline{U}_{Qi} \sin(2\pi \underline{Q}_i \cdot \underline{\ell} + \phi_i)$$

Then, if $P(\underline{\ell})$ is a periodic function, and has only a finite number of discontinuities in each period, Fourier's Theorem may be applied, and the function expressed as an infinite sum of sinusoidal components:

i.e. $\underline{r} = \underline{\ell} + \sum_{i} \sum_{n=1}^{\infty} \underline{a}_{in} \sin(2\pi n \underline{Q}_i \cdot \underline{\ell} + \phi_{in})$ + infinite series involving combinations of the $\underline{Q}_i$.

The deformation reciprocal lattice has the same geometry as for sinusoidal deformation waves, but now combinations of all the harmonics of the distortion cell contribute to <u>every</u> reflexion. Since the modulating function can in general be resolved into an infinite series of Fourier components, it follows that there is an infinite number of terms adding to the structure factor of each reflexion.

By extending the expression (14) to an infinite number of components, the structure factor for scattering at $\underline{M} - n\underline{Q}$ becomes:

$$F(\underline{M} - n\underline{Q}) = V(\underline{K}) \prod_{i=1}^{\infty} \left\{ \sum_{m_i=-\infty}^{\infty} J_{m_i} (2\pi(\underline{M} - n\underline{Q}) \cdot \underline{a}_i) \exp(i m_i \phi_i) \right\}$$

where the multiple summation is subject to the condition on the coefficients, m_i, of Fourier components that

$$-n\underline{Q} = \sum_{i} m_i \underline{Q}_i$$

Simplification of this expression is possible only if $P(\underline{\ell})$ is a special function (for instance one of the functions dealt with in section 2.6.3). In general, however, the amplitudes $\underline{a}_i$ of the higher order Fourier components tend to zero rapidly as the order m_i increases, so that the Fourier series can be truncated to give a small finite number of components. In the two sections which follow immediately the results of adding the alternative second order components to the fundamental will be considered.

2.6.1 Fourier Components $2\underline{Q}_1$, $2\underline{Q}_2$, $2\underline{Q}_3$

This is the simplest case to study, i.e. with six Fourier components of the distortion cell altogether, $\underline{Q}_1$, $\underline{Q}_2$, $\underline{Q}_3$, $2\underline{Q}_1$, $2\underline{Q}_2$, $2\underline{Q}_3$. Using a notation now with $\underline{U}_{Q_i}$ for the amplitude rather than $\underline{a}_i$, we have that the Fourier transform of the charge density is:

$$\rho(\underline{K}) = V(\underline{K}) \prod_{i=1}^{6} \left\{ \sum_{n_i=-\infty}^{\infty} \delta_{\underline{K} + n_i\underline{Q}_i, \underline{M}} \cdot J_{n_i}(2\pi \underline{K}.\underline{U}_{Q_i}) \exp(i n_i \phi_i) \right\}$$

where in order to simplify the expression, the following substitutions have been made: $\underline{Q}_4 = 2\underline{Q}_1$, $\underline{Q}_5 = 2\underline{Q}_2$, $\underline{Q}_6 = 2\underline{Q}_3$.

Thus <u>each</u> term in the summation is a product of <u>six</u> Bessel functions and a phase factor. In order to determine the scattering at a first order satellite reflexion, the summation is restricted to all values of the n_i $(i = 1,\ldots 6)$ which satisfy:

$$-\underline{Q}_1 = \sum_{i=1}^{6} n_i\underline{Q}_i = \sum_{i=1}^{3} n_i\underline{Q}_i + 2\sum_{i=1}^{3} n_i\underline{Q}_i$$

for the satellite reflexion at say $\underline{M} - \underline{Q}_1$.

It is important to note that although the Fourier components with wave vectors $2\underline{Q}_i$ $(i = 1,\ldots 3)$ form their own fundamental satellites at $\underline{M} \pm 2\underline{Q}_i$, they also give rise to contributions at other satellites, particularly those at $\underline{M} \pm \underline{Q}_i$ where the relevant combination of deformation wave vectors is:

$$\pm \underline{Q}_i = \underline{Q}_i - (2\underline{Q}_i)$$

This is in fact the largest term involving $\underline{U}_{2Q}$ contributing to the scattering at $\underline{M} - \underline{Q}_i$, ($\underline{U}_{2Q}$ being the amplitude of the second harmonic of the deformation wave.) The magnitude of this term is proportional to $J_1(2\pi\underline{K}.\underline{U}_Q)\ J_{-1}(2\pi\underline{K}.\underline{U}_{2Q})$. It is instructive to determine how this term adds to the fundamental term in the expression for the structure factor at $\underline{M} \pm \underline{Q}_i$ as the phases ϕ_Q and ϕ_{2Q} are varied. Assuming longitudinal displacements, it is found (Fig. 23) that the contributions add for $2\pi\underline{K}.\underline{U}_Q > 0$ and subtract for $2\pi\underline{K}.\underline{U}_Q < 0$ when $\phi_{2Q} = 0$, and vice versa when $\phi_{2Q} = \pi$. Changing ϕ_Q from 0 to π changes the <u>overall</u> sign.

When this is combined with the result shown in Fig. 22 it can be seen that for $\phi_Q = \pi$, $\phi_{2Q} = 0$, all the terms so far considered (i.e. the three largest for the six deformation wave model) <u>add</u> together for $\underline{M} + \underline{Q}_1$, and the second two <u>subtract</u> from the fundamental term for $\underline{M} - \underline{Q}_1$. This gives a large asymmetry in the scattering for pairs of satellites, so that

$$F(\underline{M} + Q_1) > F(\underline{M} - \underline{Q}_1).$$

Such an asymmetry is observed in the satellite intensities for $1T_2$ TaS_2 (section 7.2.5) and will prove to be a very important pointer to a model for the deformation structure of this material.

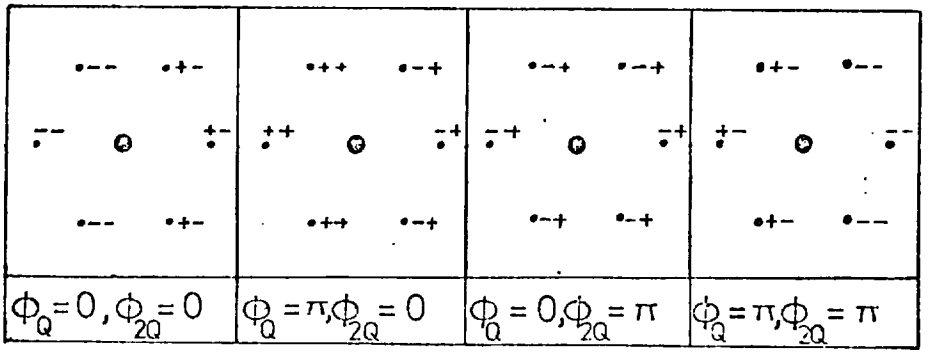


Figure 23

2.6.2 <u>Fourier Components $\underline{P}_1$, $\underline{P}_2$, $\underline{P}_3$</u>

The wave vectors $\underline{P}_i$ are defined thus:

$$\underline{P}_1 = \underline{Q}_2 - \underline{Q}_3, \quad \underline{P}_2 = \underline{Q}_3 - \underline{Q}_1, \quad \underline{P}_3 = \underline{Q}_1 - \underline{Q}_2.$$

The satellite reflexions corresponding to the wave vectors, $\underline{P}_i$ must lie in the matrix hk.ℓ plane irrespective of whether the $\underline{Q}_i$ do, since if the latter each have a component $\underline{S}_\perp$ parallel to $\underline{c}^*$, the $\underline{S}_\perp$ cancel out when the difference of two $\underline{Q}_i$ is taken. Fig. 24 below shows the configuration of the satellites corresponding to the $\underline{P}_i$.

In direct space the $\underline{P}_i$ correspond to the (11.0) planes of the deformation cell, and their magnitude is given by $P = \sqrt{3}\,Q$. They therefore have the next largest wave vector after the fundamental Q. Although these higher order Fourier components primarily scatter radiation at $\underline{M} \pm \underline{P}_i$, they also contribute to the scattering at $\underline{M} \pm \underline{Q}_i$ through combination with the $\underline{Q}_i$ etc.. For instance scattering at $\underline{M} + \underline{Q}_1$ can arise from

$$\underline{Q}_1 = \underline{Q}_3 - \underline{P}_2$$

and

$$\underline{Q}_1 = \underline{Q}_2 + \underline{P}_3$$

These combinations give rise to scattering which may add to or subtract from the fundamental scattering at $\underline{M} \pm \underline{Q}_i$. One instance which will prove to be of importance later is when ϕ_Q and ϕ_P take the values π and 0 respectively. Then the contributions once again (cf section 2.6.1) add for the satellite at $\underline{M} + \underline{Q}_1$ and subtract from the fundamental at $\underline{M} - \underline{Q}_1$, thus enhancing the asymmetry in the pair of reflexions.

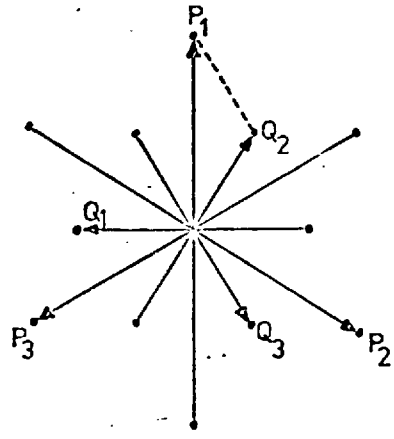


Figure 24

2.6.3 Special Non-Sinusoidal Functions

There are a number of 1-D periodic modulating functions whose Fourier components are readily calculated. Three such

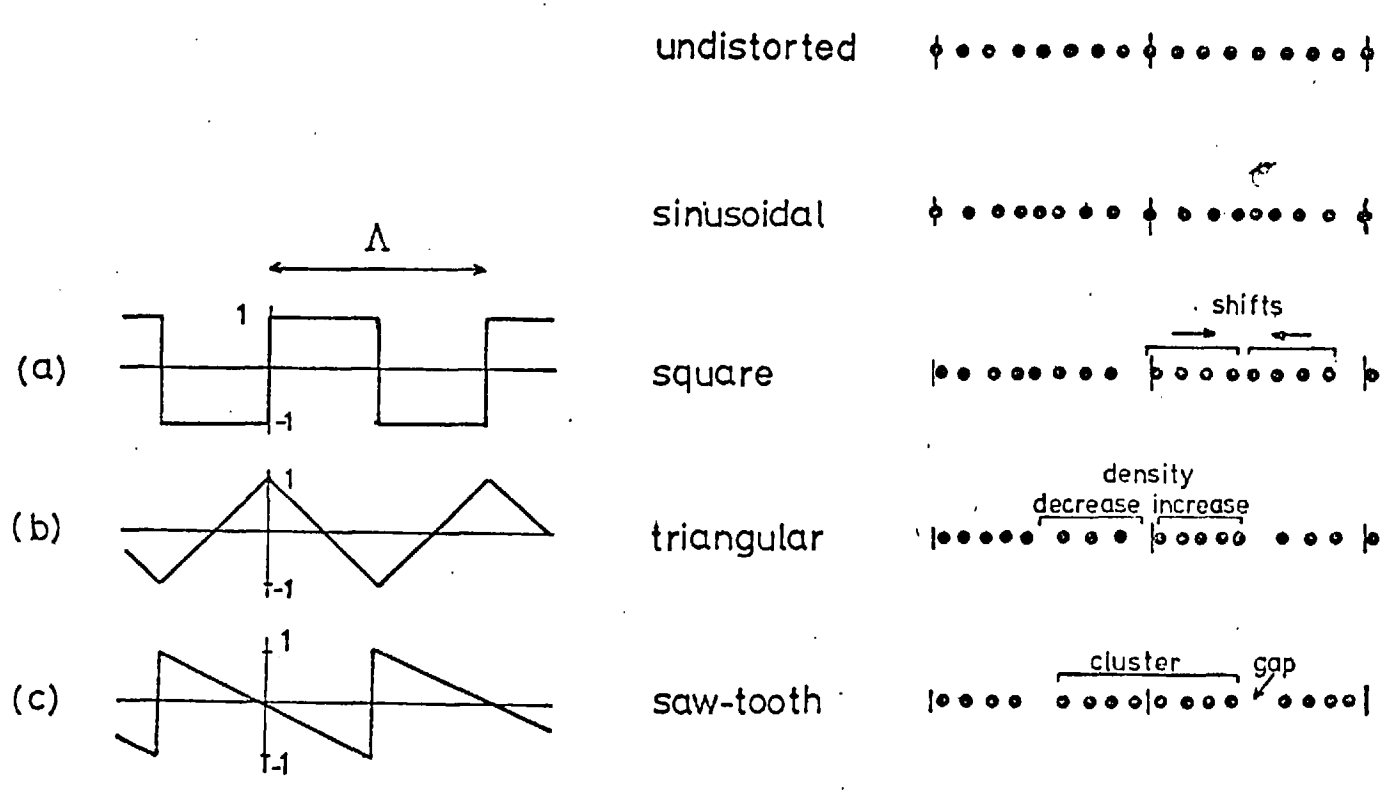


Figure 25 Deformation of 1-D lattice produced by various modulating functions discussed in the text.

functions are illustrated in Fig. 25. The two symmetrical functions (a) and (b) are considered by Böhm (1975). The experimental data presented in later chapters show very clearly that it is necessary also to consider asymmetrical modulation.

(a) Square Wave

This can be expanded as a Fourier series thus:

$$P(x) = \sum_{n=1}^{\infty} \frac{4}{n\pi} \sin(2\pi nx/\Lambda) \quad \text{for n odd only.}$$

Here Λ is the wavelength of the deformation. This expression is readily extended to the more general case of a rectangular wave.

(b) Triangular Wave

For this function the Fourier expansion is:

$$P(x) = \sum_{n} \frac{8}{\pi^2 n^2} \cos(2\pi nx/\Lambda) \quad \text{for n odd only.}$$

(c) Saw-Tooth Wave

The expansion as a Fourier Series is:

$$P(x) = \sum_{n} (-1)^n \frac{2}{n\pi} \sin(2\pi nx/\Lambda) \quad \text{n even and odd.}$$

The saw-tooth differs from functions (a) and (b) in that its Fourier expansion contains both even and odd harmonics, and this reflects its lack of symmetry ($P(x) \neq P(-x)$ irrespective of choice of origin).

Fig. 25 also shows a 1-D crystal perturbed by longitudinal deformations of these three types, as well as by a sinusoidal modulating function. From the Figure it can be seen that the longitudinal square wave shifts groups of atoms, while the triangular wave gives alternating regions of high and low density rather similar to the sine wave. The sawtooth wave however gives extended regions of increased density ('clusters') separated by narrow regions of very low density ('gaps').

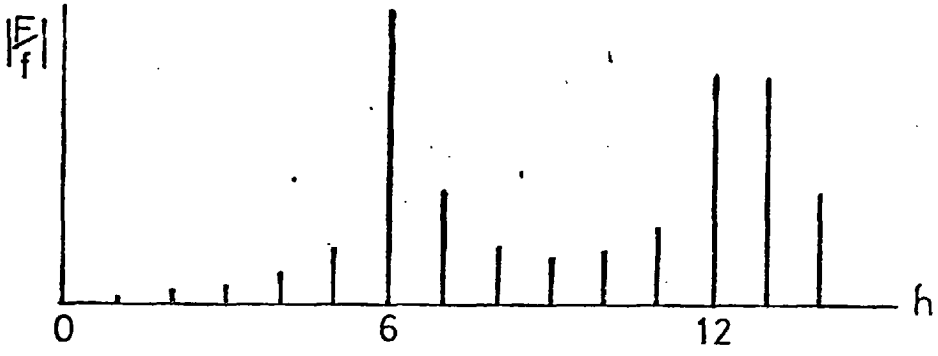
For simplicity only the 1-D case has been illustrated here. The situation in a layer material is essentially 2-D and will be

discussed when the experimental data are interpreted in chapter 7. There the analysis is far less simple, although it can still be viewed as an extension of the 1-D case.

2.6.4 Diffraction from 1-D Commensurate Clusters

The calculation for 1-D commensurate clusters is outlined in Appendix 1(a). For a 6-a distortion superlattice which has the interatomic separation within the clusters reduced from a to 0.96 a, the calculated structure factors for the first 14 reflexions are as shown in Fig. 26.

Figure 26



From this simple model a number of important observations can be made. First it may be noted that at small scattering vectors the structure factor is large for h = 6, i.e. at a'matrix' reflexion, corresponding to the undistorted interatomic separation. The scattering of radiation is relatively insensitive to the deformation at small scattering vector.

Secondly, the 'matrix' and 'satellite' structure factors are equal for h = 12 and h = 13 respectively. In this region of reciprocal space the structure factor is very sensitive to the deformation, and the radiation is effectively being scattered from an average spacing corresponding to h = 12.5 rather than h = 12, i.e. to $\frac{12}{12.5}$ a = 0.96 a rather than to the interatomic spacing a. 0.96 a is in fact the interatomic distance in the clusters. The interatomic spacings within clusters can therefore readily be estimated by determining the scattering vector at

which the matrix and first order satellite reflexions become approximately equal in intensity.

Thirdly, it can be seen that clustering produces a marked asymmetry in the satellites, the one at h = 6n + 1 being stronger in general than the one at h = 6n - 1. This reflects the asymmetry in the modulating function. 'Negative clusters', when interatomic spacings increase, would clearly make the 6n - 1 satellite stronger than the 6n + 1 satellite.

These three important observations carry over to an incommensurate deformation wave, and in 2 or more dimensions; they prove to be very indicators as to the type of modulating function.

2.6.5 Diffraction from 1-D Incommensurate Clusters

The calculation for an incommensurate deformation wave of almost equal periodicity and producing similar displacements to the commensurate one, is considerably longer and the details are given in Appendix 1(b). The results of the calculation of the structure factor are displayed graphically in Fig. 27, where it can be seen that there are the same general characteristics for the six reflexions studied. The agreement with Fig. 26 is however poorer for h = 2 than for h = 1, where reflexions are now indexed on the matrix cell. This confirms that, since for h = 2 the argument of the Bessel function $2\pi\underline{K}.\underline{U}_Q \sim 1$, the two analyses must diverge (section 2.4.4). Calculations for 2-D incommensurate and commensurate clusters are compared in section 7.7 (see especially Fig. 92).

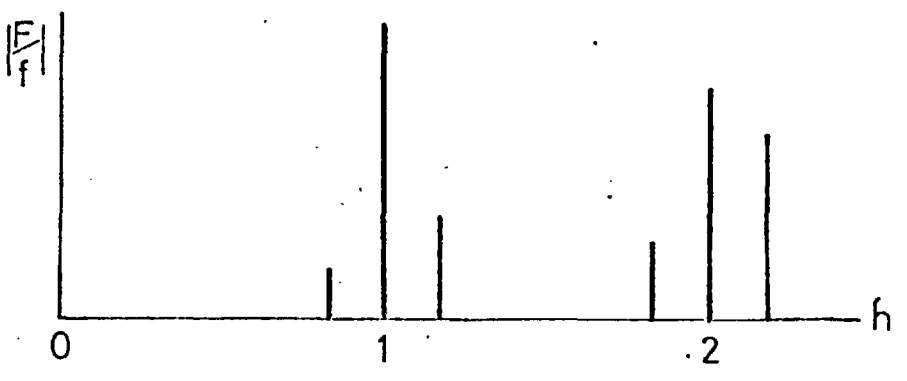


Figure 27

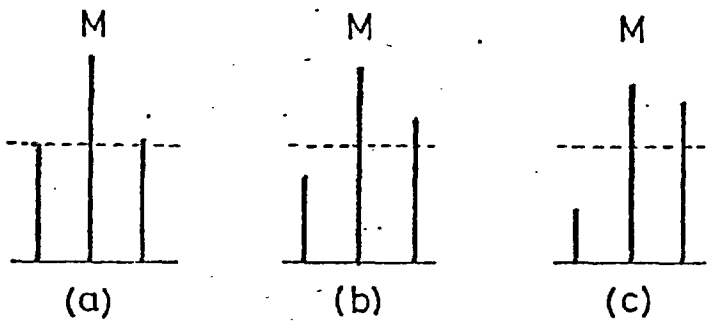


Figure 28 Showing the effect of omitting higher Fourier components of the distortion for a group of matrix and satellite reflexions.
(a) single sinusoidal deformation wave;
(b) fundamental plus second harmonic, with $\underline{U}_{2Q} = -\frac{1}{2}\underline{U}_{Q}$;
(c) 'sawtooth' deformation wave.

2.6.6 Effect of Omitting Higher Fourier Components

Finally in this chapter the effects in the diffraction pattern of omitting the higher order Fourier components will be studied with reference to a 1-D sawtooth wave. To illustrate the consequences of this, the following three models will be taken. In each case the periodicity $\Lambda \triangleq 6a$ (cf. 2.6.5).

(a) A single sinusoidal distortion with amplitude, $\underline{U}_Q = 0.08\,\underline{a}$. Then the satellites and the parent matrix reflexion at h = 2, for which $2\pi\underline{K}.\underline{U}_Q \simeq 1$, appear as in Fig. 28(a).

(b) When the fundamental periodic distortion has added to it the second harmonic with $\underline{U}_{2Q} = -\frac{1}{2}\underline{U}_Q$, (here the negative sign denotes opposite phase) the symmetry of the pair of satellites at $\underline{M} \pm \underline{Q}$ is destroyed (Fig. 28(b)).

(c) If the sawtooth wave of section 2.6.5 is now applied to the lattice, the asymmetry of the pair of satellites is enhanced.

In summary, the disparity between the structure factors for the satellites at $\underline{M} \pm \underline{Q}$ becomes progressively larger as more of the higher Fourier components of the sawtooth modulation are included in the calculation. Another effect of including the higher components is progressively to decrease the magnitude of the matrix reflexion.

In appendix 1(b) it is shown that summing all the higher order contributions to the scattering at $\underline{M} + \underline{Q}$ is approximately equivalent to summing the series:

$$(\pi\underline{K}.\underline{U}_Q)^2\left\{\sum_{n=1}^{\infty}\frac{1}{n(n+1)}\right\} = \pi^2(\underline{K}.\underline{U}_Q)^2$$

The first term in this series is $\frac{1}{2}\pi^2(\underline{K}.\underline{U}_Q)^2$. The result therefore of including the second harmonic, $2\underline{Q}$, but excluding the rest is to halve their effect on the asymmetry of the satellites. If the third harmonic is also included, $\frac{2}{3}$ of the effect is produced, etc.

3 THE KOHN ANOMALY AND CHARGE-DENSITY WAVES

3.1 Electronic Susceptibility and Screening

Suppose that a free electron gas is subjected to a time dependent perturbation, so that the external potential experienced by an electron whose position is $\underline{r}$ at time t is:

$$\delta V(\underline{r},t) = V\, e^{i\underline{q}\cdot\underline{r}}\, e^{i\omega t}\, e^{\alpha t} + \text{complex conjugate}$$

The perturbation thus has angular frequency ω, wave vector $\underline{q}$, and is slowly growing with time constant α.

As a result of the perturbation the existing electron states become mixed with other states to give a new set of wave functions. There is consequently a change in the charge-density distribution in response to the external perturbing potential. This variation in charge-density itself gives rise to a potential which acts on the electrons, i.e.

$$\delta\Phi(\underline{r},t) = \Phi e^{i\underline{q}\cdot\underline{r}}\, e^{i\omega t}\, e^{\alpha t}$$

The total potential experienced by the electrons is thus:

$$\delta U(\underline{r},t) = \delta V(\underline{r},t) + \delta\Phi(\underline{r},t)$$

i.e. the electrons screen out the external potential δV by moving to produce a screening potential term $\delta\Phi$.

It can be shown (see Ziman 1972) that by using perturbation theory, the electronic susceptibility $\chi(\underline{q},\omega)$ can be written:

$$\chi(\underline{q},\omega) = \frac{4\pi e^2}{q^2} \sum_{\underline{k}} \frac{f^o(\underline{k}) - f^o(\underline{k}+\underline{q})}{E(\underline{k}) - E(\underline{k}+\underline{q}) + \hbar\omega - i\hbar\alpha}$$

The electronic susceptibility is defined by:

$$\Phi = \chi U$$

$E(\underline{k})$ is the energy of an electron in state $\underline{k}$, and $f^o(\underline{k})$ is the probability that the state $\underline{k}$ is occupied in the unperturbed metal. $f^o(\underline{k})$ would normally by the Fermi-Dirac function.

Then, since $U = V + \Phi$

$$\therefore\ U(1 - \chi) = V$$

i.e. $$U = \frac{V}{\epsilon}$$

where $\epsilon = 1 - \chi$ is the dielectric constant, so that

$$\epsilon(\underline{q},\omega) = 1 + \frac{4\pi e^2}{q^2}\left\{\sum_{\underline{k}} \frac{f^o(\underline{k}) - f^o(\underline{k}+\underline{q})}{E(\underline{k}+\underline{q}) - E(\underline{k}) - \hbar\omega + i\hbar\alpha}\right\}$$

The electrons experience not the external applied potential V, but an effective potential $U = V/\epsilon(\underline{q},\omega)$, which is reduced in value because of the screening effect of the electrons. It is to be noted that this expression for the dielectric constant is quite general, both as regards the nature of the perturbation and as regards the density of states and their occupation.

If the perturbation is a static one (i.e. $\omega = 0$), the the dielectric constant can be written (Ziman 1972):

$$\epsilon(\underline{q},0) \doteq 1 + \frac{\lambda^2}{q^2}$$

where λ^2 = constant, so that $\epsilon \to \infty$ as $q \to 0$. This means that very long wave-length perturbations are almost entirely screened out to give $\bar{U} \to 0$. $1/\lambda$ is a measure of how effective the screening is, and is known as the screening parameter.

Suppose that there is a perturbing potential δU at a point $\underline{r}$ relative to the origin. Then the Fermi distribution of electrons at $\underline{r}$ is lifted by a relative amount δU. But this means that the Fermi level is higher in this region of the metal unless electrons flow away from it. There is therefore a net flow of negative charge away from $\underline{r}$ so as to keep E_f constant throughout the material. This is illustrated schematically in Figure 29.

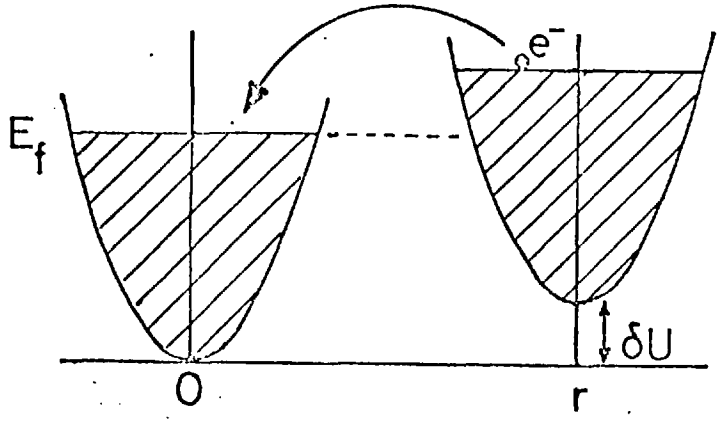


Figure 29

3.2 Phonons and the Kohn Anomaly

The previous section saw a general perturbation function being considered. Lattice vibrations, phonons, constitute examples of functions which perturb the electron gas periodically in a metal, and this section will deal exclusively with them.

3.2.1 Free Electron Model - Spherical Fermi Surface

This model was first considered by Kohn (1959). The lattice vibrations of the ions in a metal are partially screened by the conduction electrons, the degree of screening depending on the wavelength of the phonon.

The expression for the dielectric constant $\epsilon(\underline{q},\omega)$ is in general a very complex one to evaluate. Evaluation is however relatively simple for a free electron gas at absolute zero, i.e. for which the Fermi surface is a sphere in $\underline{k}$-space. The result at zero frequency is:

$$\epsilon(\underline{q},0) = 1 + \frac{4\pi e^2}{q^2} \cdot \frac{n}{\frac{2}{3}E_f} \left\{ \frac{1}{2} + \frac{4k_f^2 - q^2}{8k_f q} \ln\left|\frac{2k_f + q}{2k_f - q}\right| \right\}$$

where k_f is the radius of the Fermi sphere, and there are n electrons per unit volume. This expression can be expressed in terms of a screening parameter as before:

$$\epsilon(\underline{q},0) = 1 + \frac{\lambda^2}{q^2}$$

$$\text{i.e. } \lambda^2 = c\left\{ 1 + \frac{4k_f^2 - q^2}{4k_f q} \ln\left|\frac{2k_f + q}{2k_f - q}\right| \right\}$$

where $c = 2\pi e^2 n / \frac{2}{3}E_f$ is a constant.

It is interesting to consider the variation of λ^2 over certain ranges of q:

(a) As $q \to 0$. This can be obtained by expanding the logarithms for small $q/2k_f$:

$$\lambda^2 = c\left\{ 1 + \frac{4k_f^2 - q^2}{4k_f q} \ln\left|1 + q/2k_f\right| - \ln\left|1 - q/2k_f\right| \right\}$$

This expression, for small $q/2k_f$, can be approximated by:

$$\lambda^2 = c\left\{1 + \frac{4k_f^2 - q^2}{4k_f^2}\right\}$$

$\rightarrow 2c$ in the limit as $q \rightarrow 0$.

(b) As $q \rightarrow \infty$. This can be obtained by expanding the logarithms for small $2k_f/q$:

$$\lambda^2 = c\left\{1 + \frac{4k_f^2 - q^2}{4k_f q} \ln\left|1 + 2k_f/q\right| - \ln\left|1 - 2k_f/q\right|\right\}$$

$$\rightarrow c\left\{1 + \frac{4k_f^2 - q^2}{q^2}\right\}$$

$\rightarrow 0$ in the limit as $q \rightarrow \infty$.

(c) As $q \rightarrow 2k_f$. The critical factors in the expression for the screening parameter are $(2k_f - q)$, since these tend to zero. There are two such factors, one inside the logarithm, and one multiplying the logarithm. i.e. although there is a logarithmic infinity as $q \rightarrow 2k_f$, this is multiplied by a term which tends to zero more rapidly:

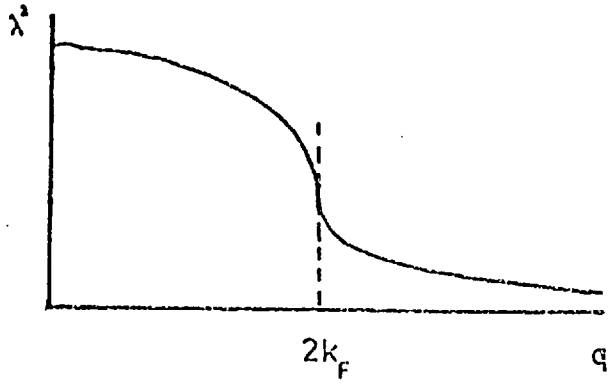
$$\text{As } q \rightarrow 2k_f, \quad (2k_f - q)\ln(2k_f - q) \rightarrow 0.$$

$\therefore \lambda^2 \rightarrow c.$

The screening parameter thus remains finite at $q = 2k_f$. The derivative of λ^2 however has a singularity in it, since $\frac{d}{dq}(\lambda^2) \propto \ln(2k_f - q) \rightarrow -\infty$ as $q \rightarrow 0$.

The overall behaviour of the screening parameter with wave vector can be seen in Figure 30. This shows that for q very small, the electrons effectively screen out the lattice vibration completely. As q increases, the effective screening length, $1/\lambda$, increases to infinity, i.e. it becomes progressively more and more difficult to screen out potentials with shorter wave-length.

Figure 30



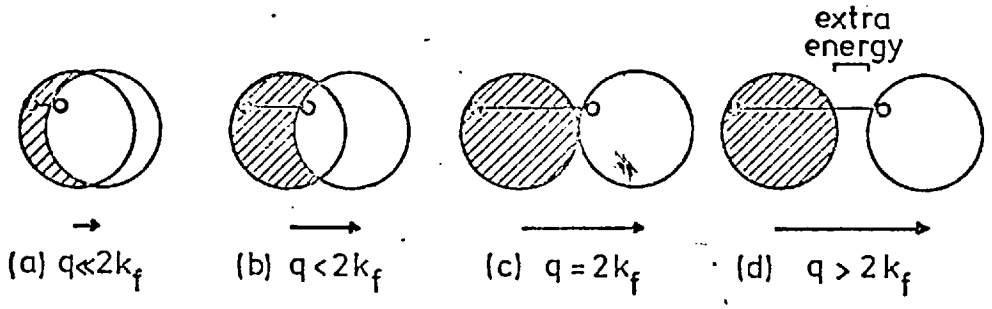


Figure 31 The Kohn Anomaly for a spherical Fermi Surface, as the perturbing wave vector $\underline{q}$ is increased through the critical value $2\underline{k}_f$

3.2.2 The Kohn Anomaly

From the consideration of the screening parameter in the previous section it can be seen that the most interesting effect occurs at $q = 2k_f$. It was shown that there is a logarithmic singularity in $d\epsilon/dq$ at this value, which gives rise to what is known as the Kohn Anomaly (Kohn 1959). The way the singularity comes about can be visualised by again studying the mechanism by which the electrons attempt to screen out the perturbation.

As a result of the perturbation, electrons are scattered from occupied states with wave vector $\underline{k}$ to unoccupied states, $\underline{k} + \underline{q}$, — the numerator in the expression for the electronic susceptibility in section 3.1 contains $\sum_{\underline{k}} \{f^o(\underline{k}) - f^o(\underline{k}+\underline{q})\}$.

For $q \ll 2k_f$, these lie in small regions covering the surface of the Fermi sphere - Figure 31(a). As q increases, these two regions increase in size as the summation in the numerator increases (b), in order to screen out the shorter wavelength vibrations. At $\underline{q} = 2\underline{k}_f$ all the states on the surface of the sphere contribute to the summation, and therefore to the electronic susceptibility (c). However, as $\underline{q}$ approaches $2\underline{k}_f$ the number of *new* states contributing to the screening becomes progressively smaller. The number of *new* states contributing is zero for $q > 2k_f$. Because the number of *new* states in the summation does not abruptly become zero at $\underline{q} = 2\underline{k}_f$ the Kohn anomaly is not very marked for a spherical Fermi surface.

As soon as q exceeds $2k_f$ there is a marked decrease therefore in the ability of the electrons to screen out the perturbation. When q is less than twice the Fermi surface radius the screening must be by virtual excitations across the Fermi surface (energy conserving) as in Figure 31 (a). For $q > 2k_f$

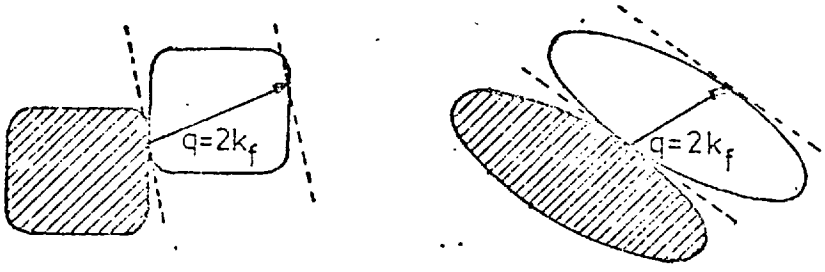
the electron has to be excited to a state above the Fermi level — Figure 31 (d) — and this require extra energy which is proportional to $(q - k_f)^2 - (k_f)^2 = q(q - 2k_f)$ — Kohn 1962.

3.2.3 Non-Spherical Fermi Surfaces

The theory outlined in 3.2.1 and 3.2.2 was for a spherical Fermi Surface, i.e. a free electron gas. The Fermi surface for electrons in a periodic lattice rarely even approximates to a sphere, except for a few simple metals.

Within a lattice, translational invariance must be taken into account. This is reflected in reciprocal space by the fact that the relationship $\underline{q} = 2\underline{k}_f$ must be replaced by $\underline{q} + \underline{K} = 2\underline{k}_f$, where $\underline{K}$ is any reciprocal lattice vector. This relationship holds whatever the shape of the Fermi Surface, in the following manner. The vector $\underline{q}$ now must connect two points on the Surface which have parallel tangential planes, and may now be said to "span" the Fermi Surface. Some examples of "spanning" vectors are given in Figure 32. It needs to be noted that if the Surface is multi-segmented there may be several values of $\underline{q}$ which span different segments for a given direction.

Figure 32



The expression for the dielectric constant $\epsilon(\underline{q},\omega)$ has to be evaluated separately for each Fermi Surface geometry, which is extremely laborious. Afanasev and Kagan (1963) have however considered the general form of the dielectric constant function, and therefore of the Kohn Anomaly, for three general cases. Their results will prove extremely useful in Chapter 11.

(a) Approximately Spherical Fermi Surface

This case has already been dealt with in some detail in the preceeding sections. To summarise, the dielectric constant remains a smooth function of $\underline{q}$ throughout, even at $\underline{q} = 2\underline{k}_f$. The Kohn Anomaly manifests itself through the logarithmic singularity in $d\epsilon/dq$:

$$d\epsilon/dq \rightarrow \ln(q - 2k_f) \quad \text{close to } \underline{q} = 2\underline{k}_f.$$

Although ϵ remains finite, its differential becomes infinite, giving rise to a relatively weak Kohn Anomaly. This explains why attempts to observe the effect in alkali metals have been relatively unsuccessful (see Overhauser, 1971).

In this approach it is useful to think of a spherical Surface as having two radii of curvature at right angles, which are equal and of the same sign. The case of a Surface with radii of curvature of opposite sign (leading to a saddle point with zero curvature) is considered in the next section.

(b) Approximately Cylindrical Fermi Surface

The change to cylindrical symmetry from spherical changes the dependence of $\epsilon(\underline{q},\omega)$ on $\underline{q}$ in a very significant way. A cylindrical Surface (or more generally, one with a constant cross section) has at any point only a curvature in one direction. Afanasev and Kagan show that close to $\underline{q} = 2\underline{k}_f$:

$$\lambda^2 \propto \left\{1 - \frac{(q^2 - 4k_f^2)^{\frac{1}{2}}}{q}\right\}$$

Since $$\epsilon(\underline{q},0) = 1 + \lambda^2/q^2,$$

the dielectric constant remains finite at $\underline{q} = 2\underline{k}_f$.

The predominant term in $d\epsilon/dq$ is proportional to:

$$(q^2 - 4k_f^2)^{-\frac{1}{2}} \rightarrow \infty \quad \text{as} \quad q \rightarrow 2k_f.$$

Hence, although the dielectric constant remains finite, its differential shows a singularity, which is stronger, being of the form $\frac{1}{(q - 2k_f)^{\frac{1}{2}}}$, rather than logarithmic (spherical case).

(c) Approximately Planar Fermi Surface

The parts of a Fermi Surface which are approximately planar (corresponding to 1-D conductivity) have zero curvature. The predominant term in the screening near $q = 2k_f$ gives:

$$\lambda^2 \propto \ln\left|\frac{1}{(q - 2k_f)^{\frac{1}{2}}}\right|$$

Thus $\epsilon(\underline{q},0) = 1 + \lambda^2/q^2 \to \infty$ as $q \to 2k_f$,

and $d\epsilon/dq \propto (q - 2k_f)^{-1} \to \infty$ as $q \to 2k_f$.

It can be seen that the singularity in the differential of the dielectric constant is even stronger than in the cylindrical case. What is more important however is the behaviour of $\epsilon(\underline{q},0)$. In this case alone, this function has a singularity at $\underline{q} = 2\underline{k}_f$, with a logarithmic divergence to infinity. In terms of screening potentials, this means that since $U = V/\epsilon$, therefore $U = 0$.

i.e. $\Phi = -V$.

The electronic response, Φ, to the external field, V, is such as to cancel it out exactly, giving zero resultant field. In other words there is an instability arising from the interaction between lattice phonons and the conduction electrons, which gives rise to a permanent static distortion of the ions in the lattice coupled to an equal distortion of the electronic charge density. This case corresponds in fact to a Peierls (1955) distortion. The distortion is spontaneous and does not require an external field.

3.2.4 Radius of Curvature of the Fermi Surface

Fehlner and Loly (1974) have considered in more detail the

form of the Kohn Anomaly in the susceptibility $\chi(\underline{q})$ close to $\underline{q} = 2\underline{k}_f$, and how it varies with the curvature of the Fermi Surface. In the limit of a Fermi Surface consisting of flat parallel sheets (known as 'nesting'), the Anomaly takes the form of a logarithmic divergence in $\chi(\underline{q})$ at $\underline{q} = 2\underline{k}_f$ — Figure 33.

Figure 33

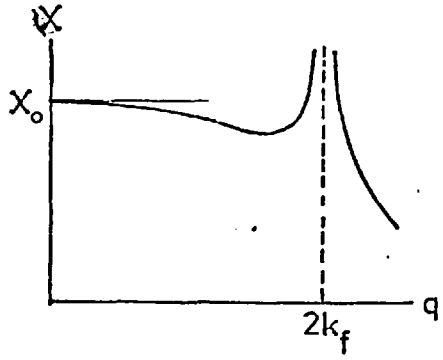
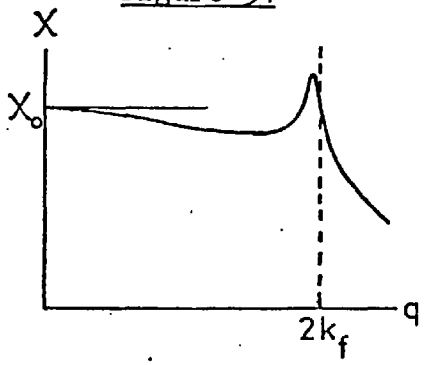


Figure 34



They then consider sheets of Fermi Surface of large, but finite radius of curvature. The sheets are doubly curved and approximate to being spherical. The calculations give a function for $\chi(\underline{q})$ rather as shown in Figure 34, which is drawn with a radius of curvature, $R = 15\,k_f$. There is now a finite peak in the susceptibility, which is shifted slightly to a value of q slightly less than $2k_f$. As R increases (tending to a flat surface) the peak becomes higher, shifting closer to $2k_f$. As R decreases the peak persists at least until $R = 9k_f$.

More recently Rice and Scott (1975) have pointed out that a 2-D energy band with saddle points can also have a logarithmic divergence in the electronic susceptibility at $\underline{q} = 2\underline{k}_f$, joining the saddle points.

3.2.5 Phonon Image of Fermi Surface

Kohn originally predicted that the Anomaly at $\underline{q} = 2\underline{k}_f$ should be visible in the phonon spectra of metals, and furthermore should in principle give rise to an 'image' of the Fermi Surface. In practice, however, as Fehlner and Loly (1974) have

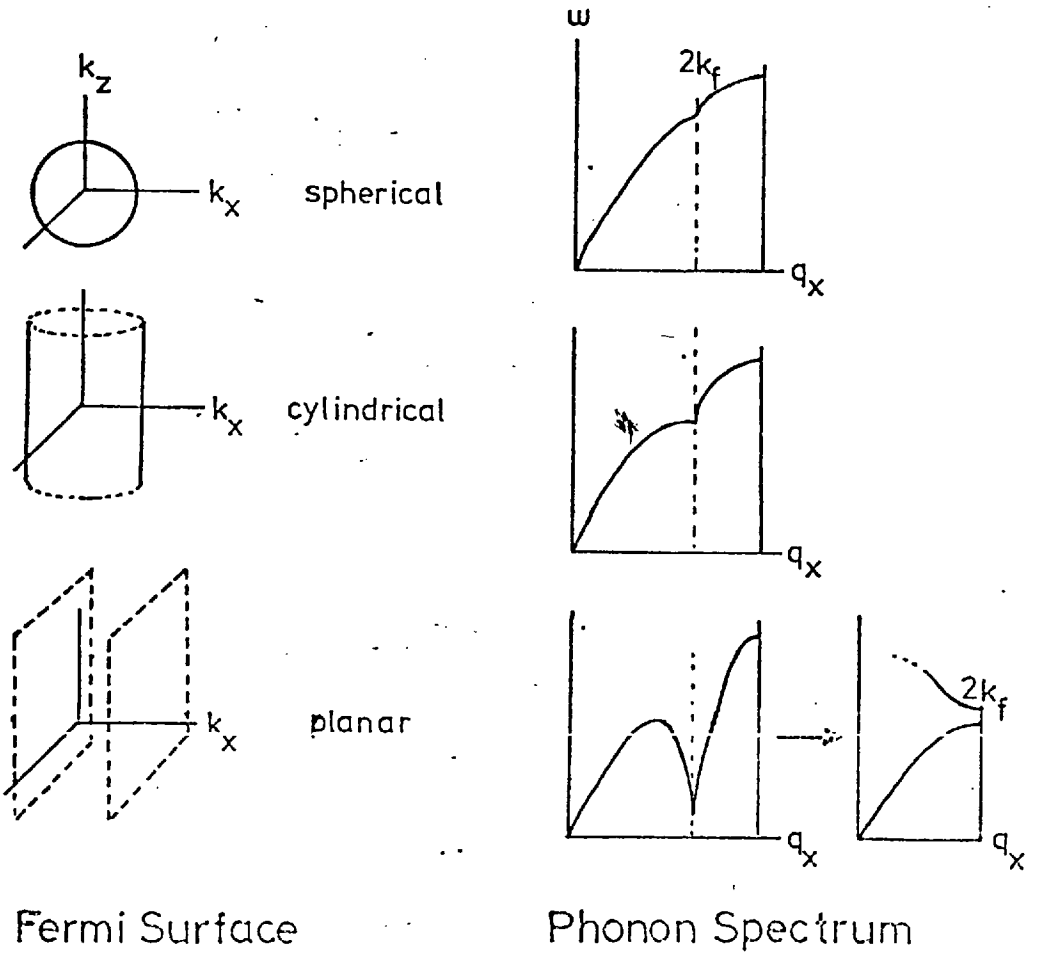


Figure 35 The Kohn Anomaly in the phonon spectrum for three general types of Fermi Surface (Afanasev & Kagan).

calculated, the effect in the phonon spectrum is extremely small unless the Surface has a very special geometry, and consists in part of planar sheets. Thus, only those parts of the Surface with small curvature are mapped out.

The Kohn anomaly is effective in producing mode softening (i.e. reducing the frequency of a mode at fixed $\underline{q}$ to zero) close to $\underline{q} = 2\underline{k}_f$. This can be understood as follows: when the electrons move to screen out the field produced by the displacements of the ion cores, they alter the strength of the electrostatic interaction between the ions. The screening effect in general tends to reduce to forces between ions, so that the mode frequency must be modified. The magnitude of the reduction in frequency is dependent on the strength of the screening, i.e. on $\epsilon(\underline{q})$. If there is a singularity in $\epsilon(\underline{q})$ so that the dielectric constant becomes infinitely large, in the limit, there must be a large decrease in frequency corresponding to this value of $\underline{q}$ (in the limit, a decrease to zero).

Suppose that Ω_p is the frequency of a mode of oscillation of the lattice in the absence of conduction electron effects. When the conduction electrons are added, the crystal field must be modified by a factor $1/\epsilon(\underline{q},\omega)$. Since the frequency of oscillation is proportional to the square root of the force field between the ions, the mode frequency, ω_p, must now be given by:

$$\omega_p^2 = \frac{\Omega_p^2}{\epsilon(\underline{q},\omega)}$$

This expression shows clearly that when the dielectric constant increases, ω_p^2 decreases and the mode is softened.

The form of phonon spectrum in the presence of a Kohn Anomaly is shown in Figure 35 for three general cases: spherical, cylindrical and planar Fermi Surfaces (from Afanasev and Kagan, 1963). In the last case $\epsilon(\underline{q}) \to \infty$ as $\underline{q} \to 2\underline{k}_f$, and so the mode is

completely softened to give a static deformation of the lattice. This is equivalent to the appearance of a new Bragg plane in $\underline{k}$-space.

The first experimental measurements confirming the existence of the Kohn Anomaly were carried out by Brockhouse, Rao and Woods (1961) on the metal lead.

3.3 Ordering and the $\underline{q} = 2\underline{k}_f$ Instability

Because of its relevance to this investigation, the emphasis in the present Chapter is on periodic perturbations of the conduction electrons arising from periodic displacements of the ions from their ideal sites. The divergence of the electronic susceptibility at $\underline{q} = 2\underline{k}_f$ can however be caused by any periodic perturbation of the potential, and so it can equally well be produced by variations in ionic charge, e.g. in an ordered alloy. The theory has in fact been applied successfully to ordering in copper-gold alloys (see for instance Sato and Toth, 1968). In these materials $\underline{q} = 2\underline{k}_f$ corresponds to the observed long-period superlattices.

The theory of the instability of the electronic susceptibility at $\underline{q} = 2\underline{k}_f$ could well apply to the ordering of an intercalate superlattice within the interlamellar space of a layer material, although other energy terms might predominate over electronic ones.

An important difference between ordered and deformation superstructures is that the former must generally speaking be commensurate with the lattice whilst the latter can also be incommensurate. It might therefore be expected that in an ordered superstructure, the value of $\underline{q}$ chosen will be that of a commensurate vector as close as possible to $2\underline{k}_f$, rather than $2\underline{k}_f$.

3.4 Charge-Density Waves and Spin-Density Waves

In this Chapter we are principally concerned with a pair of coupled systems: the electrons and the phonons in a metal. The nature of the electron-phonon interaction is not to be studied in detail here, since it is somewhat complex. Barisic (1972) and Ziman (1959) discuss it in some depth.

Having discussed how the Kohn Anomaly manifests itself in the phonon spectrum, in Section 3.2, it is proposed in this Section to study its effect on the conduction electron system. In the act of screening out a periodic potential, the electronic charge must itself assume periodic fluctuations in density (Fig. 36). The deformation of the lattice gives rise to a varying E_f, and the electrons respond by redistributing to make E_f uniform throughout the metal. The periodic fluctuations in electronic charge density was first called a charge-density wave by Overhauser (1968).

The effect of each deformation wave or phonon is to modulate the average ionic density of the lattice. In the case of an incommensurate wave, the density modulations can be taken to be in 'jellium' - a continuous positive charge distribution. In order to maintain neutrality, the electronic charge density must follow the modulations in the jellium.

For the simple model of a LA deformation wave in a lattice, the wave can be represented by a periodic function $f(\frac{2\pi r}{\Lambda})$ where Λ is the wavelength of the deformation, and r is measured in the direction of propagation.

Given that the charge density in the undistorted lattice is ρ_o, an expression can be quickly derived for the charge-density when the lattice is distorted by f, i.e.

$$\rho(r) = \rho_o(1 - \frac{df}{dr})$$

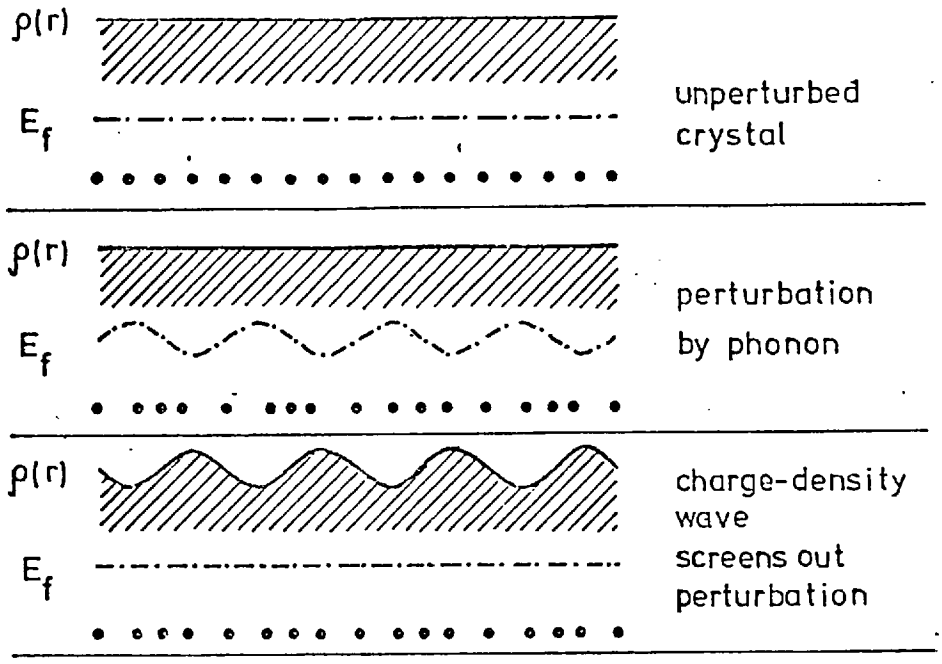


Figure 36 Formation of a charge-density wave in response to a perturbing phonon in a 1-D lattice.

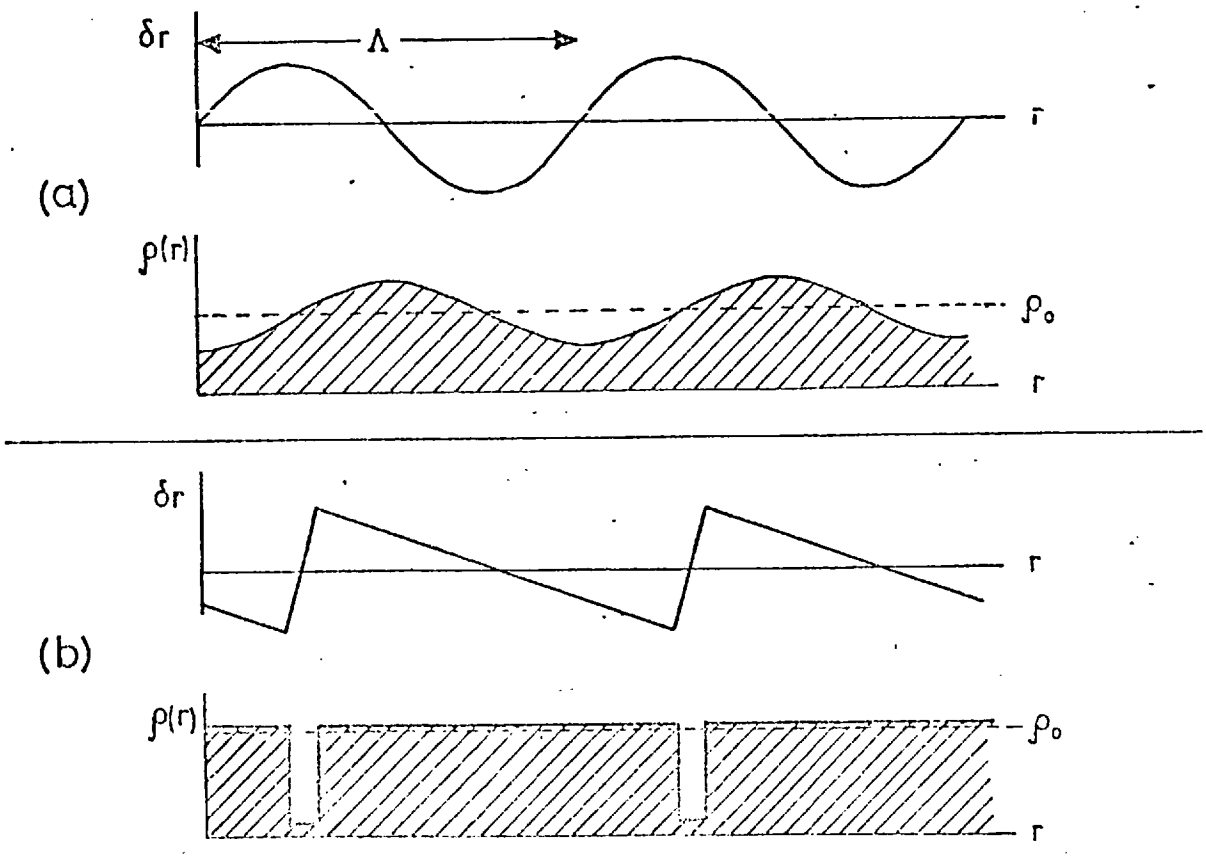


Figure 37 The form of the CDW for a sinusoidal (a) and a sawtooth (b) modulating deformation function.

This simple relationship is very important, for it shows that the maxima in the charge-density occur, not where the maximum displacements are but where the function f is changing most rapidly since differentiation is involved. This is best understood by taking the example of a pure sinusoidal deformation wave, such that:

$$f(r) = U \sin(2\pi r/\Lambda)$$

$$\therefore \quad \rho(r) = \rho_o\left[1 - \frac{2\pi U}{\Lambda}\cos(2\pi r/\Lambda)\right]$$

There is a shift of $\pi/2$ in the phase of the density fluctuations relative to the deformation wave, Figure 37 (a).

For a sawtooth wave - Figure 37(b) - the charge-density function is a constant over most of the range, except at the periodic 'gaps', where the electronic charge-density drops very low. If the sawtooth function itself had an infinitely steep slope at $(2n+1)\pi/2$, then the gaps in the charge-density would become δ-functions. Since this is physically rather unrealistic, the sawtooth has been drawn with a finite slope.

If three symmetry-related deformation waves are taken (as in section 2.5.3) the positions of the maxima and minima in the charge-density depend on the relative phase of the waves. For $\phi = \pi$ the maxima occur at the positions (0,0) and the minima at $(\frac{2}{3},\frac{1}{3})$ and $(\frac{1}{3},\frac{2}{3})$ in the hexagonal layer deformation cell.

It is possible to calculate the amplitude of the charge density fluctuations, given the amplitude of the deformation wave. For the sinusoidal charge-density wave:

$$\rho_{max} = 2\pi\rho_o U/\Lambda$$

For the sawtooth charge-density wave, ρ_{max} is the increase in charge density in the clusters and is given approximately by:

$$\rho_{cluster} = 2\rho_o U_{max}/\Lambda$$

where U_{max} is the maximum displacement due to the sawtooth. The charge-density in the 'gap' clearly depends on its width.

Overhauser (1968) considered a general model for perturbation of the conduction band, in which there are combinations of exchange and correlation interactions between the electrons (coupling via phonons is an example of a correlation interaction). He takes an electronic ground state for which the spin-up and spin-down electron densities are:

$$\rho^{+}(\underline{r}) = \tfrac{1}{2}\rho_{o}[1 + p\cos(\underline{q}.\underline{r} + \psi)]$$
$$\rho^{-}(\underline{r}) = \tfrac{1}{2}\rho_{o}[1 - p\cos(\underline{q}.\underline{r} - \psi)]$$

The mean electron density is therefore ρ_o, and the fractional modulation created by the perturbation of wave vector $\underline{q}$, is p. As the phase, ψ, is modulated the following kinds of situation arise:

(a) $\psi = 0$, spin-up and spin-down are modulated with the same phase, giving rise to fluctuations in the charge density:

$$\rho^{+}(\underline{r}) + \rho^{-}(\underline{r}) = \rho_{o}[1 + p\cos(\underline{q}.\underline{r})]$$

This constitutes a charge-density wave (CDW).

(b) $\psi = \pi/2$, spin-up and spin-down are modulated in opposite phase so that there are fluctuations in the spin density, but not in the charge density:

$$\rho^{+}(\underline{r}) - \rho^{-}(\underline{r}) = \rho_{o}\, p\, \sin(\underline{q}.\underline{r})$$
$$\rho^{+}(\underline{r}) + \rho^{-}(\underline{r}) = 0$$

This constitutes a spin-density wave (SDW).

(c) $0 < \psi < \pi/2$ For intermediate values of phase, there is a mixed charge and spin density wave . There are both spin and charge variations in the lattice.

The charge-density wave involves a redistribution of charge. The consequent increase in electrostatic energy prevents a CDW from existing without other energy terms to balance this out. The formation of a CDW may be energetically favourable if it is

coupled to a periodic deformation of the crystal lattice so that ionic charge is also re-arranged as a balance. The circumstances under which a spin-density wave is stable must clearly differ. It is not possible to discuss the criteria for the stability of CDW, SDW and mixed CDW/SDW states here: they are all discussed in some detail by Chan and Heine (1973) and Overhauser (1968). Spin-density waves have been known to exist for some time, the first to be observed being in chromium, using spin-sensitive neutron scattering (Lomer, 1962).

3.5 Charge-Density Waves and Energy Gaps

The periodicities associated with the CDW in the conduction electrons introduce Bragg planes at $\pm\frac{1}{2}\vec{q}$ in an exactly analogous way to the lattice periodicities in the crystal. The deformation periodicities therefore also define Brillouin zones. Using perturbation theory it can be shown (see for example Ziman 1972) that a discontinuity or gap in the electron energy is produced at the zone boundaries. The two values of the energy function at the boundaries correspond to the bonding and anti-bonding states in a periodic crystal. The theory is essentially the same whether the gaps result from crystal periodicities or deformation periodicities.

In Figure 38 the formation of energy discontinuities is shown for an incommensurate deformation in a 1-D crystal. If it were commensurate, we should have to consider a reduced Brillouin zone. This is not possible otherwise, and the two sets of zone boundaries (from the lattice and from the deformation) exist independently.

The magnitude, ΔE, of the energy gap is a function of the fractional modulation of the charge-density, and thus of the deformation amplitude. It needs to be emphasised that the

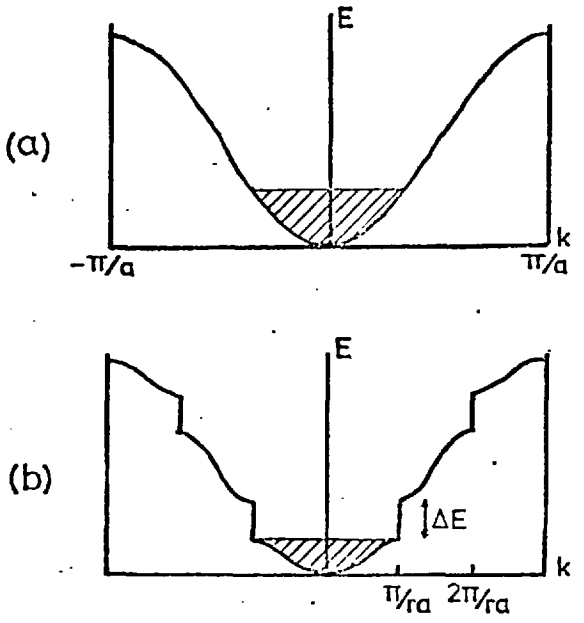


Figure 38 Distortion of a lattice produces gaps in the electronic energy band structure.

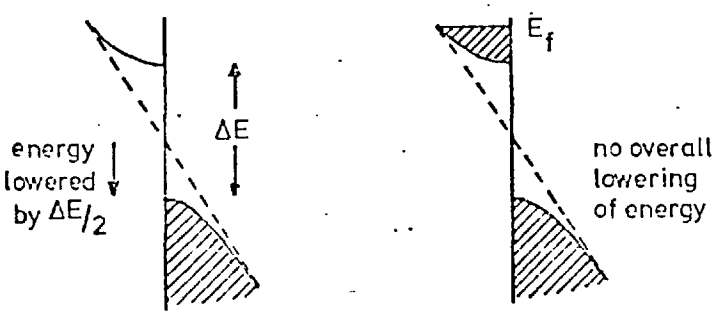


Figure 39 An overall lowering of energy for the conduction electrons only occurs when the boundary introduced by the perturbation coincides with the Fermi level.

energy gaps are produced at $\pm \frac{1}{2} n\underline{q}$, i.e. that the gaps are directional, and do not necessarily extend round the entire Fermi Surface. In this respect the 1-D figures can be rather misleading.

For a charge-density wave, $\underline{q} = 2\underline{k}_f$, since the phonon spans the Fermi Surface; i.e. all the states up to $\underline{k}_f$ are occupied in that direction. The energy discontinuity thus appears at $\pm \underline{k}_f$ at the Fermi Surface. The CDW is therefore able to effect an overall reduction in energy, since occupied states close to the gap have had their energy lowered - see Figure 38. This lowering in energy can only occur at the points where the Bragg plane intersects the Fermi Surface. At other points on the Bragg plane a notional gap is introduced, but there is no lowering in energy since states both above and below the gap are occupied, and are raised and lowered in energy by equal amounts (Figure 39). The way that a CDW introduces gaps at the Fermi Surface is considered in more detail by Overhauser (1968).

There must be a slight distortion of the Fermi Surface at, and in the immediate vicinity of, the point at which it touches the new zone boundary. The distortion of a free electron sphere is shown in Figure 40.

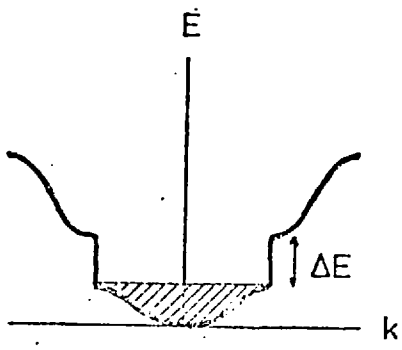
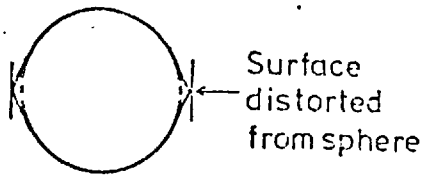


Figure 40



3.6 Metal-Insulator Transitions

In the previous section it was pointed out that the charge-density wave introduces gaps into the energy bands. If a gap extends all the way round the Fermi Surface then the material will have undergone a transition from metal to insulator (or more correctly to a semiconductor, since the gap must necessarily be small). In a material which has charge-density waves in a number of symmetry related directions with a large fractional modulation, p, this could indeed happen. In general however it is more probable that gaps would exist around some of the Fermi Surface, but not all of it. In this case anisotropy in electrical and magnetic properties might be expected. For instance a reduction in conductivity would be predicted for directions parallel to the CDW wave vectors.

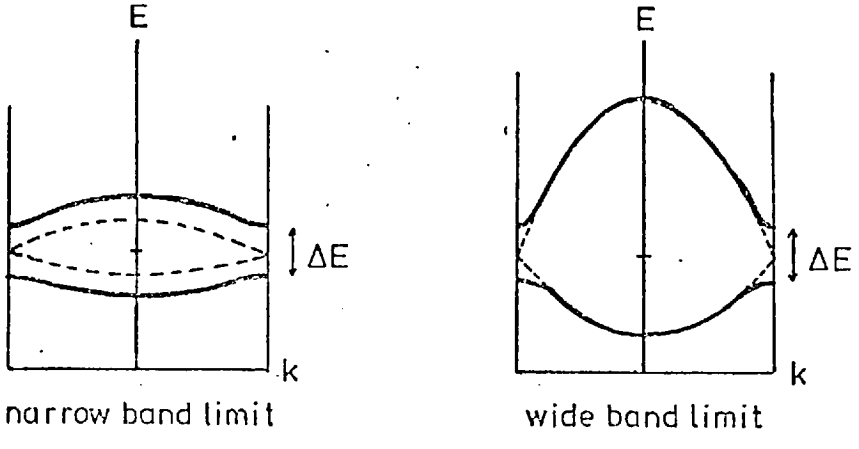
The one-dimensional case has been considered in some detail by Peierls (1959). He showed that a linear metal with a partially filled conduction band could never be stable since a distortion could always be found to produce an energy gap at the edge of the Fermi distribution. The most favourable case energetically for a Peierls distortion would be with an exactly half-filled band. In this case the metal atoms are displaced to form pairs. For a smaller fractional filling of the band, the Peierls distortion leads to clusters (i.e. 1-D groups) of atoms.

In a three-dimensional metal such effects are likely to be weak in general. They would however be enhanced if appreciable areas of Fermi Surface are approximately planar. A metal whose Fermi Surface approximates to a cube could become semiconducting as a result of symmetry-related CDWs with wave vectors spanning this Surface. The condition for there to be a large Peierls distortion thus proves to be the same as that for an enhanced

Kohn Anomaly. In fact the Peierls distortion can most simply be considered as a Kohn Anomaly in the limit as the phonon frequency is softened to zero.

Adler and Brooks (1967) discuss which metals are most likely to undergo metal-insulator transitions. They conclude from their calculations that if the conduction bands are extremely narrow (as happens for example in transition and rare earth metals), the distortion depresses the entire lower band and raises the entire upper band. The energy gap thus tends to open up along the whole of the Fermi surface at once. The transition to an insulating (semiconducting) state is consequently a favourable one. With a wide conduction and valence band the distortion however only introduces small gaps where the Surface crosses the boundaries of the reduced first Brillouin zone, and so only a small fraction of each band is displaced near the zone edge. Here then the electronic energy gained is proportionally smaller, and cannot dominate the loss in strain energy due to the distortion which is introduced in the lattice. Figure 41 attempts to illustrate the difference between narrow and broad band metals. Narrow band metals are in principle energetically more likely to undergo a Peierls-like distortion.

Figure 41



3.7 Superconductivity and Charge-Density Waves

It is worthwhile taking a little space to think about the relationship between these two phenomena, especially since some of the materials of interest exhibit both.

The theory of superconductivity (Bardeen, Cooper and Schrieffer, 1957) is based on the fact that the interaction between electrons resulting from a virtual exchange of phonons is attractive, provided that the energy difference between the electron states involved is less than the phonon energy ($\hbar\omega$). In order for there to be a superconducting phase, this interaction must dominate the repulsive screened Coulomb interaction. In the ground state of a superconductor the electrons are in pairs of opposite spin and momentum, and are coupled by the virtual phonon so as to have a lower energy than in the normal state. There are excited states in which the 'Cooper pairs' - i.e. the electron-phonon collective mode - move through the crystal with small velocities. Below the transition temperature T_c to the superconducting phase, there is a small energy gap for single particle excitations, i.e. for those which would break the pair, which decreases to zero as the temperature is raised through T_c. The transition from the superconducting to the normal state is second order thermodynamically. Frohlich (1953) showed that a coupled electron-phonon mode has position invariance and can move through the crystal, carrying current, without attenuation, and therefore giving rise to infinite conductivity. Expressed another way, the phonons which normally scatter the electrons and giving rise to resistance, do not have sufficient energy at these low temperatures to break up the electron pairs.

The charge-density wave ground state (as defined above, with a static distortion) is in many respects very similar to

the superconducting ground state. In both cases there is a coupling between electron states at the Fermi surface by a distortion of the lattice, although spin correlation is not essential for a CDW. In both cases the theory shows that an energy gap is produced at the Fermi level.

Lee, Rice and Anderson (1974) consider conductivity from charge and spin-density waves, particularly for 1-D systems, and conclude that the condition of translational invariance must hold for an incommensurate CDW (since this is basically the same condition as for a CDW in 'jellium'). There must therefore by conduction by coupled electron-phonon collective modes as in a superconductor. They note that the charge-density wave system can carry current since it consists of pairs of similarly charged electrons, whereas the excitonic state cannot do so because the electron-hole system is electrically neutral. The current-carrying collective electron-phonon mode can be broken by short phonon lifetimes, impurity scattering, or by the CDW becoming commensurate with the lattice.

If impurity scattering is to be included then a lifetime for the collective mode which is proportional to $\exp(E_g/kT)$ is introduced. $2E_g$ is the energy gap for single electron excitations. Impurity scattering, the authors argue, thus becomes negligible for low temperatures. When the collective mode is scattered by the impurity centre it gives up momentum $q = 2k_f$ to the impurity. In other words the impurities damp out the coupled electron-phonon mode, by interaction with the phonon via modulation of the charge-density surrounding the impurity.

If the CDW becomes commensurate with the crystal lattice then translational invariance is immediately lost. There is

now an energy gap in the collective mode spectrum, so that this type of conductivity by coupled electrons ceases. In 3-D as before, there clearly needs to be a gap extending around the entire Fermi surface.

Thus superconductivity would appear to arise from a spin-correlated CDW electron-phonon mode, at sufficiently low temperatures that there is negligible excitation of single electrons. A CDW formed at higher temperatures will also conduct by collective modes, but there will be severe damping by impurities, etc., since single electron excitations are energetically possible. One factor which distinguishes the two states is clearly therefore temperature and the dependent stability of coupled electrons. It would also seem that similar criteria might be applied when attempting to predict which materials might superconduct or might be subject to large amplitude CDWs. It is also interesting to speculate whether a transition to a commensurate CDW would inhibit superconductivity in the material in the direction of the commensurate deformation wave vector. Such conjectures must however be treated with the caution deserving of a subject as yet only partially understood.

4 EXPERIMENTAL PROCEDURES

4.1 Materials

Of the transition metal layer dichalcogenides studied in this investigation, only molybdenum disulphide occurs in appreciable quantities in nature, and flakes of naturally occurring molybdenite were used in the lattice resolution studies (this occurs as a mixture of the 2H and 3R polytypes).

Crystals of the other materials are most readily grown by chemical vapour transport (Schafer, 1964) using a halogen carrier in two- or three-zone furnaces — for experimental details see DiSalvo(1971). The heavy metal sulphides (e.g. TaS_2) are particularly difficult to grow as good single crystals, partly because of the huge difference in the metal and sulphur vapour pressures, and partly because their natural anisotropy leads to extremely thin,hexagonal, plate-like crystals. While thin flat crystals which undergo ready cleavage are ideal for electron microscopy, their shape is very far removed from the ideal equiaxed shape required for quantitative X-ray studies. The crystals are generally speaking much too thin for routine neutron scattering experiments also.

The present work relied very much on the supply of crystals from other laboratories (noted in the Acknowledgements). The results obtained proved not only to be reproducible within the same growth batch, but also between batches from quite different origins. Special care was taken over the investigation of 2H $NbSe_2$, since the reported electrical and magnetic anomalies are known to be susceptible to crystal impurity. Only crystals which had previously been shown to exhibit the correct electrical properties (i.e. a sign reversal of the Hall coefficient at 26 K) were subjected to full diffraction examination.

At the temperature used for the vapour transport growth of tantalum disulphide crystals, the octahedrally co-ordinated 1T polytype is the stable one. Rapid quenching to room temperature after growth ensured that the material remained in the now metastable 1T form. Transformation to 2H tantalum disulphide was effected by annealing the crystals at about 400 °C for about a week, followed by slow cooling. Although the gold colour of the 1T phase changes to black in 2H TaS_2, this was not taken as the main criterion of conversion. X-ray diffraction was used to confirm finally that the interpolytypic transformation had fully taken place.

4.2 Intercalation

The intercalation complex of pyridine with 2H TaS_2 was prepared by refluxing small hexagonal crystal plates of the host material with pyridine at 110 °C for about a day. Intercalation was considered to be complete when the crystals doubled in thickness and changed in colour from black to gold. Full details of experimental techniques for intercalation with pyridine and a wide range of other organic nitrogen compounds are given in Gamble, Osiecki and DiSalvo (1971), and Di Salvo (1971). After intercalation, excess pyridine was washed off in methanol. X-ray diffraction confirmed not only that the intercalation process was complete, but that the complex remained stable for at least six months. There was no reason to suppose that it would not be permanently stable at room temperature. Reproducible results were obtained from intercalation experiments carried out on different batches of crystals at different times.

4.3 Electron Diffraction Studies

Crystals of pure and intercalated layer materials cleave extremely easily along the basal plane. All the materials

were prepared for electron diffraction and microscopy by successive cleavage using adhesive tape, until there were extremely thin (i.e. of the order of 500 Å) areas of crystal which were transparent to electrons. Great care was taken during cleavage to avoid undue deformation of crystals, for instance by bending. Whether the crystals were relatively deformation-free was also checked by studying the dislocation structure in the electron microscope before proceeding to diffraction or high resolution studies. The solvent generally used to soak the specimens off the adhesive tape and on to copper grids was trichloroethylene. Adequate soaking to remove most of the traces of adhesive usually took about an hour.

Most of the diffraction studies were carried out using a JEOL JEM 7A electron microscope (incident electron beam energy 100 keV). This instrument could be fitted with both a liquid nitrogen cold stage and a heating stage, so that selected area diffraction patterns could be monitored over a wide range of temperature, from about 150 K to about 800 K if necessary. The lower end of the temperature range was extended down to about 16 K, using modified Siemens 1A and Hitachi instruments in other laboratories. The former had helium gas cooling, which gave relatively quick specimen changes but less ability to reach really low temperatures. The Hitachi instrument was generally slower to use, but had the greater temperature range. All the stages used on the three instruments had limited facilities for tilting the specimen.

4.4 High Resolution Phase Contrast Electron Microscopy

Areas of crystal, which were prepared in a similar manner to those for diffraction studies (4.3), were also studied at screen magnifications of up to 500 000 times in the JEOL JEM 100B

electron microscope. Areas of thickness about 100 Å on the edge of a somewhat thicker crystal were usually chosen for high resolution study. The nearby edge aided focusing, while the thick adjacent crystal acted both as a support and as a heat sink for the area under study.

The cleavage properties of the crystals meant that it was generally possible (in the absence of a tilting facility for the specimne stage) only to record data with the electron beam at normal incidence to the dichalcogenide layers. The small deviations from normal incidence required to image the distortions in some of the materials were obtained by finding locally tilted regions, close for instance to dislocations or bend (Bragg) contours. In what will be called the'bright-field' technique the beams admitted by the diffraction aperture included the zero-order, undeviated beam). The phrase'dark-field' technique will be reserved for the case where the beams transmitted by the aperture to form the image did not include (as a result of double tilting the incident beam)the zero-order beam. Since there was complete consistency between the bright and dark field n-beam lattice images of the materials, the latter technique was usually employed for the tantalum disulphide polymorphs, since the reduction in background illumination considerably aided the visibility of the weak deformation fringes.

Although (because of the weakness of the fringes) exposures of up to 60 s were sometimes necessary, resolution better than 2 Å was maintained by working at times of minimum external vibration. Beam heating instabilities were reduced by keeping the intensity of illumination constant on the area of interest for several minutes prior to exposing the plates.

Different sizes of diffraction aperture were employed for

each material in order to check the consistency of the results as more beams contributed to the image. The maximum size of aperture and therefore number of beams which could be used, was limited by spherical aberration (C_s for the instrument, quoted as being about 1.6 mm). Phase corrections for spherical aberration were not computed since detailed structural information was not required here. The diameter of the maximum size of aperture which can be used must correspond to the resolution limit of the instrument: in fact it is inversely proportional to a first approximation. The effect of using an aperture larger than this is merely to raise the background level of the image with unresolved Fourier components, and obscure the information already present.

A through-focal series of plates was exposed in each case, although not for the express purpose of correcting for spherical aberration phase shifts. The micrographs which are presented in Chapter 10 have the optimum degree of underfocus for the periodicities of interest. Diffraction patterns were systematically checked for signs of Moiré fringes, and the instrument's double tilt system was used to ensure that the interfering beams passed symmetrically through the aperture and down the column of the microscope. The voltage centre and astigmatism were also periodically adjusted.

4.5 X-ray Diffraction Studies

The crystals of the 2H TaS_2(pyridine) intercalation complex which were examined by X-ray diffraction, were small hexagonal prisms, with edge dimensions of about 0.15 mm and with no obvious external defects. They were in fact approximately equiaxed, and therefore suitable for X-ray diffraction studies. The crystals of 1T TaS_2 on the other hand were far from ideal in shape for

study by this technique. The hexagonal platelets had a breadth of between 3 and 6 mm, and thickness in the range of 200 μm down to about 1 μm for the thinnest.

The crystals were all mounted on glass fibres. Shellac was used as the adhesive except for high temperature work when epoxy resin was found to be more suitable. Diffraction patterns were recorded either photographically using Mo Kα radiation or by counter diffractometer. For the photographic studies the crystals were mounted on the arcs of a Unicam S25 single crystal goniometer, and oscillated about the a-axis. The incident beam was oriented either perpendicular to the c-axis to study the 00.ℓ reflexions, or parallel to the c-axis for recording the hk.0 reflexions.

The zirconium β-filter was placed immediately front of the film rather than in the beam collimator, as this improved the quality of the films obtained after the long exposures often necessary. The chief reason for these was the high absorption of X-radiation at the wavelengths employed by the tantalum disulphide matrix. The absorption coefficient, μ, for pure TaS_2 in Mo Kα radiation is about 60 mm^{-1}, while it is reduced by the lower density of the intercalation complex to about 27 mm^{-1}.

For low temperature studies, liquid nitrogen was dripped slowly onto the crystal from a dewar immediately above the crystal. Shielding was introduced to try and reduce condensation of moisture and the formation of ice crystals. In the absence of an automatic system for maintaining the level of the nitrogen in the dewar, exposure times were limited to about eight hours without allowing the crystal to regain room temperature. For extending the temperature range of observation above room temperature a small electrically heated furnace was used.

The temperature was monitored by a standardised thermocouple, and thus steady temperatures could be maintained up to about 420 K. The main beam entered and left the furnace by as small apertures as possible to reduce heat losses and draughts. Steady temperatures were maintained for periods of several weeks in order to test the stability of the high temperature phase of 1T tantalum disulphide.

For quantitative measurements, the crystals were transferred to a Siemens type F diffractometer, modified for the study of single crystals and fitted therefore with a Eulerian cradle so as to produce a four-circle instrument. Diffracted radiation was detected by a scintillation counter, backed by a conventional single channel pulse counting system. Molybdenum Kα radiation was again used when studying the octahedral polymorph of TaS_2. During the course of the experiment the absorption effect of the very thin crystal on the main beam was measured. It was discovered that the crystal (whose area was sufficient to more than cover the main beam) absorbed 3 % of the radiation. This enables a value of 0.03 to be calculated for μt. Thus the thickness of the crystal was estimated to be rather less than 1 μm. Absorption corrections were therefore deemed to be unnecessary.

Copper Kα radiation was used in order to increase the dispersion of the 00.l and 01.l reflexions in the pyridine intercalation complex. Absorption effectswere however enhanced with this longer wavelength radiation, and $\mu = 53\ mm^{-1}$, so that $\mu t = 10$. The data from TaS_2(pyridine) presented in Chapter 5 are nevertheless uncorrected for absorption and this should be borne in mind. An additional complication in attempting accurate intensity measurement was the proximity of the 01.l reflexions and their broadening for l odd.

5 DIFFRACTION RESULTS AND INTERPRETATION: TANTALUM DISULPHIDE (PYRIDINE)

5.1 Introduction

The experimental results comprise both electron and X-ray diffraction data, and for the latter both photographic and diffractometer data, and they will be considered as follows:

First to be studied will be the change in the tantalum disulphide matrix structure resulting from the intercalation process. This will include changes in cell dimensions, symmetry, and interatomic distances. It will be convenient to deal separately in some sections with changes within the layers and changes in the stacking of the layers. Secondly the radiation scattered by the pyridine molecules will be considered, both with regard to 'superlattice' reflexions associated with periodicities of the pyridine superstructure, and with regard to contributions to the intensity of the matrix reflexions. While it will be possible to characterise the structure of the 'host' lattice reasonably well, it will be found that the limited data specifically relevant to the pyridine superstructure allow only tentative conclusions about the packing of the pyridine molecules. In the final section of the chapter the structural results are discussed in terms of a charge transfer model for intercalation.

5.2 Tantalum Disulphide Matrix Structure

5.2.1 Change in Cell Dimensions on Intercalation

The structure of pure 2H TaS_2 was analysed by Jellinek (1962), who referred the structure to the hexagonal space group $P6_3/mmc$ with the Ta atoms located at $\pm(0,0,\frac{1}{4})$ and the sulphur atoms at $\pm(\frac{1}{3},\frac{2}{3},z)$ and $\pm(\frac{1}{3},\frac{2}{3},\frac{1}{2}-z)$. He gave as the value of the variable parameter, $z \simeq 1/8$. Thus the stacking sequence is AcA BcB. The unit cell dimensions were a = 3.315 Å, c = 12.10 Å.

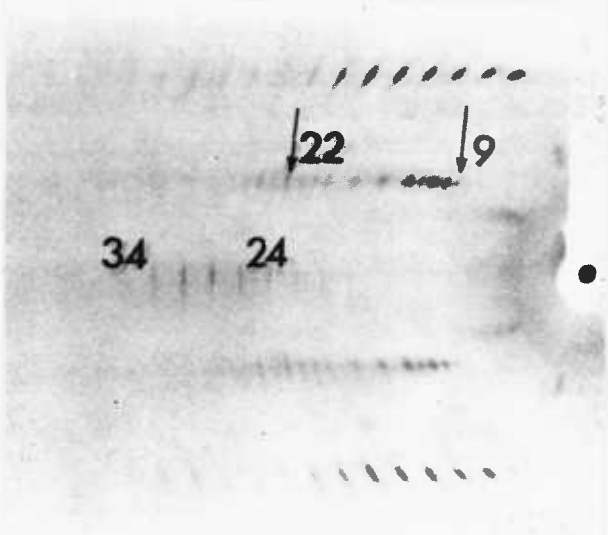


Figure 42 Oscillation X-ray diffraction photograph of TaS_2 (pyridine), showing part of the 10.ℓ row (with 10.9 and 10.22 marked), and part of the 00.ℓ row (with 00.24 and 00.34 marked).

The 00.ℓ reciprocal lattice row shown in Fig 42 implies that after intercalation there is a doubling of the spacing between TaS_2 layers. Diffraction photographs also show that the a-spacing undergoes very little change. Excluding the pyridine scattering, all the X-ray diffraction photographs from the intercalation complex can be indexed on the basis of a hexagonal unit cell, and referred to the same space group, $P6_3/mmc$, as the pure material, 2H TaS_2. In particular there are systematic absences among the 00.ℓ reflexions for ℓ odd, and indeed for all hk.ℓ reflexions for which $h - k \equiv 0 \pmod 3$.

The unit cell dimensions for the intercalation complex were determined from diffractometer measurements as $a = 3.32_7$ Å, $c = 23.7_4$ Å. There is thus a slight increase in a of about 0.35% due to the intercalation with pyridine.

The unit cell still contains two TaS_2 layers, but the c spacing has increased by 96% from 12.10 to 23.74 Å. This implies that the distance between layers has increased by 5.82 Å (i.e. from 6.05 to 11.87 Å) in order to accommodate the pyridine.

5.2.2 Tantalum - Sulphur Layer Distance

The 00.ℓ reflexions are independent of the x and y co-ordinates of the atom positions within the unit cell, and therefore to the stacking sequence of the layers. These reflexions are most conveniently used then to determine the z co-ordinates of the atoms in the cell. It should be emphasised that at this stage, just the 'empty lattice' is being considered.

In the structure analysis for 2H TaS_2, Jellinek (1962) gave only an approximate value for the separation of neighbouring Ta and S planes of $c/8 = 1.51$ Å. This simply assumes that all the sulphur planes are equally spaced. Since the stacking

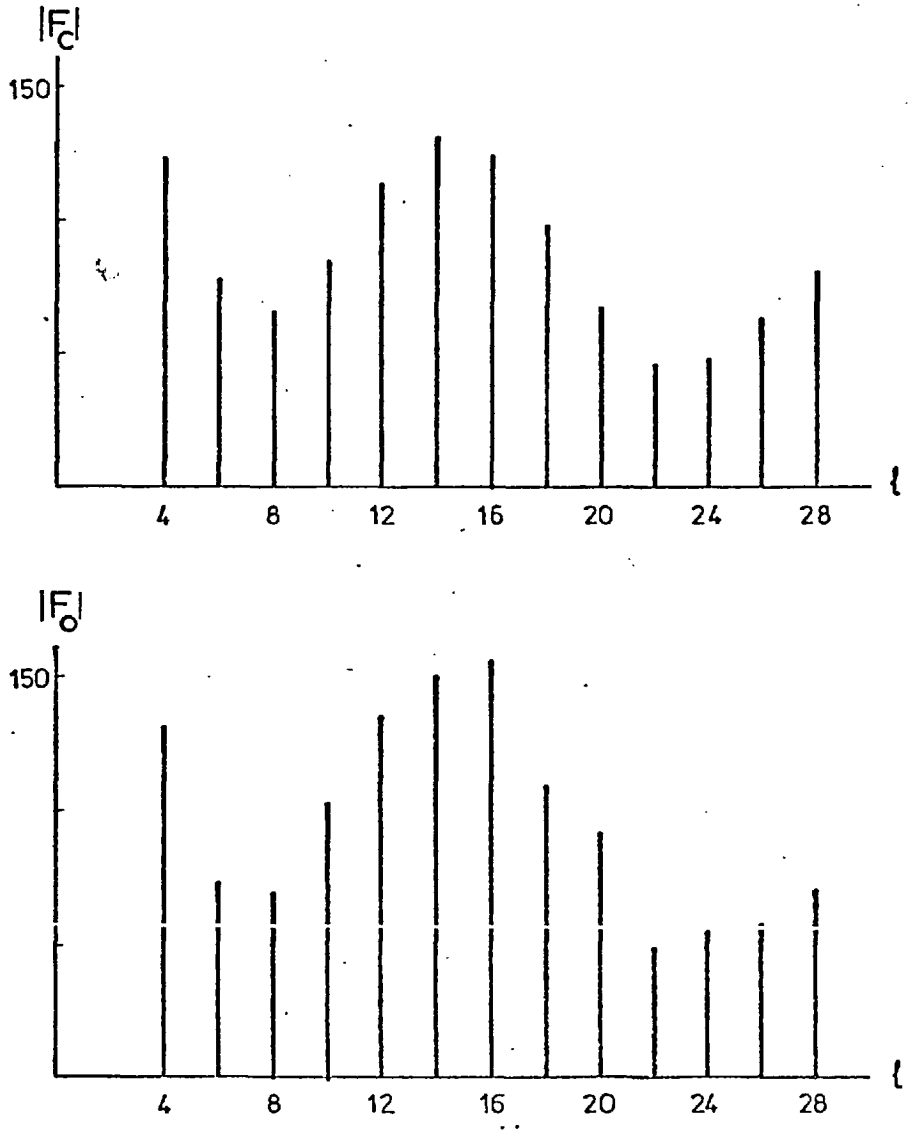


Figure 43 Comparison of observed and calculated structure factors for the 00.ℓ reflexions (data from Table 5)

sequence of the sulphur layers alone is AABB, this is unlikely to be true in reality: the spacing between layers in the same orientation, AA or BB, is likely to be larger than those which are close packed, AB or BA. For the current investigation however a value of 1.57 Å was used. This was obtained after correcting the half-layer height of 2H $TaSe_2$ (1.68 Å, Bjerkelund and Kjekshus, 1967) by the difference in half-layer heights (1.57 - 1.68)Å of NbS_2 and $NbSe_2$ (Jellinek 1960, Brown and Beerntsen, 1965).

Assuming that this separation remains essentially unchanged in the intercalated material, this gives:

$$z(Ta) - z(S) = \pm \frac{1.57}{23.74}$$

$$= \pm 0.066$$

With the origin at the centre of symmetry, $z(Ta) = \pm\frac{1}{4}$ as in the pure material. Thus:

$$F(00.\ell) = 2f_{Ta}\cos(\frac{2\pi\ell}{4}) + 2f_S[\cos 2\pi\ell(\tfrac{1}{4} + .066) + \cos 2\pi\ell(\tfrac{1}{4} - .066)]$$

$$= 0 \quad \text{for } \ell \text{ odd}$$

$$= (-1)^{\frac{1}{2}}[\, 2f_{Ta} + 4f_S \cos(2\pi\ell\, .066)\,]$$

The effect of the sulphur contribution is to produce oscillations in the magnitude of the structure factor with period $\ell = (0.066)^{-1} \simeq 15$. Table 5 (and Figure 43) show the measure of agreement between structure factors calculated for $00.\ell$ reflexions on this model and those observed. Since the observed data are uncorrected for absorption, no allowance for thermal vibrations has been made. F_o and F_c show the same variation with index ℓ; no marked improvement in fit between calculated and observed data can be obtained by changes in the z parameter.

ℓ	F_o	F_c
4	129	122
6	73	77
8	68	65
10	101	84
12	127	112
14	150	129
16	154	123
18	109	97
20	91	66
22	47	46
24	55	47
26	57	63
28	70	80

Table 5 Comparison of observed and calculated structure factors for the 00.ℓ reflexions. F_o corresponds to diffractometer data, and F_c has been calculated for the 'empty lattice' (i.e. expanded TaS_2 matrix).

5.2.3 Stacking of the Tantalum Disulphide Layers

It was found to be most convenient to determine the TaS_2 layer stacking sequence from the 01.ℓ (equivalent under hexagonal symmetry to 10.ℓ) row. Structure factor data will be calculated for a number of stacking sequences consistent with the symmetry of the space group:

AcA|BcB

This assumes that the sequence in the intercalated material is the same as in pure 2H TaS_2. Then with z(Ta) - z(S) = z' = .066, the structure factor for the 01.ℓ reflexions is given by:

$$F(01.\ell) = 2f_{Ta}\cos(\tfrac{\ell\pi}{2}) + 2f_s[\cos(\tfrac{\ell\pi}{2} + \tfrac{4\pi}{3} + 2\pi\ell z') + \cos(\tfrac{\ell\pi}{2} + \tfrac{4\pi}{3} - 2\pi\ell z')]$$

For ℓ even

$$F(01.\ell) = (-1)^{\frac{1}{2}\ell}[2f_{Ta} - 2f_S\cos(2\pi\ell z')]$$

This is in fact a similar expression to that for the 00.ℓ structure

factor, but with the sulphur contribution multiplied by a phase factor, $\cos(4\pi/3) = -\frac{1}{2}$.

For ℓ odd

$$F(01.\ell) = (-1)^{\frac{1}{2}(\ell-1)}\sqrt{3}\, f_s \cos(2\pi\ell z')$$

Thus there is no tantalum contribution, so that the structure factor depends only on sulphur scattering. This follows of course from the fact that the metal atoms are stacked in the same orientation in alternate layers. It would thus be expected that the 01.ℓ reflexions would be very weak for ℓ odd, as in the pure material.

Reference again to Figure 42 reveals very clearly that this situation does not obtain in the intercalated material. For instance, when $\ell \sim 15$, only the odd reflexion can be seen. Thus there must have been a change in stacking sequence. If changes in co-ordination of the metal within the TaS_2 layers are ruled out, then there are only 2 other stacking sequences which can be generated within the same space group, $P6_3/mmc$. These are

(i) AcA|CaC, and (ii) AcA|AbA.

AcA|CaC

Of the two possible sequences this would appear the more likely in that it is the sequence adopted by some of the Group VIa materials, such as 2H MoS_2. This model for the intercalated host lattice has tantalum and sulphur on alternating sites in successive layers. Thus the phase factor introduced when moving from the 00.ℓ row to 0k.ℓ rows affects Ta and S contributions alike:

For ℓ even

$$F(01.\ell) = (-1)^{\frac{1}{2}\ell+1}[2 f_{Ta} + 4 f_S \cos(2\pi\ell z') \cos\pi/3]$$

For ℓ odd

$$F(01.\ell) = (-1)^{\frac{1}{2}\ell-\frac{1}{2}}[2 f_{Ta} - 4 f_S \cos(2\pi\ell z') \sin\pi/3]$$

Since the sign of the sulphur contribution changes from even ℓ to odd ℓ, the variation of $F(01.\ell)$ with ℓ is in opposite phase for even ℓ compared with odd ℓ. Reference to Table 6 shows that this model predicts similar values of the structure factor for even and odd ℓ when $\ell \sim 14$. This situation is not found however in the observed data.

AcA|AbA

In this model for the stacking of TaS_2 layers, all the sulphur planes are in the same orientation. This would clearly be an unfavourable sequence in the pure material since it would require AA stacking around the Van der Waals gap. This sequence is however energ etically favourable in certain intercalation complexes (see for instance, Huisman, De Jonge, Haas and Jellinek, 1971).

The structure factors for this model are given by:

For ℓ even

$$F(01.\ell) = (-1)^{\frac{1}{2}\ell \pm 1} \left[2 f_{Ta} \cos \pi/3 - 4 f_S \cos(2\pi\ell z') \right]$$

For ℓ odd

$$F(01.\ell) = (-1)^{\frac{1}{2}\ell - \frac{1}{2}} [2 f_{Ta} \sin \pi/3]$$

Because the sulphur atoms are stacked identically in successive layers, their contribution must be zero for ℓ odd. Their only contributions is to the even reflexions, where they produce oscillations with ℓ in the magnitude of $F(01.\ell)$. It can be seen from Table 6 that the structure factors are approximately equal for ℓ even and odd when $\ell \sim 7$ and $\ell \sim 22$.

This gives the best agreement with the behaviour of the observed data implying therefore that the host TaS_2 lattice undergoes a stacking change on intercalation with pyridine to the sequence AcA|AbA.

ℓ	$\|F_o\|$	$\|F_c\|$ AcA|AbA Model ii	$\|F_c\|$ AcA|CaC Model i	$\|F_c\|$ AcA|BcB Expanded 2H
5	90	94	113	19
6	97	89	36	125
7	82	91	127	36
8	89	93	31	124
9	68	87	116	29
10	62	70	39	109
11	54	83	88	5
12	28	37	52	89
13	48	79	60	20
14	10	13	60	74
15	51	75	46	29
16	14	11	58	69
17	54	71	51	20
18	25	29	46	75
19	51	68	69	1
20	47	52	32	83
21	52	65	85	20
22	57	65	22	87
23	54	61	86	25
24	63	59	22	81

Table 6 Comparison of observed and calculated structure factors for the 01.ℓ reflexions. $|F_o|$ is from diffractometer data while $|F_c|$ is given for the three possible stacking sequences in the 'empty' expanded TaS_2 lattice.

This sequence may be referred to the space group $P6_3/mmc$, placing the tantalum atoms at $\pm(\frac{1}{3},\frac{2}{3},\frac{1}{4})$, and the sulphur atoms at $\pm(0,0,z)$ and $\pm(0,0,\frac{1}{2}-z)$, where:

$$z(S) = z(Ta) - z' = 0.184.$$

The agreement for ℓ even is reasonable, especially when it is remembered that no absorption correction has been made to F_o, and that neither pyridine scattering nor thermal diffuse scattering have been taken into account. Figure 44 enables the three models to be compared graphically with experiment.

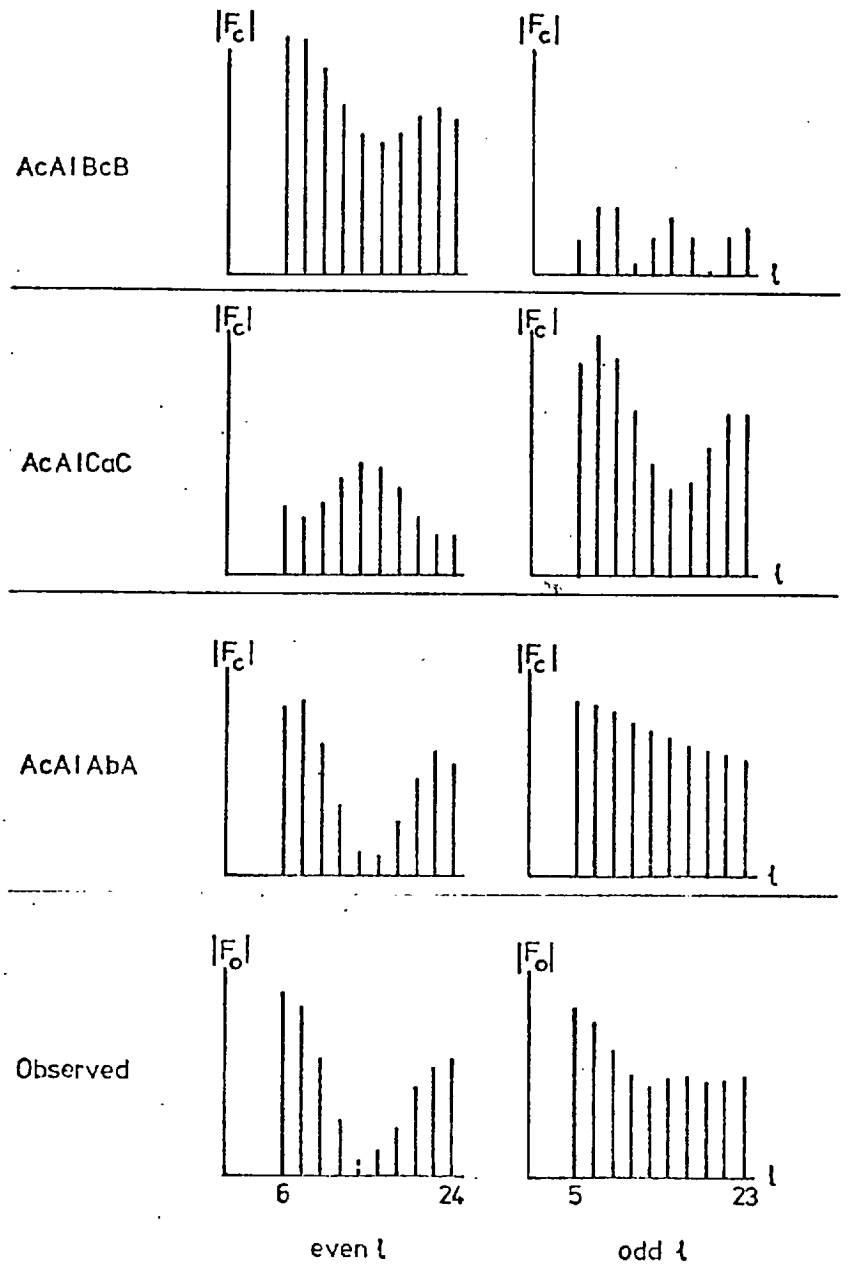


Figure 44 Comparison of observed and calculated structure factor data for the three possible stacking sequences for the 'empty' expanded TaS_2 lattice (data from Table 6).

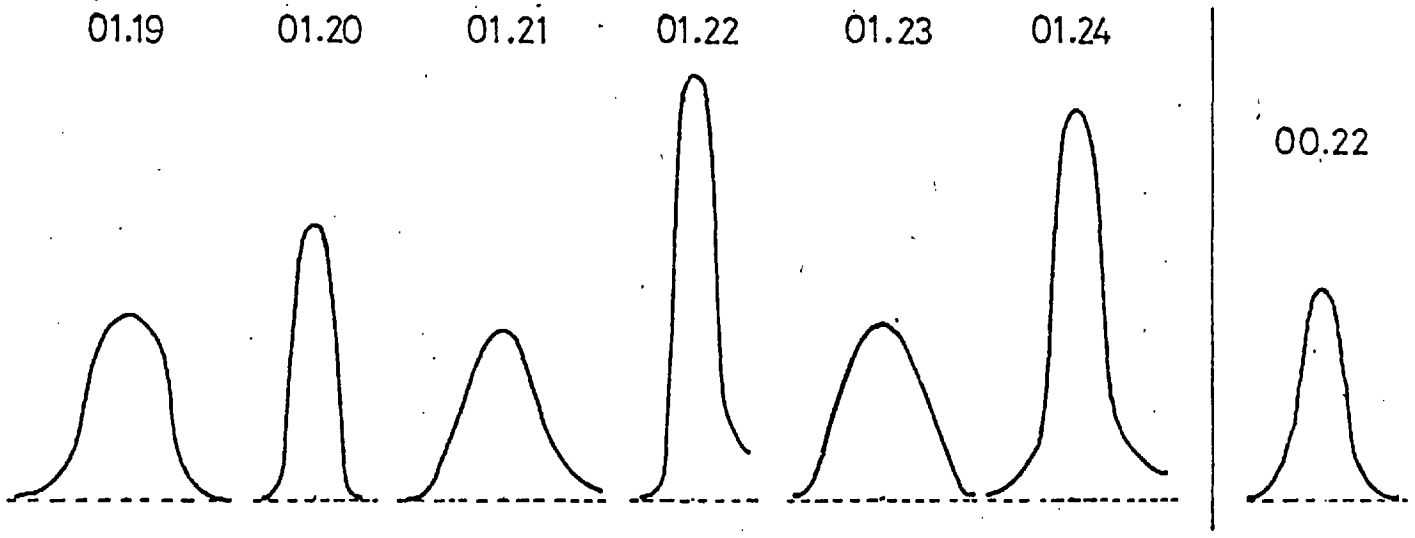


Figure 45 Profiles of 01.ℓ reflexions from diffractometer measurements. A typical 00.ℓ reflexion is given for comparison.

The agreement for ℓ odd is however somewhat inferior. Since all the sulphur planes are in the same orientation for this model, $|F_c|$ should be a slowly decreasing function of (i.e. proportional to the tantalum scattering factor). The variations in $|F_o|$ rather suggest that there may in fact be scattering from the sulphurs and that the sulphur planes are not all stacked A/A. Furthermore the definition of reflexions with ℓ odd is inferior to those with ℓ even (Figure 45, obtained during diffractometer measurements of intensity). The breadths of the 00.ℓ and 01.ℓ (ℓ even) reflexions are however of very similar magnitude.

This broadening for odd ℓ must be due to stacking disorder in the idealised structure, AcA|AbA, and it is possible to interpret this in terms of an average distance over which the stacking sequence AcA|AbA is maintained. Using the measured breadths of the reflexions, this distance is calculated to be approximately 72 Å $\simeq$ 3 c, i.e. about 6 TaS_2 layers. This figure indicates a relatively poor maintenance of the stacking sequence.

5.3 Ordering of Pyridine Molecules

5.3.1 Pyridine Lattice

Additional satellite reflexions were observed in the hk.0 section of the 2H TaS_2 reciprocal lattice both by electron and X-ray diffraction. The selected area diffraction pattern in Figure 46 shows many reflexions additional to the hexagonal matrix. The reflexions R and the weaker S also shown on the accompanying diagram (Figure 47) can be observed on well-exposed X-ray diffraction photographs such as Figure 48. The superlattice, due to the presence of the pyridine, appears in the three symmetry-related orientations (Figure 47). In

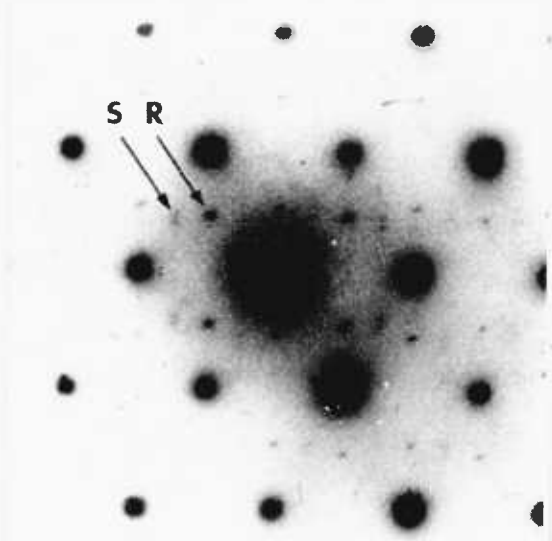


Figure 46 Selected area electron diffraction pattern which shows the pyridine superlattice in one orientation. Reflexions R and S are discussed in the text.

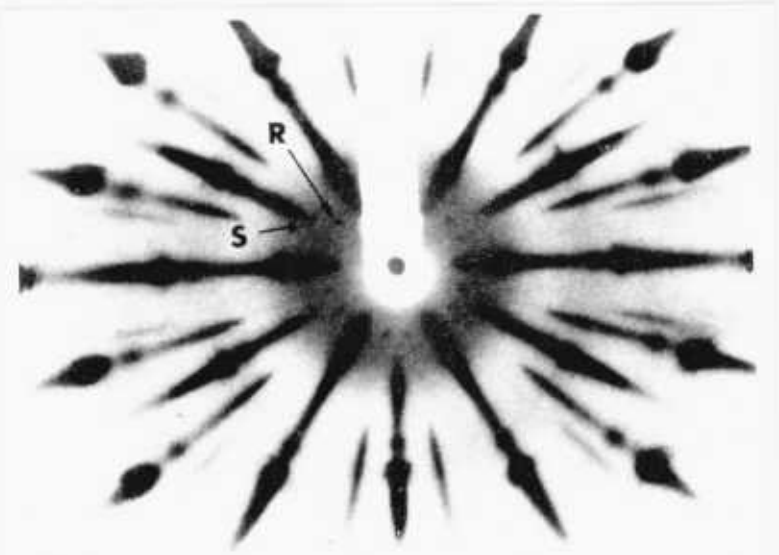


Figure 48 Oscillation X-ray diffraction pattern showing the superlattice in three orientations (cf. Figure 47b) Reflexion R & S are the same as in Figure 46.

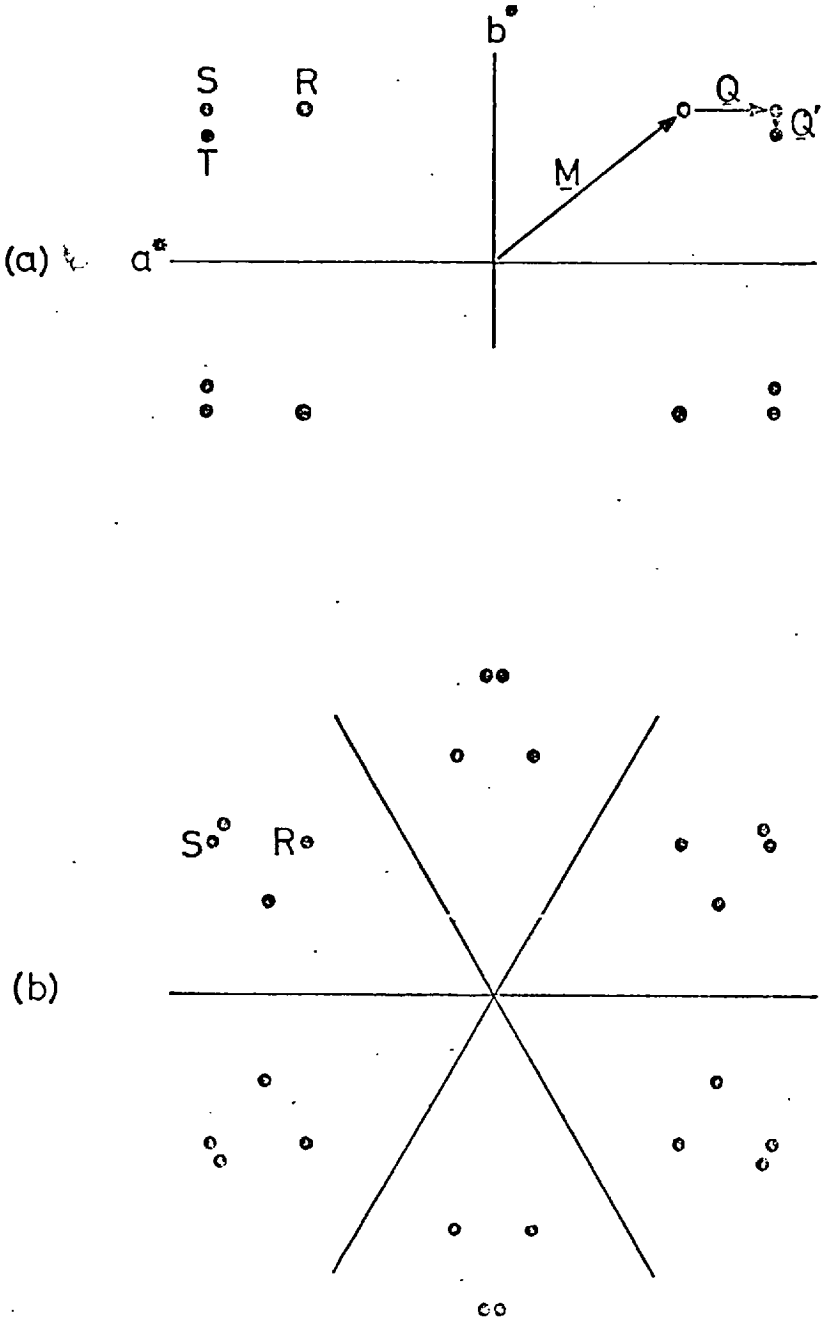


Figure 47 Accompanying diagram for Figure 46 and 48; (a) and (b) show the pyridine superlattice in one and three symmetry-related orientations respectively. Q and Q' are disucssed in the text.

electron diffraction the pattern of satellite reflexions is repeated around each matrix reflexion. Since this effect is not observed in X-ray diffraction (in marked contrast to the deformation superstructures discussed in later Chapters), it most likely to be due in this material to double diffraction of the electron beam. This is, furthermore, strong evidence that the superlattice is primarily due to the ordering of pyridine molecules rather than to displacements or ordering of atoms in the TaS_2 'sandwiches'. Some additional, very weak satellites (e.g. T) are visible in electron diffraction alone: these will be discussed later, although it is clear that they must arise from the greater sensitivity of electron diffraction to scattering by light atoms.

Electron diffraction observations at room temperature, when the superlattice pattern rapidly disappears, confirm that the behaviour of all four reflexions of type R is identical. The simplest model therefore must be based on a centred rectangular cell (2-D), with the indices of type R reflexions {1,1}. The dimensions of the cell (Figure 49) would be:

$$a' = 5.76\ \text{Å} = \sqrt{3}\, a_{TaS_2}$$

$$b' = 7.21\ \text{Å} = 2\tfrac{1}{6}\, a_{TaS_2}$$

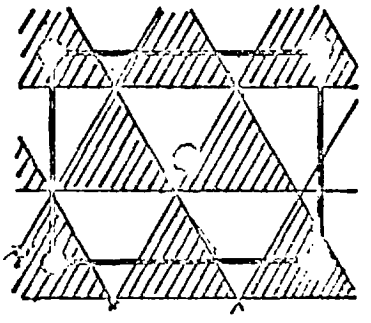


Figure 49

The chief problem with this simple model is that it predicts an infinite series of superlattice reflexions, such as (2,0),(0,2),(2,2) etc, while in practice only (1,1) is observed. This lack of data may be partly due to most of the satellites being too weak for observation ((1,1) is the

reflexion with smallest scattering angle). It is however unlikely to be due entirely to this, and some other reason for the absence of data must be sought. In view of the fact that the supercell does not form a simple coincidence mesh with the matrix lattice, a very probable consequence would be disorder in the positions of the pyridine molecules. Such disorder would be consistent in general terms with the absence of sharp higher order superlattice reflexions..

If a pyridine molecule is associated with each position in the supercell, i.e. so that there are two molecules in the centred rectangular cell, then the corresponding stoichiometry is $TaS_2(pyridine)_{6/13}$. This is in quite good agreement with the measured stoichiometry of TaS_2 $(pyridine)_{\frac{1}{2}}$ - Gamble et al, 1970. According to the diffraction data the pyridine molecules are not sited on an ideal $\sqrt{3}a \times 2a$ superlattice, but on non-ideal sites with respect to the matrix lattice. This can be seen most clearly from the coincidence cell of Figure 50; the smallest coincidence is with $13\underline{a} = 6\underline{b}'$, so that the coincidence length in this direction is 43.6 Å.

Disorder resulting from pyridine molecules trying to move closer to ideal sites, would destroy the order at large distances. In order to balance charge, etc. within the pyridine cell, it seems most logical to associate the pyridine molecules at the cell corners with the TaS_2 layer one side of the van der Waals gap (upper), and the pyridines at the cell centres with the other layer (lower). It follows from this however that it is not possible to have both the upper and lower layer pyridine molecules adjacent to similar sites in the matrix lattice, because the cell corner and centre are separated by a distance of $a\sqrt{3}/2 < 2a/\sqrt{3}$, resolved parallel to $\underline{a}'$.

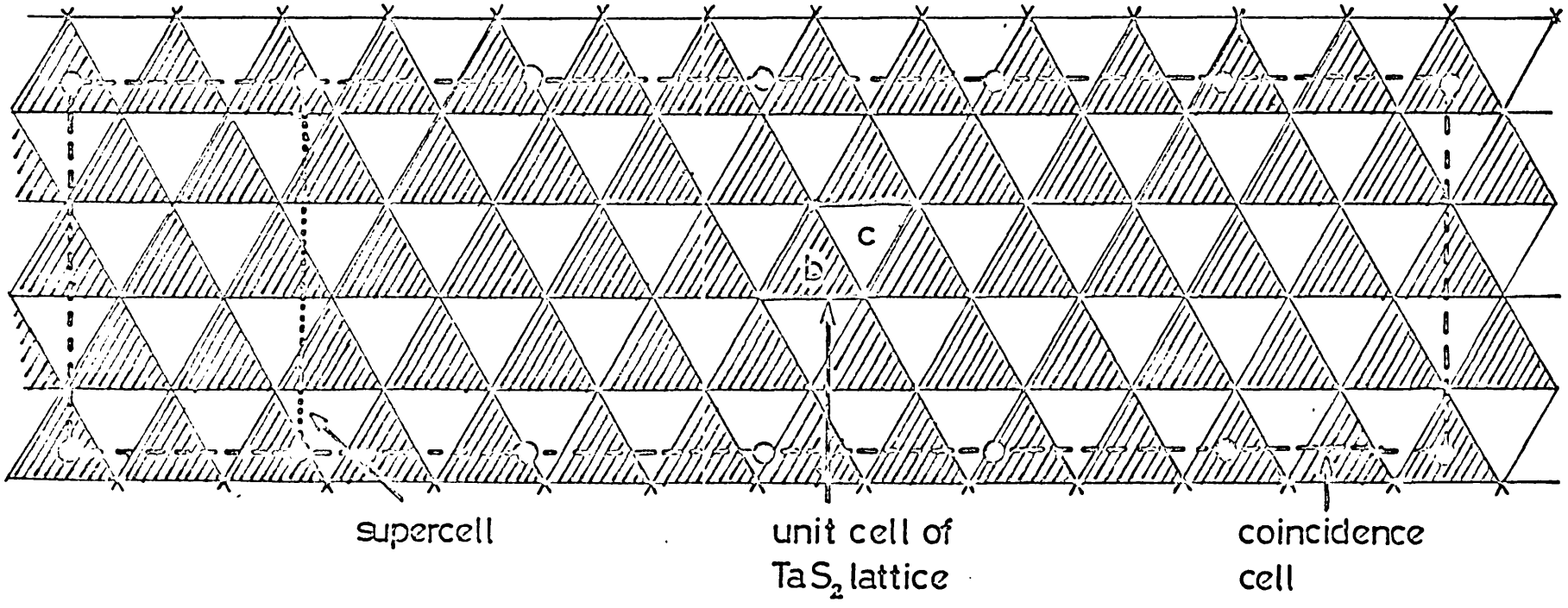


Figure 50 Coincidence cell for the TaS_2 lattice and the pyridine superlattice.

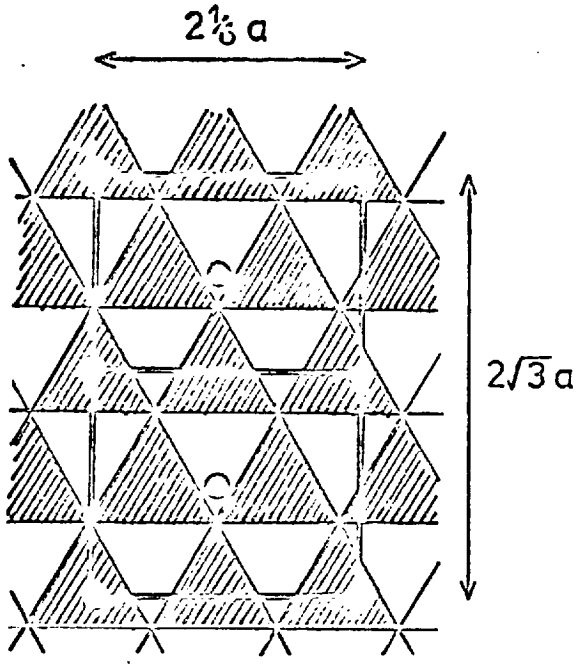


Figure 51 $2\sqrt{3}$a x 2½a pyridine supercell, corresponding to reflexions R and S in Figures 46 & 48.

If the shaded sulphur prisms (Figures 49, 50) contain a tantalum atom, then the unshaded sulphur prisms in the lower layer must do the same, so that it is impossible for all the pyridine molecules (i.e. at corner and centre positions) to be adjacent to the metal atoms. This fact would also be expected to give rise to displacements of the pyridine molecules from ideal positions: this time however the displacements would probably be in the a' direction as well as in the b' direction. Although pyridine molecules have been associated with the upper and lower TaS_2 layers, there has been no discussion of their orientation and what this association means geometrically. This point is taken up in section 5.3.2.

The above interpretation has been based solely on the reflexions of type R, which are in fact the strongest superlattice reflexions. Reflexions labelled S (Figures 46, 48) are however also common to X-ray and electron data, although much weaker. On the X-ray diffraction photograph (Figure 48) they appear very close to the white radiation streak from the matrix (11.0) reflexions. By lowering the X-ray tube voltage to 35 kV it was confirmed that the reflexions are independent of the white radiation. When the S reflexions are incorporated into the model for the pyridine supercell, they cause the a' axis to double in magnitude so that (Figure 51):

$$a' = 2\sqrt{3}\, a_{TaS_2} = 11.52 \text{ Å}$$

$$b' = 2 \times a_{TaS_2} = 7.21 \text{ Å}$$

On the basis of this rectangular supercell, the reflexions R and S are indexed as (2,1) and (3,1) respectively.

The reflexion (1,1) on this basis is either very weak or absent. This, coupled with the fact that (3,1) is much weaker than (2,1), rather suggests that the doubling of the cell may be due to small displacements of the molecules from sites

which would otherwise define the smaller $\sqrt{3}$ a x 2½a supercell. This is in effect saying that the $\sqrt{3}$ a x 2½a cell (defined by the reflexions at M) is subjected to a deformation of wavevector $\underline{Q} = \frac{1}{2}\underline{a}'^{*}$ (Figure 47 a).

With this extremely simplified model it is possible to estimate the order of magnitude of satellite reflexion intensities. If it is assumed that the displacements are of magnitude U in a direction parallel to $\underline{a}'$, then treating (2,1) as a pyridine 'matrix' reflexion, and (1,1) & (3,1) as satellites of this, their intensities are given by (Section 2.4):

$$I(2,1) \propto |J_0(4\pi QU)|^2 ,$$
$$I(1,1) \propto |J_1(2\pi QU)|^2 ,$$
$$I(3,1) \propto |J_1(6\pi QU)|^2 ,$$

where the substitution $\underline{a}'^{*} = 2\underline{Q}$ has been made.

Suppose that (3,1) is about 10 times weaker than (2,1) (which is probably an upper limit on the strength of (3,1)):

Then $$\frac{I(3,1)}{I(1,1)} \simeq \frac{\frac{1}{4}(6\pi QU)^2}{\frac{1}{4}(2\pi QU)^2}$$ since $J_1(x) \simeq \frac{1}{2}x$ for small x.

$$= 9$$

The intensity of (1,1) is therefore nearly 100 times smaller than (2,1), and would probably be too weak to be observed.

Taking again the approximate estimate that (3,1) is 1/10 the intensity of (2,1), then by approximating also the zero order Bessel Function by unity for small argument:

$$\frac{I(3,1)}{I(2,1)} \simeq \frac{1}{4}(6\pi QU)^2$$
$$= 0.1$$
$$\therefore \quad QU = 1/9$$
$$\therefore \quad U = 0.13\ a = 0.4\ \text{Å}.$$

This may be compared with the average distance either corner or centre molecules are from ideal sites. Resolved parallel to $\underline{a}'$, this distance is $\frac{1}{2}(\frac{2a}{\sqrt{3}} - \frac{a\sqrt{3}}{2}) = 0.14\ a$.

Although this calculation has been somewhat speculative, and must be treated as such, it is interesting to note that it gives an estimate of molecular displacements within the pyridine supercell which are at least of the right order of magnitude to satisfy a condition which requires the molecular positions to be as close as possible to Ta atoms.

It is now necessary to consider the scattering which appears in electron diffraction patterns (Figure 46) but not in X-ray (Figure 48). This extra scattering takes the form of faint diffuse streaks parallel to $\underline{b}'^{*}$ and passing through the reflexions S etc.. There are also weak reflexions of type T on these streaks, adjacent to S and of similar strength.

The streaking indicates superlattice disorder in the direction of $\underline{b}'$, i.e. disorder in the y co-ordinates of the pyridine molecules.

The spacing of the satellite T adjacent to S, given by the scattering vector, $\underline{Q}'$ (Figure 47 a), is the same as that of the coincidence cell, i.e. $13\,\underline{a} = 6\,\underline{b}'$.

$$\therefore \quad \underline{Q}' = \frac{1}{6}\,\underline{b}'^{*}$$

$$= \frac{1}{13}\left(a^{*}\sqrt{\frac{3}{2}}\right)$$

This spacing is best interpreted in terms of displacements of the pyridine molecules in the $\underline{b}'$ direction with the periodicity of the coincidence cell. As it was pointed out earlier since $\underline{b}' = 2\tfrac{1}{6}\underline{a}$ for the average cell, molecules could be expected to be displaced towards more favourable sites energetically, corresponding to integral multiples of $\underline{a}$. The diffuse streaks would then show that this ordering is only short range.

In summary, the diffraction data suggest that the pyridine molecules suffer considerable disorder and displacements from positions on a simple superlattice, given by the average positions.

5.3.2 Orientation of the Pyridine Molecules

In the previous section no reference has been made to pyridine orientation because nothing can be inferred about this from the very limited hk.0 superlattice diffraction data. Furthermore, when the TaS_2 matrix reflexions wereconsidered in Section 5.2, no allowance was made for scattering from the pyridine. It is reasonable to ask whether the omission of the pyridine contribution affects to any great extent the conclusions then reached.

In order to do this it is necessary to set up a model for the structure of the pyridine layers, with particular attention to the orientation of the pyridine molecules relative to the TaS_2 layers. Alternative proposals have been made for this orientation, that it is:

(a) parallel to the TaS_2 layer - Gamble, Osiecki, Di Salvo (1971), and Acrivos & Salem (1974),

(b) perpendicular to the TaS_2 layer - Gamble, Di Salvo, Klemm & Geballe (1970).

In both cases a double layer structure is envisaged, in which alternate pyridine molecules are associated with the host layers above and below the interlamellar space.

At first sight it might be supposed that the question of pyridine orientation could be resolved from measurement of the increase in the host interlayer separation on intercalation, and comparison with the diemnsions of the molecule. Regrettably this approach fails because the length and breadth of the pyridine molecule are both almost exactly twice its thickness (3.35 Å) - Bowen et al 1958. Thus either orientation would give a similar c-axis expansion of about 6 Å, assuming still a double layer.

If the study of the effect of pyridine scattering is restricted to the matrix 00.ℓ reflexions, it is not necessary to include the x and y co-ordinates of the pyridine molecules, thereby enormously simplifying the model. The essential difference between the two models is revealed as follows:

(a) When the pyridine molecules are parallel to the host layers, all the atoms in every pyridine layer scatter in phase for each 00.ℓ reflexion - they all have the same z co-ordinate because pyridine is a planar molecule.

(b) When the pyridine molecular plane is perpendicular to the host layers, the atoms in the pyridine molecules have different z co-ordinates. They can only even approximately scatter in phase for 00.ℓ reflexions with spacings equal to interatomic separations. Since these are between 1 and 2 Å, the atoms first scatter in phase for $\ell \sim 12$.

From this it can be concluded that only model (a) is likely to produce a large effect in the range of intermolecular spacings, 3 - 4 Å, i.e. $4 < \ell < 10$. It is possible to make the two models more quantitative as follows:

Model (a) - Parallel Orientation

For a quantitative model with the pyridine molecules in this orientation, the planes of the molecules can be placed $2.9 = \frac{1}{2} \times 5.8$ Å apart in the centre of the gap (Figure 52) so that z(pyridine) = 0.189 and $(\frac{1}{2} - 0.189)$. The initial choice of this separation for the planes of pyridine molecules is based on the increase of 5.8 Å in the gap between TaS_2 layers on intercalation. Thus also the pyridine - tantalum layer distance can be calculated as about 4.5 Å.

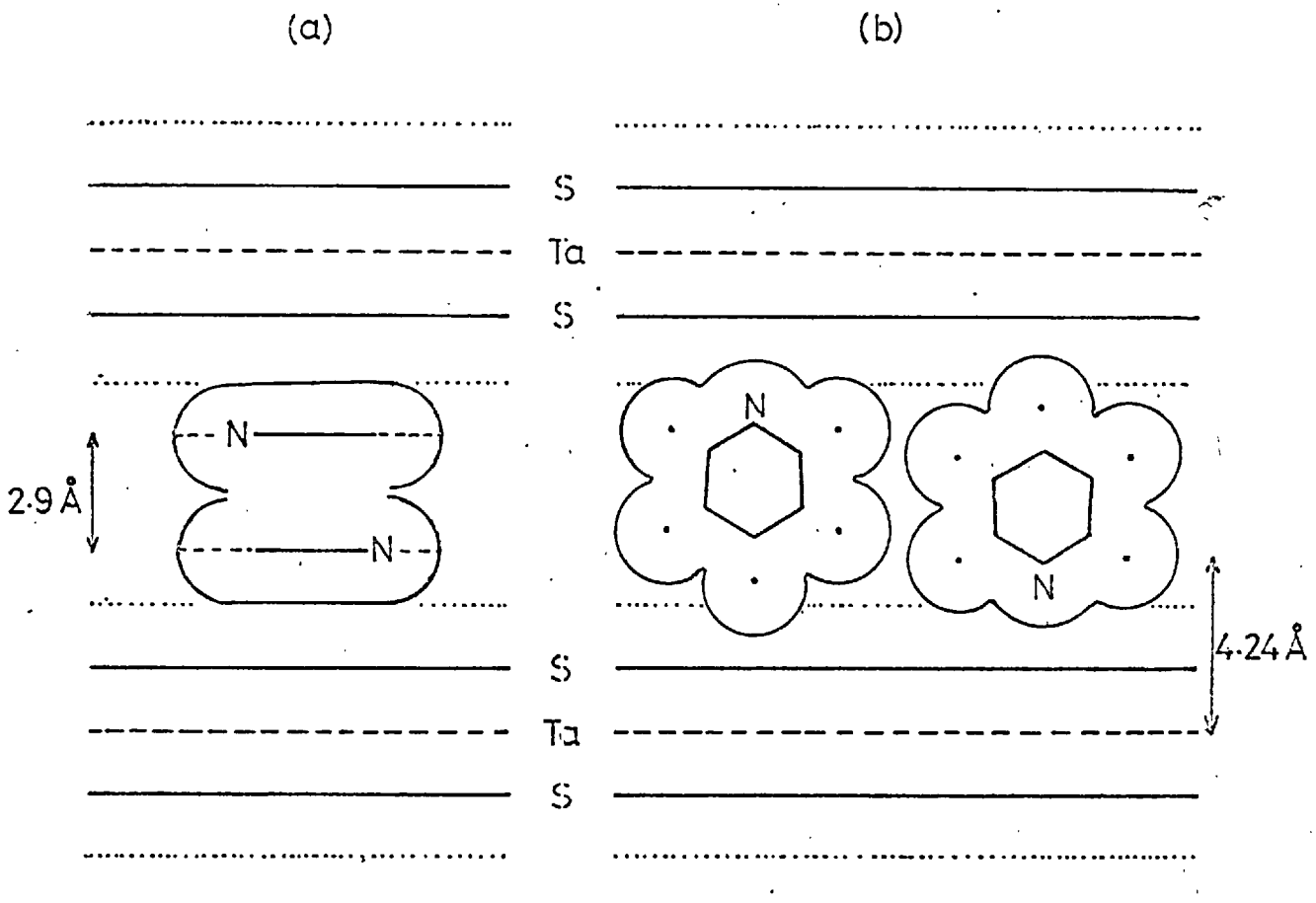


Figure 52 Model (a), for parallel orientation of pyridine molecules.

Figure 53 Model (b) for perpendicular orientation of pyridine molecules.

The stoichiometry of the complex suggests that it is correct to assume one pyridine molecule per unit cell (which itself contains two TaS_2 formula units). Then the scattering by the planar molecules into the 00.ℓ reflexions is given by:

$$F_a = (5f_C + f_N) \cos(2\pi\ell \times 0.189)$$

Values of the pyridine contribution to the structure factor based on this expression are given in Table 7. The expression is in fact not very sensitive to small changes in z parameter for values of $\ell \leqslant 10$. In Table 7, probable limits for z of 0.179 and 0.199 have also been included to illustrate this. These values correspond to moving the pyridine molecular planes 0.5 Å respectively further apart and closer together. Geometrical considerations would preclude much larger displacements.

ℓ	F_a			F_c	$F_c + F_a$
	z = 0.179	z = 0.189	z = 0.199	(empty)	(z = 0.189)
4	-7	1	9	122	123
6	26	20	10	77	97
8	-20	-25	-21	65	40
10	5	17	22	84	101

Table 7 Calculated structure factors based on model with pyridine molecules parallel to TaS_2 host layers, for 00.ℓ reflexions.

Model (b) - Perpendicular Orientation

The pyridine molecules are placed so as to be approximately equally spaced from the two host layers, i.e. with the Ta - N distance 4.24 Å (Figure 53). Then there is in each unit cell on average half a pyridine molecule in one orientation (with the nitrogen pointing towards one layer) and half a pyridine in the opposite orientation. The z co-ordinates of the atom positions in the pyridine molecules can be calculated from Bowen et al (1958), so that the pyridine contribution to scattering is given by:

$$F_b = f_N \cos(2\pi l \times 0.179) + f_C\{2\cos(2\pi l \times 0.208) + 2\cos(2\pi l \times 0.267) + \cos(2\pi l \times 0.297)\}$$

For this orientation also small displacements of the pyridines were tried parallel to c, so that there were changes in z(N) of ± 0.01. Again it was found (Table 8) that the pyridine contribution to the structure factor was not very sensitive to these.

l	F_b			F_c	$F_c + F_b$
	z = 0.169	z = 0.179	z = 0.189	(empty)	(z = 0.179)
4	14	16	17	122	138
6	1	0	-2	77	77
8	2	-6	-3	65	59
10	5	8	10	84	92

Table 8 Calculated structure factors for 00.l reflexions based on model with pyridine molecules perpendicular to TaS_2 host layers.

The average Ta - N distance used in model (b) is about 0.25 Å less than in model (a): this is consistent with the nitrogen being able to approach the tantalum more closely in this model by assuming a position on the axis of the sulphur trigonal prism.

In the final columns of Tables 7 and 8 the pyridine contributions have been added directly to the structure factor for the 'empty' host lattice. This assumes coherency of scattering from pyridine and host lattice. There is in fact considerable disorder in the pyridine layer in the Van der Waals gap, so that a certain amount of incoherent scatter might be expected, and which would tend to reduce differences between intensities calculated from the two models. The interlayer separation of the matrix however places a severe constraint on movement of pyridine molecules in the c direction, so that the scattering from them must be predominantly coherent

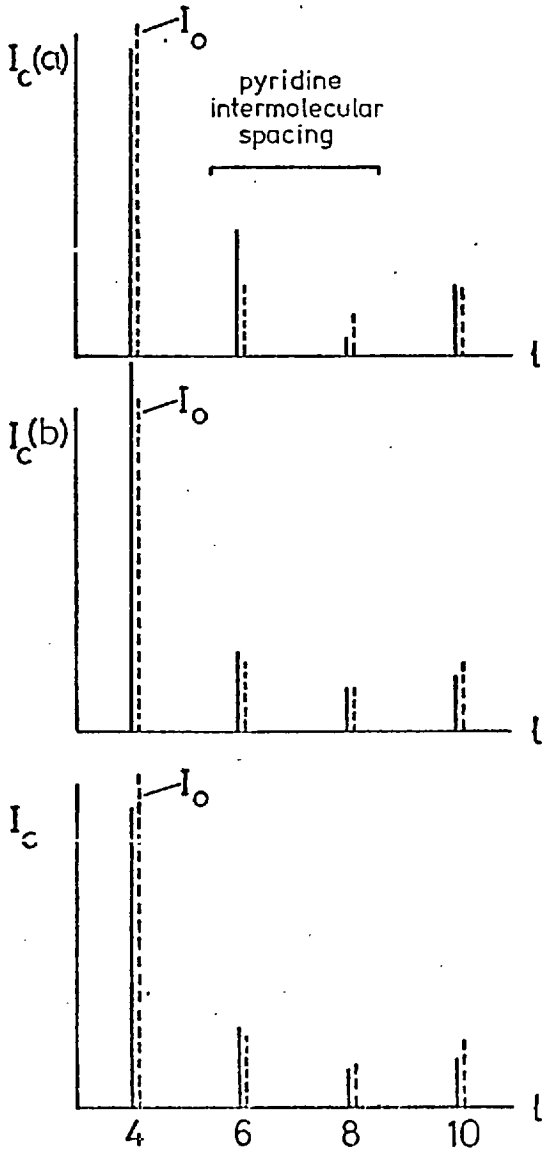


Figure 54 Comparison of observed 00.ℓ intensity data with calculated values for the empty host lattice (I_c) and models (a) & (b). Data from Table 9.

with that of the matrix.

Table 9 enables the intensities predicted on the basis of the two models to be compared with experimental data. Calculated data has been included also for the empty host lattice, so that an estimate is obtained for the magnitude of the corrections produced by including the pyridine scattering.

d(Å)	ℓ	I_c	$I_c(a)$	$I_c(b)$	I_o
6	4	56	57	69	62
4	6	15	23	15	13
3	8	7	3	8	8
2.4	10	9	13	10	13

Table 9 Comparison of observed 00.ℓ intensity data with calculated intensities for the empty host lattice (I_c), models (a) and (b). The data are arbitrarily scaled.

The increased intensity of 00.6 and reduced intensity of 00.8 for model (a) are contrary to observation. They are also basic to the model and cannot significantly be altered even when the pyridine molecular separation is changed by 0.5 Å (Table 7). From this it is concluded that in model (a), where all the atoms in the pyridine scatter in phase, the predicted result should be detectable but is not consistent with experimental observation, the agreement between I_o and I_c having been worsened compared with that for the empty lattice. Column $I_c(b)$ on the other hand shows that it is possible to insert pyridine into the empty host lattice, in the perpendicular orientation, without significantly altering the agreement with observed data. Figure 54 illustrates this agreement.

As well as effectively eliminating model (a), with all the pyridine molecules parallel to the TaS_2 layers, this calculation has also shown that the omission of the pyridine contribution earlier on is in fact not important at this stage of the investigation. The calculation on the other hand does not

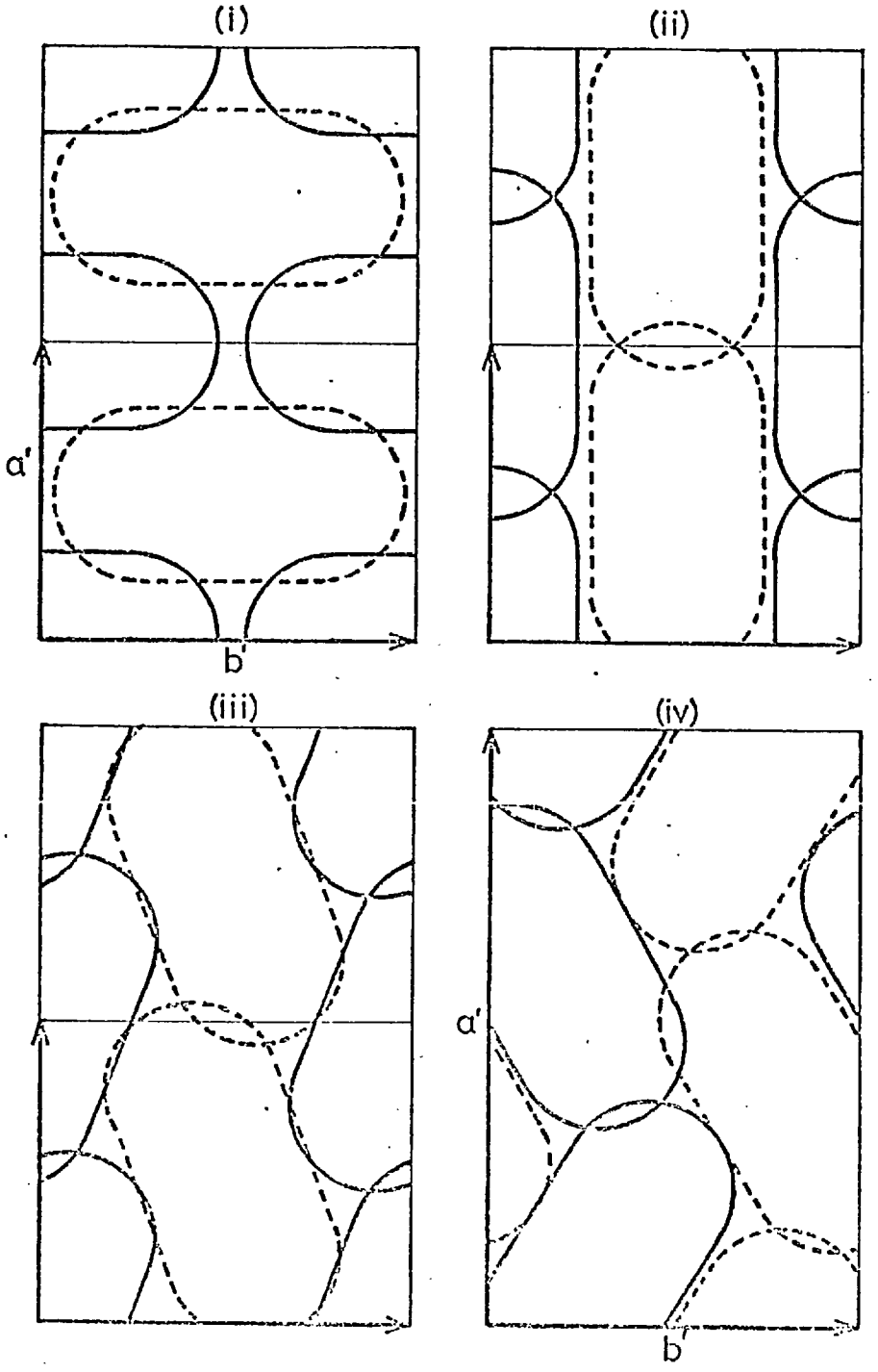


Figure 55 Four simple models for the packing of the pyridine molecules in the interlamellar space (perpendicular orientation), and discussed in the text.

in any way prove that the pyridine molecules are perpendicular to the host layers: it only shows that this orientation is possible, and it certainly does not rule out a structure in which the pyridine molecular planes are oriented at some angle between 0° and 90°. Geometrical considerations (coupled with the reflection symmetry of the pyridine superlattice) do tend to point to perpendicular orientation as being the most probable. It is clear that while model (a) has its most marked effect on the 00.ℓ reflexion intensities, model (b) must have its effect chiefly on reflexions in the hk.0 plane, since this is where entire molecules can scatter in phase. Quantitative hk.0 superlattice intensity measurements are therefore required in order to identify the orientation of the pyridine molecules positively.

The question of pyridine molecular orientation is a sufficiently important one, that it is felt to be worthwhile to explore what perpendicular orientation might mean, in terms of the packing of the molecules, a little further. Although quantitative superlattice intensity measurements are not available, there are the qualitative observations of Figures 46 & 48). For the perpendicular orientation of model (b) to be acceptable, there must be a possible packing model for the pyridine molecules, which is consistent both with geometrical considerations and the limited experimental data available.

It is assumed that there are four pyridine molecules per unit supercell (i.e. which has $a' = 2\sqrt{3}\, a_{TaS_2}$ and $b' = 2a_{TaS_2}$) and that the molecules are oriented with the 2-fold axis perpendicular to the host layer, and with the nitrogen atom as close as possible to a tantalum atom (i.e. model (b)). Then Figure 55 gives a number of possible dispositions of the pyridine molecules within the supercell. The two simplest have

the molecular planes parallel to b' (i) or parallel to a' (ii). Both have orthorhombic symmetry consistent with the diffraction pattern, but in each case the unit cell is half the size of the one deduced from diffraction. Full lines and broken lines are used to differentiate between molecules associated with upper and lower host layers and therefore in opposing orientation, and it can be seen that there is bad steric hindrance between the hydrogen atoms in the molecules.

In models (iii) and (iv) the molecules are canted slightly so as to reduce this steric hindrance, and therefore fill the interlamellar space more effectively. The chief advantage of (iv) is that the unit cell contains the correct number (four) of pyridine molecules. The other appeal of this model is that the axes of the molecules are displaced so as to bring the nitrogen atoms closer to ideal sites adjacent to tantalum atoms (as proposed in section 5.3.1 on the basis of the diffraction pattern). Furthermore the molecules now tend to form dipole pairs, which are known often to be a stable configuration.

5.4 Discussion of Structural Results

The most prominent result of this study of the TaS_2(pyridine) intercalation complex is that the expansion of the interlayer separation and the occupation by the pyridine of the interlamellar space are accompanied by a stacking change in this host matrix structure (Figure 56):

$$AcA\ BcB \longrightarrow AcA|AbA$$

This displacement of alternate tantalum disulphide layers has two important consequences:

(1) The superimposed cc stacking sequence of the metal atoms - which is characteristic of Group Va materials in general - has been replaced by an alternating cb sequence. This is found, rather, in the pure Group VIa materials.

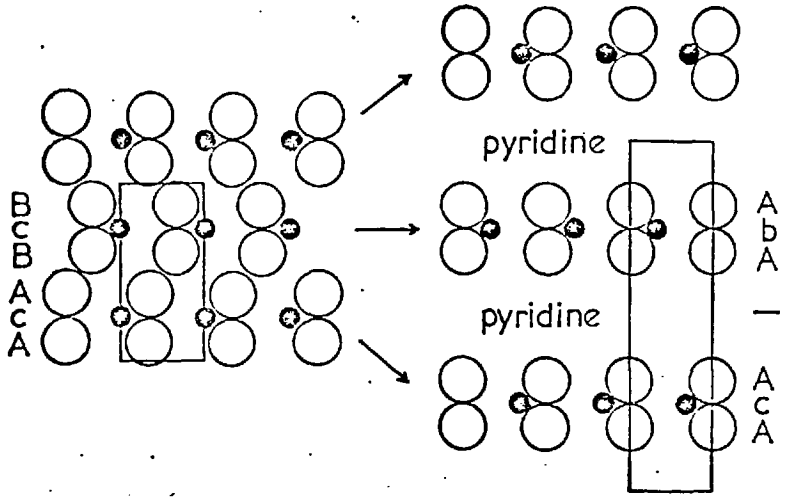


Figure 56 The expansion of the layer separation when 2H TaS_2 is intercalated with pyridine is accompanied by a stacking change. The (11$\bar{2}$0) sections in this Figure also permit comparison of the unit cells adopted before and after intercalation; ● Ta; O S.

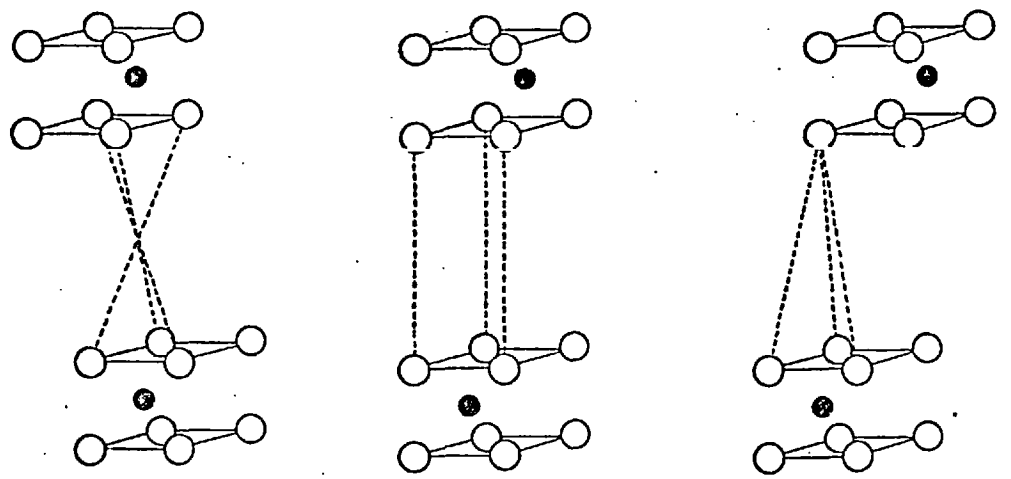


Figure 57 The three possible stacking sequences for the expanded 2H TaS_2 lattice, showing (a) octahedral, (b) trigonal prismatic, (c) tetrahedral environments associated with an interlamellar site adjacent to a Ta atom in the lower layer. ● Ta; O S.

(2) The sulphur atoms move to AA stacking about the Van der Waals gap, and thereby divide the interlamellar space into trigonal prisms. This can be compared with the trigonal prismatic co-ordination of the alkali metals in their intercalation complexes with tantalum and niobium dichalcogenides, discussed by Omloo and Jellinek (1969).

The results also favour a model in which the pyridine molecules are oriented perpendicular to the TaS_2 layers, rather than the model in which they are parallel to these layers.

These findings are consistent in general terms with the following interpretation. The perpendicular alignment of the pyridine molecule allows the nitrogen atom in the ring to approach more closely to a tantalum atom in the layer than if the molecule were parallel. Moreover the sp^2 hybrid orbital containing the nitrogen lone pair is then in a favourable position to interact with the tantalum conduction d-band. Such interaction would then allow some degree of charge transfer to place, consistent with the findings of Beal and Liang (1973).

The proposal that the nitrogen atoms in alternate molecules are associated with opposite surface of the gap, and that there are equal populations of molecules with opposing orientations (i.e. 'up' or 'down') means that the dipole moments on adjacent molecules tend also to be opposed, and thereby satisfy electrostatic energy considerations.

The model which was very tentatively proposed for the packing of the pyridine molecules in the interlamellar space does indeed consist of paired dipoles. There is still however the intriguing fact that each pyridine molecule occupies on average the area of 2½ TaS_2 units rather than the simpler two. Since the characteristic translation distances parallel to b' are slightly greater

than 2a (TaS_2), it might well be expected that periodic faulting of the intercalate structure, consisting of displacements of the pyridine molecules towards ideal sites, would be required to regain register between the pyridine and host structures. This faulting would occur with the periodicity of the $2\sqrt{3}$ a x 13 a coincidence cell. A possible reason why the 2½a periodicity is chosen for the pyridine superlattice is discussed in section 11.11.

When the tantalum atoms are stacked cc as in the pure 2H TaS_2 structure, the sites available for N-Ta interaction in the top and bottom surfaces of the interlamellar space superimpose (Figure 57 a). The number of possible charge transfer sites available to pyridine molecules therefore doubles when the tantalum layer stacking changes to cb. These sites now occur alternately in the upper and lower host layers. Adjacent sites have a projected separation of $a/\sqrt{3}$ = 1.9 Å, and clearly could not accommodate a pair of pyridine molecules. Other site separations can be found where the dipole pairs can be accommodated in the way discussed in the previous section.

Of the two ways in which the stacking change could in principle take place, the one deduced from experiment in fact divides the interlamellar space into trigonal prisms (Figure 57 b) whose bases provide sites for both the nitrogen and hydrogen atoms, diametrically opposite one another in the pyridine ring. The alternative stacking change (Figure 57 c) divides the space into sulphur octahedra and tetrahedra, with the tetrahedra situated over sites suitable for charge transfer. Such tetrahedra must undoubtedly provide a less favourable environment for the pyridine molecules than the trigonal prisms, but the possibility that some stacking faults of this type do occur cannot be ruled out as an explanation of the line broadening effects mentioned in section 5.2.3.

There is still controversy among authors about the orientation of the pyridine molecules, and a number assume that the molecules are parallel to the host layers, for instance Gamble, Osiecki and DiSalvo (1971), and Acrivos and Salem (1974). In attempting to reconcile this with the results of the present investigation, which favours perpendicular orientation, it seems that the answer may lie in the possibility of either orientation occurring, according to certain conditions. Indeed Gamble, Osiecki and DiSalvo (1971) reported the presence of two phases with slightly different c-axis expansions. In the present work, only one phase was detected, which corresponded to the phase with the smaller expansion. It is tempting to wonder whether the other phase has the parallel orientation. Thompson (1974) suggests that the phase corresponding to the perpendicular orientation is formed when there is a deficiency of sulphur, for instance by the reaction of pyridine with sulphur from the host lattice, while the other phase (which he also states is more stable and ordered) is formed in the presence of excess sulphur.

Perhaps the most useful systems to extend these studies to would be the substituted-pyridine intercalation complexes, which originally suggested parallel orientation to Gamble, Osiecki and DiSalvo(1971) because changes in the substituent group generally made little difference to the interlayer separation.

6 DIFFRACTION RESULTS AND INTERPRETATION: 1T TANTALUM DISULPHIDE

6.1 Introduction

Electron diffraction studies (Figure 58) established that the material exists in three distinct metastable phases over the temperature range available to experiment, each phase being characterised by additional satellite reflexions in the reciprocal lattice. Transitions between the phases, designated $1T_1$, $1T_2$, $1T_3$, took place at temperatures in agreement with the results of resistivity measurements (Thompson, Gamble, Revelli 1971). Although it was not possible to measure the transition temperature accurately in the electron microscope, the $1T_2$ phase was consistently found to be stable over a narrower range of temperature than that deduced from electrical data, (Thompson et al, 1971). The results were reproducible in crystals from several different growth batches.

The geometry of the hk.0 section of the reciprocal lattice was obtained from electron diffraction. Tilting the electron beam slightly relative to the crystal enabled limited information to be gained about the positions of the satellite reflexions out of the hk.0 plane. X-ray diffraction photographs (Fig 59) with the incident beam parallel to $\underline{c}^*$ confirmed the reciprocal lattice geometry, and showed that the direct space periodicities implied by the satellite reflexions were characteristic of the whole crystal. With the incident X-ray beam normal to $\underline{c}^*$, it was possible to locate the heights of the satellites above the hk.ℓ planes precisely (Figure 61). X-ray photographs also enabled qualitative intensity data to be obtained for all three phases. Diffractometer measurements of intensity for the room temperature $1T_2$ phase led to a more accurate characterisation of this, and these results are dealt with separately in Chapter 7.

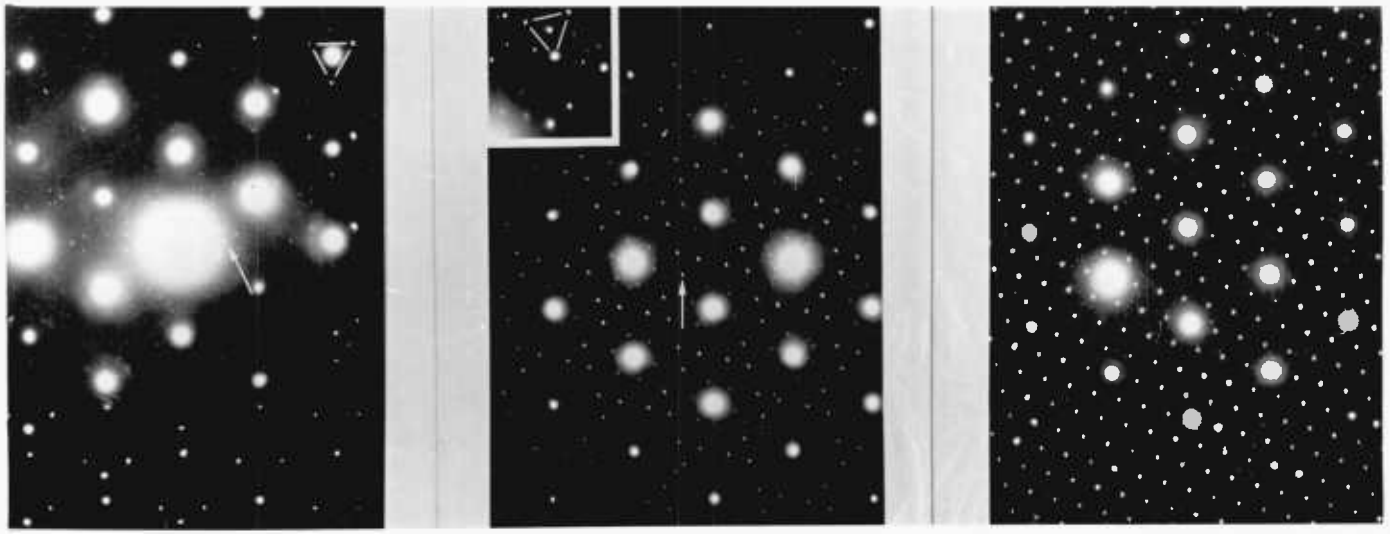


Figure 58 Selected area diffraction patterns with incident electron beam parallel to $\underline{c}^*$: (i) $1T_1$ at 340 K, identifying the triangular grouping $\{\underline{S}_M(10.1)\}$ and indicating by arrow one $\underline{S}_M(11.0)$ reflexion near the origin; (ii) $1T_2$ at 290 K, the arrow indicating a $\underline{S}_M(11.0)$ reflexion, and the inset showing a triangular grouping $\{\underline{S}_M(10.1)\}$ when the beam is tilted slightly; (iii) $1T_2$ TaS_2 at 150 K.

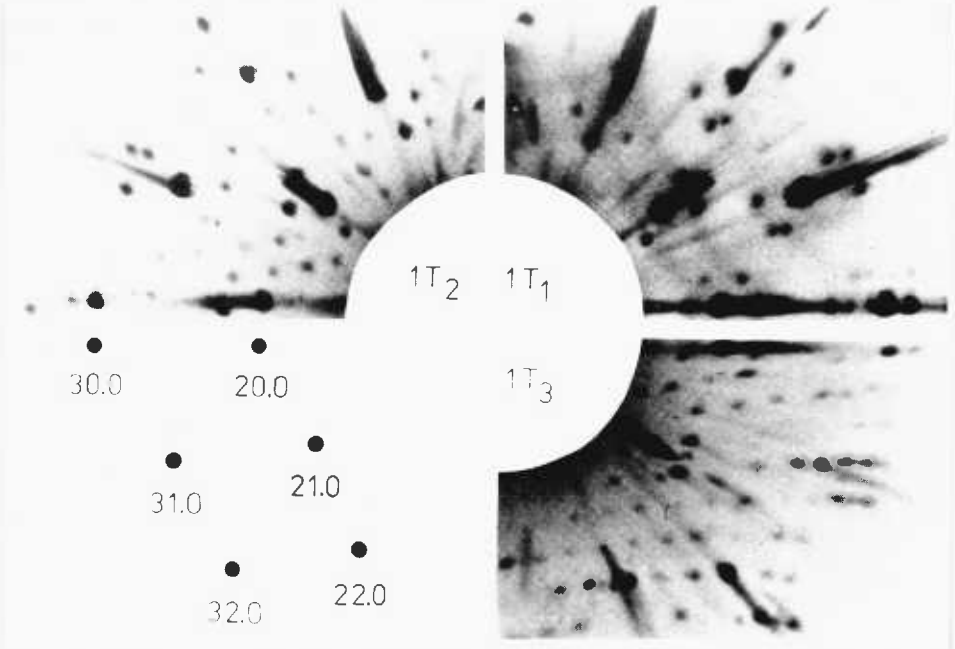


Figure 59 Oscillation X-ray photographs with incident beam in similar orientation to Figure 58 for (i) $1T_1$ at 390 K, (ii) $1T_2$ at 290 K, (iii) $1T_3$ TaS_2 at 80 K.

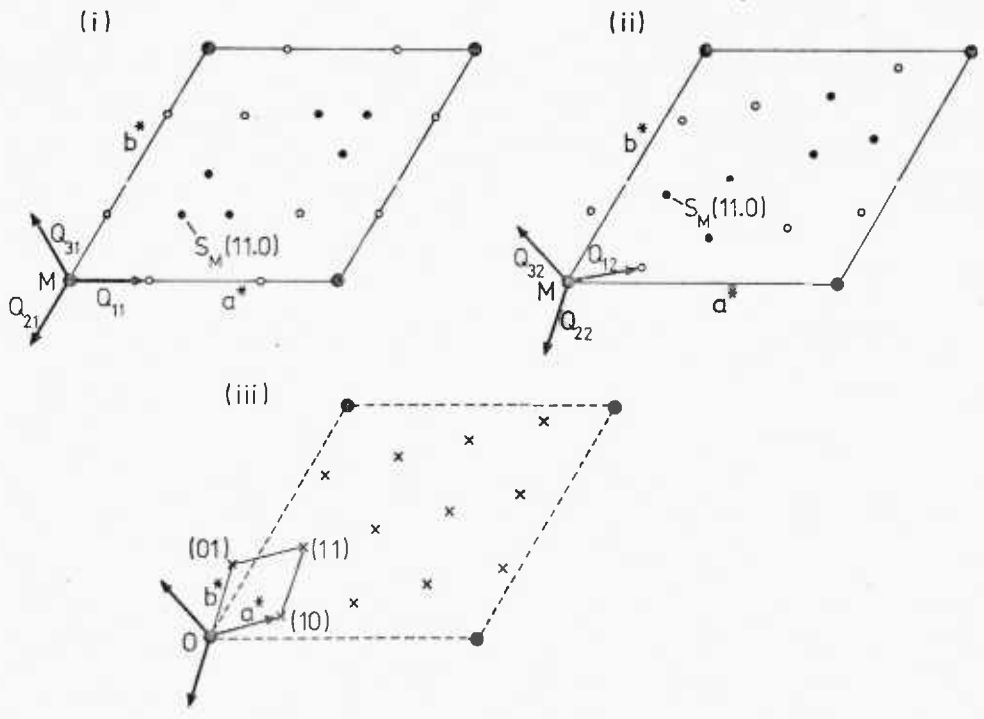


Figure 60 Reciprocal cells for each distorted 1T TaS_2 phase, where $\underline{Q}_{i1}$, $\underline{Q}_{i2}$, $\underline{Q}_{i3}$ are distortion wave vectors. In (i) $1T_1$ and (ii) $1T_2$ the unit cell is that of the matrix, satellite reflexions lying both in the hk.0 plane (●) and at $\pm\frac{1}{3}\underline{c}^*$ (○). In $1T_3$ (iii) the commensurate distortions define a reduced reciprocal cell, shown here in projection.

6.2 Reciprocal Lattice Geometry:

Matrix Reflexions

The matrix reflexions, which are the strong reflexions in Figure 58, form a hexagonal reciprocal lattice. They correspond to the average or undistorted CdI_2-like structure of the material (see section 1.2.1). Diffractometer measurements for $1T_2$ TaS_2 (the room temperature phase) showed that the base angles of the unit cell are $(120.0 \pm 0.1)^\circ$. This was confirmed by measuring the three a-axes of the cell and finding them to be equal. The angle between the c-axis and an a-axis was found to be $(90.0 \pm 0.2)^\circ$.

The $1T_2$ TaS_2 matrix is therefore trigonal and not, in any measurable way, sheared as a result of what will later be shown to be its distorted structure. Intensity measurements carried out at a later stage of the investigation, on both matrix and satellite reflexions also showed trigonal symmetry about the origin of reciprocal space.

The matrix reflexions can therefore be indexed on a trigonal unit cell (space group $P\bar{3}m$), and the cell dimensions are

$$a = 3.365 \text{ Å}, \quad c = 5.897 \text{ Å}.$$

As far as could be determined from careful measurements of the electron diffraction patterns, the projections of the unit cells (matrix) in the other two distorted phases are also trigonal. The symmetry of the $1T_3$ unit cell will be discussed later in this Chapter. The notation $\underline{M}(hk.\ell)$ will be used to index a matrix reflexion.

6.3 Reciprocal Lattice Geometry:

Satellite Reflexions in $1T_1$ and $1T_2$ TaS_2

The reflexions additional to those of the matrix, which appear in the reciprocal lattice, form clusters which are

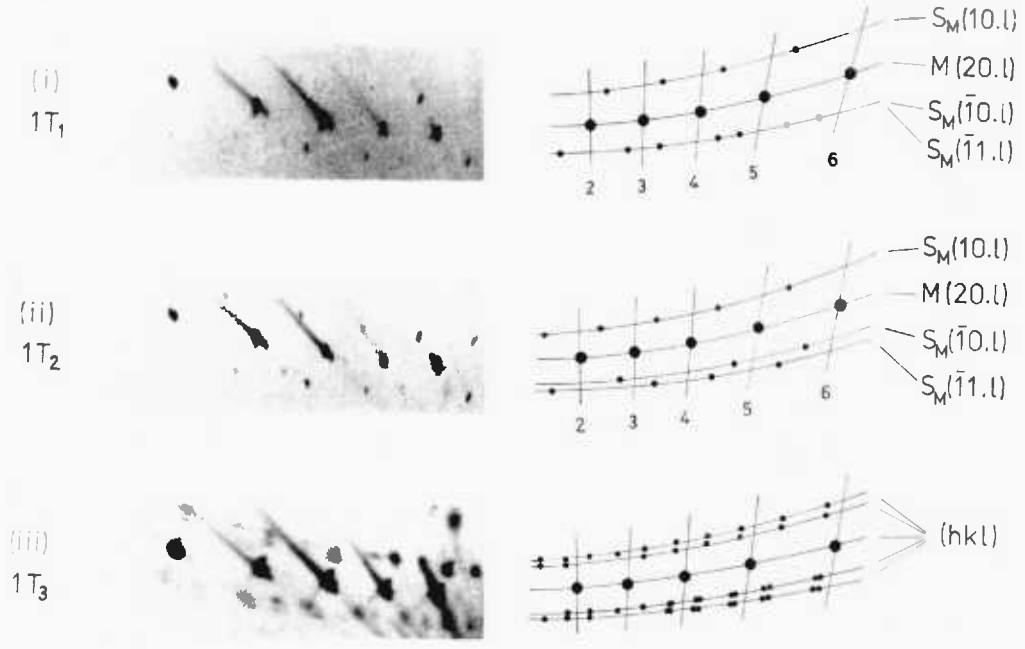


Figure 61 Oscillation X-ray photographs with incident beam approximately perpendicular to c*, and showing part of the matrix 20.ℓ row for each phase, and satellites. This can be compared with patterns predicted by rhombohedral distortion cells in $1T_1$ and $1T_2$, and by twinned triclinic cells in $1T_3$ TaS_2 (see text). The patterns for $1T_1$ and $1T_2$ differ as a result of the change in the orientation of Q.

repeated about each matrix reflexion. In $1T_1$ and $1T_2$ TaS_2 there are six first order satellites, and these are disposed in two triangular groupings which are visible in Figure 58 (i), (ii). The inset in (ii) is from the tilted area shown in full in Figure 63. In this case the Ewald sphere intersects the satellite reflexions which lie out of the reciprocal hk.0 plane. X-ray diffraction with the incident beam along $\underline{c}^*$ (Figure 61) implies that the octahedral groupings are at heights $(\ell \pm \frac{1}{3})\,\underline{c}^*$. Diffractometer measurements for $1T_2$ confirmed these heights more accurately. The positions of the six first order satellites about the matrix reflexion conform to the point group $\bar{3}m$.

In $1T_1$ TaS_2 all the symmetry elements of the octahedron of satellites are parallel to those of the matrix reciprocal lattice (Figure 62a). Although the $\bar{3}$ axis is still parallel to $\underline{c}^*$ in $1T_2$, the octahedron has changed its orientation by about 12° (Figure 62b).

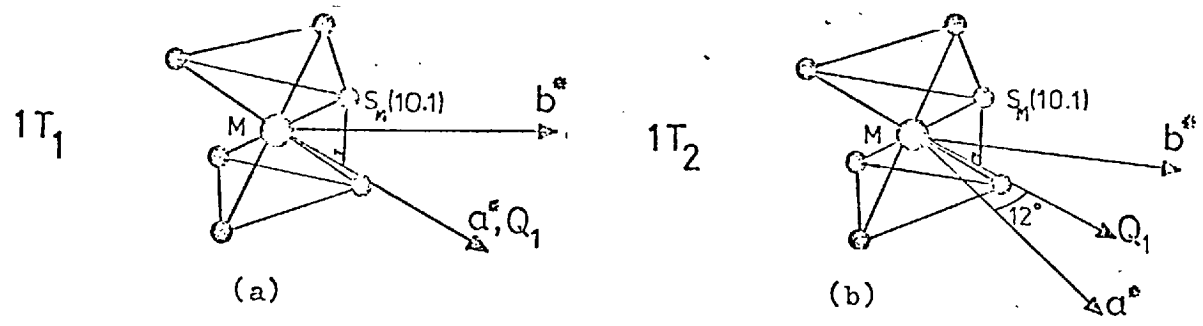


Figure 62

In each of the two phases the satellite periodicities define a cell in direct space which is rhombohedral, and which contains three layers of the matrix lattice. Both cells are in fact incommensurate (section 2.3) with the matrix lattice to the limit of measurement accuracy. The coincidence length, if it exists, must be in excess of 500 Å. For the present purposes a coincidence length of that magnitude can be forgotten and the superstructure considered as incommensurate.

The lack of commensurateness means that two independent



Figure 63 Selected area electron diffraction pattern from $1T_2$ TaS_2, with incident beam tilted away from normal incidence. First order satellites are clearly visible.

unit cells can always be defined, for the matrix and for the superstructure. It also means that the satellite reciprocal lattice is convoluted with that of the matrix, so that every matrix reflexion is 'parent' to an infinity of satellites. The notation introduced in section 2.3.2 will be used. Thus $\underline{S}_M(hk.\ell)$ refers to a satellite reflexion derived from a parent matrix reflexion $\underline{M}$, the indices h,k,ℓ here referring to the superstructure cell and <u>not</u> the matrix cell. $\{\underline{S}_M(hk.\ell)\}$ refers to the group of symmetry related satellite reflexions. The first order group for instance contains six members.

The indices of a matrix reflexion can be referred to more specifically. $\underline{S}_{30.0}(10.1)$ for example refers to the satellite reflexion (with indices (10.1)) whose parent is the matrix reflexion $\underline{M}(30.0)$. Once the unit cell of the superstructure has been defined, a satellite reflexion has a unique parent (this of course no longer applies if the two cells become commensurate). As the examples above have already implied, a hexagonal system of indices will be used for both matrix and superstructure.

Plates (i) and (ii) of Figure 58 indicate that there are satellite reflexions also in the matrix hk.0 plane. These can be indexed as $\underline{S}_M(11.0)$ when the first order group closest to the matrix reflexion is indexed $\underline{S}_M(10.1)$.

$\underline{M}$ and $\underline{S}_M$ are in fact reciprocal lattice vectors so that

$$\underline{K} = \underline{M} + \underline{S}_M$$

$$\underline{M} = h\underline{a}^* + k\underline{b}^* + \ell\underline{c}^*$$

A similar set of reciprocal axes can be defined for the superstructure (as in section 2.3.2). However, an alternative system proves to be rather more convenient for a layer material. Three reciprocal vectors $\underline{Q}_1$, $\underline{Q}_2$, $\underline{Q}_3$ which are related by trigonal symmetry are chosen. They lie within the hk.0 plane of the matrix reciprocal lattice, i.e. $\underline{Q}_i.\underline{c}^* = 0$.

Thus
$$\underline{S}_M = h'\underline{Q}_1 - k'\underline{Q}_2 + \ell\underline{c}^*$$
$$= h'\underline{Q}_1 - k'\underline{Q}_2 + \tfrac{1}{3}\ell'\underline{c}^*$$

where h',k',ℓ' are indices based on the superstructure cell. This shows that $\underline{S}_M$ has effectively been separated into an in-plane component (a linear combination of the $\underline{Q}_i$) and a perpendicular component.

6.4 Reciprocal Lattice Geometry:

Satellite Reflexions in $1T_3$ TaS_2

In $1T_3$ TaS_2, Figure 58 (iii), the octahedra of satellite reflexions are replaced by what appears from electron diffraction to be a hexagonal superlattice of side $\sqrt{13}\,a$. Figure 61 however indicates that there has also been a change in the heights of the superlattice reflexions above and below the hk.ℓ planes, compared with the other two phases. The change in height will be discussed further in section 6.7.

The transition to a commensurate superlattice implies that strictly speaking reference should always be made to the supercell. It is for purposes of comparison very useful to be able still to refer to the 'matrix' reflexions. The matrix cell is now a subcell of the true unit cell: its physical meaning is of an 'average' or undistorted structure. The shift in position of the satellite reflexions within the hk.0 plane at the $1T_2$ - $1T_3$ transition is in fact extremely small. Notwithstanding this, there is a sudden and marked change in the diffraction pattern when continuous observation is made through the transition. The act of becoming commensurate must therefore involve other changes, for instance in the heights of the satellite reflexions. After the transition to $1T_3$ had taken place, the specimen was tilted relative to the electron beam, rather as it had been at room temperature. This time however tilting produced relatively little change in the appearance of the diffraction pattern.

6.5 Evidence for a Deformation Superstructure

The satellite reflexions define a superstructure; in general this could have two origins, as discussed in section 2.3. They could be produced as a result of periodic fluctuations in density of the atoms which scatter radiation, i.e. short or possibly long range order. This would include as possibilities for this material the ordering of vacancies - these would most probably be on the sulphur sublattice, since the vapour pressure of sulphur is much more than tantalum - or the ordering of interstitial atoms - most probably of tantalum in the empty sites in the interlamellar space. It is unlikely that the ordering would be of sulphur and tantalum atoms on similar sites because of the gross differences between the two species of atom. The alternative mechanism responsible for the additional periodicities could be periodic fluctuations in atomic position, i.e. displacements from ideal sites resulting from some kind of deformation wave or large amplitude phonon.

A study of the way the intensity of radiation scattered into the satellites varies with position in reciprocal space settles beyond doubt which of these two mechanisms is chiefly responsible for the superstructure. Neglecting absorption and Lorentz-Polarisation factors for the moment, the intensity of radiation scattered by an ordering mechanism must fall off with increasing scattering angle, either as the square of an atomic scattering factor (e.g. for vacancy or interstitial ordering) or as the square of the difference of two atomic scattering factors (e.g. in a binary alloy). For a superstructure based on periodic lattice distortions, the behaviour of the satellite intensities is quite different. There is initially a build up in scattered intensity with increasing scattering

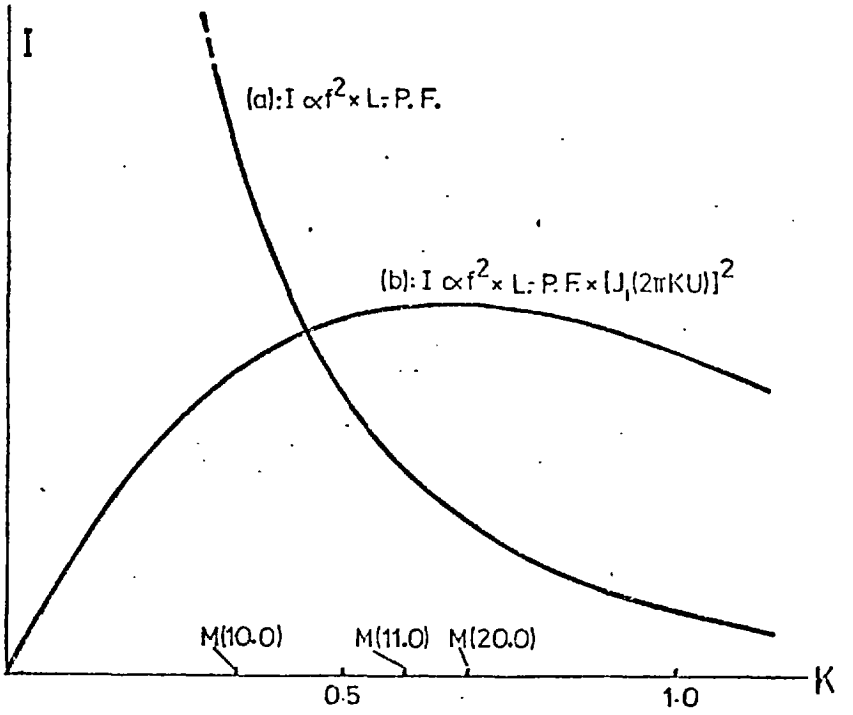
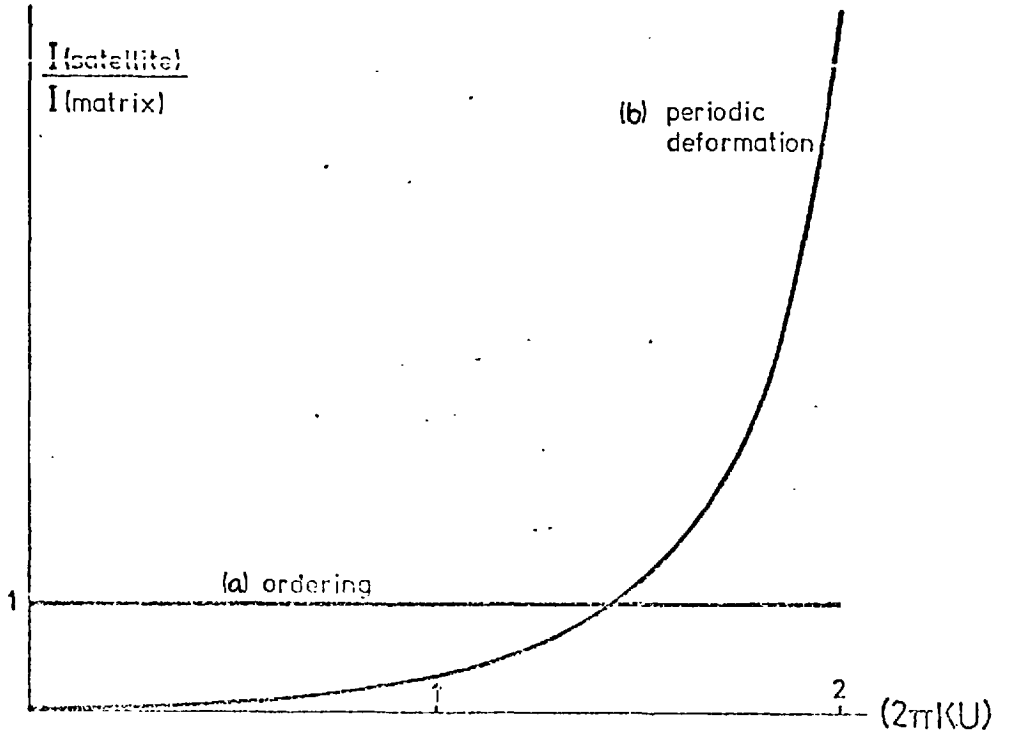


Figure 64 Intensity predicted for (a) ordering and (b) distortion mechanism for the satellite reflexions, for scattering vector $K \lesssim 1$. Variations in the geometrical part of structure factor are ignored.



Ratio of satellite to parent matrix reflexion intensities for same two mechanisms as in Figure 64.

angle, followed by a fall off in intensity at higher angles. In Figure 64 the predicted intensity from the two mechanisms is compared, without regard to variations in the geometrical part of the structure factor, and it shows clearly the difference between the two mechanisms at values of the scattering vector less than about 0.7.

A contrast in behaviour at larger values of scattering angle is more clearly seen by taking the ratio of satellite intensity to parent matrix intensity. From the theory (2.4.1):

$$\frac{I(\text{satellite})}{I(\text{matrix})} = \frac{|J_1(2\pi \underline{K}.\underline{U})|^2}{|J_0(2\pi \underline{K}.\underline{U})|^2} \quad \text{for deformations.}$$

Figure 64 shows that this ratio becomes very large for K = 2 when the mechanism is a periodic structural distortion, while the alternative ordering mechanism gives a ratio which remains on average approximately constant (again neglecting geometrical effect in the structure factor).

Examination of Figure 65 shows that the satellites associated with higher index matrix layer lines do indeed increase in intensity with scattering angle. The quantitative data considered in the next Chapter (see for instance Figure 69) very much confirm this. It found also that the diffuse scattering has the same variation in intensity with scattering angle.

Other evidence for deformation rather than ordering includes the observed specimen independence of the effects (the same physical parameters were observed in crystals from a number of different sources), the variation of the superstructure with temperature, and the fact that some phases have incommensurate superstructures. However the most important and direct evidence remains the intensity variation of the satellite reflexions, and in particular the initial increase with scattering angle.

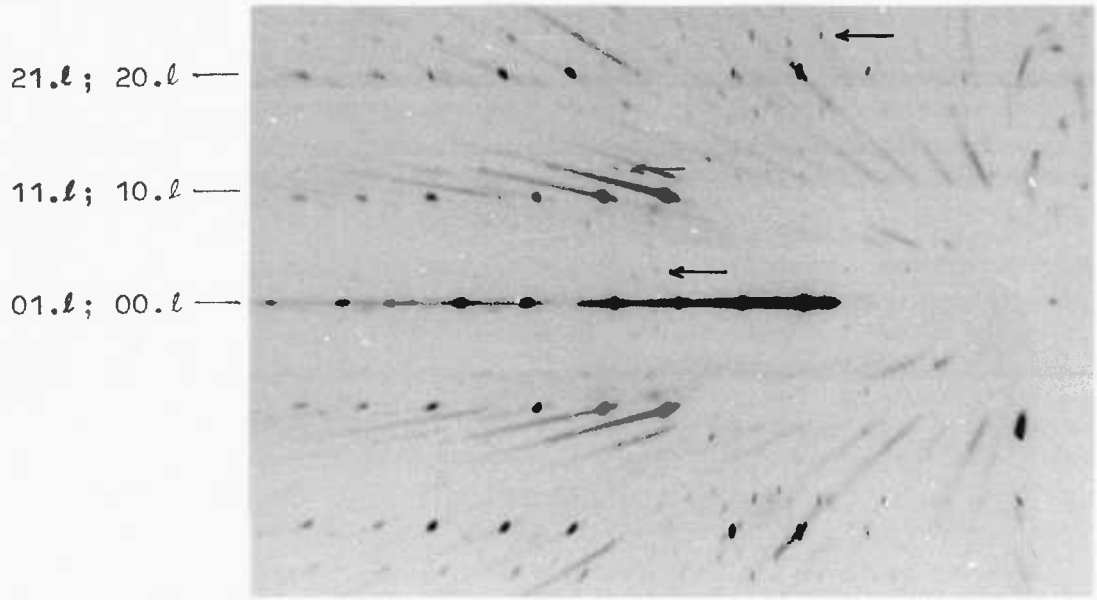


Figure 65 Oscillation X-ray photograph of $1T_2$ TaS_2 with incident beam normal to c* (cylindrical camera), and showing the relative increase in satellite intensity parallel to a (oscillation axis): compare the satellites indicated by arrows.

Since the matrix has remained strictly trigonal in $1T_1$ and $1T_2$, and individual layers in $1T_3$ are apparently also hexagonal, the concept of a shear structure as such must be ruled out. It is clear however that the periodic deformations must produce shearing on a local level, i.e. of the individual octahedra, but that the shearing is self-compensating within each unit cell of the deformation superstructure.

In section 6.3, the reciprocal lattice vector $\underline{S}_M$ was separated into an in-plane component (which is incommensurate with the matrix lattice), $h'\underline{Q}_1 - k'\underline{Q}_2$, and an out-of-plane component, $l'\underline{c}^*$. In fact the experimental evidence confirms that this separation has physical significance, since referring to Figure 65 again shows that while the satellite intensities initially build up with scattering vector parallel to $\underline{a}$ (oscillation axis), this effect is absent for increasing scattering vector parallel to $\underline{c}$. The in-plane component is therefore interpreted in terms of incommensurate periodic deformation waves, while the perpendicular component (which is commensurate with the layer spacing) is related to the stacking of the deformations in adjacent layers.

6.6 Determination of Deformation Wave Vector

The $\{\underline{S}_M(10.1)\}$ can thus be considered to arise directly from three symmetry related deformation waves. The term 'wave' is being used in a general sense to include any periodic modulating function, and not just a sinusoidal wave. The $\underline{Q}_i$ therefore take on physical significance, with $\Lambda = 1/\underline{Q}_i$ the wavelength of the deformation wave. Although strictly speaking $\underline{q}_i = 2\pi\underline{Q}_i$ is the wave vector, $\underline{Q}_i$ itself will also be referred to as this.

The vector amplitude of the deformation wave (i.e. the maximum displacement from mean position) is denoted by $\underline{U}_{Qi}$ for

$i = 1,2,3$. From the observed symmetry both of the lattice geometry and reflexion intensities:

$$\sum_i \underline{Q}_i = 0,$$
$$|\underline{Q}_i| = Q \quad \text{for all } i,$$
$$\sum_i \underline{U}_{Qi} = 0,$$
$$|\underline{U}_{Qi}| = U_q \quad \text{for all } i.$$

Symmetry will also be used in order to simplify the presentation of the results of measurements of the deformation wave vector. Only one of the three symmetry related wave vectors will be given. Thus if it is:-

$$x\underline{a}^* + y\underline{b}^*,$$

the other two are obtained as:-

$$-(x+y)\underline{a}^* + x\underline{b}^*,$$
$$y\underline{a}^* - (x+y)\underline{b}^*.$$

In the $1T_1$ phase the wave vector $\underline{Q}_{i1}$ - second subscript denoting the phase - remains directed always along the reciprocal $\underline{a}^*$ axis (Figure 50(i)). Measurements from diffraction patterns show that, within experimental error, its magnitude remains in a fixed ratio to the dimensions of the matrix reciprocal lattice throughout the range of temperature over which $1T_1$ TaS_2 exists, and that:

$$\underline{Q}_{i1} = 0.283\,\underline{a}^*$$

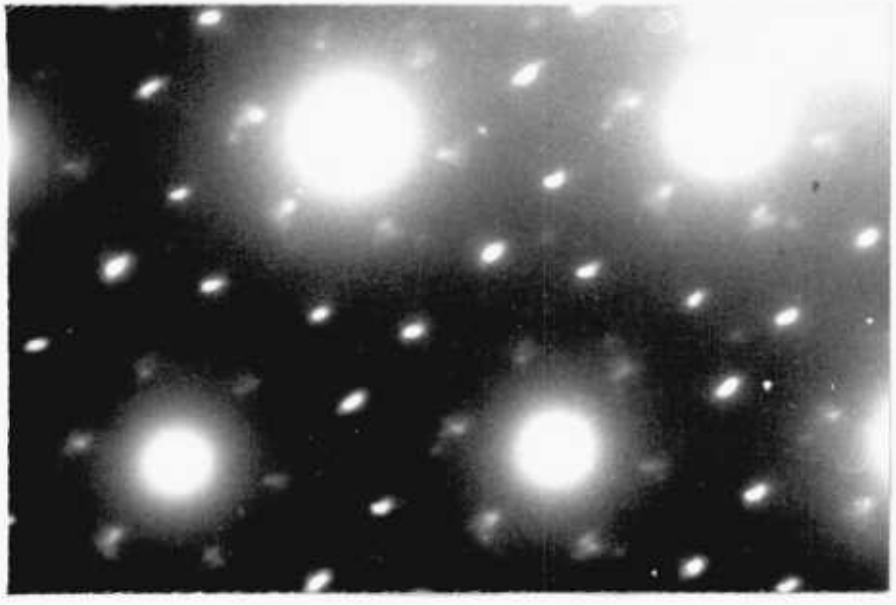
At about 340 K, the transition from $1T_1$ to $1T_2$ TaS_2 manifests itself by a discontinuous change both in the direction and magnitude of the deformation wave vector. The change in its magnitude is in fact very small and only just detectable. At room temperature measurements from electron diffraction and the X-ray single crystal diffractometer give:

$$\underline{Q}_{i2} = 0.245\,\underline{a}^* + 0.068\,\underline{b}^*$$
$$\text{i.e. } Q_{i2} = 0.285\,a^*$$

(a)



(b)



(c)

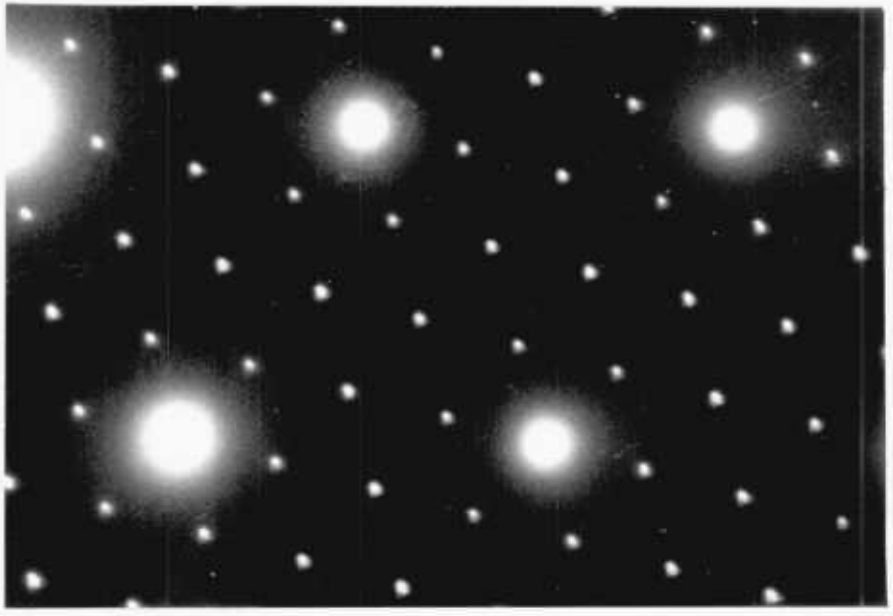


Figure 66

Temperature variation of the satellite reflexions in $1T_2$ TaS_2. In (a) at 331 K, the degree of incommensurateness is a maximum as shown by the clusters of high order satellites close to matrix reflexions, and by the lack of alignment of the $S_M(11.0)$. In (b) at ~ 250 K, the deformation wave vectors are closer to being commensurate, and the satellites <u>almost</u> lie on the superlattice of the $1T_3$ phase, given in (c) at 190 K.

As the $1T_2$ phase was cooled from 340 K towards the transition to $1T_3$ TaS_2 at about 190 K, there was a small but continuous decrease in the absolute magnitude of Q_{i2} as well as in its value relative to the reciprocal lattice. The angle between $\underline{Q}_{i2}$ and $\underline{a}^*$ increased simultaneously from 11.6 to 13.9° ($\tan^{-1}\sqrt{3}/7$)

This change in $\underline{Q}_{i2}$ on progressively lowering the temperature is most readily seen from the effect it has on the configuration of higher order $\underline{S}_M(hk.\ell)$ reflexions. Figure 66 shows the changes with temperature both in the appearance of the $\{\underline{S}_M(11.0)\}$ groupings near the centre of the matrix reciprocal cell, and of the third and fourth order clusters close to the projected positions of $\{\underline{S}_M(10.1)\}$ satellites. It was also this geometrical magnification of the changes in $\underline{Q}_{i2}$ which enabled the measurements to be made with a high relative accuracy.

Since the deformation waves are incommensurate with the matrix lattice in $1T_2$ TaS_2 there is an infinity of satellite reflexions in the vicinity of any point in reciprocal space, including one of these 'clusters', but only the strongest are observed directly. As the temperature is lowered, the progressive change towards commensurateness manifests itself in these clusters, as they tend to merge together into one superlattice reflexion.

At 190 K $\underline{Q}$ becomes commensurate, defining a $\sqrt{13}a \times \sqrt{13}a$ superlattice in $1T_3$ TaS_2 (Figure 58(iii)). The distortion wave vector does not change below 190 K (measurements were in fact made down to about 20 K).

$$\underline{Q}_{i3} = 3/13\,\underline{a}^* + 1/13\,\underline{b}^*$$
$$= 0.231\,\underline{a}^* + 0.077\,\underline{b}^*$$
$$Q_{i3} = 0.277\,a$$

Figure 60 summarises the reciprocal lattice geometries in the three metastable distorted 1T TaS_2 phases, while Table 10 summarises changes in the distortion wave vector.

Phase	Temperature	Q/a*	ϕ
$1T_1$	420 - 340 K	0.283	0°
$1T_2$	331 K	0.286	11.6°
	303 K	0.285	12.0°
	290 K	0.285	12.1°
	269 K	0.283	12.7°
	250 K	0.282	13.1°
$1T_3$	Below 190 K	0.277	13.9°

Table 10 Variation of deformation wave vector $\underline{Q}$ with temperature in 1T TaS_2; $\underline{a}^*$ is the matrix reciprocal lattice vector and ϕ is the angle between $\underline{Q}$ and $\underline{a}^*$.

6.7 Stacking of Deformation Waves in Adjacent Layers

In the previous section the in-layer distortion wave vectors $\underline{Q}_i$ were determined. The Fourier transform of the deformation wave system within a single TaS_2 layer, is a family of rods in reciprocal space which are perpendicular to the layer and hence parallel to $\underline{c}^*$. When the 3-D structure of the material is under consideration, the periodicities normal to the layers must be taken into account; in general these periodicities cause modulation of the rods. Thus the out-of-phase component of the distortion periodicity must give information on the way the waves stack together in successive layers.

The modulation of the rods in all three phases is such as to give discrete reflexions in X-ray diffraction photographs with the incident beam normal to $\underline{c}^*$. This implies a very good phase correlation between deformation waves in different layers. In both $1T_1$ and $1T_2$ the relative positions of the deformation waves in successive layers are such that there is reinforcement

of scattered radiation along the rods at $(l + \frac{1}{3})\underline{c}^*$ or $(l - \frac{1}{3})\underline{c}^*$ and destructive interference elswhere - Figure 61. In electron diffraction from $1T_1$ or $1T_2$ the $\{\underline{S}_M(10.1)\}$ satellites appear only when the beam is incident a few degrees away from normal to the layers (Figures 58 and 63).

The satellite reflexions define a deformation cell, whose dimensions within the layer are periods of the lattice deformation waves. In $1T_1$ and $1T_2$ TaS_2 the measurements of $\underline{Q}$ showed that the deformation waves were incommensurate, or commensurate with a very large unit coincidence cell. The strongest evidence for true incommensurateness comes in fact from the way the deformation wave vector changes with temperature in $1T_2$ TaS_2. This behaviour is extremely difficult to conceive of for a commensurate deformation cell, since it would involve a whole series of discrete jumps. This point has been emphasised, not only because there are important differences electrically between the two types of superstructure (which will be discussed in Chapter 11) but because there are significant structural differences too. A periodic structure modulated by a periodic deformation structure is periodic if and only if the periodicities are commensurate.

When the deformation periodicities are incommensurate with the lattice, no two atomic positions exactly superimpose as atomic positions within the infinite distorted lattice are translated into a single unit deformation cell. The result so far as Bragg scattering from the deformation wave is concerned, is therefore equivalent to scattering from a continuum. From the point of view of diffraction the reduced deformation cell may be considered to be in 'jellium'. An alternative way is to think of it as a statistical average.

The distortions in adjacent layers can therefore be regarded as forming a 3 layer stack, i.e. they stack rhombohedrally with the sequence $\alpha\beta\gamma$, where α, β, γ are conventional positions in the hexagonal, statistically defined, deformation cell. It must be noted however that α, β, γ cannot be defined uniquely within the matrix lattice. In $1T_1$ and $1T_2$ TaS_2, where $\{\underline{S}_M(hk.\ell)\}$ are referred to the local hexagonal system of reciprocal axes, the indices of all the observed satellites obey the normal rhombohedral condition, $-h+k+l = 3n$, where n is an integer.

The fact that the deformations are modulating a lattice of atoms rather than a continuum is expressed in diffraction by the deformation reciprocal lattice being convoluted with a matrix reciprocal lattice.

The satellite reflexions on the reciprocal rods parallel to $\underline{c}^*$ in $1T_3$ - Figure 61(iii) - are clearly no longer at the rhombohedral positions, $(\ell \pm \frac{1}{3})\,\underline{c}^*$, indicating that the transition to this phase from $1T_2$ has been accompanied by a change in deformation stacking. If the stacking sequence had changed from $\alpha\beta\gamma$ to $\alpha\alpha\alpha$ in $1T_3$ TaS_2 then Figure 61(iii) would show superlattice reflexions at $\ell\underline{c}^*$. If to a sequence $\alpha\beta$ there would be superlattice reflexions at $\ell\underline{c}^*$ and $(\ell+\frac{1}{2})\,\underline{c}^*$. The diffraction data support neither of these stacking sequences. The data are in fact consistent with an assumption that the origin of distortions in adjacent TaS_2 layers is shifted by $\underline{a}$. This gives a triclinic cell, whose c-axis is the stacking vector of the distortions, i.e. $\underline{c} + \underline{a}$. This cell may be compared with the triclinic cell for the low temperature phase of 1T $TaSe_2$ reported by DiSalvo, Maines, Waszczak (1974). There are alternatives for the stacking vector, $\underline{c} + \underline{a}$ and $\underline{c} - \underline{a}$, and it would

therefore be expected that twin domains would be formed. Figure 61 (iii) is in fact consistent with twinning of the $1T_3$ TaS_2 crystal.

7 DETAILED DEFORMATION STRUCTURE OF 1T TANTALUM DISULPHIDE

7.1 Introduction

This Chapter deals mainly with the interpretation of the intensities of matrix and satellite reflexions obtained by diffractometer measurements on the room temperature phase of tantalum disulphide. The quantitative data thus obtained proved to be in complete agreement with estimates of intensity made from the photographic data presented in the previous chapter. The term detailed deformation structure refers to the displacement amplitudes and directions of the periodic distortions in the lattice, and also must include their phases, together with their profiles (sinusoidal, triangular, etc.). Some of these quantities have their parallels in conventional structural determinations, although the determination of the deformation structure is generally far more complex. Its complexity derives chiefly from there being convolution of the deformation reciprocal lattice with that of the matrix structure, so that deformation parameters cannot be measured directly.

The first step in the determination is essentially to deconvolve the deformation reciprocal lattice from that of the matrix. This gives the Fourier transform of the deformation cell and the second step therefore is to make a transformation back to direct space. These two steps will involve determining certain quantities (i.e. amplitude and phase of the Fourier components) from selected parts of the reciprocal lattice, followed by an attempt at refinement. The complexity of the problem makes however a full refinement in the conventional sense impracticable.

The data for $1T_2$ TaS_2 and its interpretation will be dealt with in two major parts, based on the two régimes outlined at the end of section 2.5.5. Data acquired in and close to the

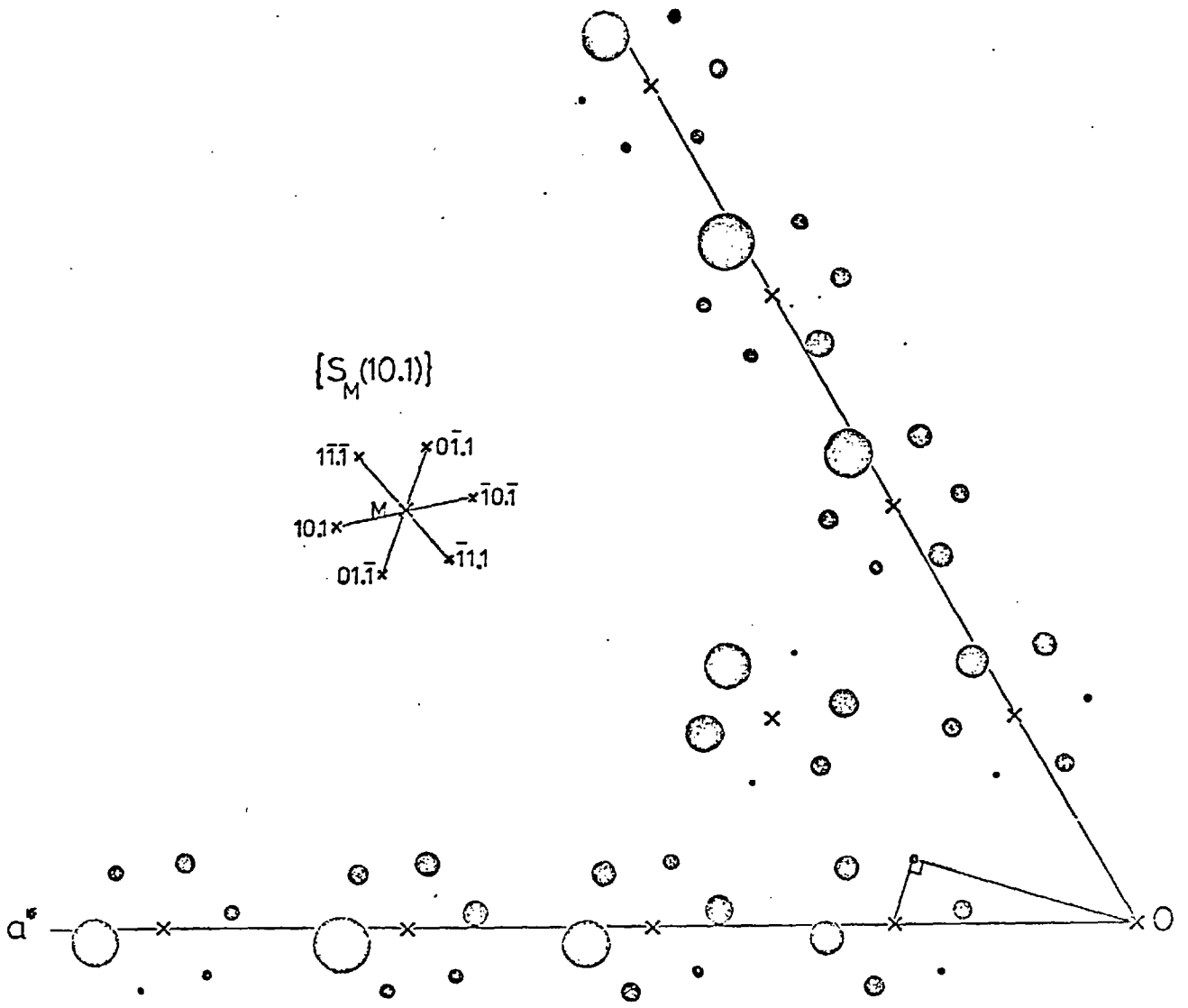


Figure 67 Hexant of matrix hk.0 plane of reciprocal lattice in $1T_2$ TaS_2. This diagram only shows matrix and $\{S_M(10.1)\}$ satellites for clarity. Radius of satellite is proportional to observed structure factor (Table 17).

matrix hk.0 reciprocal lattice plane will be used to determine displacements within the TaS_2 layers (perpendicular to $\underline{c}$). Intensities measured close to the $\underline{c}^*$ axis will be used to determine displacements perpendicular to the TaS_2 layers. This approach was found to be essential for such a complex reciprocal lattice. Wherever possible data will be presented both in table form and graphically. The relative weakness of higher order satellite reflexion meant generally the restriction of measurements to matrix reflexions, $\{\underline{S}_M(10.1)\}$ and $\{\underline{S}_M(11.0)\}$ satellites.

In the later sections of this chapter (7.5 - 7.7) a semi-quantitative discussion of the deformation structures of the other two distorted phases, $1T_1$ and $1T_3$ TaS_2 appears. This is based on photographic data and relies very much on comparison with the detailed model proposed for the room temperature phase.

7.2 Magnitude of In-Layer Displacements in $1T_2$ TaS_2

In Fig. 67 a hexant of the matrix reciprocal lattice hk.0 plane is shown. Since in-layer displacements only are being considered in this section, the $\{\underline{S}_M(10.1)\}$ reflexions at $\pm \frac{1}{3}\underline{c}^*$ have been projected on to the plane so as to give a 2-D lattice. Fig. 67 particularly shows the first order satellites and the approximate magnitude of their structure factors (proportional to the radius of the circles used to represent the reflexions). The numerical data on which these values are based appear in Table 19.

Several general points emerge from consideration of Fig. 67, all of which will be discussed in some detail in later sections: (a) There is no appreciable difference in the satellite pattern for matrix reflexions with $-h+k = 3n$ (e.g. $\underline{M}(30.0)$, $\underline{M}(11.0)$) and for those with $-h+k \neq 3n$ (e.g. $\underline{M}(10.0)$, $\underline{M}(20.0)$). Since these two types of reflexion should have different contributions to

the structure factor from the sulphur, it is inferred that the predominant scattering in the satellite reflexions is from the tantalum.

(b) Structure factors are largest where $\underline{Q}$ (i.e. the in-plane component of $\underline{S}_M$) is approximately parallel to the scattering vector $\underline{K}$, and least where $\underline{Q}$ is approximately perpendicular to $\underline{K}$. This indicates strongly that the mode of the deformation wave is predominantly longitudinal.

(c) There is a marked asymmetry in the structure factors of the satellite reflexions at $\underline{M} + \underline{Q}$ and $\underline{M} - \underline{Q}$, which cannot be explained in terms of variation of atomic scattering factor or of the orientation of the satellites. This lack of symmetry in the Fourier transform of the deformation cell suggests that the deformation function itself lacks reflection symmetry.

7.2.1 Structure Factors of M(h0.0) - Total Displacement

Comparison of Fig. 68 (a) and (b) shows clearly that the observed structure factors for the $\underline{M}$(h0.0) reflexions fall off very rapidly with increasing scattering vector. This trend is far too marked to be due to a conventional Debye-Waller factor and must be a consequence of the periodic lattice deformations. This decrease in matrix structure factor essentially monitors the scalar deviations from, or disorder in the matrix lattice planes. It cannot give detailed information about the deformation structure.

The fact that the structure factors approximates to zero in the region of $\underline{M}$(70.0), i.e. at spacings of the order of 0.4 Å, suggests that displacements in $1T_2$ TaS_2 are sufficient to bring on average half the atoms into antiphase with the other half. This elementary reasoning gives a magnitude for gross displacements of about 0.2 Å.

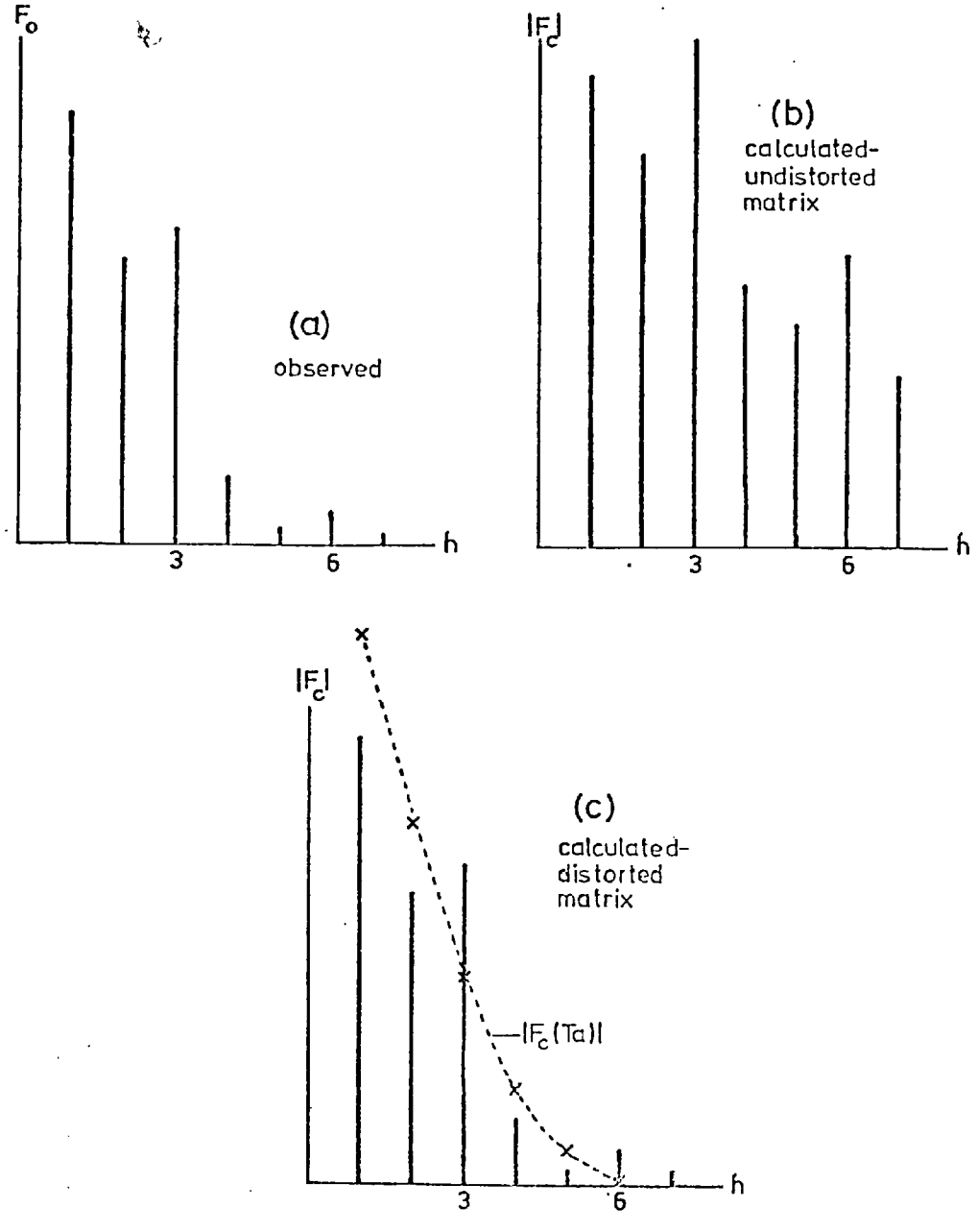


Figure 68 Observed (a) and calculated structure factors for the M(h0.0) reflexions: (b) for the undistorted TaS_2 matrix, and (c) for the distorted model of the matrix. Also shown is the Ta contribution to the structure factor alone. (Values from Table 11).

If a simple model with three symmetry related sinusoidal deformation waves of amplitude 0.2 Å is taken, and distortion of the Ta sublattice is assumed to predominate, then the fit between calculated and experimental data is quite good for matrix reflexions with h = 1, 2, 3. The agreement rapidly deteriorates however for h ≥ 4, where the structure factor is necessarily more sensitive to the detailed deformation structure.

Better agreement is in fact obtained by combining the 3 symmetry related distortions of the Ta sublattice with a slightly reduced amplitude, with temperature factors for both the tantalum and sulphur scattering. With this model, the best fit to experimental data was gained with a distortion amplitude of 0.173 Å, a temperature factor for the Ta sublattice of $e^{-0.127K^2} = e^{-0.015h^2}$, and a temperature factor for the S sublattice of $e^{-0.20K^2} = e^{-0.024h^2}$.

The tantalum 'temperature factor' implies RMS thermal displacements of about 0.08 Å. This is rather high, but must in fact take into account all other displacements, both thermal disorder and distortion waves of other periodicities. The exponential term for this 'temperature factor' can in fact be replaced by a zero order Bessel function: $J_o(0.63K)$, with little change in the fit to experimental data. The choice of a Bessel function rather than an exponential function suggests that the scattering is due to a specific deformation wave, rather than to general thermal motion. Clearly the 'temperature factor' both for the tantalum and sulphur sublattices must be thought of as including both at this stage.

Table 11 enables observed structure factors to be compared with those calculated from the model outlined above. These numerical values have also been used for Fig. 68, where agreement can be assessed graphically. Observed values have been scaled

to calculated by equating the sums of the structure factors.

h	F_o	F_c
1	47.0	48.2
2	31.1	31.2
3	34.4	34.4
4	7.4	6.5
5	1.8	1.4
6	3.4	3.6
7	1.5	1.3

Table 11 Observed and calculated structure factors for h0.0 matrix reflexions from $1T_2$ TaS_2, assuming three symmetry related sinusoidal deformation waves, $\underline{U}_Q$ = .173 Å.

From the agreement obtained we may conclude that the maximum displacements, U, of the tantalum atoms produced by the distortions is approximately 0.17 Å. The other static distortions included above in the 'temperature factor' together with thermal vibration, will later be shown to be higher harmonics of the deformation cell. For instance deformation waves with wave vectors $\underline{Q}_2 - \underline{Q}_3$, $\underline{Q}_3 - \underline{Q}_1$, $\underline{Q}_1 - \underline{Q}_2$, scattering radiation primarily into the in-plane $\{\underline{S}_M(11.0)\}$ reflexions. The larger value for total displacement of 0.2 Å estimated earlier takes into account the three distortions of wave vector $\underline{Q}$ together with all other displacements of the lattice.

7.2.2 Structure Factors of $\underline{S}_{h0.0}(10.1)$ and $\underline{S}_{h0.0}(\bar{1}0.\bar{1})$ — determination of U_Q, Fundamental Distortion Amplitude

The values of the structure factors for these pairs of satellites (Fig. 69 and Table 12) show clearly the marked asymmetry between $F(\underline{M} + \underline{Q})$ and $F(\underline{M} - \underline{Q})$. In section 2.6 it was shown that such an asymmetry is linked with a deformation wave whose profile lacks reflection symmetry, for instance the 'sawtooth' wave of section 2.6.3. A simple sinusoidal periodic deformation must

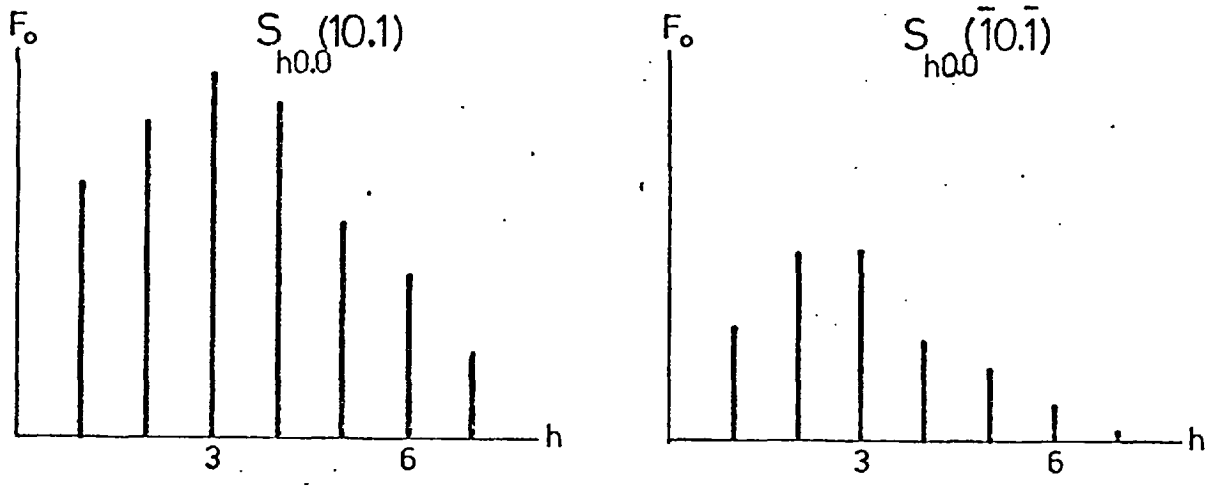


Figure 69 Observed structure factors for first order satellites of M(h0.0) reflexions, at $\underline{M} + \underline{Q}_1$ and $\underline{M} - \underline{Q}_2$.

therefore be excluded as a possibility.

A more complex deformation profile can be analysed to give a series of Fourier components with different amplitudes. In diffraction these additional Fourier components (e.g. with wave vector $\underline{Q}_2 - \underline{Q}_3$, $3\underline{Q}_1$) give rise to scattering contributions which are added to or subtracted from those of the fundamental distortions according to their phase. In the case of a wave with a sawtooth profile, approximately equal values are added to $F(\underline{M}+\underline{Q})$ and subtracted from $F(\underline{M}-\underline{Q})$. Thus the <u>average</u> of the structure factors of the paired satellites, $\underline{S}_{h0.0}(10.1)$ and $\underline{S}_{h0.0}(\bar{1}0.\bar{1})$ should give just that part which is due to the fundamental component of the deformation wave. It is convenient to use the following notation:

$$\langle F(S_M)\rangle = \tfrac{1}{2}\left\{|F(S_M(10.1))| + |F(S_M(\bar{1}0.\bar{1}))|\right\}$$

$F_{Ta}(M)$ = the Ta contribution to the matrix structure factor, shown in Fig.68(c).

$$r = \frac{\langle F(S)\rangle}{F_{Ta}(M)}$$

Then since all the other factors (mostly zero order Bessel functions) should approximately cancel out, r can be written:

$$r = \frac{J_1(2\pi\underline{K}.\underline{U}_Q)}{J_0(2\pi\underline{K}.\underline{U}_Q)} .$$

We can therefore determine $|\underline{U}_Q|$ directly from r, which can itself be calculated from the structure factors as outlined in the following Table:

h	$\lvert F(S_M(10.1))\rvert$	$\lvert F(S_M(\bar{1}0.\bar{1}))\rvert$	$\langle F(S)\rangle$	$F_{Ta}(M)$	r	$2\pi\underline{K}.\underline{U}_Q$	$\lvert\underline{U}_Q\rvert$
1	10.9	4.8	7.8	59.4	0.132	0.26	0.12
2	13.6	8.0	10.8	39.2	0.275	0.53	0.12
3	15.5	8.1	11.9	22.4	0.531	0.92	0.14
4	14.3	4.2	9.2	11.3	0.817	1.27	0.15

Table 12 Determination of $|\underline{U}_Q|$ from observed structure factors of $S_{h0.0}(10.1)$ and $S_{h0.0}(\bar{1}0.\bar{1})$ reflexions from $1T_2$ TaS_2.

The calculated value of U_Q increases with h from an initial 0.12 Å. This is therefore the amplitude of the fundamental Fourier component of the deformation structure. The apparent increase in U_Q results from the approximations no longer holding for large scattering vector.

If the calculation for U_Q is carried out using $F(S_M(10.1))$ instead of the average $\langle F(S_M)\rangle$, then a value of 0.17 Å is obtained. This is very close to the value derived from the matrix intensities of the previous section (7.2.1) for the reason that the contributions from all the higher Fourier components are in phase for the $S_{h0.0}(10.1)$ satellites, so that radiation is scattered by maximum displacements of the atoms. These contributions are out of phase for $S_{h0.0}(\bar{1}0.\bar{1})$ satellites, so that radiation is scattered by reduced displacements at this value of $\underline{K}$.

7.2.3 In-Layer Distortion of Sulphur Sublattice

When Fig. 67 was being discussed at the beginning of section 7.2, it was commented that the satellite reflexions in the hk.0 section of the reciprocal lattice give little direct indication of distortion of the sulphur sublattice. Reference to Fig. 68 gives the effect of sulphur scattering on the structure factors of the matrix reflexions. For the undistorted structure:

$$\begin{aligned} F(h0.0) &= f_{Ta} + 2f_S \cos(2\pi h/3) \\ &= f_{Ta} + 2f_S \quad \text{when } h = 3n \\ &= f_{Ta} - f_S \quad \text{when } h \neq 3n \end{aligned}$$

Consequently $\underline{M}(30.0)$, $\underline{M}(60.0)$, etc are stronger than the remainder of the $\underline{M}(h0.0)$, due to the sulphur contribution. This effect is completely absent from the satellite reflexions, confirming the conclusion that tantalum scattering predominates and that sulphur scattering can be ignored at this stage. Since the sulphur scattering factor is some 5 or 6 times smaller than

that of tantalum, the deformation amplitude on the sulphur sublattice would have to be of the same order of magnitude in order to be readily observable, even when the sulphur is scattering directly in phase or antiphase with the tantalum.

When the calculated structure factors were being fitted to the observed values for the M(h0.0) reflexions in section 7.2.1, a 'temperature factor' was found necessary for the sulphur scattering. This corresponds to displacements of the sulphur atoms of about 0.1 Å. In section 7.2.1 it was not possible to determine what fraction of this was due to thermal disorder and what to periodic lattice distortions. If there were in fact deformation waves of amplitude 0.05 Å on the sulphur sublattice and in phase with those on the tantalum sublattice, then there should be an approximately 20% difference due to sulphur scattering, between satellite reflexions of matrix reflexions with $h = 3n$ and $h \neq 3n$. Such a difference is not observed, so that 0.05 Å is very much an upper limit on the deformation amplitude (assumed in phase). The need for small in-layer displacements of the sulphur atoms is consistent with the close packing of the sulphur layers.

The possibility of the sulphur scattering out of phase (e.g. $\phi_Q = 90^\circ$ or 120°) cannot be excluded however. Indeed evidence from the study of other layer materials such as niobium diselenide (section 9.2) strongly points to this being the case there, while the fact that the $TA_\perp$ deformation of the sulphur sublattice (section 7.4) is out of phase by 120° also suggests that the in-layer component is out of phase. If this were the case, at least part of the sulphur scattering would be in the imaginary part of the structure factor, and so its detection would prove even more difficult.

7.2.4 Direction of $\underline{U}_Q$ and Mode of Deformation Waves

Fig. 67 clearly showed that the fundamental deformation mode is predominantly longitudinal acoustic within the layer. If however it were a pure LA mode (i.e. $\underline{U}_Q$ parallel to $\underline{Q}$) then the structure factor of the satellite $S_{10.0}(01.\bar{1})$ would be extremely small since for this reflexion $\underline{Q}$ is almost perpendicular to the scattering vector $\underline{K}$ and hence $\underline{K}.\underline{U}_Q \triangleq 0$. However, both Fig. 67, and Table 17 show that this is manifestly not the case, although the reflexion is weaker than most in the set of six. From this it is concluded that $\underline{U}_Q$ must also have a $TA_{//}$ component.

If, as before we take the average* structure factor for $F(\underline{M} + \underline{Q})$ and $F(\underline{M} - \underline{Q})$ for the $\{S_{10.0}(10.1)\}$ and $\{S_{11.0}(10.1)\}$, in order to minimise the effect of higher harmonics of the deformation cell, we obtain the following:

M(10.0)			M(11.0)		
Satellite	F_o	Average	Satellite	F_o	Average
10.1	11.8	8.7	10.1	10.8	9.6
$\bar{1}0.\bar{1}$	5.6		$\bar{1}0.\bar{1}$	8.5	
$0\bar{1}.1$	2.8	3.9	$0\bar{1}.1$	0.3	0.4
$01.\bar{1}$	4.9		$01.\bar{1}$	0.6	
$\bar{1}1.1$	1.4	4.0	$\bar{1}1.1$	6.0	9.1
$1\bar{1}.\bar{1}$	6.6		$1\bar{1}.\bar{1}$	12.2	

Table 13 Observed structure factors for $\{S_{10.0}(10.1)\}$ and $\{S_{11.0}(10.1)\}$ reflexions from $1T_2$ TaS_2.

Fig. 70 shows the disposition of these values about the two matrix reflexions:

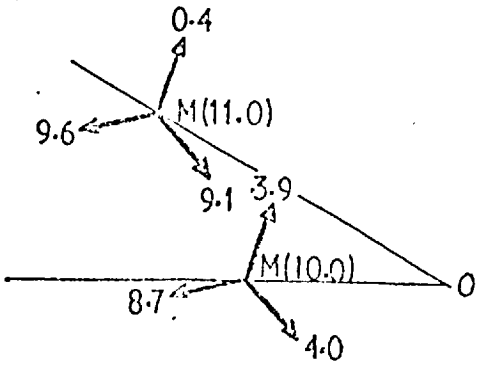


Figure 70

The fact that the structure factors for the $\underline{Q}_2$ satellites of $\underline{M}(11.0)$ are extremely small can only imply that

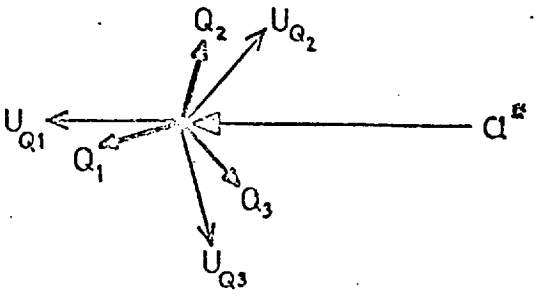
$$\underline{M}(11.0).\underline{U}_{Q_2} \triangleq 0.$$

This condition is satisfied if $\underline{U}_Q$ is parallel to $\underline{a}^*$, the matrix reciprocal lattice basis vector, as shown in Fig. 71. This is also confirmed by noting that:

$$\underline{M}.\underline{U}_{Q_2} \triangleq \underline{M}.\underline{U}_{Q_3} \quad \text{where } \underline{M} = \underline{M}(10.0)$$
$$\underline{M}.\underline{U}_{Q_1} \triangleq \underline{M}.\underline{U}_{Q_3} \quad \text{where } \underline{M} = \underline{M}(11.0)$$

i.e. the angle between $\underline{U}_{Q_i}$ and $\underline{Q}_i$ is 12°.

Figure 71



7.2.5 Higher Fourier Components

(a) Wave Vector a Multiple of Fundamental $\underline{Q}_i$

Earlier it was noted that the asymmetry of the first order satellite reflexions implies the presence of higher order Fourier components and a non-sinusoidal deformation profile. In this case the simplest way of determining the amplitudes of these higher components should be by measuring the intensities of the higher order satellite reflexions, e.g. with scattering vector $\underline{M} \pm 2\underline{Q}_i$. The procedure is unfortunately not as straightforward as this, since purely sinusoidal deformation waves give rise to infinite series of satellites (section 2.4.1) whose contributions to the structure factor must also be taken into account. It is however possible to make approximation when the scattering vector, $\underline{K}$, is small. Under these conditions the structure factor at $\underline{M} + n\underline{Q}$ for example, has contributions both from the nth order Fourier

component of the deformation cell with amplitude $\underline{U}_{nQ}$ and from the fundamental with amplitude $\underline{U}_Q$. The first is proportional to $J_1(2\pi\underline{K}.\underline{U}_{nQ})$, while the second is proportional to $J_n(2\pi\underline{K}.\underline{U}_Q)$.

For small K, the nth order Bessel function can be approximated

$$J_n(2\pi\underline{K}.\underline{U}_Q) = \frac{(2\pi\underline{K}.\underline{U}_Q)^n}{n!.2^n} \ll 1$$

since $z^n \ll z$ for $z = 2\pi\underline{K}.\underline{U}_Q < 1$.

therefore $J_n(2\pi\underline{K}.\underline{U}_Q) \ll J_1(2\pi\underline{K}.\underline{U}_{nQ})$

The higher order satellite reflexions close to the origin of reciprocal space ought consequently to give the amplitudes, $\underline{U}_{2Q}$, $\underline{U}_{3Q}\cdots\ \underline{U}_{nQ}$, directly. This means in practice restricting meansurements to $K \lesssim 0.26$, i.e. $\theta \lesssim 5^o$, for $\underline{U}_Q$ of the order of 0.1 Å. Not only is the amount of data in this region limited, but the high background intensity makes accurate measurement extremely difficult. The values thus obtained must be taken to be approximate only, and to be refined later.

The three satellite reflexions used to estimate $\underline{U}_{2Q}$ are shown in Fig. 72. The structure factor of $S_{10.0}(\bar{2}0.1)$ is very small, rather suggesting that $\underline{U}_{2Q}$ is almost perpendicular to the scattering vector, i.e. $\underline{K}.\underline{U}_{2Q} \sim 0$.

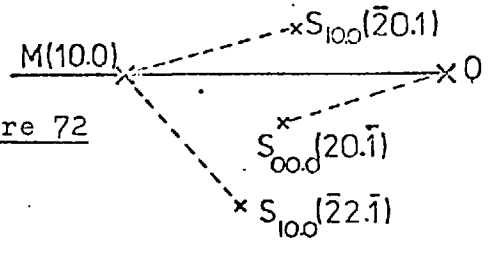
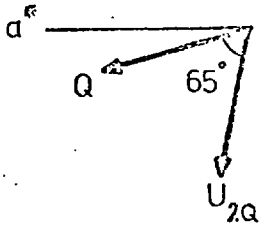


Figure 72



In this case, $\underline{U}_{2Q}$ must be approximately parallel to $\underline{K}$ for the $S_{10.0}(\bar{2}2.\bar{1})$ reflexion, enabling U_{2Q} to be estimated as 0.03 Å. Taking the angle between $\underline{U}_{2Q}$ and $\underline{Q}$ to be -65° the calculated structure factors in Table 14 are obtained:

Table 14 F_o and F_c for selected $S_{h0.0}(20.\bar{1})$ reflexions.

Reflexion	F_o	F_c
$S_{00.0}(20.\bar{1})$	0.4	0.5
$S_{10.0}(\bar{2}0.1)$	0	0
$S_{10.0}(\bar{2}2.\bar{1})$	1.4	1.5

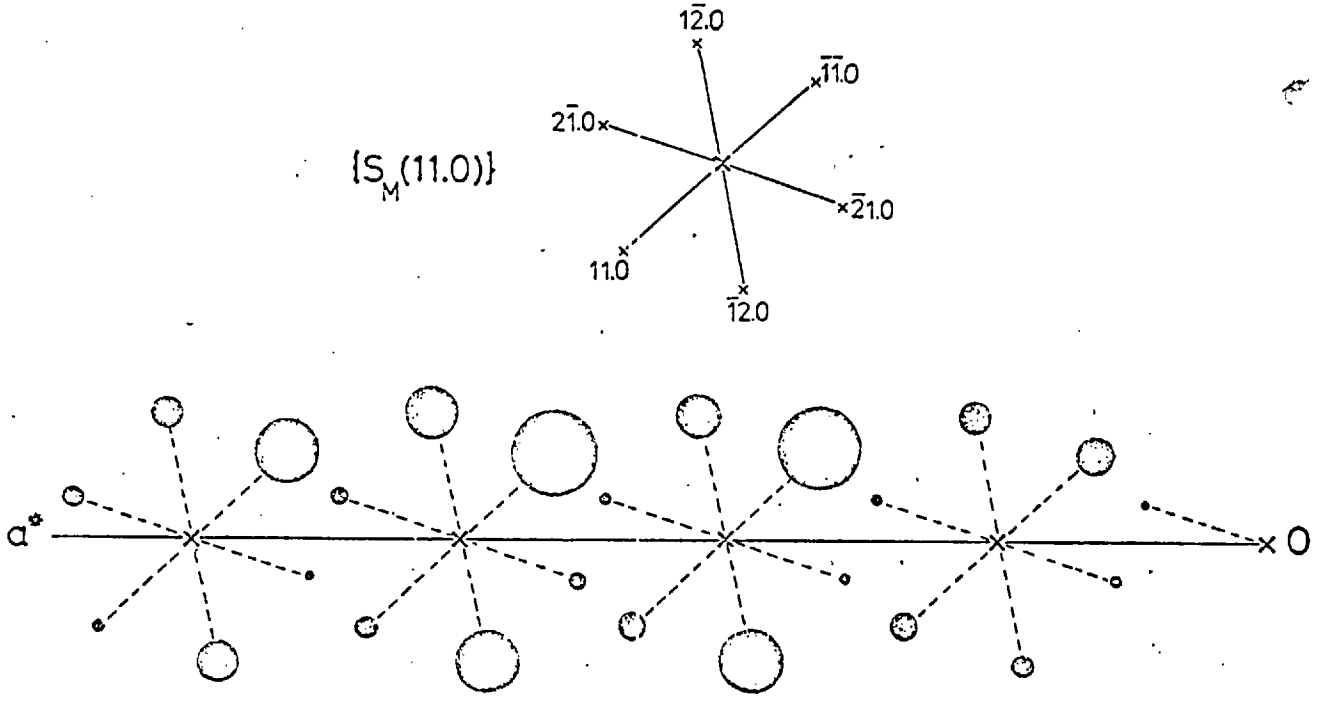


Figure 73 Observed structure factors for $\{S_{\pm h0.0}(11.0)\}$ satellites (radius proportional to structure factor).

Attempts were also made to estimate the values of $\underline{U}_{3Q}$ and $\underline{U}_{4Q}$ close to the origin, but the intensities of the respective satellites were too small for reliable measurement.

7.2.6 Higher Fourier Components

(b) Wave Vectors $\underline{P}_i$

The $\underline{P}_i$ are defined as in section 2.6.2, e.g. $\underline{P}_1 = \underline{Q}_2 - \underline{Q}_3$. For the 2-D distortion cell, the reciprocal lattice vector with the next largest magnitude after the fundamental $\underline{Q}_i$ is that corresponding to the(11.0) planes of the cell, i.e. $\underline{P}_i$.

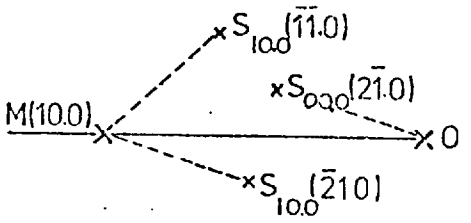
$$|\underline{P}_i| = \sqrt{3}|\underline{Q}_i|$$

Electron diffraction patterns (e.g. Fig. 58(b)) show that the $\{S_M(11.0)\}$ satellites are quite strong, immediately suggesting the presence of Fourier components with this wave vector. The same problem however arises with interpreting these satellites as with those discussed in part (a) of this section, namely that the fundamental distortions also scatter radiation into them.

The structure factor variation for $\{S_M(11.0)\}$ which is illustrated in Fig. 73, is quite different from the $\{S_M(10.1)\}$ (Fig. 67). Notably the maximum values occur when the scattering vector $\underline{K}$ is perpendicular to $\underline{P}$ rather than when parallel. This is very much indicative of a transverse mode ($TA_{//}$), in marked contrast to the fundamental LA mode.

Following similar reasoning to the first part of this section, we consider $S_M(11.0)$ reflexions with $K < 0.25$, as shown in Fig. 74.

Figure 74



Taking $\underline{U}_P$ = 0.05 Å, and the angle between $\underline{U}_{P_i}$ and $\underline{P}_i$ as 80° (i.e. angle between $\underline{U}_{P_i}$ and $\underline{Q}_i$ of 170°), we obtain the calculated structure factors shown in Table 15, where they can be compared with observed values. The agreement of these values suggests that this estimate of $\underline{U}_P$ can be used later for refinement of the deformation structure.

Table 15 Structure factors for selected $S_{h0.0}(11.0)$ reflexions.

Reflexion	F_o	F_c
$S_{00.0}(2\bar{1}.0)$	0.3	0.3
$S_{10.0}(\bar{2}1.0)$	0.6	0.8
$S_{10.0}(\bar{1}\bar{1}.0)$	2.5	2.5

7.2.7 Phases of Deformation Waves

The phases vary according to the relative origins of the different distortions within the deformation cell (see section 2.5.4). Reference to Figures 67 and 73 again, shows that the structure factors of the satellite reflexions undergo large variations in magnitude with changes in orientation about the parent matrix reflexions. This suggests that the phases are either 0 or π, or close to these values, since they give the maximum effect in adding or subtracting the contributions to the scattering from higher Fourier components. Phases close to $\pi/2$ or $3\pi/2$ tend to minimise this and produce satellites with approximately even intensity.

The most marked effect is shown for the pair of satellites at $\underline{M} \pm \underline{Q}_1$, i.e. that

$$F(\underline{S}_M(10.1)) > F(\underline{S}_M(\bar{1}0.\bar{1})) \qquad \text{where } \underline{M} = \underline{M}(h0.0)$$

To maximise this for the calculated structure factors, the phases of the distortion waves considered so far must be:

$$\phi_Q = \pi, \phi_P = 0, \phi_{2Q} = 0.$$

(See sections 2.5.4, 2.6.1, 2.6.2).

7.3 Calculations Based on Detailed Model for Distorted Layers

7.3.1 Summary of Initial Values for Parameters

Preliminary interpretation of the observed structure factor data in section 7.2. has enabled a model for the layer deformation cell to be set up. This model consists of three symmetry-related deformation waves (with wave vectors $\underline{Q}_1$, $\underline{Q}_2$, $\underline{Q}_3$) together with two sets of symmetry related higher order Fourier components ($\underline{P}_1$, $\underline{P}_2$, $\underline{P}_3$, $2\underline{Q}_1$, $2\underline{Q}_2$, $2\underline{Q}_3$). The initial values of the parameters to be used in the quantitative model are summarised in the following Table:

Wave Vector	Amplitude, $\underline{U}_Q$		Phase
	Magnitude U	Direction θ	ϕ
$\underline{Q}_i$	0.12	+ 12°	180°
$\underline{P}_i$	0.05	+170°	0°
$2\underline{Q}_i$	0.03	- 65°	0°

Table 16 Summary of initial values for the parameters for the deformation cell in $1T_2$ TaS_2. θ is the angle between the vector amplitude and the distortion wave vector.

7.3.2 Deformation Wave Combinations

The model as outlined above consists of 9 deformation waves all of which scatter radiation. From chapter 2, and section 2.6 in particular we can determine the scattering produced by these. The structure factor of a satellite reflexion at some scattering vector $\underline{K}$ is given by:

$$F(\underline{K}) = V(\underline{K}) \sum_{n_i} \left\{ J_{n_1}(2\pi \underline{K}.\underline{U}_{Q_1}) \ldots J_{n_9}(2\pi \underline{K}.\underline{U}_{Q_9}) . \exp(i \sum_{n_i} n_i \phi_i) \right\}$$

The summation is over all values of n_i ($i = 1,\ldots 9$) which satisfy the constitutive relationship:

$$-\sum_i n_i \underline{Q}_i = \underline{K} - \underline{M} .$$

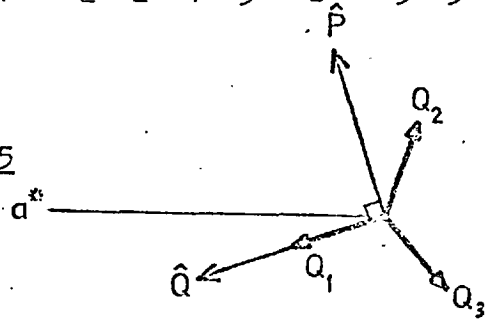
The expression for $F(\underline{K})$ shows that there are contributions to the scattering at $\underline{K}$ from different combinations of the 9 deformation

waves, and that each term in the summation is a product of 9 Bessel Functions and a phase factor. For the nine deformation waves in the model under consideration, the relationship between the wave vectors becomes:

$$\sum_i n_i \underline{Q}_i + \sum_i m_i \underline{P}_i + 2\sum_i l_i \underline{Q}_i = \underline{M} - \underline{K}$$

$$\underline{Q}_1(n_1-m_2+m_3+2l_1) + \underline{Q}_2(n_2+m_1-m_3+2l_2) + \underline{Q}_3(n_3-m_1+m_2+2l_3) = \underline{M} - \underline{K}$$

Figure 75



Resolving the vectors in the directions of $\hat{\underline{Q}}$ and $\hat{\underline{P}}$, which are orthogonal as shown in Fig. 75, and have moduli $|\hat{\underline{Q}}| = |\hat{\underline{P}}| = 1/Q$ we obtain two scalar equations:

$$2n_1 - n_2 - n_3 - 3m_2 + 3m_3 + 4l_1 - 2l_2 - 2l_3 + 2(\underline{K} - \underline{M}).\underline{Q} = 0$$

$$n_2 - n_3 + 2m_1 - m_2 - m_3 + 2l_2 - 2l_3 + 2(\underline{K} - \underline{M}).\underline{P} = 0$$

To obtain the relationship between the coefficients for a matrix reflexion, we substitute $\underline{K} - \underline{M} = 0$, i.e.

$$2n_1 - n_2 - n_3 - 3m_2 + 3m_3 + 4l_1 - 2l_2 - 2l_3 = 0$$

$$n_2 - n_3 + 2m_1 - m_2 - m_3 + 2l_2 - 2l_3 = 0$$

To obtain the relationship for a satellite $\underline{S}_M(10.1)$ we substitute $\underline{K} - \underline{M} = \underline{Q}_1$, i.e.

$$2n_1 - n_2 - n_3 - 3m_2 + 3m_3 + 4l_1 - 2l_2 - 2l_3 + 2 = 0$$

$$n_2 - n_3 + 2m_1 - m_2 - m_3 + 2l_2 - 2l_3 = 0$$

To obtain the relationship for a satellite $\underline{S}_M(1\bar{2}.0)$ we substitute $\underline{K} - \underline{M} = \underline{P}_1$, i.e.

$$2n_1 - n_2 - n_3 - 3m_2 + 3m_3 + 4l_1 - 2l_2 - 2l_3 = 0$$

$$n_2 - n_3 + 2m_1 - m_2 - m_3 + 2l_2 - 2l_3 + 2 = 0$$

Thus relationships between the cofficients can be obtained for the six $\{\underline{S}_M(10.1)\}$ and six $\{\underline{S}_M(11.0)\}$ satellites by substituting

$\pm \underline{Q}_1, \pm \underline{Q}_2, \pm \underline{Q}_3, \pm \underline{P}_1, \pm \underline{P}_2, \pm \underline{P}_3$, and performing cyclic permutations with i on the n_i, m_i, and l_i. For each reflexion we therefore require all the values of the coefficients n_i, m_i, l_i (i.e. the orders of the Bessel functions) which satisfy the pairs of equations. As the problem stands (9 unknowns, 2 equations) there is an infinite number of solutions. It is therefore necessary to place limits on the values the n_i, m_i, l_i can take. These can be determined practically by considering the order of magnitude of the Bessel functions.

It can readily be shown that for a finite argument z,

$$J_n(z) \rightarrow 0 \quad \text{as} \quad n \rightarrow \infty$$

This convergence of the Bessel function to zero with n is very rapid for small z. Thus if values of n are restricted so that for instance $|n| < N$, only very small contributions to the scattering are being omitted.

With the values given in 7.3.1 for the deformation amplitudes and a maximum value of scattering vector $\underline{K}$ of about 1.5 (corresponding to the reflexion $\underline{S}_{40.0}(hk.\ell)$) the arguments of the Bessel functions are respectively:

$$z_Q < 1.2, \; z_P < 0.5, \; z_{2Q} < 0.3$$

To maintain an accuracy of about 1% we can restrict the magnitude of the orders as follows:

$|n_i| \leqslant 3$ (since $J_4(z_Q) \triangleq 0.01\, J_1(z_Q)$)

$|m_i| \leqslant 2$ (since $J_3(z_P) \triangleq 0.01\, J_1(z_Q)$)

$|l_i| \leqslant 2$ (since $J_3(z_{2Q}) \triangleq 0.004\, J_1(z_Q)$)

The term in $J_1(z_Q)$ is generally the largest, and the errors introduced by this truncation of higher terms cannot be more than a few percent.

A further neccessary restriction is on the sum of all the orders, i.e.

$$\sum_i |n_i| + \sum_i |m_i| + \sum_i |l_i| \leqslant 7$$

This eliminates terms of overall order 8 and above, and introduces negligible error.

A computer programme was written to determine the sets of values of n_i, m_i, l_i which satisfy all these conditions. The Fortran programme, and a listing of the computed combinations are to be found in Appendix 2. 153 combinations of deformation waves must be considered for scattering at $\underline{K} = \underline{M}$, a matrix reflexion, 151 for scattering at $\underline{K} = \underline{M} + \underline{S}_M(10.1)$ a first order satellite, and 137 for scattering at $\underline{K} = \underline{M} + \underline{S}_M(11.0)$. The programme was checked by using it to calculate the $\{n_i\}$ for the simpler problem of three distortion waves and comparing the result with with that of hand calculation.

7.3.3 Details of Structure Factor Calculation

A second Fortran programme was written to calculate the structure factors for the $\underline{M}(hk.0)$, $\underline{S}_{hk.0}(10.1)$, and $\underline{S}_{hk.0}(11.0)$ reflexions. The full programme can be found in Appendix 3, but an outline of the logic is presented in Fig. 76. Disc storage facilities were used both to store this programme and to store temporarily the results of the preliminary programme prior to their use here. The Bessel functions were computed using a standard sub-routine (called BESJ) which uses backwards recursion followed by normalisation; the recursion formula is -

$$J_{n+1}(x) = J_{n-1}(x) - \frac{2n}{x} J_n(x)$$

The variables $\underline{U}_Q$, $\underline{U}_P$, $\underline{U}_{2Q}$ were varied in order to try and obtain for the model the best fit to observed structure factor data. The reflexions used for this lie within the range prescribed in the previous section, i.e. $\underline{M}(h0.0)$, $\{\underline{S}_{h0.0}(10.1)\}$, $\{\underline{S}_{h0.0}(11.0)\}$ with $h < 5$. Using just these variables it was found that the degree of fit was limited, and could not be improved beyound a certain value. A comparison of observed and calculated

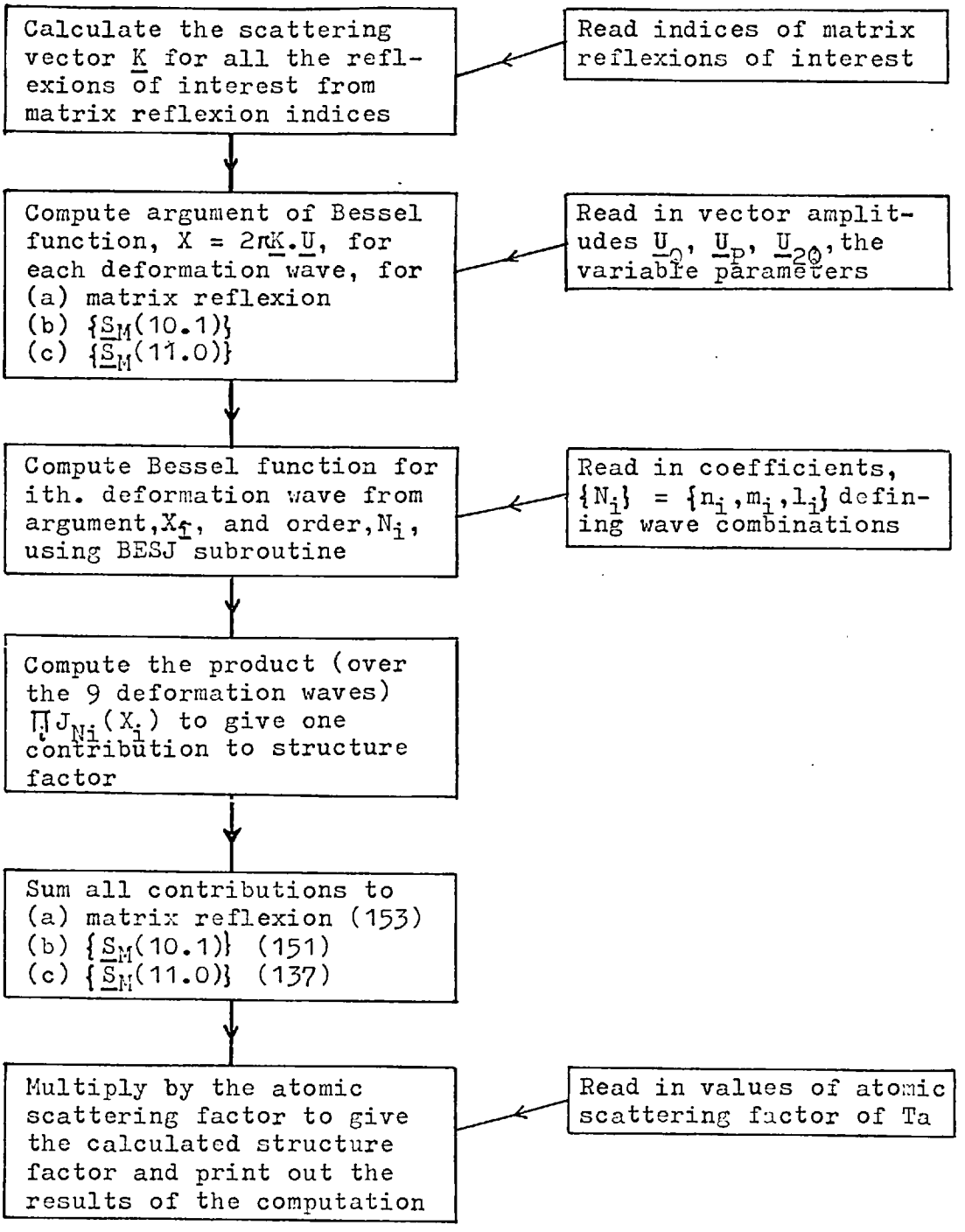


Figure 76 Summary of the computer programme written to calculate structure factors for the model of $1T_2$ TaS_2 with 9 deformation waves.

Reflexion	F_o	F_c
M(10.0)	47.0	46.9
$S_M(10.1)$	11.8	11.3
$S_M(1\bar{1}.\bar{1})$	6.6	6.4
$S_M(0\bar{1}.1)$	2.8	2.5
$S_M(\bar{1}0.\bar{1})$	5.6	6.0
$S_M(\bar{1}1.1)$	1.4	2.2
$S_M(01.\bar{1})$	4.9	5.9
$S_M(1\bar{2}.0)$	2.4	2.2
$S_M(\bar{1}\bar{1}.0)$	2.5	2.9
$S_M(\bar{2}1.0)$	0.6	0.8
$S_M(\bar{1}2.0)$	1.5	3.1
$S_M(11.0)$	2.1	1.1
$S_M(2\bar{1}.0)$	0.4	1.0
M(20.0)	31.1	31.0
$S_M(10.1)$	14.6	15.1
$S_M(1\bar{1}.\bar{1})$	7.1	6.7
$S_M(0\bar{1}.1)$	5.0	5.9
$S_M(\bar{1}0.\bar{1})$	8.4	9.0
$S_M(\bar{1}1.1)$	3.8	4.8
$S_M(01.\bar{1})$	6.3	5.6
$S_M(1\bar{2}.0)$	3.2	2.7
$S_M(\bar{1}\bar{1}.0)$	5.6	5.9
$S_M(\bar{2}1.0)$	0.8	1.1
$S_M(\bar{1}2.0)$	4.2	4.2
$S_M(11.0)$	2.0	0.4
$S_M(2\bar{1}.0)$	0.7	2.2

Reflexion	F_o	F_c
M(30.0)	34.4	34.0
$S_M(10.1)$	15.7	15.1
$S_M(1\bar{1}.\bar{1})$	6.0	5.2
$S_M(0\bar{1}.1)$	6.7	6.6
$S_M(\bar{1}0.\bar{1})$	8.1	8.0
$S_M(\bar{1}1.1)$	4.2	4.9
$S_M(01.\bar{1})$	4.6	3.6
$S_M(1\bar{2}.0)$	3.4	1.8
$S_M(\bar{1}\bar{1}.0)$	5.7	7.3
$S_M(\bar{2}1.0)$	1.0	1.3
$S_M(\bar{1}2.0)$	4.9	3.5
$S_M(11.0)$	1.5	0.7
$S_M(2\bar{1}.0)$	1.4	2.9
M(40.0)	7.4	7.3
$S_M(10.1)$	14.1	12.7
$S_M(1\bar{1}.\bar{1})$	4.1	2.9
$S_M(0\bar{1}.1)$	5.6	5.5
$S_M(\bar{1}0.\bar{1})$	4.2	5.5
$S_M(\bar{1}1.1)$	2.9	3.8
$S_M(01.\bar{1})$	2.1	1.5
$S_M(1\bar{2}.0)$	2.2	0.7
$S_M(\bar{1}\bar{1}.0)$	4.5	7.1
$S_M(\bar{2}1.0)$	0.3	1.4
$S_M(\bar{1}2.0)$	2.9	2.1
$S_M(11.0)$	0.8	1.1
$S_M(2\bar{1}.0)$	1.4	2.9

Table 17 Observed and calculated structure factors for the M(h0.0) reflexions and associated satellites. A temperature factor has been included in the calculated data, U_Q = 0.13 Å, U_P = 0.055 Å, U_{2Q} = 0.07 Å.

Reflexion	F_o	F_c
M(10.0)	47.0	46.6
$S_M(10.1)$	11.8	11.9
$S_M(1\bar{1}.\bar{1})$	6.6	6.7
$S_M(0\bar{1}.1)$	2.8	2.7
$S_M(\bar{1}0.\bar{1})$	5.6	5.9
$S_M(\bar{1}1.1)$	1.4	2.1
$S_M(01.\bar{1})$	4.9	5.9
M(20.0)	31.1	30.2
$S_M(10.1)$	14.6	16.4
$S_M(1\bar{1}.\bar{1})$	7.1	7.3
$S_M(0\bar{1}.1)$	5.0	5.9
$S_M(\bar{1}0.\bar{1})$	8.4	8.3
$S_M(\bar{1}1.1)$	3.8	4.3
$S_M(01.\bar{1})$	6.3	5.5

Reflexion	F_o	F_c
M(30.0)	34.4	33.7
$S_M(10.1)$	15.7	16.5
$S_M(11.1)$	6.0	5.2
$S_M(01.1)$	6.7	6.4
$S_M(10.1)$	8.1	7.3
$S_M(11.1)$	4.2	4.2
$S_M(01.1)$	4.6	3.4
M(40.0)	7.4	7.1
$S_M(10.1)$	14.1	14.1
$S_M(1\bar{1}.\bar{1})$	4.1	3.2
$S_M(0\bar{1}.1)$	5.6	5.2
$S_M(\bar{1}0.\bar{1})$	4.2	4.8
$S_M(\bar{1}1.1)$	2.9	2.8
$S_M(01.\bar{1})$	2.1	1.3

Reflexion	F_o	F_c
M(11.0)	60.2	59.8
$S_M(10.1)$	10.8	12.0
$S_M(1\bar{1}.\bar{1})$	12.2	13.4
$S_M(0\bar{1}.1)$	0.3	0.3
$S_M(\bar{1}0.\bar{1})$	8.5	8.4
$S_M(\bar{1}1.1)$	6.0	6.3
$S_M(01.\bar{1})$	0.6	0.4

Table 18 Observed and calculated structure factors for the M(h0.0) reflexions and first order satellites. A temperature factor has been included in the calculated data, U_Q = 0.13 Å, U_P = 0.06 Å, U_{2Q} = 0.10 Å.

Reflexion	F_o	F_c
M(10.0)	47.0	47.0
$S_M(1\bar{2}.0)$	2.4	2.1
$S_M(\bar{1}\bar{1}.0)$	2.5	2.5
$S_M(\bar{2}1.0)$	0.6	0.8
$S_M(\bar{1}2.0)$	1.5	3.1
$S_M(11.0)$	2.1	1.1
$S_M(2\bar{1}.0)$	0.4	1.0
M(20.0)	31.1	31.2
$S_M(1\bar{2}.0)$	3.2	2.5
$S_M(\bar{1}\bar{1}.0)$	5.6	5.0
$S_M(\bar{2}1.0)$	0.8	0.6
$S_M(\bar{1}2.0)$	4.2	4.5
$S_M(11.0)$	2.0	0.6
$S_M(2\bar{1}.0)$	0.1	2.1

Reflexion	F_o	F_c
M(30.0)	34.4	33.9
$S_M(1\bar{2}.0)$	3.4	2.0
$S_M(\bar{1}\bar{1}.0)$	5.7	6.3
$S_M(\bar{2}1.0)$	1.0	0.1
$S_M(\bar{1}2.0)$	4.9	4.3
$S_M(11.0)$	1.5	0.3
$S_M(2\bar{1}.0)$	1.4	2.5
M(40.0)	7.4	10.9
$S_M(1\bar{2}.0)$	2.2	1.3
$S_M(\bar{1}\bar{1}.0)$	4.5	6.2
$S_M(\bar{2}1.0)$	0.3	0.3
$S_M(\bar{1}2.0)$	2.9	3.2
$S_M(11.0)$	0.8	0.6
$S_M(2\bar{1}.0)$	1.4	2.4

Table 19 Observed and calculated structure factors for the M(h0.0) reflexions and $\{S_M(11.0)\}$ satellites. A temperature factor has been included in the calculation data, U_Q = 0.13 Å, U_P = 0.05 Å, U_{2Q} = 0.03 Å.

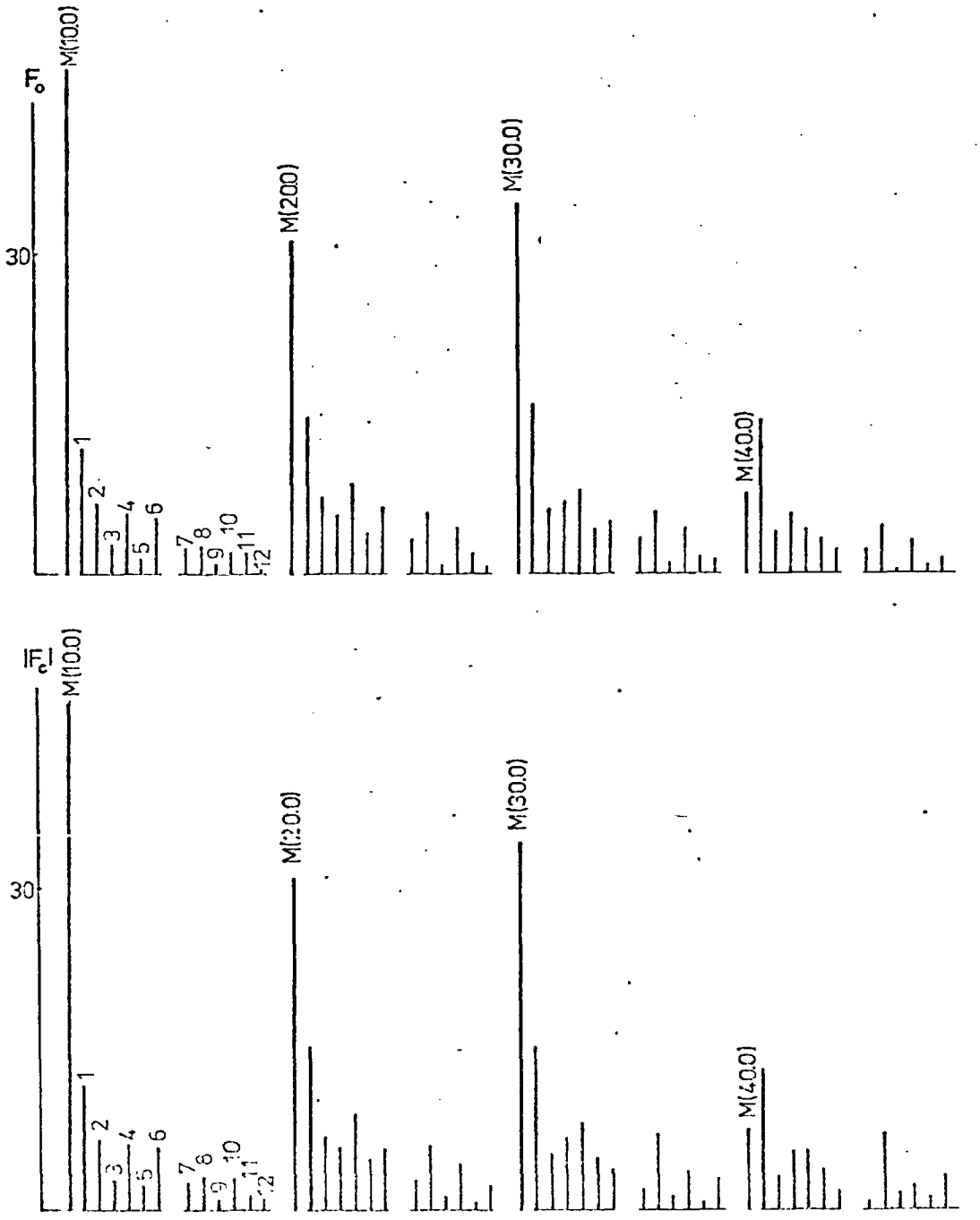


Figure 77 Comparison of observed and calculated structure factors for matrix and satellite reflexions (from Table 17). For each matrix reflexion there is a group of six $\{\underline{S}_M(10.1)\}$ reflexions (labelled 1 to 6) and a group of 6 $\{\underline{S}_M(11.0)\}$ reflexions (labelled 7 to 12). The twelve satellites correspond in order to those in Table 17 , and it must be remembered also that they are symmetrically disposed about each matrix reflexion.

data is presented both in Table 17 and Figure 77 using the best overall values for the deformation amplitudes, i.e.

	Magnitude	Direction	Phase
$\underline{U}_Q$	0.13 Å	+ 12°	180°
$\underline{U}_P$	0.055Å	+169°	0°
$\underline{U}_{2Q}$	0.07 Å	- 65°	0°

These give a value of R of about 9%, where R is given by:

$$R = \frac{\sum|F_o - F_c|}{\sum|F_o|}$$

The agreement is however much better, i.e. 5%, if only the matrix and first order satellite reflexions are considered. This serves to emphasise a point which became evident during calculation, that with the present limited model (9 distortion waves) it is not possible to obtain a good fit on the $\{\underline{S}_M(10.1)\}$ and the $\{\underline{S}_M(11.0)\}$ reflexions simultaneously.

Ignoring the $\{\underline{S}_M(11.0)\}$ reflexions for the moment, a better agreement (R = 4%) results from increasing $\underline{U}_{2Q}$ to 0.1 Å (see Table 18), where it is possible to confirm the agreement by also comparing calculated with observed values for the $\{\underline{S}_{11.0}(10.1)\}$ satellites. This increase in $\underline{U}_{2Q}$ particularly improves the fit on the asymmetrical pairs $F(\underline{M} + \underline{Q})$ and $F(\underline{M} - \underline{Q})$ as $\underline{K}$ increases, and this point will be referred to again later. Although it has not been presented here, the agreement for the $\{\underline{S}_M(11.0)\}$ does in fact seriously deteriorate as $\underline{U}_{2Q}$ is allowed to increase.

Reference back to Table 16 shows that values for the deformation amplitudes tabulated above agree quite well with the preliminary values, with one important exception. This is that the best value of $\underline{U}_{2Q}$ is approximately double the preliminary value. Furthermore, the better agreement on just the first order satellites means assigning an even larger value to $\underline{U}_{2Q}$. Before attempting to give an explanation for this, it is valuable

to vary the parameters so as to give as good an agreement as possible for the $\{\underline{S}_M(11.0)\}$ reflexions. It is found that the best fit is obtained when $\underline{U}_{2Q} = 0.03$ Å, which agrees with the preliminary value for this parameter. The calculated data based on this modification can be compared with observed data in Table 19.

The disparity between values of $\underline{U}_{2Q}$ required to obtain agreement for the $\{\underline{S}_M(10.1)\}$ satellites on the one hand, and for the $\{\underline{S}_M(11.0)\}$ on the other, must stem from the inherent limitations of the proposed model. Its description in terms of 9 Fourier components only, and the omission of higher order components, must make significant differences to the agreement as the scattering vector $\underline{K}$ increases in magnitude. A study of the data of Table 17 and Figure 77 shows how the errors build up as clusters of satellite reflexions further from the origin are taken.

In section 2.6.6 it was demonstrated that a 1-D deformation wave with a sawtooth profile produces a characteristic asymmetry in the structure factors of the pairs of satellites, i.e. that $F(\underline{M} + \underline{Q}) > F(\underline{M} - \underline{Q})$. Furthermore the effect of excluding most of the higher harmonics and approximating the function to its first two terms:

$$- \underline{U}_Q \sin(2\pi \underline{Q}.\underline{\ell}) + \underline{U}_{2Q} \sin(2\pi \underline{Q}.\underline{\ell})$$

is to halve the difference $\{F(\underline{M} + \underline{Q}) - F(\underline{M} - \underline{Q})\}$. This can be compensated for by doubling the magnitude of $\underline{U}_{2Q}$; i.e. so far as the <u>first order</u> satellites are concerned, the higher harmonics can be omitted from the calculation and replaced by taking $2\underline{U}_Q$. Although the situation is necessarily more complex in 2-D distorted layers, the same principles must apply. The discussion above indicates that this indeed the case for $1T_2$ TaS_2. In order to have good agreement for the first order $\{\underline{S}_M(10.1)\}$ satellites

$\underline{U}_{2Q}$ needs multiplication by a factor of between 2 and 3, compared with the true value, i.e. the one which gives the best fit on the second order satellites, 0.03 Å.

The values of the distortion amplitudes are in fact:

$$\begin{cases} U_Q = (0.13 \pm .005)\ \text{Å} \\ U_P = (0.05 \pm .005)\ \text{Å} \\ U_{2Q} = (0.03 \pm .01)\ \text{Å} \end{cases}$$

The value for U_P has been taken to be 0.05 Å the value giving the best fit for the second order satellites. In a similar way to $\underline{U}_{2Q}$, $\underline{U}_P$ also needs to be increased when fitting the calculated to the observed data for the first order satellites because of the omission of higher harmonics of the deformation cell.

The higher harmonics individually have deformation amplitudes much smaller than $\underline{U}_Q$, and therefore extremely difficult to measure, but when taken together they contribute significantly to the structure factors of the first and second order satellites, especially as $\underline{K}$ increases. While a partial compensation can be made for these by increasing $\underline{U}_{2Q}$ for the first order satellites, large variations in phase make the agreement worse for higher order satellites.

7.3.4 Interpretation in terms of Metal Atom Clusters

It was shown in sections 2.6.3 - 2.6.5 that the 1-D deformation wave with a sawtooth profile produces 'clusters' of atoms in the matrix, separated by 'gaps'. The results as discussed in the previous sections of this chapter strongly suggest that a 2-D analogue of the sawtooth deformation wave exists in $1T_2$ TaS_2. The amplitudes and phases of the Fourier components included in the model are consistent with this approach, the strongest evidence for cluster formation coming from the asymmetry in the magnitudes of the structure factors for satellites at $\underline{M} + \underline{Q}$ and

Figure 78

Pattern of displacements in the $1T_2$ TaS_2 distortion cell from 9 deformation waves of proposed model.

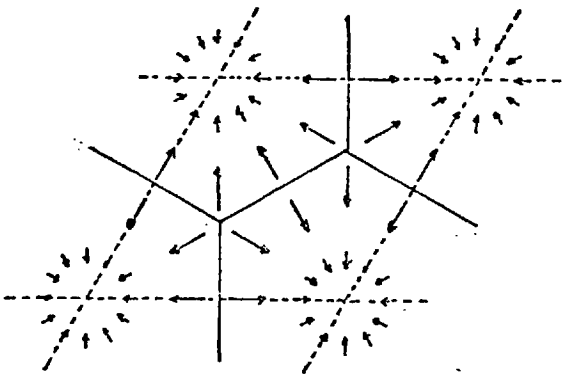


Figure 79

Distribution of average density of Ta atoms resulting from deformation structure of $1T_2$ TaS_2. Broad regions of slightly increased density are separated by narrow regions of decreased density ('gaps').

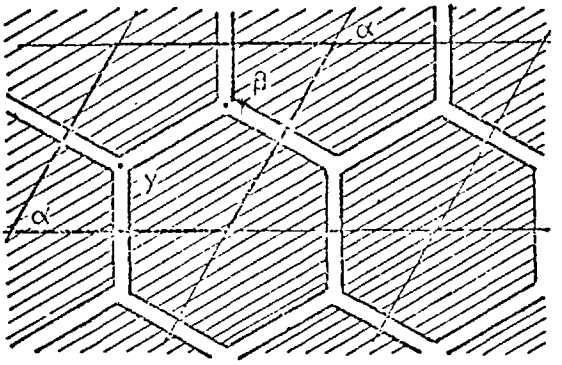
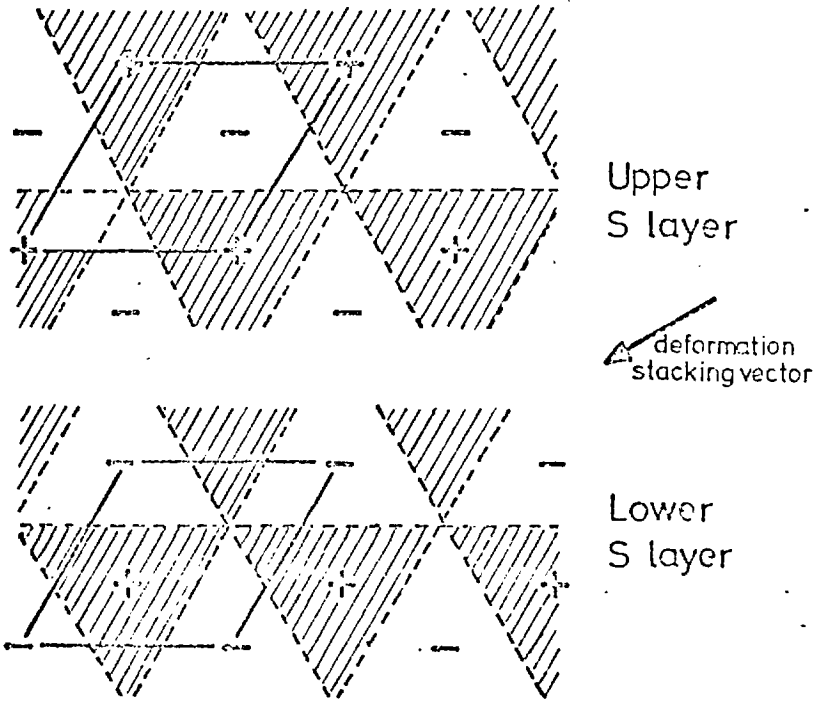


Figure 80

Displacements of the S atoms (+ve or -ve) in the two layers surrounding the Ta layer. Note that displacements in both layers are outward from the Ta layer at the centre of the metal atom cluster (cf. Figure 79).



$\underline{M} - \underline{Q}$. The magnitude of this effect implies significant clustering of the metal atoms.

Figure 78 shows the pattern of displacements from the nine deformation waves of the proposed quantitative model. This confirms that the overall effect is to displace atoms to form clusters centred on the deformation lattice points. There are consequently broad regions where the average density of Ta atoms is increased, separated from one another by narrow regions of decreased density (Figure 79). Because the deformation structure is incommensurate with the matrix lattice, a continuum 'jellium' of matter is more appropriate than discrete atoms. The calculated magnitudes and directions of the deformation amplitudes, $\underline{U}_Q$, $\underline{U}_P$, $\underline{U}_{2Q}$, suggest that regions of increased density, the clusters, are probably not uniform and that rotations as well as linear displacements are involved. The simplified model of Figure 79 is however likely to be a reasonably good approximation.

An estimate of the average spacing between Ta atoms in the clusters can be derived from the data in two different ways:

(a) The Ta part of the structure factors of $\underline{M}(40.0)$ and $\underline{S}_{40.0}(10.1)$ are approximately equal. The radiation is equally strongly scattered by spacings in the lattice corresponding to the matrix reflexion as to the satellite. The Ta interatomic distance (i.e. the a-axis of the matrix unit cell) is 3.365 Å. The equivalent spacing for the satellite reflexion is

$$3.365 \times \frac{|\underline{M}|}{|\underline{S}_M|} = 3.143 \text{ Å}.$$

The average of these two values is 3.26 Å, and this must represent the tantalum interatomic distance in the cluster, i.e. a decrease of about 3%.

(b) Taking the maximum displacements of the Ta atoms to be ±0.17 Å (see section 7.2.1), there must be a decrease of twice this, i.e. 0.34 Å, over the period of a wavelength,

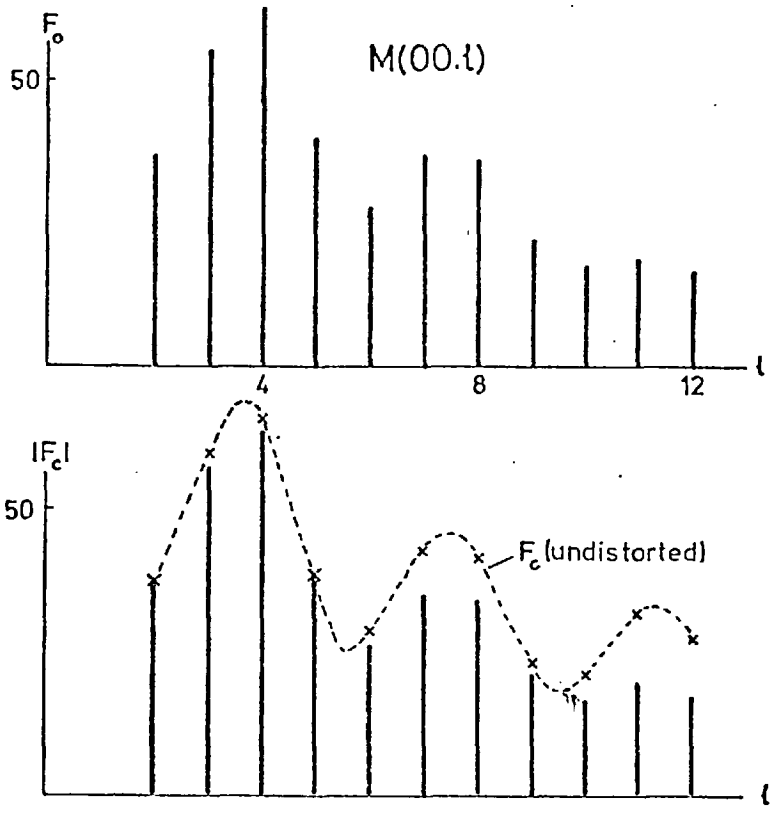


Figure 81 Comparison of observed and calculated structure factors for $\{\underline{M}(00.\ell)\}$ reflexions (from Table 20).

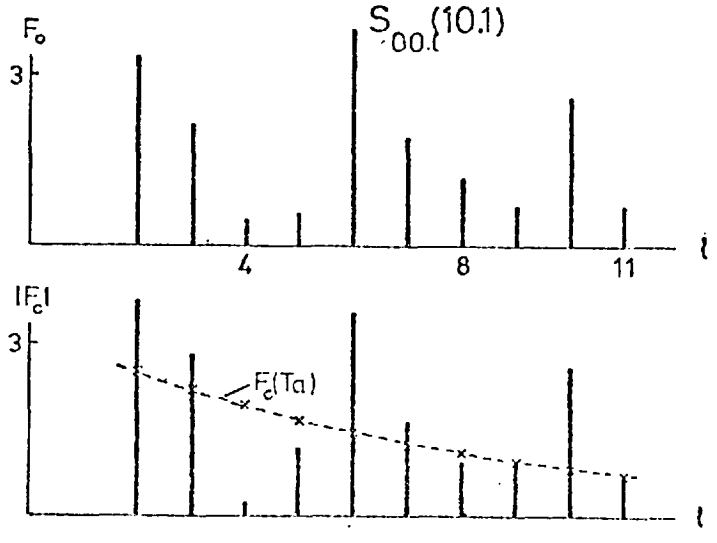


Figure 82 Comparison of observed and calculated structure factors for $\underline{S}_{00.\ell}(10.1)$ reflexions (Table 21). The Ta contribution to the structure is also given.

10.2 Å. This again gives a decrease of about 3% and an interatomic distance of 3.26 Å.

7.4 Displacements Perpendicular to the Layers in $1T_2$ TaS_2

These are necessarily linked to the $TA_\perp$ modes in the layers, and it will be assumed that there may be displacements on both metal and sulphur sublattices. In order to find their magnitude it is most convenient to restrict study to the $\underline{M}(00.\ell)$ reflexions and their satellites, $\underline{S}_{00.\ell}(10.1)$ with $2 \leq \ell \leq 12$. As explained in section 2.5.5, this effectively separates the variation in structure factor due to the $TA_\perp$ component of the distortion from the other components.

In the absence of distortion of the matrix lattice, the structure factor for the $\underline{M}(00.\ell)$ reflexions is given by:

$$F(00.\ell) = f_{Ta} + 2 f_S \cos(2\pi\ell z)$$

where z is the height of one sulphur, -z of the other, and $z \pm \frac{1}{4}$.

If there are three symmetry related deformation waves on both the tantalum and sulphur sublattices, with displacement amplitudes, perpendicular to the layers, of $\underline{U}_{Ta}$ and $\underline{U}_S$, then the matrix reflexion structure factors become

$$F(00.\ell) = f_{Ta} e^{-\alpha_{Ta} K^2} J_o(2\pi\ell c^* U_{Ta})^3 + 2 f_S e^{-\alpha_S K^2} J_1(2\pi\ell c^* U_S)^3 \cos(2\pi\ell z)$$

where the two exponential terms are temperature factors.

When z is varied, then the period of the modulation of the $F(00.\ell)$ caused by the scattering from the sulphur atoms, is changed. The best fit for this was obtained when z = 0.258 (Fig. 81). It is also very clear from this Figure that the observed structure factors fall off in magnitude when compared with calculated data for an undistorted lattice. The general reduction in structure factor is due to the tantalum contribution, while the reduced modulation at larger scattering vector is due to the sulphur contributions. This effect must be due to a combination

ℓ	$\lvert F_o \rvert$	$\lvert F_c \rvert$ distorted	$\lvert F_c \rvert$ undistorted
2	36.8	37.5	37.5
3	55.2	57.4	60.4
4	62.1	63.5	66.6
5	39.7	38.7	39.0
6	27.6	26.4	28.8
7	36.8	34.9	43.7
8	35.6	34.2	42.0
9	21.9	21.2	23.6
10	17.0	16.5	21.7
11	19.1	19.6	31.9
12	16.5	17.5	27.6

Table 20 Observed and calculated structure factors for M(00.ℓ) reflexions. Calculated values for a model without $TA_{\perp}$ distortions are also given.

ℓ	$\lvert F_o \rvert$	$\lvert F_c \rvert$	$\lvert F_c(Ta) \rvert$
2	3.3	3.8	2.5
3	2.1	2.8	2.3
4	0.5	0.3	2.0
5	0.6	1.2	1.8
6	3.8	3.5	1.5
7	1.9	1.7	1.3
8	1.2	0.9	1.1
9	0.7	0.9	1.0
10	2.6	2.6	0.8
11	0.7	0.7	0.7

Table 21 Observed and calculated structure factors for $S_{00.\ell}(10.1)$ satellites. Values for the tantalum contribution to the structure factor are also given.

of $TA_{\perp}$ displacements of Ta and S atoms and of temperature factors. The exact balance between these can be determined from a study of the structure factors of the $S_{00.\ell}(10.1)$ satellites.

The intensities of these satellites were very small indeed, for instance:

$$\text{Intensity}(\underline{S}_{00.4}(10.1)) \sim \text{Intensity}(\underline{M}(00.4)) \times 10^{-5}$$

and consequently the observed values of the structure factors in Table 21 cannot generally be considered as at all accurate. The weakest reflexions may have errors as large as 50%.

Figures 81 and 82 shows that there has been a shift in phase of almost π in the modulation of the satellites compared with the matrix reflexions. Expressing the structure factor for the matrix reflexion as:

$$F(00.\ell) = \mathcal{F}(Ta) + 2\,\mathcal{F}(S)\cos(2\pi\ell z)$$

where $\mathcal{F}(Ta)$ and $\mathcal{F}(S)$ represent the scattering from tantalum and sulphur, and therefore include atomic scattering factors, temperature factors and distortion Bessel functions, then a similar equation may be written for the structure factor of the satellite:

$$F(S_{00.\ell}) = \mathcal{F}(Ta) + 2\,\mathcal{F}(S)\cos(2\pi(\ell+\tfrac{1}{3})z + \phi')$$

The variable ϕ' in this equation is the phase of the deformation waves on the sulphur sublattice (assumed centresymmetric) relative to those on the tantalum sublattice (see section 2.5.2). The best fit for the shift in the modulation of the structure factors is obtained when

$$\phi = \phi' + 2\pi z/3 = 0.84$$

$$\text{i.e.}\ \phi'/2\pi = 0.33$$

$$\therefore\ \delta x = \tfrac{1}{3}\Lambda$$

The origin of the TA distortion wave on the upper sulphur layer (at $+z$) is shifted by $\delta x = +\frac{1}{3}\Lambda$, and on the lower sulphur layer (at $-z$) by $-\delta x = -\frac{1}{3}\Lambda$ relative to the origin of the tantalum deformation wave. This means that the perpendicular displacements

of the sulphur atoms are zero at the β site $(\frac{1}{3},\frac{2}{3})$ in the upper layer and at the γ site $(\frac{2}{3},\frac{1}{3})$ in the lower. Maximum positive displacements in the upper layer and maximum negative displacements in the lower occur at the α site (0,0) as drawn in Figure 80.

No $TA_{\perp}$ component of the distortion wave on the tantalum sublattice could be detected. The limits of experimental error therefore make $\underline{U}_N(Ta) \lesssim 0.01$ Å. It is clear that if there were a significant tantalum component perpendicular to the layers, it would cause the tantalum part of the structure factor to increase with $\underline{K}$, while the experimental evidence (Fig. 82) shows a steady decrease throughout the range measured.

The best fit with experimental data was obtained with a value of$(0.05 \pm .005)$ Å for the sulphur deformation amplitude normal to the layers. Calculated values of the structure factors for the $\underline{M}(00.\ell)$ and $\underline{S}_{00.\ell}(10.1)$ reflexions can be compared with observed in Tables 20 & 21, and Figures 81 & 82. The temperature factors used in the calculation were $\exp(-0.11K^2)$ and $\exp(-0.16K^2)$ for tantalum and sulphur respectively.

Summary

The tantalum layer in each TaS_2 sandwich is distorted by in-layer deformation waves whose chief effect is to produce clusters of metal atoms (average spacing 3.26 Å in clusters) at the deformation cell lattice points. They are separated by narrow regions of reduced metal atom density on average, i.e. corresponding to increased bond lengths across the 'gaps'. Typical increased bond lengths would be ~ 3.7 Å (i.e. the undistorted length + 2 x 0.17 Å).

The sulphur layers are distorted by $TA_{\perp}$ deformation waves giving displacements at right angles to the layers. It is likely that there are also in-plane displacements: these must be small in

amplitude and/or out of phase with the displacements of the tantalum atoms (section 7.2.3). The shift in origin of the deformation waves on the sulphur sublattice implies that while the upper sulphur layer is displaced upwards at the centre of the tantalum cluster, the lower layer is displaced downwards, Figure 80. These periodic variations in layer thickness are such that when the deformations are stacked rhombohedrally, the sulphur layers either side of the interlamellar space fit closely together.

7.5 Deformation Structure of $1T_1$ TaS_2

7.5.1 Introduction

Neither of the other two distorted phases of tantalum disulphide was studied with the single crystal diffractometer. It is however possible to gain insight into the detailed deformation structure of both $1T_1$ and $1T_3$ TaS_2 by careful comparison of the photographic data for these phases with that obtained for $1T_2$ TaS_2. As an aid to this photographs were obtained from the same crystal, and under similar conditions of exposure, for each of the two phases being compared. One crystal was used for the study of $1T_1$ and $1T_2$, and a different one for the study of $1T_3$ and $1T_2$.

7.5.2 Direction of Deformation Amplitude, $\underline{U}_Q$

In each set of six first order satellite reflexions, those with greatest intensity lie on the reciprocal axes, i.e. when $\underline{Q}$ is parallel to $\underline{M}$, Figure 59. This immediately suggests a predominantly LA mode for the fundamental deformation waves. The mirror symmetry about the matrix reciprocal axis of for instance the $\{\underline{S}_{20.0}(10.1)\}$ shown in the enlargement (Figure 83), confirms that $\underline{U}_Q$ must be directed along $\underline{a}^*$.

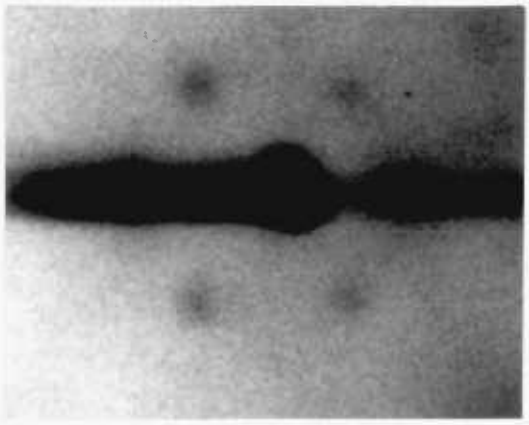


Figure 83 Enlargement from Figure 59 (i) showing $\{S_{20.0}10.1)\}$ satellites in $1T_1$ TaS_2.

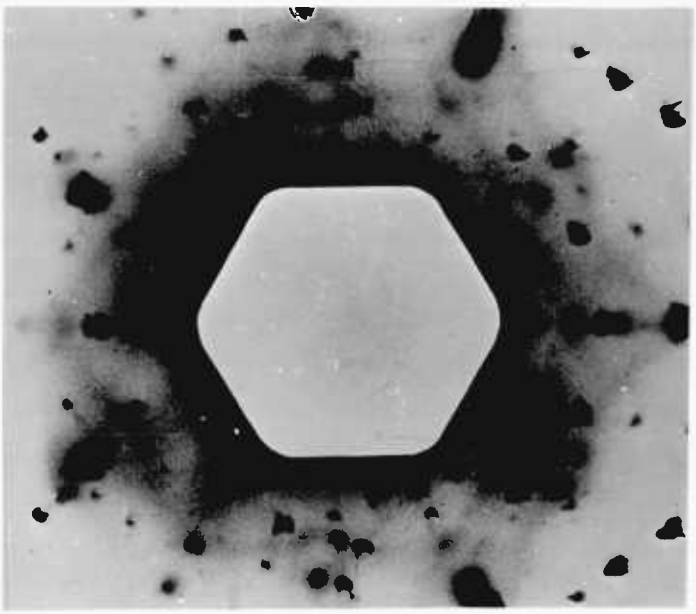


Figure 84 Stationary X-ray diffraction photograph (beam approximately parallel to c*) to show diffuse streaks in $1T_1$ TaS_2.

Thus when the material transforms from the $1T_1$ phase to $1T_2$ the direction of the deformation wave vector changes, but the direction of $\underline{U}_Q$ remains unchanged. Although the magnitudes of the displacements of the metal atoms produced by the deformation waves increase during this transition, their directions stay the same.

7.5.3 Magnitude of the Displacements

A direct comparison of the electron diffraction patterns for the two phases (Fig. 58 (i),(ii)) shows that the $\{\underline{S}_M(11.0)\}$ are far weaker in the higher temperature ($1T_1$) phase. In fact these second order satellites are too weak to be visible, even on well-exposed X-ray photographs of $1T_1$ TaS_2 (Fig. 59). This suggests a smaller deformation amplitude in $1T_1$ than in $1T_2$ TaS_2. An estimate of $\underline{U}_Q$ can be obtained by comparing photographic data for the two phases. Microdensitometer traces were taken from the original X-ray film in order to measure the intensities of the satellite reflexions. The exposure conditions for each of the two phases were checked by comparing matrix reflexion intensities. No correction for variations in exposure was found to be necessary.

An intensity 'envelope' can be calculated for the radiation scattered into satellite reflexions based on a simple distortion model, in which the deformation amplitude is $\underline{U}$. Then the intensity of a first order satellite is given by:

$$I = [f_{Ta}\, J_1(2\pi \underline{K}.\underline{U})]^2 \times(\text{Lorentz-polarisation factor})\times(\text{temperature factor})\times(J_0 \text{ terms from other distortions})$$

If we restrict values of the scattering vector K, i.e. $K < 1$, then the last two terms can be approximated to unity.

For $U \sim 0.15$ Å, the argument of the first order Bessel function is less than unity, and so may be approximated in the usual way

i.e. $J_1(2\pi \underline{K}.\underline{U}) = \pi \underline{K}.\underline{U}$

Thus $I = U^2 \times$ (function of K)

This, the intensity envelope, is in fact shown in Fig. 64, where the equivalent intensity function for a conventional structure is given for comparison.

In the range $0.5 \leqslant K \leqslant 0.9$ it can be seen that the dependence on K is negligible, since the decrease in I from the variations of f_{Ta} and the L-P factor is counterbalanced by the increase with K^2 from $(J_1(2\,\underline{K}.\underline{U}))^2$. The intensity is therefore approximately constant (i.e. to within 5%) over this range, so that

$$I \propto U^2$$

The reflexions $\{\underline{M}(11.0)\}$ and $\{\underline{M}(20.0)\}$ come within this range and comparison of intensities will be restricted to their satellites. This is simplified by the fact that $\underline{U}_Q$ is in the same direction in $1T_1$ and $1T_2$, and that the rotation of 12° in $\underline{Q}$ can be neglected. From microddensitometer measurements, the following intensity values were obtained (Table 22):

Table 22

Comparison of satellite intensities in $1T_1$ and $1T_2$ TaS_2. Two reflexions were too close to white radiation streaks to enable measurement.

Reflexion	$I(1T_1)$	$I(1T_2)$
$S_{11.0}(10.1)$	3.2	6.8
$S_{11.0}(1\bar{1}.\bar{1})$	3.3	-
$S_{11.0}(\bar{1}1.1)$	2.4	3.5
$S_{2\bar{1}.0}(10.1)$	3.3	-
$S_{2\bar{1}.0}(01.\bar{1})$	3.4	7.2
$S_{2\bar{1}.0}(0\bar{1}.1)$	2.3	4.4

If we take the average intensity for pairs of satellites at $\underline{M} \pm \underline{Q}$ in order to reduced the effect of higher Fourier components, we find that the satellite intensities in $1T_1$ are about half the magnitude of those in $1T_2$ TaS_2. Since $I \propto U^2$, this must mean that

$$\underline{U}_Q(1T_1) \triangleq \underline{U}_Q(1T_2) \times 0.7$$

i.e. $\underline{U}_Q(1T_1) \triangleq 0.09$ Å at 390 K.

Since the intensities of the $\{\underline{S}_M(11.0)\}$ reflexions are to a first approximation proportional to the fourth power of the deformation amplitude $\underline{U}_Q$, their intensities must be at least four times smaller on average in $1T_1$ TaS_2 than in $1T_2$, explaining their apparent absence from the X-ray diffraction photographs.

7.5.4 Metal Atom Clusters in $1T_1$ TaS_2

The next question to consider is whether the distortion is sinusoidal or a complex clustering as in the room temperature phase. The asymmetry in intensity is certainly less marked for the $\underline{M} \pm \underline{Q}$ satellites in $1T_1$ than in $1T_2$ TaS_2, but this must be due partly to the smaller deformation amplitude. In order to try and settle this, the intensities of the first order satellites of $\underline{M}(20.0)$ were also measured. It was found that

$$\frac{\text{Intensity of } \underline{S}_{20.0}(10.1)}{\text{Intensity of } \underline{S}_{20.0}(\bar{1}0.\bar{1})} = \frac{2.7}{2.0} = 1.35$$

The mean of this and the values of the ratio for the two pairs in Table 22 is 1.4.

A region of reciprocal space has been chosen in which satellite intensity is approximately independent of K for a sinusoidal deformation wave (Figure 64). The larger intensity at $\underline{M} + \underline{Q}$ must therefore be interpreted again in terms of clustering of the metal atoms. The ratio 1.4 is consistent with a deformation structure very similar to that of $1T_2$ TaS_2 as described in 7.3, but with all the displacements reduced by about 30%. Thus in $1T_1$ TaS_2 $\underline{U}_Q$ = 0.09 Å and maximum displacements are approximately 0.12 Å, compared with the respective values of 0.13 Å and 0.17 Å for $1T_2$ TaS_2.

To summarise, the transition from $1T_1$ to $1T_2$ TaS_2 is accompanied by a rotation of the wave vector $\underline{Q}$ and an increase of 30% in

deformation amplitude, although the deformation structure apparently remains otherwise unchanged.

7.6 Diffuse Scattering in $1T_1$ TaS_2

Diffuse scattering was only observed to occur in highest temperature distorted phase (Figs. 58 and 59): this point will be discussed in Chapter 11. There are in general two possible origins for the diffuse streaks — it must either be due to density variations (short range order, probably of interstitial tantalum atoms or sulphur vacancies), or else due to atomic displacements. The discrete satellite reflexions have been successfully interpreted in terms of periodic displacements of the atoms, and this suggests that a similar interpretation should be considered for the streaks also. Confirmation that the origin of the diffuse scattering is in phonons rather than short range order can be found from the intensity variation of the scattering with increasing scattering angle. Streaks due to short range order would have their intensity maxima at small scattering angles as the matrix reflexions have. Careful study of oscillation and stationary X-ray diffraction photographs (Figs 59, 84) shows that the diffuse scattering has maximum intensity over a fairly broad range of K from about 0.5 to 0.9, i.e. close to the $\{\underline{M}(11.0)\}$ and $\{\underline{M}(20.0)\}$ reflexions. Reference again to Fig.64 confirms that this is the behaviour expected for scattering by phonons.

It was not possible to measure any modulation of intensity of the streaks in a direction parallel to $\underline{c}^*$. Recent diffractometer measurements (Yamada et al, 1975) have in fact shown some modulation at $(\ell \pm \frac{1}{3})\,\underline{c}^*$. This suggests limited phase correlation between the deformation waves in different layers.

Electron diffraction shows that the deformation amplitude of the fundamental LA deformation waves (as measured by the

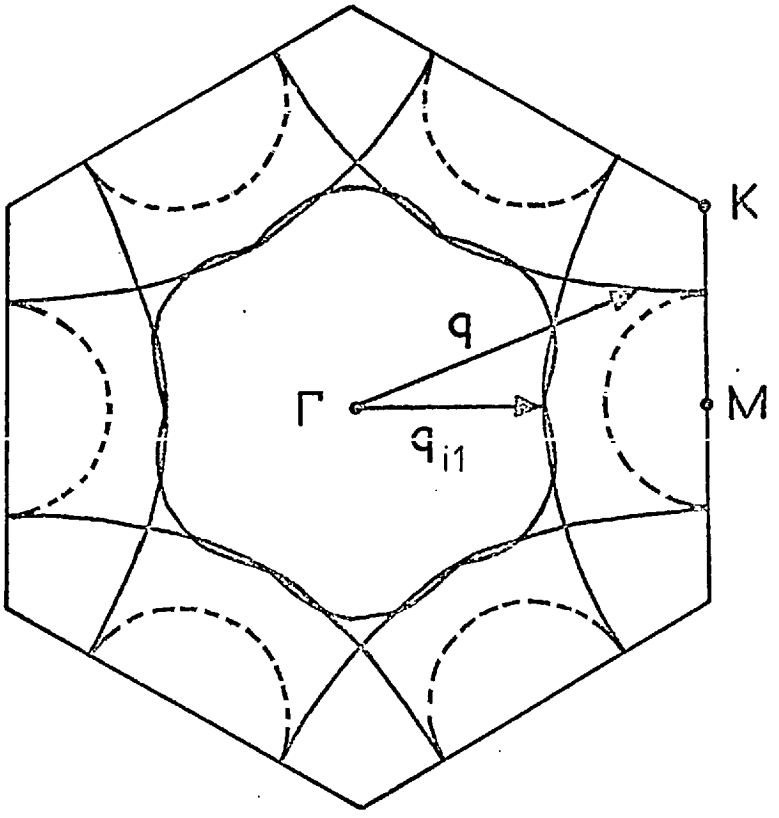


Figure 85 Pattern of diffuse scattering in first Brillouin zone of matrix reciprocal lattice.

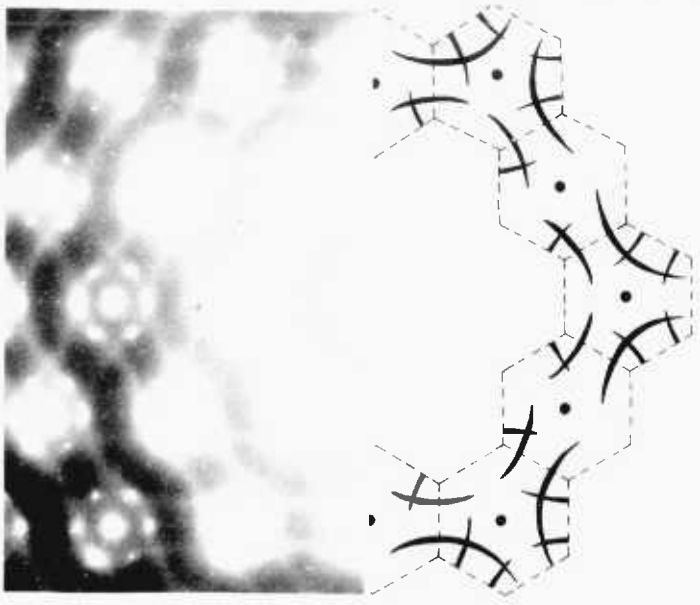


Figure 86 (a) S.A.D.P. for $1T_1$ TaS_2 at 420 K, showing diffuse streaking which images the Fermi Surface. All six $\underline{S}_M(10.1)$ satellites are visible because of crystal buckling. (b) Plot of phonon wave vectors which satisfy $\underline{q} \triangleq 2\underline{k}_f$ for Fermi Surface of Figure 110, and are in $TA_\perp$ modes with $|\underline{k}.\underline{U}_q|^2$ large.

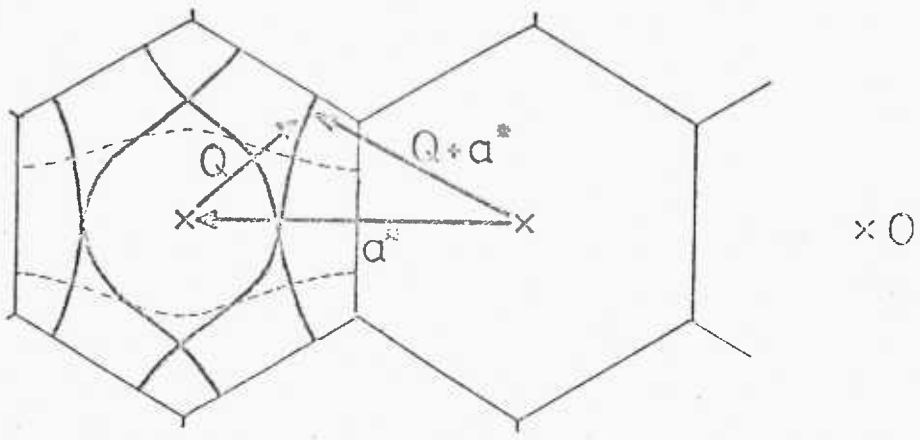


Figure 87 The diffuse streaking can either be described by $TA_\perp$ N-phonons, with wave vector $\underline{Q}$; or as LA U-phonons with wave vector $\underline{Q} + \underline{a}^*$, depending on which matrix reflexion is taken as origin.

intensity of the first order satellites) decreases progressively as the temperature is raised from 350 K to 450 K, above which an interpolytypic transition to the 2H or $4H_b$ phase occurs. The intensity of the diffuse scattering however appears to increase at first, just above the transition temperature, before decreasing as the temperature is further raised.

Figure 85 shows the pattern of diffuse scattering in one Brillouin zone of the matrix reciprocal lattice (ignoring intensity modulation). The reciprocal co-ordinates of the streaks have been more accurately measured by Yamada et al, 1975 using a 4-circle diffractometer. The modulation of the diffuse streaks is such as to produce maxima where $\underline{K}$ is approximately perpendicular to $\underline{Q}$, and minima where it is parallel. The streaks parallel to central reciprocal lattice rows are consequently very weak, while tangential streaks are strong, giving rise to the characteristic pattern of small and large almost circular arcs. Such an intensity variation is consistent with the phonons being in predominantly $TA_{//}$ modes with respect to the first Brillouin zone for phonons, i.e. associated with the nearest matrix reflexion. In Fig. 86 the diffuse scattering calculated for $TA_{//}$ modes can be compared directly with the electron diffraction pattern.

If the phonons are now referred to an adjacent matrix reflexion (and Brillouin zone), so that they are now Umklapp phonons, they can be described as longitudinal. As LA modes they give rise directly to the incomplete 'circles' observed in parts of the diffraction pattern (see Fig. 87).

7.7 Deformation Structure of $1T_3$ TaS_2

When the X-ray diffraction patterns for $1T_2$ and $1T_3$ are studied (Fig. 59) they reveal a marked similarity between the two reciprocal lattices when the incident beam is parallel to $\underline{c}^*$,

in spite of deformation structure only being commensurate in $1T_3$ TaS_2. In this phase the satellite reflexions ought strictly speaking to be indexed on the supercell, but in order to make comparison easier the system of indexing used for the incommensurate superstructures will also be referred to in this section. It is particularly difficult to note from the X-ray diffraction photographs which of the two phases is the commensurate one. The pattern of intensities is also very similar, except that in $1T_3$ TaS_2 the $\{\underline{S}_{hk.0}(11.0)\}$ superlattice reflexions are relatively stronger, and this gives a slightly more even spread of scattered intensity over the diffraction pattern. These observations imply that there must be a strong resemblance between the deformation structures in the two phases. Most important of all, there must be clusters of tantalum atoms in the commensurate $1T_3$ phase also.

There must however be one key difference in the structure of the distorted layers, which arises from formation of a commensurate superlattice. In $1T_3$ TaS_2 each metal atom cluster must be identical since there is one per layer supercell, and also have sixfold symmetry about an axis perpendicular to the layer. In the incommensurate phase however the clusters are not identical on a local level, and they only have hexagonal symmetry on average. This point will be returned to later in the general discussion (11.9).

Comparative intensity measurements were carried out using a microdensitometer from photographs of similar exposure for each phase. After normalising the intensities by using the matrix reflexions, the $\{\underline{S}_{11.0}(10.1)\}$ and $\{\underline{S}_{20.0}(10.1)\}$ were compared. Following a similar approach to that adopted when comparing $1T_1$ and $1T_2$, the mean intensity of a pair of satellites at $\underline{M} \pm \underline{Q}$ was calculated for each phase, and it was found that the satellite

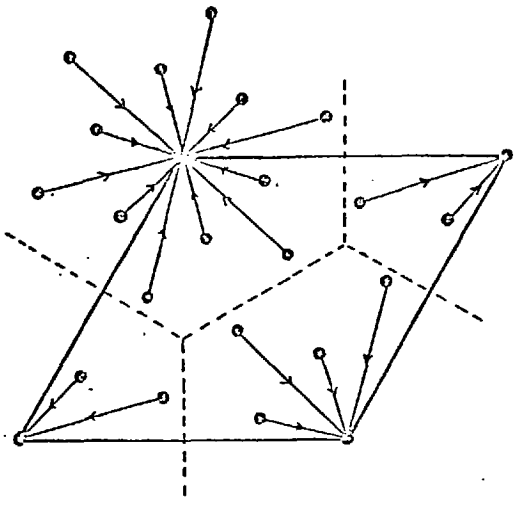


Figure 88 The metal atoms are drawn together into clusters which lie on a $\sqrt{13}$a x $\sqrt{13}$a superlattice in $1T_3$ TaS_2.

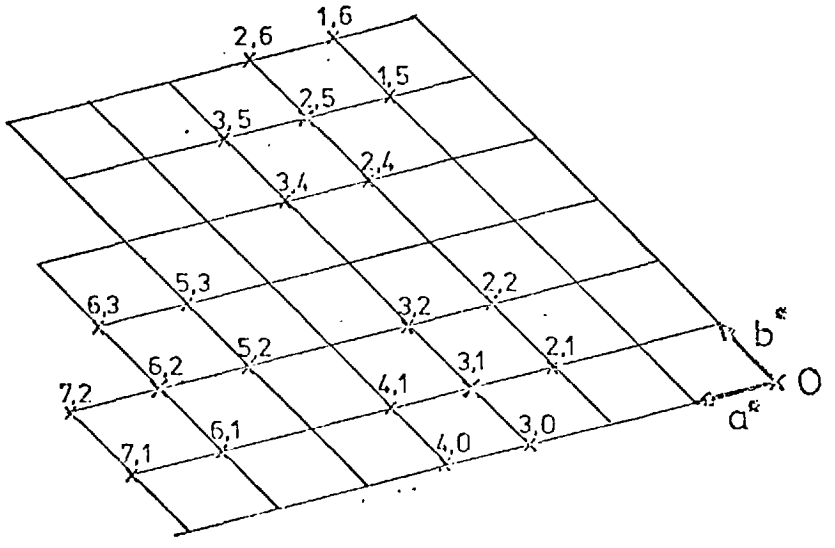


Figure 89 Showing the indices of the matrix and satellite reflexions from $1T_3$ TaS_2 which are referred to in Table 23.

intensities were about 30% higher in $1T_3$ than in $1T_2$ TaS_2. Since measurements were again restricted to the region of reciprocal space in which the intensity is proportional to the square of the deformation amplitude, it may be concluded that deformation amplitudes in $1T_3$ are about 15% larger than in $1T_2$ TaS_2. This implies a fundamental deformation amplitude of about 0.15 Å, and maximum displacements of about 0.2 Å.

The difference in the intensities of the pairs of satellite reflexions at $\underline{M} \pm \underline{Q}$ was greater than in $1T_2$ TaS_2, and this is consistent with more pronounced clustering of metal atoms in $1T_3$. It is important to note at this point that in this region of reciprocal space, $2\pi\underline{K}.\underline{U}_Q \simeq 0.7 < 1$, and so the comparison of commensurate and incommensurate intensities is meaningful (section 2.4.4). In order to make a semi-quantitative comparison with the experimental data the following simple model for a commensurate $\sqrt{13}\,a \times \sqrt{13}\,a$ cluster formation will be studied. The tantalum atoms are considered to be drawn into 13 atom clusters centred on the lattice points (Fig. 88). Estimated maximum displacements of 0.2 A mean a 4% decrease in Ta - Ta distances within the clusters. Thus the x and y co-ordinates of the atoms in the deformation cell must all be multiplied by a factor $0.96 = r$. The 13 atoms therefore occupy the following positions:

$$(0, 0);$$
$$\pm(.3077r, .0769r) \; ; \quad \pm(.5385r, .3846r);$$
$$\pm(.2308r, .3077r) \; ; \quad \pm(.1538r, .5385r);$$
$$\pm(-.0769r, .2308r) \; ; \quad \pm(-.3846r, .1538r).$$

For r = 0.96, this model gives the values shown in Table 23 for structure factor and intensity (no correction for absorption or temperature factor). The indexing of the $1T_3$ superlattice is given in Fig. 89. The equivalent deformation indices (Table 23) enable comparisons to be made with $1T_2$ TaS_2.

Supercell Indices	Equivalent Deformation Indices	$F_{c/13}$	I_c
3,1	M(10.0)	47.4	18 200
4,1	$S_{10.0}$(10.1)	10.3	650
3,2	(1$\bar{1}$.$\bar{1}$)	7.0	320
2,2	(0$\bar{1}$.1)	1.4	16
2,1	($\bar{1}$0.$\bar{1}$)	1.7	240
3,0	($\bar{1}$1.1)	1.8	31
4,0	(01.$\bar{1}$)	4.4	140
6,2	M(20.0)	34.9	4 600
7,2	$S_{20.0}$(10.1)	16.6	880
6,3	(1$\bar{1}$.$\bar{1}$)	9.9	330
5,3	(0$\bar{1}$.1)	3.9	60
5,2	($\bar{1}$0.$\bar{1}$)	7.4	240
6,1	($\bar{1}$1.1)	2.8	33
7,1	(01.$\bar{1}$)	4.2	62
2,5	M(11.0)	64.3	18 300
3,5	$S_{11.0}$(10.1)	10.7	440
2,6	(1$\bar{1}$.$\bar{1}$)	14.7	809
1,6	(0$\bar{1}$.1)	2.2	20
1,5	($\bar{1}$0.$\bar{1}$)	6.9	240
2,4	($\bar{1}$1.1)	4.9	130
3,4	(01.$\bar{1}$)	0.3	0

Table 23 Calculated structure factors and intensities for hk.0 reflexions from a commensurate deformation model of $1T_3$ TaS_2. Values have been scaled for one metal atom per unit cell, to assist comparison with Table 17.

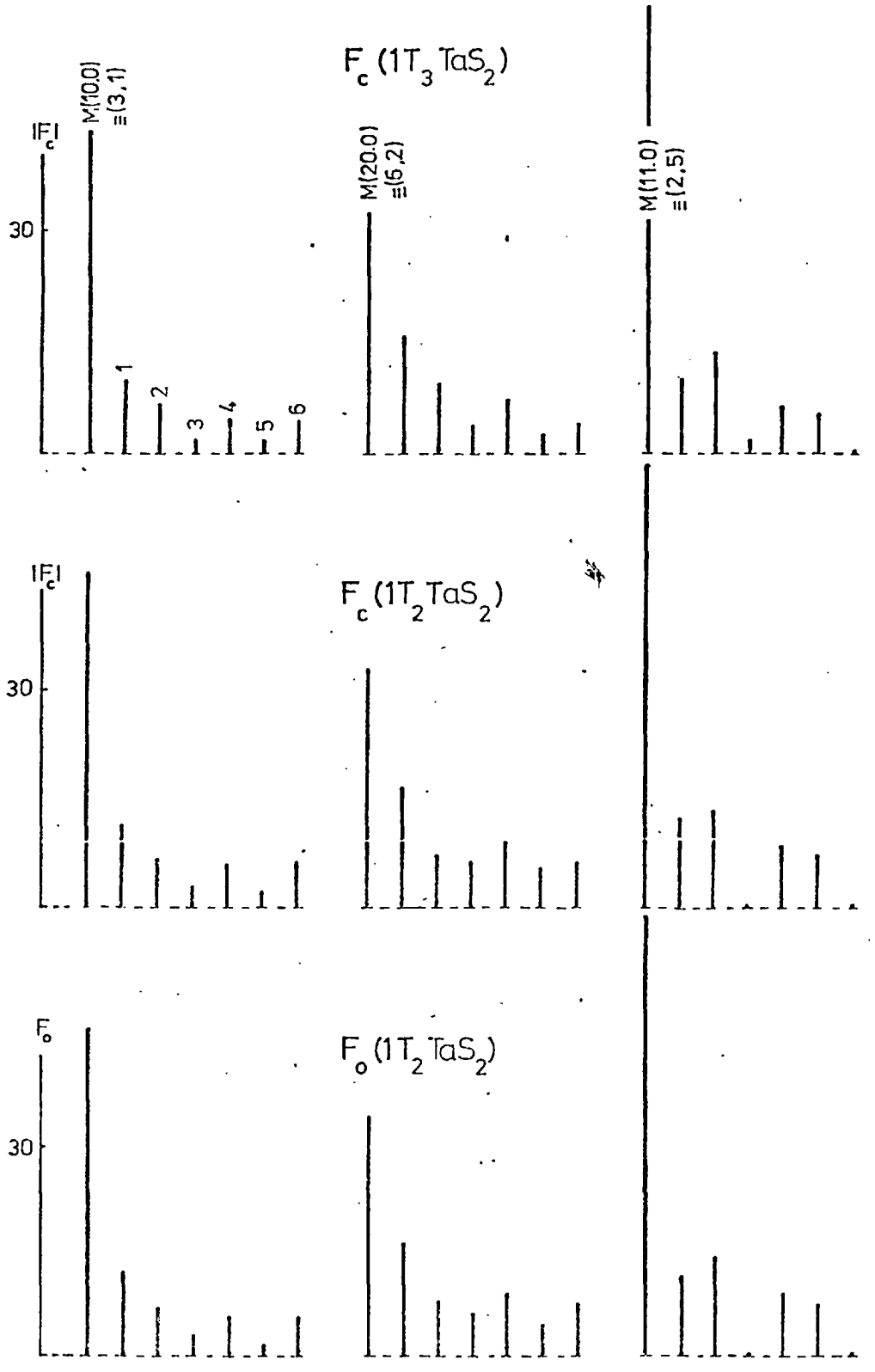


Figure 90 Comparison of calculated structure factors for $1T_3$ and $1T_2$ TaS_2. The commensurate and incommensurate models give good agreement at small scattering vector. Observed values for $1T_2$ are also given.

The calculated intensities can be compared with the photographic data of Figure 59. There is also good qualitative agreement for the first order satellites surrounding the matrix reflexions: M(10.0), M(11.0), M(20.0). The calculated structure factors for $1T_3$ TaS_2 are plotted out in Figure 90 (a), where they can be directly compared with calculated values for the incommensurate $1T_2$ TaS_2 distortion model (b), and with observed structure factors also for $1T_2$ TaS_2 (c). The data for this phase are reproduced from Fig. 77, and Table 17.

It can be seen from Figure 90 that there is close agreement between calculations based on commensurate and incommensurate models for values K less than about 0.8, and thus proof of the equivalence of the two kinds of model close to the limiting case has been extended to a 2-D superstructure. Furthermore, the close similarity between photographic intensities from $1T_2$ and $1T_3$ TaS_2 suggests that the commensurate model proposed above gives a good description of the deformation structure of this phase, and that if quantitative data were available, then the agreement between observed and calculated data would be as good for $1T_3$ as for $1T_2$ TaS_2. Outside this limited range of scattering angle, the calculations based on the two models necessarily diverge, and the differences due to commensurateness become significant.

7.8 Coherence Length of the Deformation Waves

Diffractometer measurements of the room temperature $1T_2$ TaS_2 phase showed no difference in width or profile between matrix and satellite reflexions. This must mean that the deformation waves maintain good phase correlation within each crystal grain, and that their coherence length is controlled by grain size alone. This applied both within the layers and perpendicular to the layers.

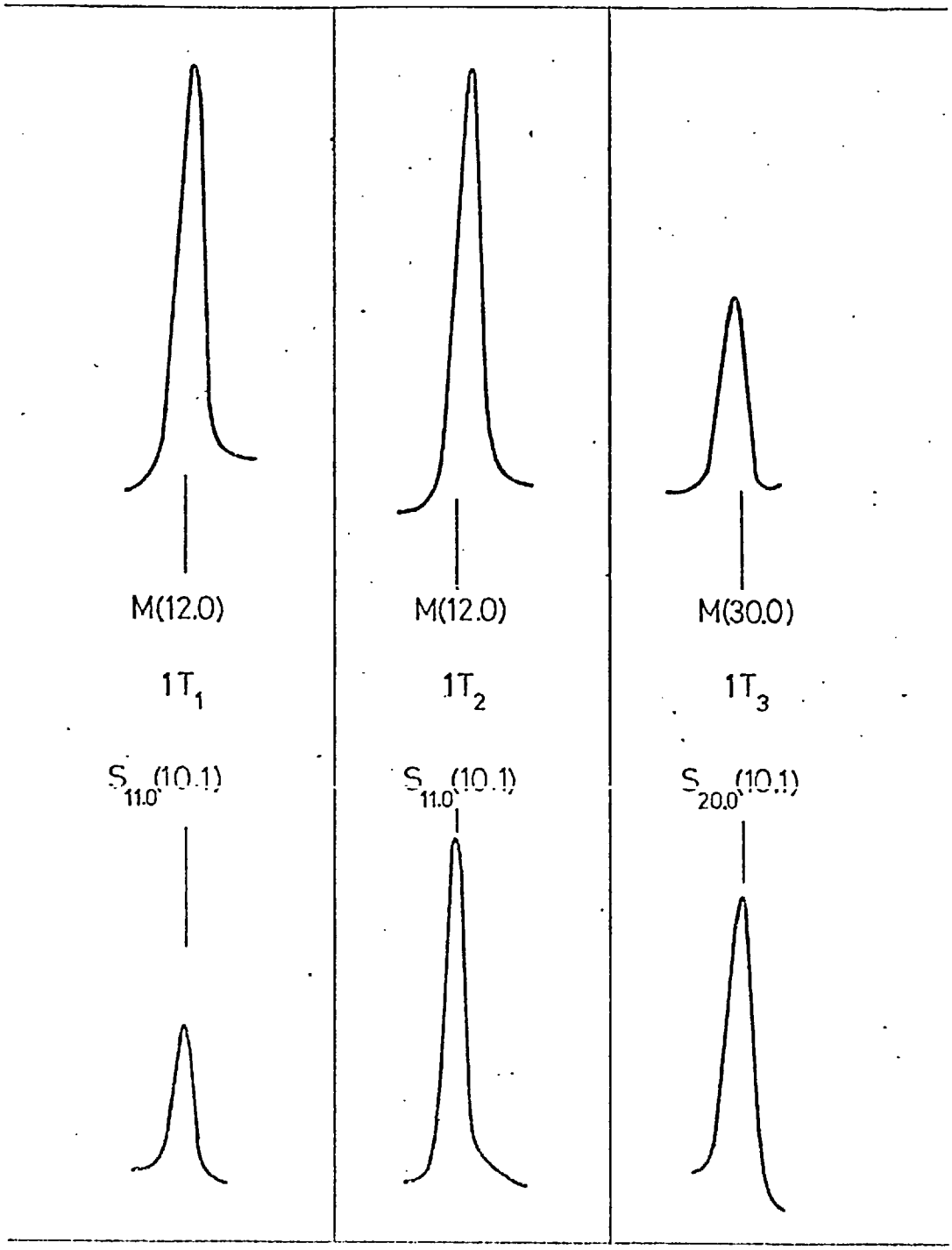


Figure 91 Microdensitometer traces for matrix and satellite reflexions from all three phases of 1T TaS_2.

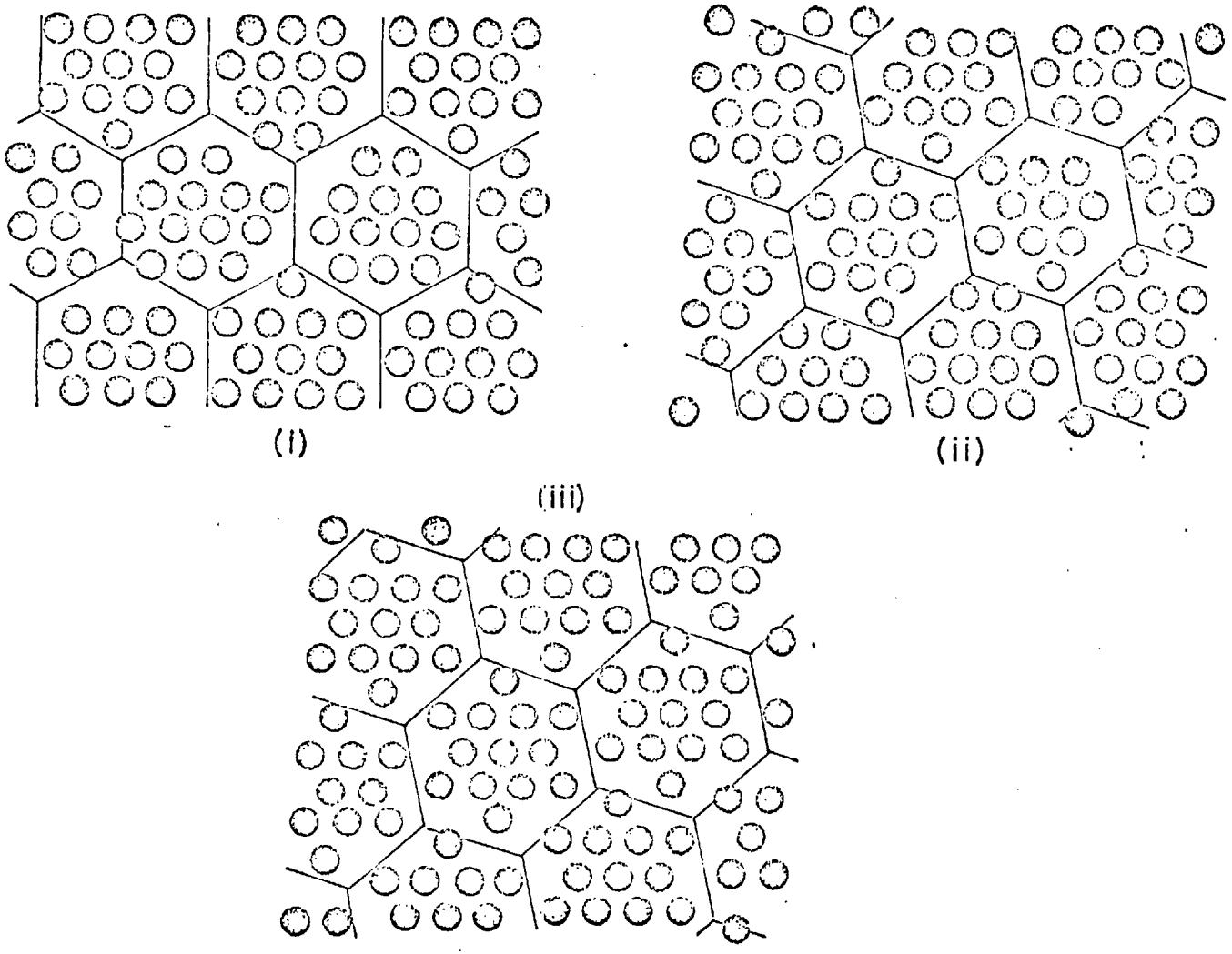


Figure 92 Cluster deformation structures proposed for (i) $1T_1$, (ii) $1T_2$, (iii) $1T_3$ TaS_2, and based on calculations outlined in Chapter 7. Note that the clusters are identical only in $1T_3$ TaS_2. For clarity the structures are drawn with an exaggerated distortion amplitude of 10 %.

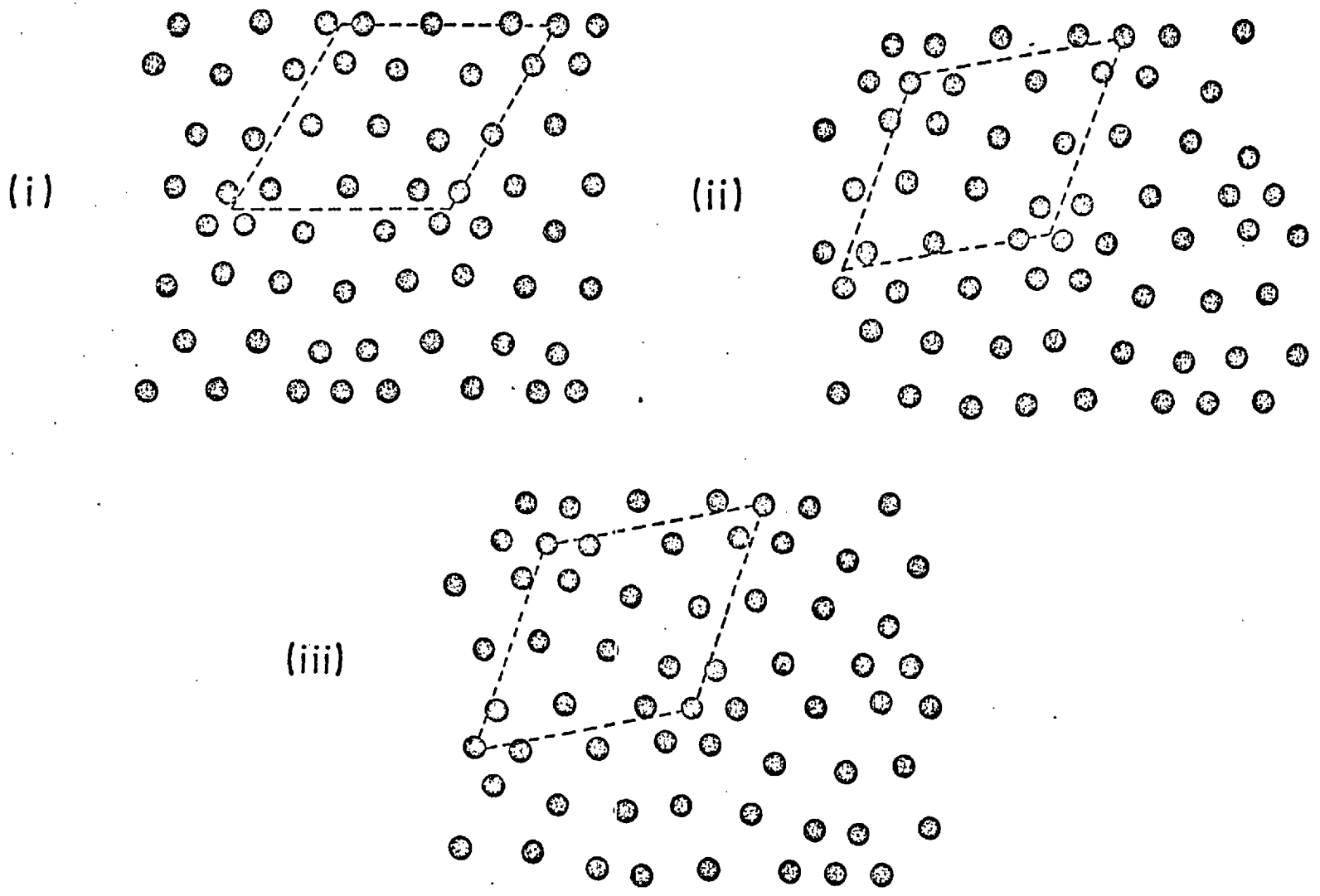


Figure 93 Deformation structures based on purely sinusoidal distortion waves, with U_Q = 0.1 a. This should be compared with Figure 92.

In particular, this implies that the correlation between deformation waves in adjacent layers is as good as the packing of the TaS_2 layers.

Microdensitometer traces from all three phases (Fig. 91) strongly suggest equally good phase coherence in $1T_1$, $1T_2$ and $1T_3$. This does not of course apply to the phonons giving rise to the diffuse scattering in $1T_1$ TaS_2, which apparently have partial coherence both within and perpendicular to the layers.

7.9 Distorted Layer Models for the Three Phases

Cluster deformation structures based on the experimental data for each of the three phases are shown in Fig. 92. In order to accentuate the effect of the deformation waves in the layers, the structures have been drawn with an exaggerated 10% distortion in each case. It should be remembered that the deformation amplitude increase progressively from $1T_1$ to $1T_2$ to $1T_3$. An important difference to note is that the clusters are identical only in $1T_3$ TaS_2, and that the number of Ta atoms per cluster varies in the two incommensurate phases. The most noticeable effect overall however, is not the decreased interatomic distance in the clusters, but the increased bond lengths between clusters. Fig. 92 should be compared with Fig. 93, in which deformation structures are drawn for the fundamental sinusoidal deformation waves alone, and in which the interatomic distances vary more slowly.

Whilst it seems likely that almost perfect (i.e. with atoms equally spaced within each cluster) clustering occurs in the $1T_3$ phase, as shown in Fig. 92 (iii), it seems more probable that only partial clustering occurs in $1T_1$ and $1T_2$, and that the true situation is intermediate between that represented in Fig. 92 and Fig. 93. In particular the tantalum atoms in the proximity

of the 'gaps' and especially of where three gaps meet, could be expected to be drawn together slightly, thereby reducing interatomic distances. This would certainly be consistent with the measured value of $\underline{U}_p$ (i.e. 0.05 Å) being somewhat less than the value predicted for a perfect cluster model (i.e. 0.78 $\underline{U}_Q$ = 0.1 Å, see section 7.3.5 and Appendix 3).

8 DIFFRACTION RESULTS AND INTERPRETATION: OTHER OCTAHEDRAL MATERIALS

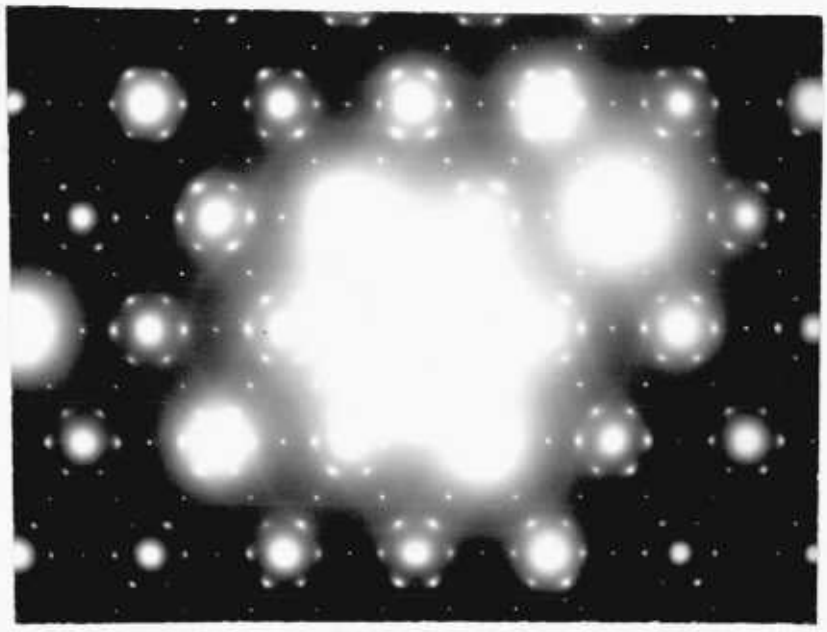
8.1 Introduction

Two other materials in Group Va which have octahedral co-ordination of the transition metal atoms were studied, $4H_b$ TaS_2 and 1T VSe_2. The first of these in fact has alternate layers with octahedral and trigonal prismatic co-ordination (see section 1.2). The materials could only be studied by electron diffraction because the satellite reflexions are far weaker than in 1T TaS_2, and a focusing, monochromatic X-ray system would be required to observe them using this radiation. It was just possible to detect the superlattice in $4H_b$ TaS_2 at room temperature without this facility, but a combination of high background intensity (due to necessary long exposures) and poor single crystal quality made for extremely unsatisfactory results. Regrettably the same situation also obtained for the trigonal prismatic materials (Chapter 9), where conditions were worsened by the weak satellite reflexions lying on the reciprocal axes, and therefore often coinciding with the white radiation streaks which result from the use of non-monochromatic radiation.

8.2 $4H_b$ Tantalum Disulphide

The behaviour of this polymorph of tantalum disulphide in diffraction is somewhat similar to that of the octahedral polymorph, although with important differences. Within the temperature range of observation, 150 - 450 K, there is a transition on cooling at about 415 K direct from a $1T_1$ - like phase to a $1T_3$ - like phase, without the intermediate equivalent of the incommensurate $1T_2$ TaS_2 phase. The behaviour of $4H_b$ TaS_2 is in this respect more closely related to that of 1T $TaSe_2$ (Wilson et al, 1975), which also has only the two distorted metastable

(a)



(b)

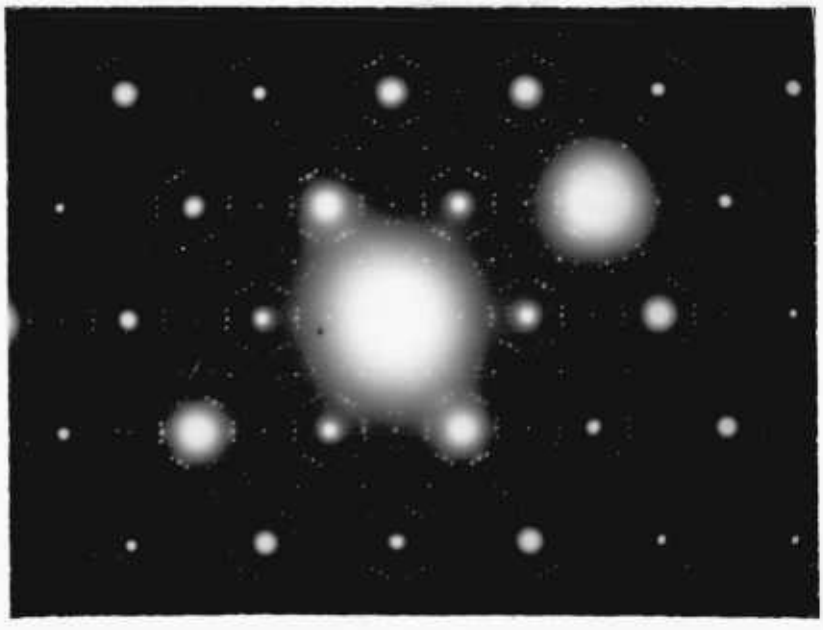
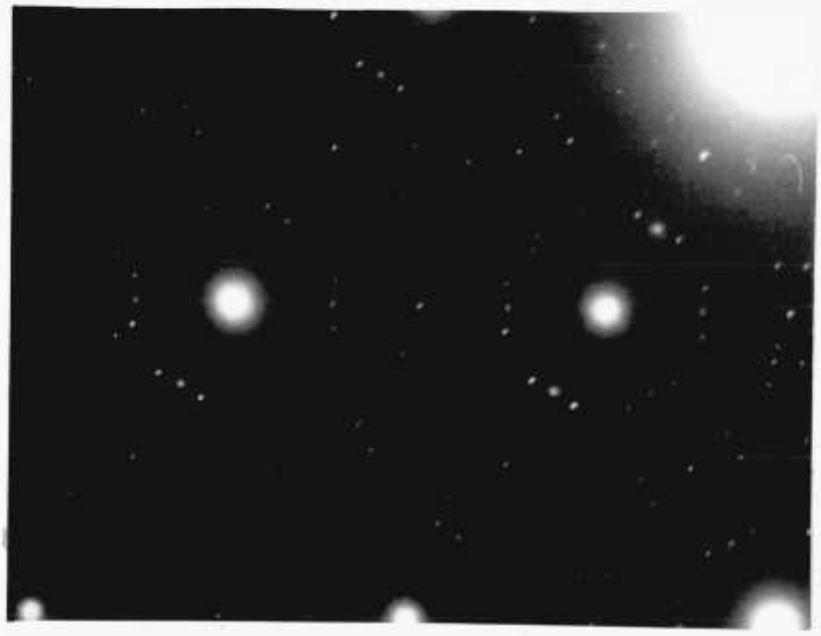


Figure 94 Selected area diffraction patterns from $4H_b$ TaS_2 at (a) about 430 K and (b) about 415 K. Plate (b) is from an area of crystal enclosing transformed and untransformed material.

(b)



(c)

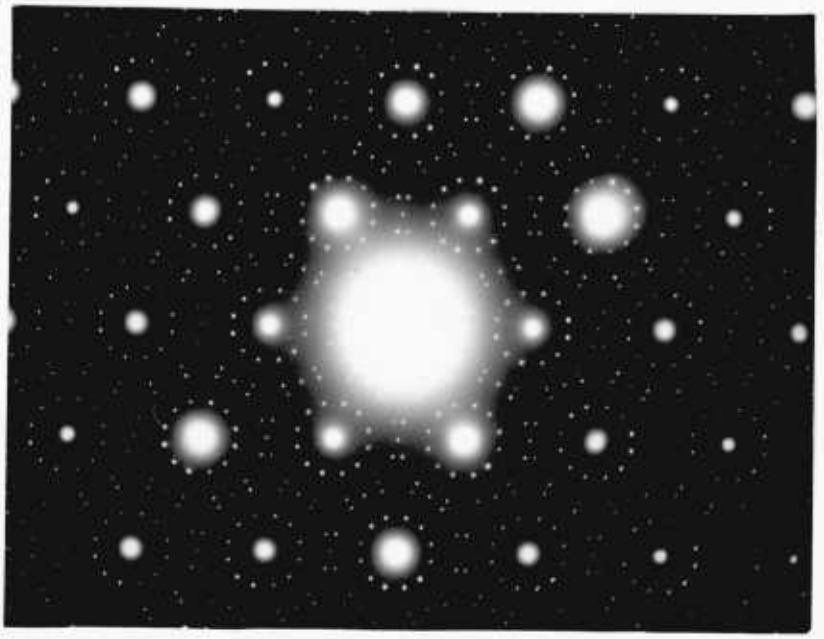


Figure 94 (continued) Selected area diffraction patterns from $4H_b$ TaS_2 at (b) about 415 K (enlargement) and (c) 290 K.

phases. The similarities with the 1T material (compare Fig. 94 with Fig. 58) mustimply that the observed diffraction effects are due to deformation of the alternate octahedrally co-ordinated TaS_2 layers. The transition occurs at a temperature which agrees well with the results of electrical measurements (DiSalvo, Bagley, Voorhoeve, Waszczak, 1973), which also show a second transition around 20 K, which is most likely to be taking place in the trigonal prismatic layers. This low temperature transition would then be the parallel of the one in 2H TaS_2, all of whose layers have this co-ordination (see footnote*below).

The high temperature phase with distortion of the octahedral layers (fig. 94(a)) clearly shows satellite reflexions lying on the matrix reciprocal axes (i.e. as in $1T_1$ TaS_2). Tilting the crystal in the electron microscope however confirmed that the satellites lay in the matrix hk.0 plane of the reciprocal lattice rather than at $\pm \frac{1}{3}\underline{c}^*$. They can therefore be indexed as $\{S_{hk.0}(10.0)\}$ It seems likely that the distortion waves are stacked with the same periodicity perpendicular to the layers as the matrix itself.

The satellite reflexions are weaker than in $1T_1$ TaS_2, and consequently the $\{S_M(11.0)\}$ are too weak to be observed even on well-exposed electron diffraction plates. This suggests immediately that the deformation amplitudes in this polytype are smaller, although it must be remembered that intensities of satellites are halved purely as a result of only alternate layers being distorted. The intensity pattern in each group of $\{S_M(10.0)\}$ reflexions again indicates longitudinal deformation waves, i.e. that $\underline{Q}$, $\underline{U}_Q$ and $\underline{a}^*$ are all parallel.

* Very recent low temperature electron diffraction (Tatlock, to be published) has detected this transition at 24 K. The incommensurate superstructure has periodicities very similar to those of 2H TaS_2.

Measurements from the plates of the magnitude of the distortion wave vector give

$$\underline{Q} = 0.265\ \underline{a}^*$$

This value is in fact $6\frac{1}{2}\%$ smaller than in $1T_1$ TaS_2.

Diffuse scattering is observed also, but it is again weaker in intensity than in $1T_1$ TaS_2 and therefore barely visible in Fig. 94 (a). As the temperature was further raised the satellites and the diffuse scattering weakened, and eventually disappeared as the material transformed to the stable 2H polytype at 450 - 500 K.

On cooling the crystal through 415 K a rather sluggish transition took place giving a commensurate distorted phase (Fig. 94(c)). It was possible as a result to obtain a pattern (Fig. 94(b)) from an area of crystal enclosing transformed and untransformed material. This effect was never observed in 1T TaS_2 where the transformation was far quicker. A 2 x 2 superlattice is also frequently observed in diffraction patterns from $4H_b$ TaS_2. This is most likely to be associated with the presence also of trigonal prismatic layers, and is therefore discussed in Chapter 9.

The breadth of the satellite reflexions in the incommensurate phase is larger than in the commensurate room temperature phase, suggesting a loss in deformation wave coherence within the layers at temperatures close to the transition. This increase in breadth in the higher temperature incommensurate phase was not observed for 1T TaS_2. Both this and the sluggishness of the transition could well be due to the influence of the (supposedly) undistorted trigonal prismatic layers. The loss of register between the layers would make long coherence lengths for the incommensurate deformation wave rather unfavourable. In 1T TaS_2 the deformation waves are able to maintain register with their

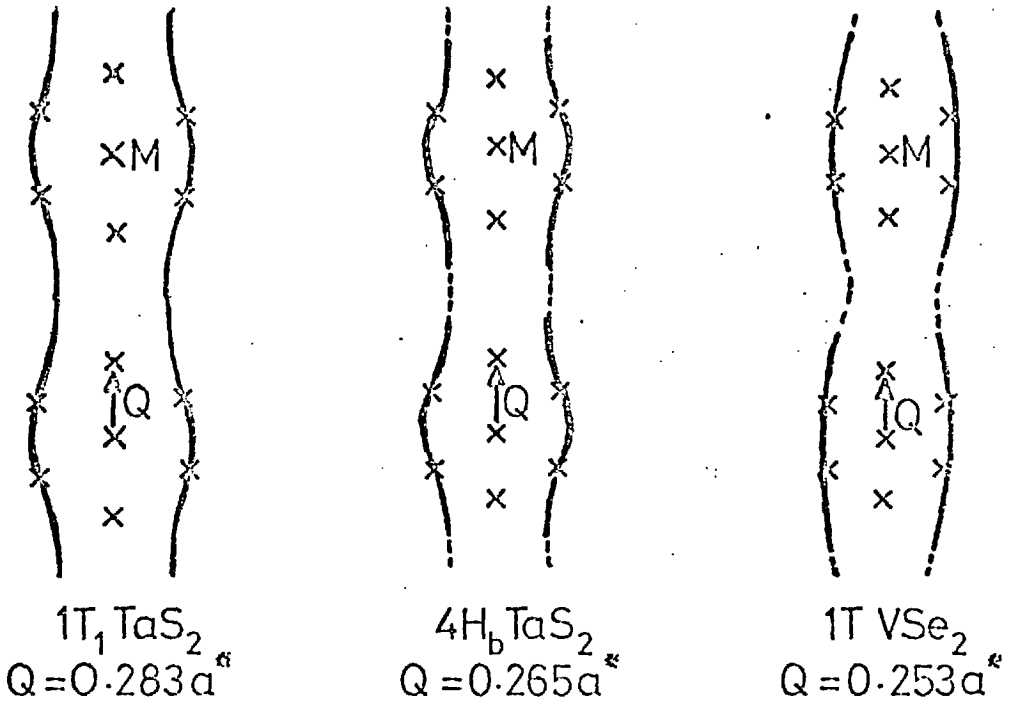


Figure 95 Comparison of the form taken by the diffuse scattering in three octahedral materials, and based on electron diffraction data.

neighbours through the rhombohedral stacking of distortions in adjacent layers.

The diffuse streaking disappears at the transition, and a careful study of well-exposed electron diffraction plates confirm that it is generally of the same form as in 1T TaS_2, although slightly closer to the parent matrix reflexion (Fig 95).

The commensurate phase (stable down to 150 K, the limit of experiment) usually has the two mirror-symmetry related orientations of the $\sqrt{13}a \times \sqrt{13}a$ superlattice with approximately equal intensity. The pattern closely resembles $1T_3$ TaS_2, except for the two orientations and being rather weaker — this may just be due to only half the layers being distorted; or more probably the deformation amplitude is smaller in this polymorph also. Small, very thin, areas of the crystal have been found which show one orientation stronger than the other, e.g. Fig. 108. Finally at the transition the wave vector $\underline{Q}$ increases discontinuously from $0.265\,\underline{a}^*$ to the coincidence value $1/\sqrt{13} = 0.277\,\underline{a}^*$.

It is extremely tempting to interpret the diffraction patterns from this material as arising from deformation structures very similar to those of $1T_1$ and $1T_3$ TaS_2, i.e. clusters of metal atoms in the octahedral layers. However, while there can be no doubt that there are periodic lattice deformations in the layers, there is as yet no direct diffraction evidence for clustering. The deformation profiles could be sinusoidal rather than 'sawtooth'. Quantitative X-ray or neutron diffraction studies are required in order to settle this uncertainty.

8.3 1T Vanadium Diselenide

Weak diffuse scattering can be seen on well-exposed diffraction patterns of this material at room temperature (Fig. 96(a)). The regular variation of the matrix reflexion intensity is due to the stacking sequence AbC AbC of vanadium and selenium atoms

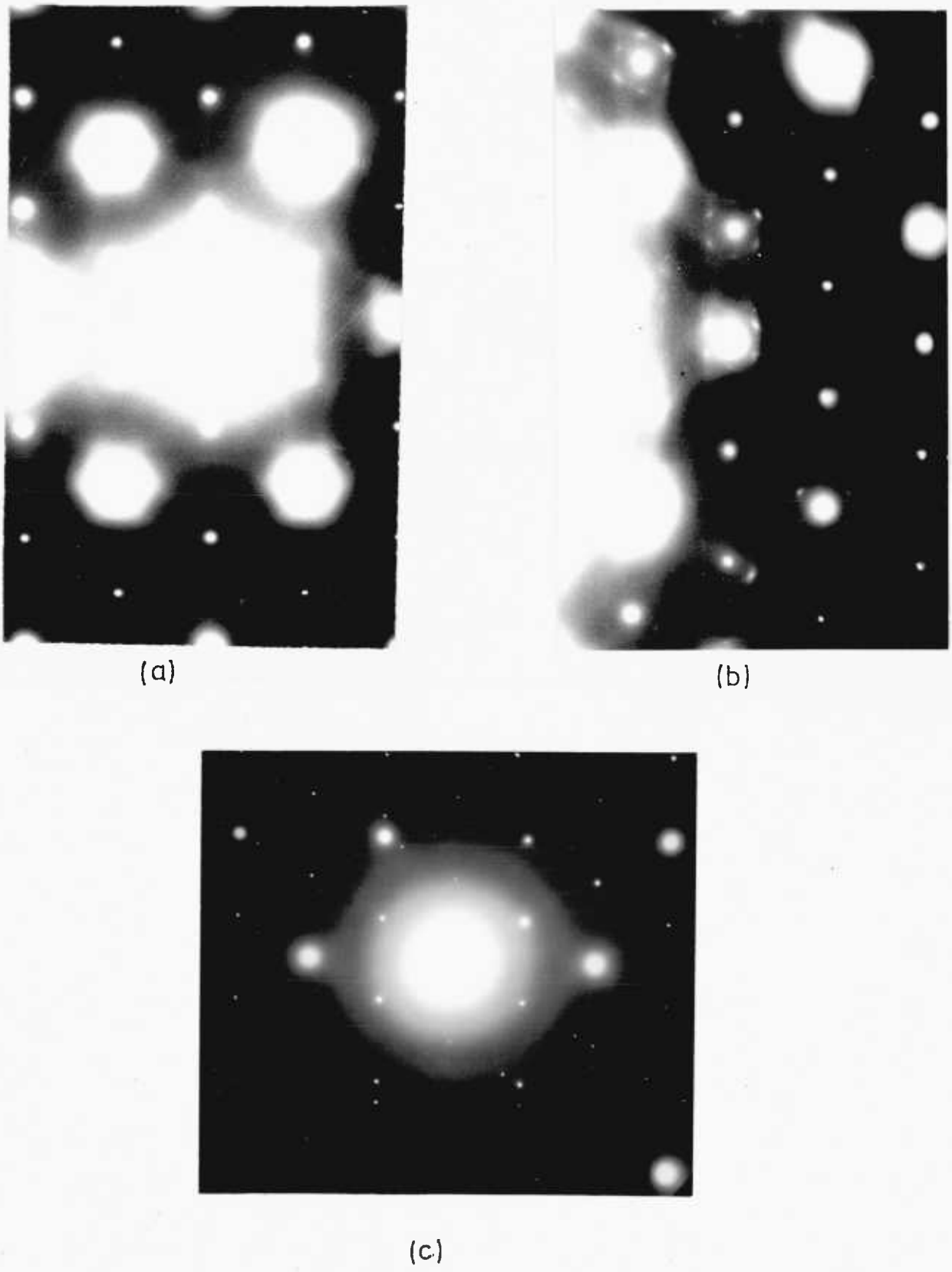


Figure 96 Selected area diffraction patterns from 1T VSe_2 at (a) 290 K, (b) 150 K and (c) about 40 K.

which have similar atomic scattering factors. Because of what approximates, as far as electron scattering is concerned, to rhombohedral stacking, the hk.0 reflexions are weak for $h - k \neq 0$ and strong for $h - k = 0$. This regular pattern of intensities was used to check that the crystal layers were oriented perpendicular to the incident radiation.

When the material was cooled to 150 K the intensity of the diffuse scattering increased, and as Fig. 96(b) shows it is now accompanied by rather broad satellite reflexions $\{S_M(10.\ell)\}$, which lie along the matrix reciprocal axes. The disposition of the satellites is therefore similar to that of the high temperature metastable phases of the other octahedral materials. Tilting experiments suggested that the $\{S_M(10.\ell)\}$ reflexions lie on modulated rods perpendicular to the layers, while the breadth of the satellites implies that phase correlation within each layer is somewhat limited. The general lack of coherence of the deformation waves argues for their not being static at this temperature.

Careful measurements show that at 150 K, $\underline{Q}$ is incommensurate with the matrix lattice and that

$$\underline{Q} = 0.255\,\underline{a}^* .$$

The intensity variation of the $\{S_M(10.\ell)\}$ is indicative of longitudinal deformation waves, since maxima occur where $\underline{K}$ is parallel to $\underline{Q}$ and minima where $\underline{K}$ is perpendicular to $\underline{Q}$. In this respect the deformation structure of VSe_2 is similar to that of $1T_1$ TaS_2 although the deformation amplitudes are weaker and the deformation waves *may* not be static.

The intensity dependence on $\underline{K}.\underline{Q}$ of the diffuse scattering implies that, as in $1T_1$ TaS_2, it arises as a result of scattering from $TA_\perp$ phonons in the layers. The geometry of the streaks differs from the other octahedral materials slightly: the

curvature of the streaks does not change sign (i.e. they are convex with respect to the parent reflexion throughout) whereas parts of the diffuse streaks in $1T_1$ TaS_2 are concave. The geometry of the diffuse scattering in the three octahedral materials considered so far can be compared in Fig. 95.

On further cooling to about 40 K the $\{S_M(10.\ell)\}$ were found (96d) to define a 4 a x 4 a superlattice. Tilting experiments clearly showed that the now very sharp satellite lie out of the matrix hk.0 reciprocal plane. It is not possible for them to be at $\pm \frac{1}{3}c^*$(matrix) — see section 11.10 — and it seems likely that they define a 4 layer repeat and are located at $\pm \frac{1}{4}c^*$.

The change in Q giving a commensurate superlattice is only 2% (from 0.255 a^* to 0.25 a^*) and it was not possible to detect any discontinuity in $\underline{Q}$ at the transition. The transition did however occur in a range of temperature consistent with NMR data (Silbernagel, 1974, unpublished work). As with the transitions in the other materials, the diffuse scattering disappeared when the material was cooled through the transition.

8.4 1T Tantalum Diselenide

Although it was not possible to obtain crystals of this material, the results of other workers (Wilson et al. 1975) are included in this Chapter for completeness, and to simplify discussion at a later stage. the 1T polytype of tantalum selenide ideally has the CdI_2 structure, and therefore should be isostructural with 1T TaS_2. Wilson et al (1975) discovered that 1T $TaSe_2$ has two metastable distorted phases, with a transition at 473 K corresponding to the one observed from resistivity and susceptibility data. The upper phase exhibits a superstructure almost identical to that of $1T_1$ TaS_2, except that the distortion wave vector, $\underline{Q}$ = 0.278 $\underline{a}^*$, slightly smaller than in the sulphide (0.283 $\underline{a}^*$).

The diffuse scattering is also very similar in the two materials. However the selenide transforms on cooling directly to a $\sqrt{13}a \times \sqrt{13}a$ superlattice (compare $1T_3 TaS_2$). DiSalvo, Maines and Waszczak (1974) have shown that this phase has a triclinic unit cell, and this again agrees with the conclusions which were drawn for $1T_3$ TaS_2 in section 6.7.

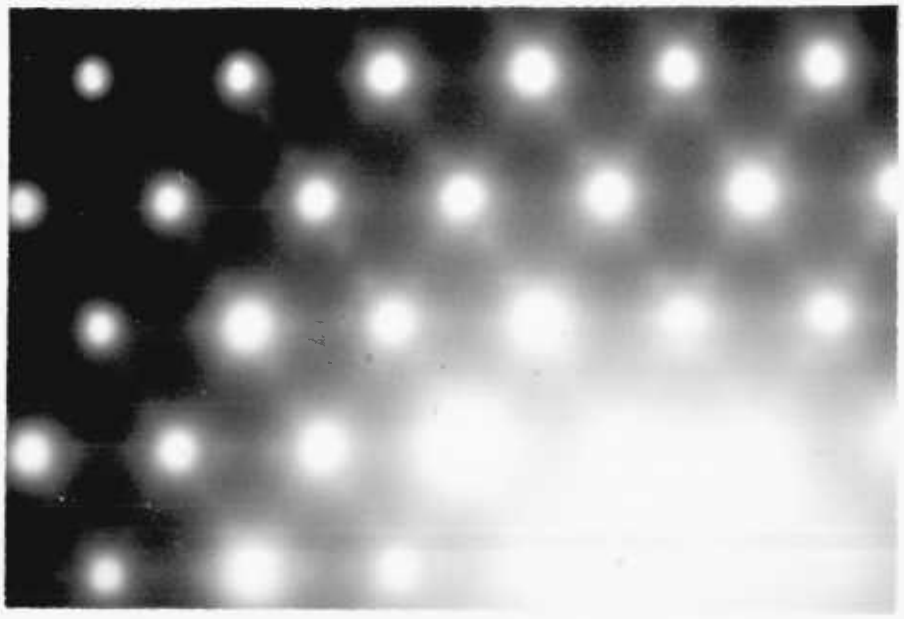
9 DIFFRACTION RESULTS AND INTERPRETATION: TRIGONAL PRISMATIC MATERIALS

9.1 Introduction

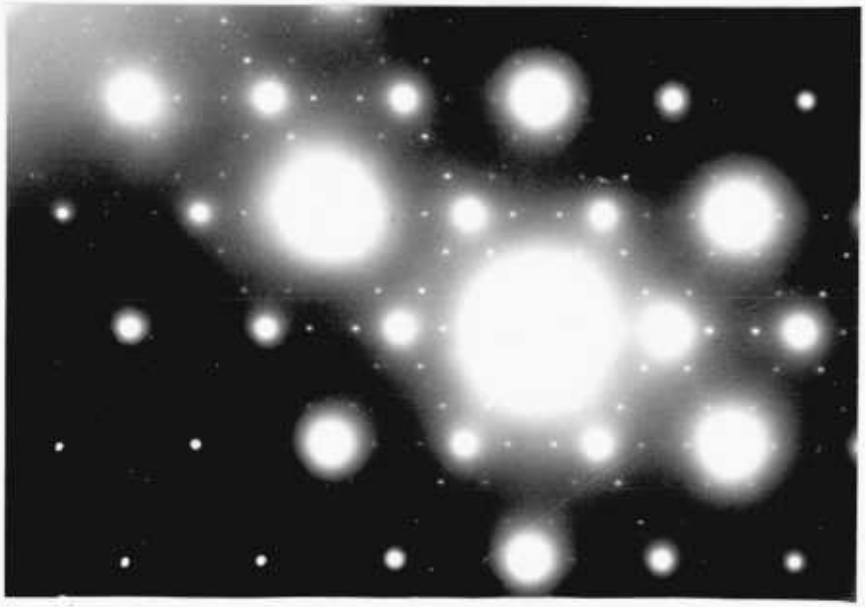
Group Va materials with trigonal prismatic co-ordination of the metal by the chalcogen atoms were also investigated. In general they also have phases with distorted structures, but these tend to be associated with smaller deformation amplitudes and to occur at lower temperatures. As the results show, the deformation wave vectors in the materials studied are always parallel to the matrix reciprocal axes. In this respect they appear to be similar to the octahedral materials, but the different patterns of diffuse scattering for the two types of co-ordination indicate that the mechanism responsible for the distortion of the lattices must be dependent on crystal symmetry. The diffuse streaks appear in fact to join up the matrix reflexions. Incommensurate-commensurate phase transitions are also observed for some trigonal prismatic materials. As it was remarked in the introduction to chapter 8, the orientation and very low intensity of the satellite reflexions make their observation very difficult without using monochromatic, focused X-rays. The materials were therefore studied by electron diffraction only.

9.2 2H Niobium Diselenide

Room temperature diffraction patterns of $NbSe_2$ showed just the hexagonal matrix reflexions. On cooling the sample to about 150 K however diffuse streaks appeared between the matrix reflexions with maxima in the streaks at approximately $\underline{M} \pm \frac{1}{3}\underline{a}^*$, as shown in Fig. 97(a). When crystals of the material were further cooled, using a liquid helium cold stage, the diffuse satellites became sharper to give an incommensurate superstructure. Figure 97(b) at 16 K shows this. At this transition, which



(a)



(b)

Figure 97 Selected area diffraction patterns from 2H $NbSe_2$ at (a) 150 K and (b) 16 K.

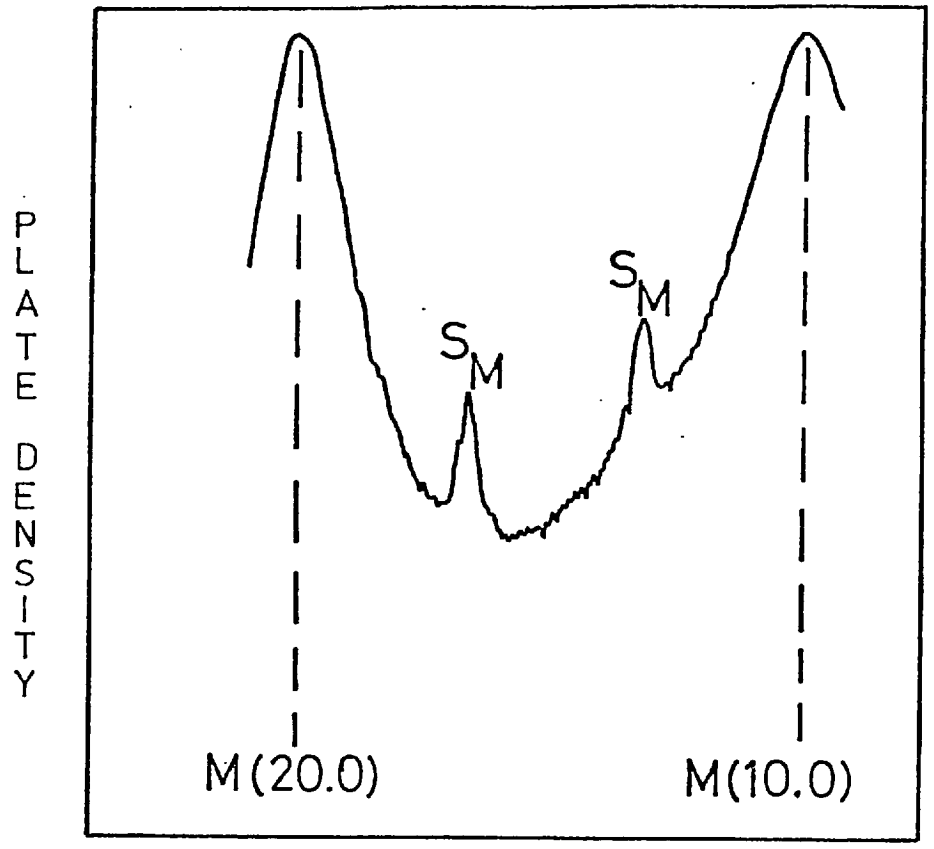


Figure 98 Microdensitometer trace along a central reciprocal lattice row, showing two satellite reflexions.

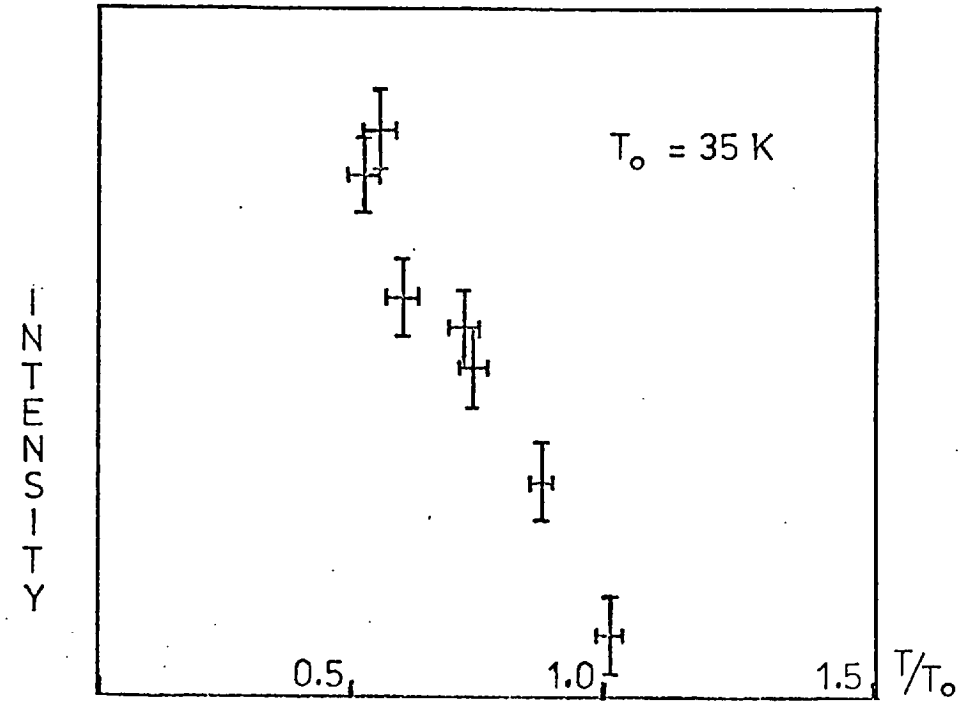


Figure 99 Normalised intensity (after subtraction of inelastic background) of satellites shown in Figure 98 as a function of reduced temperature.

started at about 35 K, there was a very big increase in the coherence length of the deformation waves, the satellite reflexions having become much sharper. The intensities of the satellites also showed a marked temperature dependence, and became very weak when the crystal was warmed above 35 K. This behaviour was reproducible from sample to sample, and also reversible within the same crystal.

Careful measurement shows that $\underline{Q} = (0.328 \pm .002)\ \underline{a}^*$. This is less than $\frac{1}{3}\underline{a}^*$ by 1 - 2 %, showing that the deformation waves must be incommensurate with the matrix lattice. Second or higher order satellite reflexions are never observed, even with very long exposures, and this is consistent with modulation of the lattice by an incommensurate deformation superstructure of small amplitude.

As can be deduced from the symmetrical distribution of matrix reflexion intensity in Figure 97(b), the crystal was oriented with the layers perpendicular to the incident electron beam. By also observing areas of crystal tilted at several degrees away from normal incidence, it was established that the satellite reflexions lie on families of reciprocal lattice rods parallel to $\underline{c}^*$. There may well be modulation of the rods to give maxima at $l\underline{c}^*$, but even so it would seem that there is far less correlation between deformations in neighbouring layers than in the octahedrally co-ordinated materials.

A microdensitometer was used to measure relative intensities of satellite reflexions and Figure 98 reproduces a typical trace along a $\underline{M}(h0.0)$ direction. After due allowance for the inelastic background, the variation in relative intensity as a function of reduced temperature, T/T_o, is shown in Figure 99. From this, T_o was estimated to be approximately 35 K. The variation in satellite intensity is interpreted as an increase in deformation

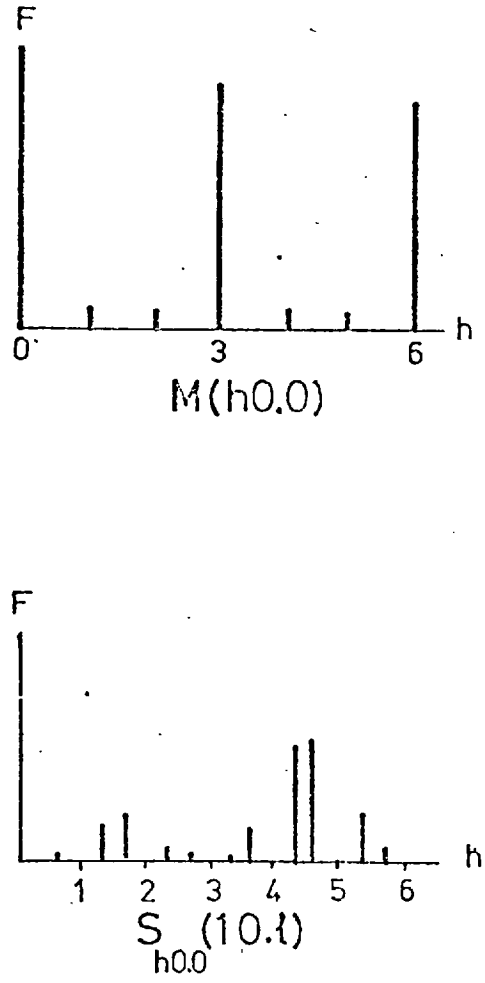


Figure 100 Calculated matrix and satellite reflexion structure factors, based on model discussed in text. The variation with h is π out of phase for the satellites relative to the matrix.

amplitude as the temperature decreases. A careful study of the intensity distribution in the set of satellites surrounding a matrix reflexion reveals that the largest intensity occurs when $\underline{Q}$ is parallel to $\underline{M}$. This again suggests a predominantly LA distortion.

Perhaps more noticeable on well-exposed plates is the variation of $S_{hk.0}(10.0)$ intensity with the indices of the matrix reflexion, h and k. There was no variation in satellite intensity with h,k in 1T TaS_2, where it was concluded that in-plane sulphur sublattice deformations were either very small or else out of phase with the tantalum sublattice. It was however deduced from other data that $TA_\perp$ modes on the sulphur sublattice were $2\pi/3$ out of phase with the tantalum LA modes. The sulphur was such a weak scatterer that its contributions to satellite intensity were extremely difficult to measure. In the case of niobium selenide however the selenium atoms scatter almost as strongly as the niobium so that their contributions to satellite intensity must be of the same order of magnitude. Consequently the variation in satellite intensity with matrix indices is readily interpreted in terms of distortion of the selenium sublattice.

The maximum satellite intensities for the $\underline{M}(h0.0)$ row occur midway between h = 1 and h = 2. The minima occur for h = 3n (n is an integer), i.e. where the matrix reflexions have their maxima. This situation, which is illustrated by Figure 100, can only mean that the displacements of the selenium atoms are opposed to the displacements of the niobium atoms, i.e. that there is a difference in phase factor of $\phi = \pi$. This follows from section 2.5.2, i.e.

$$F[M(h0.0)] = F_{Nb} + 2F_{Se}.\cos(2\pi h/3)$$

$$\text{and} \qquad F[S_{h0.0}(\pm 10.\ell)] = F_{Nb} + 2F_{Se}\cos(2\pi h/3 + \phi) \Big\}$$
$$= F_{Nb} - 2F_{Se}\cos(2\pi h/3)$$
$$\therefore \qquad \phi = \pi$$

Using the same notation as in Chapter 7, F_{Nb} and F_{Se} represent the niobium and selenium scattering contributions.

The temperature of the transition agrees well with the NMR measurements of Valic, Abdolall and Williams 1974. They show that $NbSe_2$ undergoes a transition centred on a temperature of 26 K. The reversal in the sign of the Hall coefficient in niobium selenide also occurs at about the same temperature (Lee, Garcia, McKinzie and Wold, 1970).

9.3 Niobium Disulphide

2H niobium disulphide was subjected to a similar investigation to the selenide. There was no diffraction evidence of for the existence of periodic structural distortions in this material, even at liquid helium temperatures.

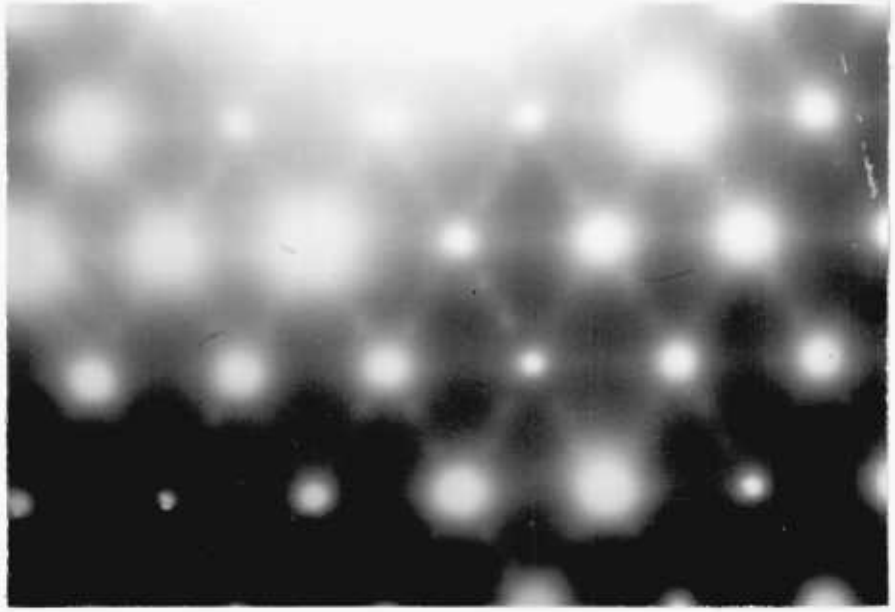
3R niobium disulphide crystals showed varying amounts of short range ordering (possibly of anion vacancies) but like the 2H polytype there was no evidence of periodic structural distortions.

These negative results are in fact important, for they are consistent with the failure of electrical and magnetic measurements to show anomalies in NbS_2 analogous with those in $NbSe_2$.

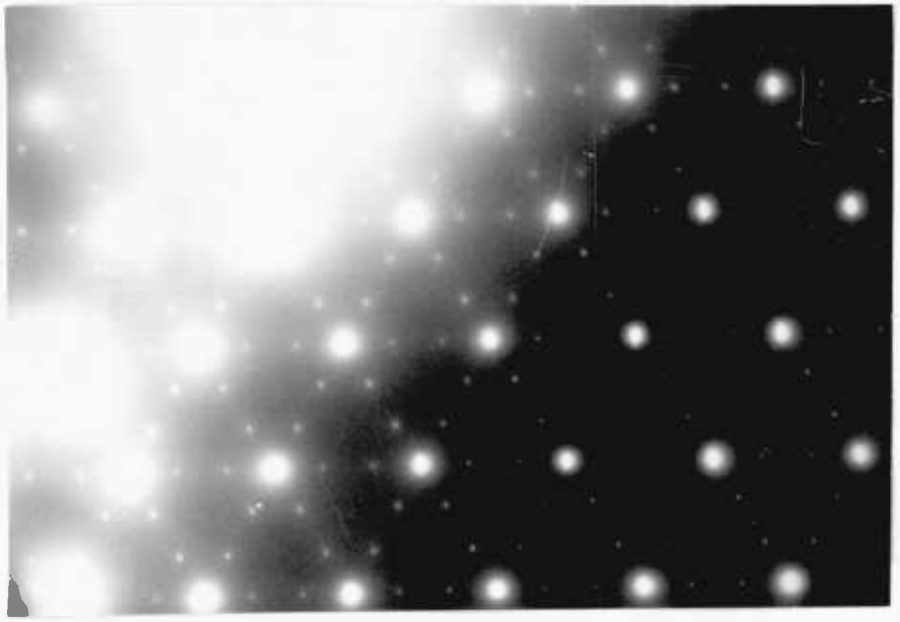
9.4 2H Tantalum Diselenide

The diffraction effects of the deformation superstructure in tantalum selenide were more pronounced at higher temperatures than in the niobium compound. At room temperature diffuse streaks are visible between the $TaSe_2$ matrix reflexions, and there are maxima on the streaks approximately at $\underline{M} \pm 0.3\underline{a}^*$ (Figure 101). This scattering is very reminiscent of niobium diselenide (Figure

(a)



(b)



(c)

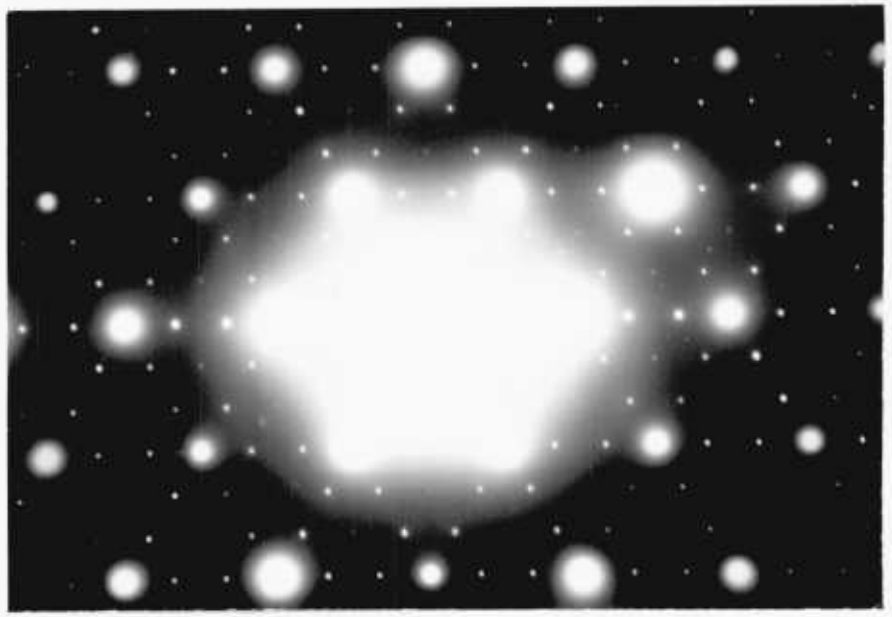


Figure 101

Selected area diffraction patterns from 2H $TaSe_2$ at (a) 290 K, (b) 150 K, and (c) about 40 K. It is interesting to compare (a) and (b) with Figure 97, 2H $NbSe_2$. The $3\underline{a} \times 3\underline{a}$ superlattice (c) does not have a parallel in $NbSe_2$.

99(a)) but in $TaSe_2$ it occurs about 120 K higher.

When the crystal is cooled to 150 K sharp satellite reflexions form. They define a superstructure with wave vector $\underline{Q} = (0.327 \pm .002)\,\underline{a}^*$, i.e. which is about 2% incommensurate (Figure 101(b)). The absence of satellite reflexions of order higher than the six fundamental ones, is consistent with the incommensurateness of the superstructure and a relatively small deformation amplitude. $\{S_M(11.0)\}$ reflexions are just visible in electron diffraction for $1T_1$ TaS_2 (Fig. 58), where $\underline{U}_Q$ is estimated to be 0.09 Å. Comparing Fig. 58(i) with Fig. 101(b) suggests therefore that at 120 K, $\underline{U}_Q$ in $TaSe_2$ is less than 0.09 Å. It is again interesting to note that the satellite diffraction pattern for 2H $TaSe_2$ at 120 K is very similar to 2H $NbSe_2$ at 16 K (Figure 97 (b)).

On further cooling a transformation takes place to a structure with a $3\underline{a} \times 3\underline{a}$ deformation superlattice (Figure 101 (c) taken at about 40 K). In this respect 2H $TaSe_2$ differs from $NbSe_2$ whose deformations remain incommensurate even at 5 K (Moncton, Axe and DiSalvo, 1975). Very weak higher order satellite reflexions (indexed $\{\underline{S}_M(11.0)\}$ on the deformation cell) are visible in Figure 101 (c). As well as confirming that a transformation to a commensurate superlattice has taken place, this also suggests an increase in $\underline{U}_Q$ on cooling (similar to the increase observed for $NbSe_2$). The comparison with $1T_1$ TaS_2 referred to in the previous paragraph implies that $\underline{U}_Q$ in 2H $TaSe_2$ is approximately the same below the transition, i.e. 0.09 Å. Neutron diffraction studies (Moncton et al 1975) have confirmed this value. They have also shown that the selenium displacements are opposed to those of the tantalum atoms (compare the results for 2H $NbSe_2$, Section 9.2) and that there are higher Fourier components of the deformation lattice, with wave vectors $2\underline{Q}$. This is rather

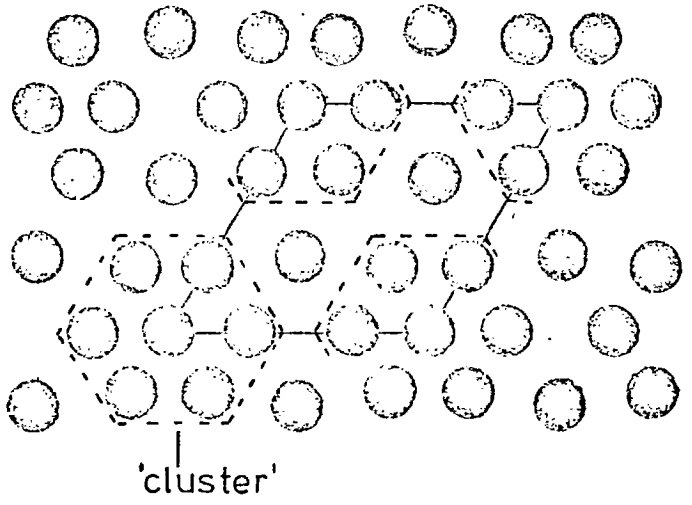


Figure 102 A model for a 3a x 3a distortion supercell in 2H $TaSe_2$ (drawn with 10 % amplitude of deformation). It can be seen that it is not possible to incorporate all the atoms in the unit cell (solid lines) into the 'clusters' (broken lines) and also maintain the hexagonal symmetry. This is in contrast to the $\sqrt{13}$a x $\sqrt{13}$a distortion supercell of Figure 92 (iii).

interesting, for it suggests that 2H $TaSe_2$ may well have a deformation structure like the octahedral materials with perhaps partial clustering of the tantalum atoms.

At the end of Chapter 7 models were proposed for the distorted layers in the three 1T TaS_2 phases, and illustrated by Figures 92 and 93. If this is also done for 2H $TaSe_2$ it is found that because the supercell is $3\underline{a} \times 3\underline{a}$ rather than $\sqrt{13}\,a \times \sqrt{13}\,a$ (cf. $1T_3$ TaS_2) it is not possible to incorporate all the tantalum atoms into hexagonal clusters (Figure 102). If the clusters are centred on a metal atom at the cell corners, then there are metal atoms at $(\frac{1}{3}, \frac{2}{3})$ and $(\frac{2}{3}, \frac{1}{3})$ which are equidistant from three clusters. This situation can only be avoided by a small shift in origin and loss of hexagonal symmetry.

The temperature of the transformation is again consistent with the transition temperature proposed on the basis of electrical and magnetic measurements (Chapter 1.3.2).

9.5 2H Tantalum Disulphide

Sufficiently good crystals of 2H TaS_2 could not be obtained in order to include it in this study. The material has however been examined in electron diffraction by Tidman, Singh, Curzon and Frindt, (1974) who show that 2H TaS_2 behaves very similarly to the selenide and undergoes a transition to a commensurate $3\underline{a} \times 3\underline{a}$ deformation superstructure at 75 K. At this temperature a discontinuity in electrical resistivity is also observed. The transition temperature is about 75 K lower than in the selenide.

10 PHASE-CONTRAST LATTICE IMAGES

10.1 Introduction

The technique of direct lattice resolution is best applied to materials with large unit cells. Ideally, the cell spacings in projection normal to the incident electrons should be much greater than the spacing corresponding to the resolution limit of the instrument. This criterion is satisfied for a number of transition metal oxides, in which n-beam lattice imaging has successfully resolved crystallographic shear and tunnel structures. For examples of this see Iijima (1971) and Allpress & Sanders (1973).

In the case of the regular transition metal layer dichalcogenides the lattice a-spacing of ~ 3 Å permits only the first Fourier components of the hexagonal cell to be resolved with present equipment. The layer materials which have distorted structures are more suitable, having spacings in the range 6 to 11 Å.

The main purpose of this part of the investigation was to complement the diffraction studies of the distorted Group Va layer dichalcogenides, especially of 1T and $4H_b$ TaS_2. 2H MoS_2 which has a regular structure, and β-$MoTe_2$ whose distorted structure has been analysed by Brown (1966), were however included mainly for the purposes of comparison. All spacings given in this Chapter are calculated from diffraction data.

10.2 Molybdenum disulphide

2H MoS_2 has a regular structure which belongs to the hexagonal space group $P6_3/mmc$, and the phase-contrast lattice image (Figure 103) shows the unit cell in projection. The diffraction pattern (inset) reveals that the image is formed from three beams: 00.0, 10.0, 01.0, transmitted by the aperture.

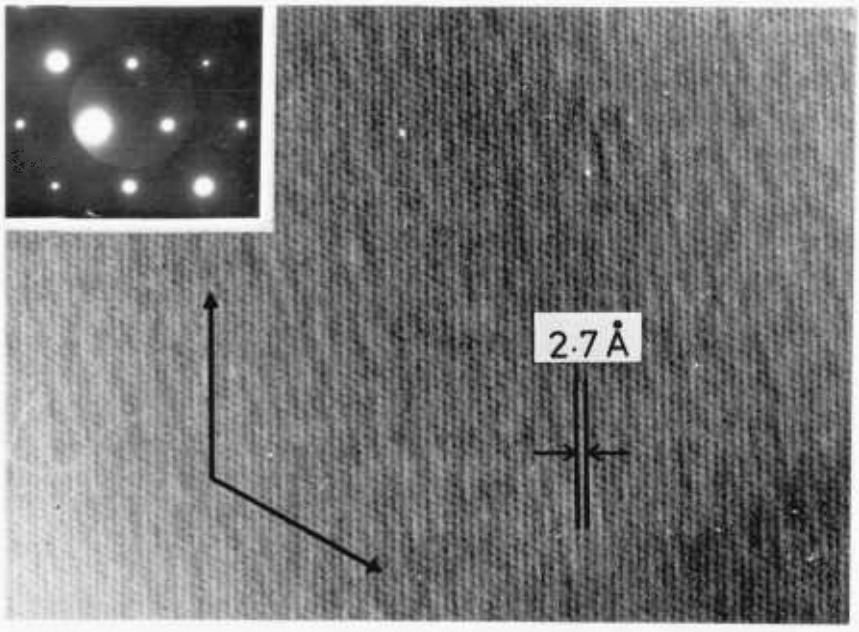


Figure 103 Phase-contrast lattice image showing the MoS_2 unit cell in projection (inset shows diffraction pattern and position of aperture).

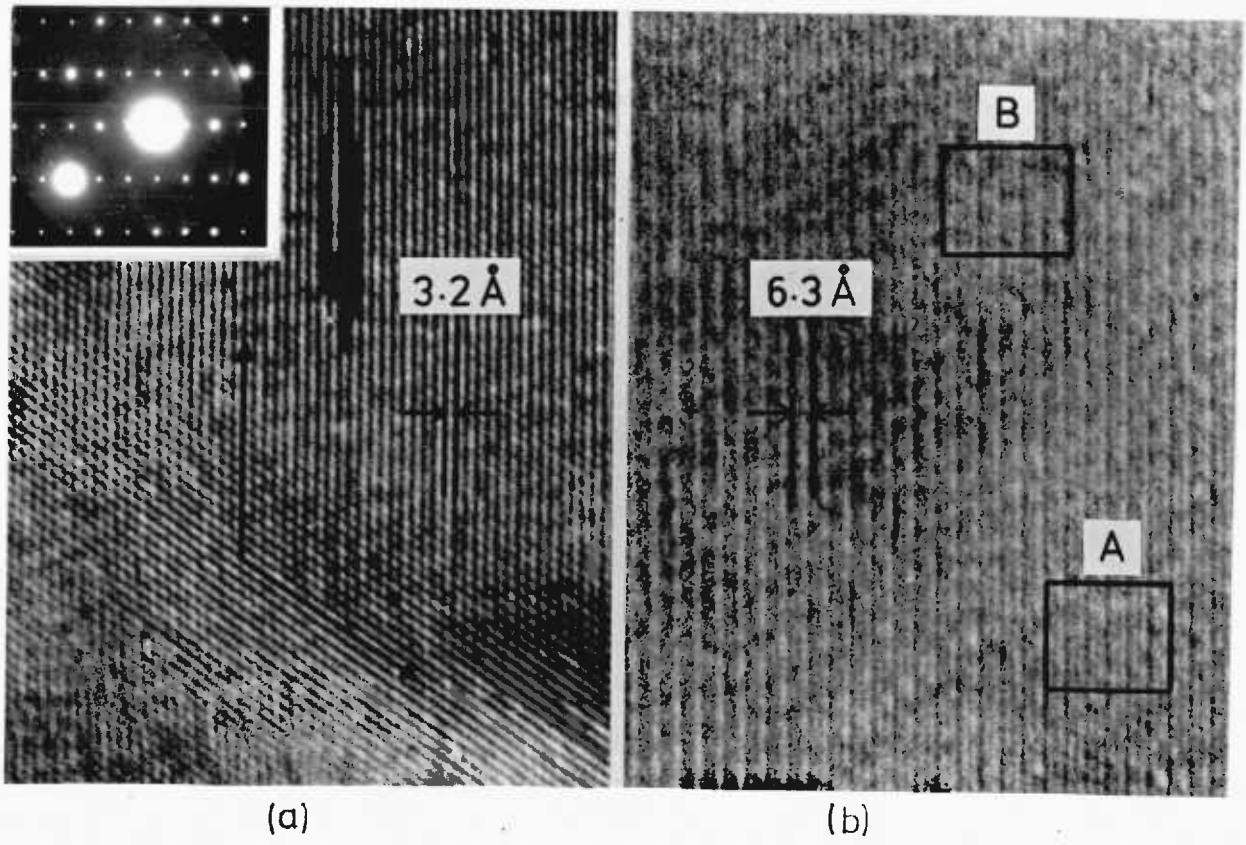


Figure 104 Phase-contrast lattice images from ρ-$MoTe_2$. In (a) the electron beam is incident normal to the layers, while in (b) it is tilted slightly. The inset shows the position of the diffraction aperture for these images.

10.3 β-Molybdenum Telluride

Comparison of the hk.0 section of the β-$MoTe_2$ reciprocal lattice (Figure 104 inset) with MoS_2 indicates that there is a doubling of the unit cell parallel to $\underline{a}^*$, and a consequent lowering of symmetry in the telluride. In fact the structure analysis of Brown (1966) places it in the monoclinic space group $P2_1/m$ with a = 6.33 Å, b = 3.47 Å, c = 13.86 Å, β = 93° 55'.

Figure 104 (a) however appears to show a hexagonal cell in projection for the telluride, rather than the monoclinic cell. The reason for this becomes clearer when the structure of β-$MoTe_2$ is examined more closely. Figure 105 shows that each CdI_2-like layer is modulated by a periodic distortion, the effect of which is to produce parallel zig-zag chains of molybdenum atoms. The unit cell which the distortion can be considered to modulate is 2-D pseudo-hexagonal (of angle 118.7°) rather than hexagonal, and the periodicity of the deformation wave is $2\underline{a}' + \underline{b}' = \underline{a}$ (monoclinic).

The stacking is such that the origin of the deformation is shifted by $\frac{1}{2}\underline{a}$ in successive layers. Thus with the electron beam incident normal to the layers, the contributions to the projected image from the distortion periodicity in adjacent layers are in antiphase. There is consequently destructive interference between these contributions, so that the image must be formed from the non-zero Fourier components which correspond to the pseudo-hexagonal cell, i.e. 200, 110. In Table 24, below, the observed values of the structure factors for the h00 reflexions (Brown 1966) clearly show this effect. The non-zero reflexions (h even) correspond to the pseudo-hexagonal cell spacing.

h	2	3	4	5	6	7	8	9	10	11
F_o	22.6	0	14.8	0	14.4	0	22.3	0	5.4	0

Table 24 Observed h0.0 structure factors (from Brown 1966).

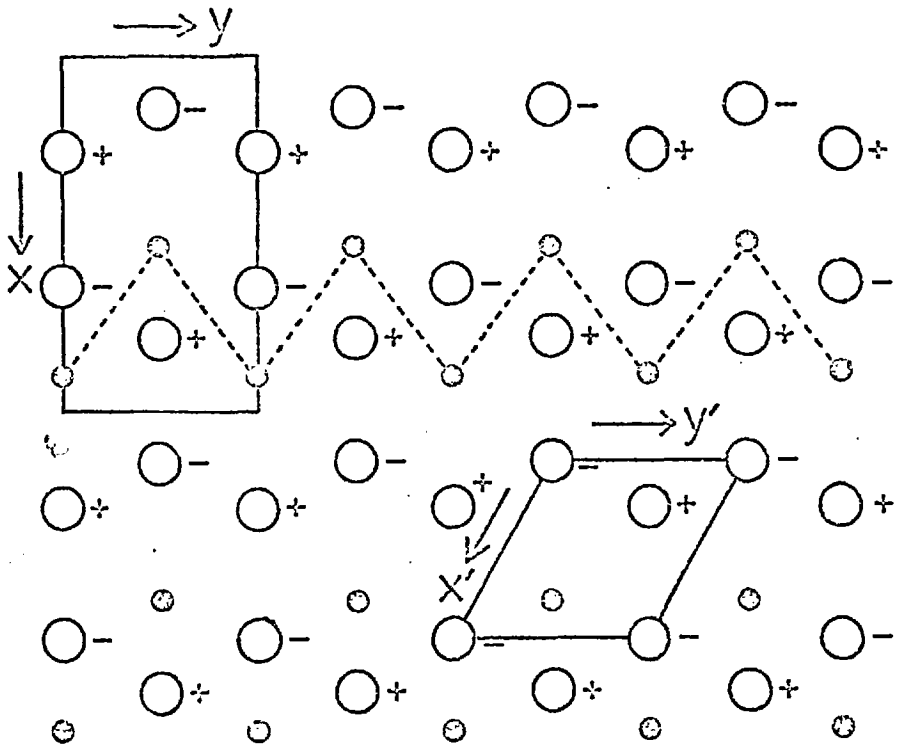


Figure 105 Diagram showing part of a single distorted β-$MoTe_2$ layer (from Brown, 1966). Also marked are axes of the monoclinic cell (x,y) and the pseudohexagonal cell (x',y'). The metal atoms, in chains, are drawn shaded, and all atoms are projected on to the plane of the paper.

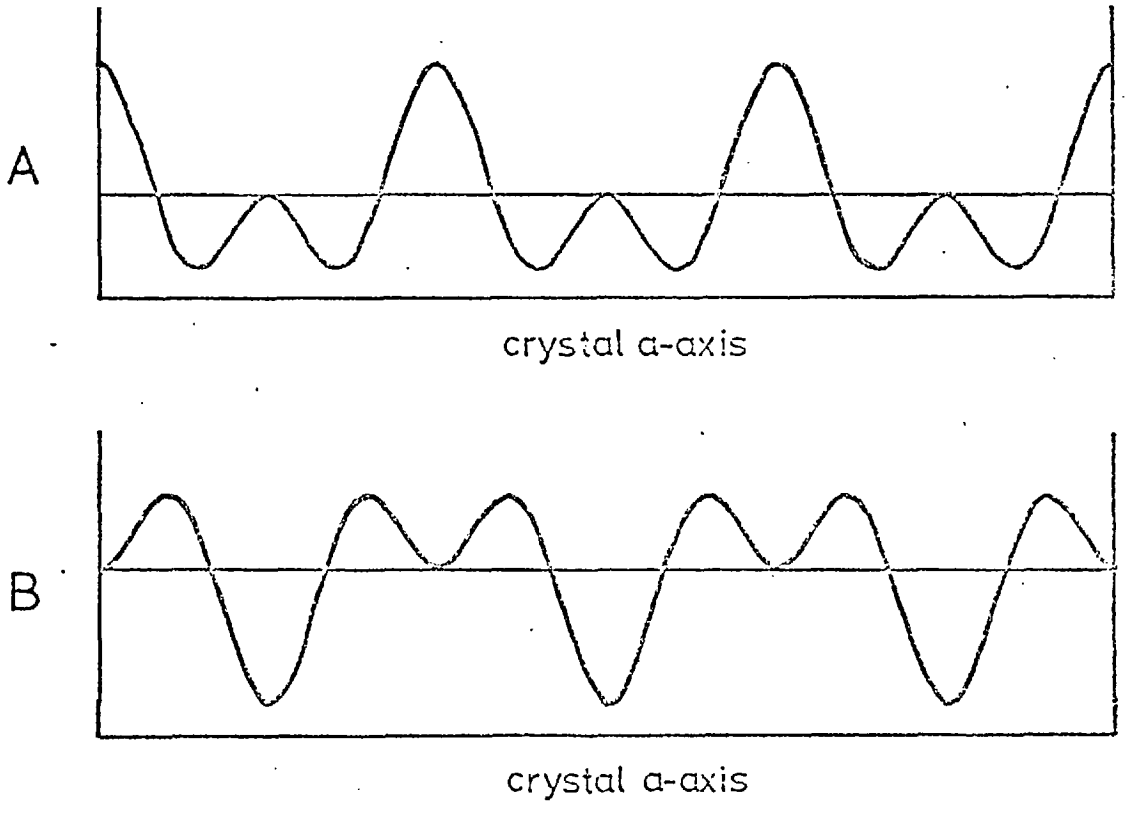


Figure 106 The result of adding together the first two Fourier components of a 1-D lattice with phase 0 (A) & $\pi/2$ (B).

With a slight change in relative orientation of incident beam and crystal, the contributions from adjacent layers no longer cancel, and the 6.3 Å deformation wave is seen to modulate the pseudo-hexagonal cell (Figure 104 (b)). The result of adding together with equal amplitude the first two Fourier components of a 1-D structure is reproduced in Figure 106. Although detailed interpretation is made difficult by the large phase shifts introduced by spherical aberration, Figure 104 does indicate that the lattice image is phase dependent and that there is quite good agreement between the areas A and B, and the limiting cases of 0 and $\pi/2$ phase difference (Figure 106). The variation in image is most probably due to local changes in orientation, although changes in specimen thickness cannot be ruled out.

Careful study of Figure 104(a) confirms that even here there is a slight modulation of the 200 fringes by the deformation periodicity. This modulation never occurs for the 110 fringes which are sinusoidal: this is consistent with the distortion being in a unique direction in the unit cell. With larger changes in crystal orientation, the distortion periodicity (i.e. the monoclinic cell a-spacing) is imaged alone.

10.4 1T Tantalum Disulphide

The area of crystal normal to incident electrons (Figure 107 (a)) has 2.9 Å (= $a\sqrt{3}/2$) lattice fringes crossing it. Superimposed on these are sets of weaker 5.9 Å fringes. The adjacent, slightly tilted area in the immediate vicinity of a Bragg contour - Figure 107 (b) - shows 10.2 Å fringes. Here the 2.9 Å lattice fringes are barely resolved. The additional reflexions in the diffraction pattern of $1T_2$ TaS_2 - Figure 58(ii) - were interpreted in terms of symmetry related deformation waves of periodicity

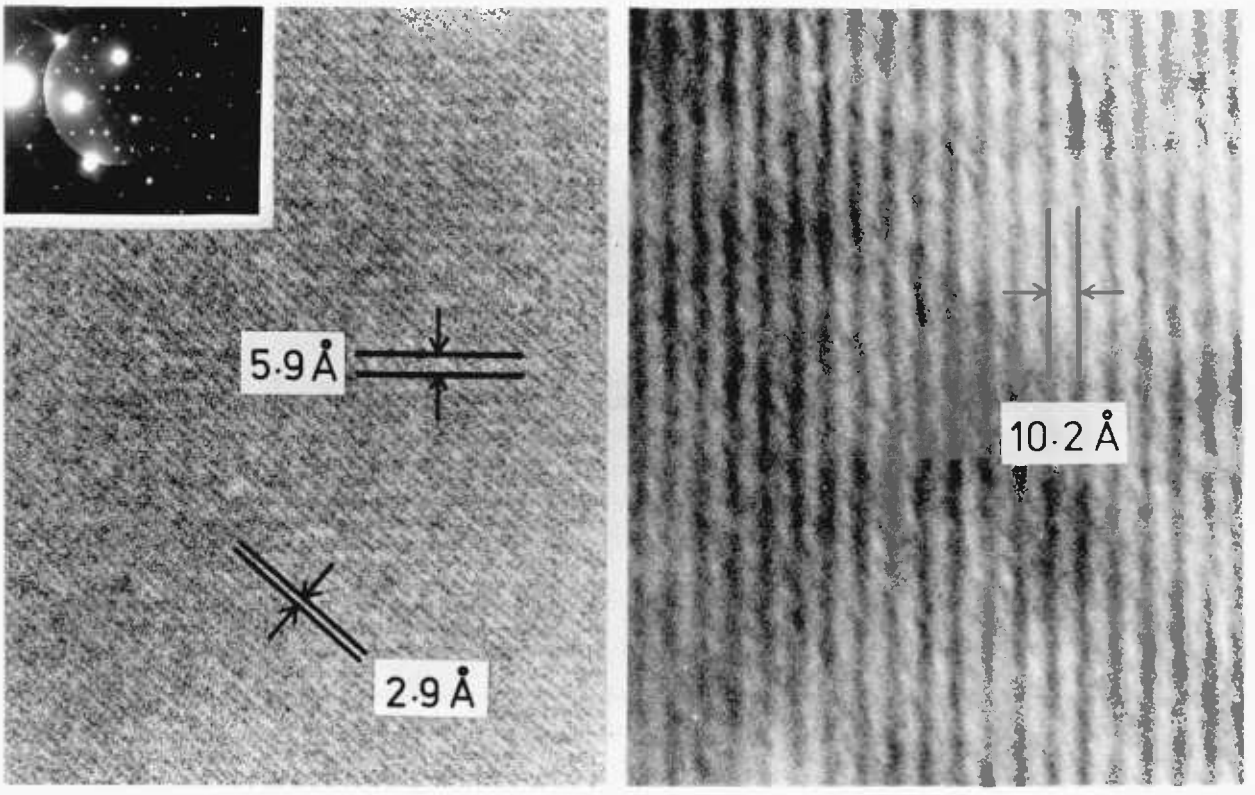


Figure 107 Phase-contrast lattice images from $1T_2$ TaS_2 (inset again showing diffraction conditions). In (a) the electron beam is incident normal to the layers, while in (b) it is tilted sufficiently for the fundamental distortion periodicity to be visible.

10.2 Å within each layer. In Chapter 6 the distortions were also seen to be incommensurate with the matrix lattice. The broad fringes of Figure 107 (b) must therefore result from the interference of the radiation scattered into a matrix reflexion and an adjacent $\underline{S}_M(10.1)$ satellite. The periodic structural deformations in $1T_2$ TaS_2 must therefore be static for this image to be formed.

The fundamental 10.2 Å periodic lattice distortion is not observed when the crystal layers are in perpendicular orientation - Figure 107(a). This argues that the distortions in adjacent layers must be stacked so that their contributions cancel out in the projected image of the deformation cell - compare Figure 104 (a), β-$MoTe_2$. This interpretation is consistent with the results of the diffraction studies, i.e. that the deformation waves stack rhombohedrally. While the contributions to the image from distortions in successive layers of β-$MoTe_2$ have phases 0, π, etc, the contributions have phase 0, $2\pi/3$, $4\pi/3$, from the rhombohedrally stacked distortions in 1T TaS_2.

The fringes which are observed when the crystal is in this perpendicular orientation have spacing $5.9 = 10.2/\sqrt{3}$ Å, and therefore correspond to the (11.0) planes of the deformation cell. These planes are in the same orientation in each layer and their contributions to the image are always in phase for this orientation.

In Section 7.2.6 , the fundamental 10.2 Å deformation wave was shown to be accompanied by a series of higher harmonics of the deformation periodicity. These included deformations with wave vector $\underline{P}_1 = \underline{Q}_2 - \underline{Q}_3$, etc, which scattered radiation into the $\{\underline{S}_M(11.0)\}$ satellites. The 5.9 Å fringes are therefore essentially an image of this higher harmonic. They are much weaker than the fundamental fringes, an observation which is

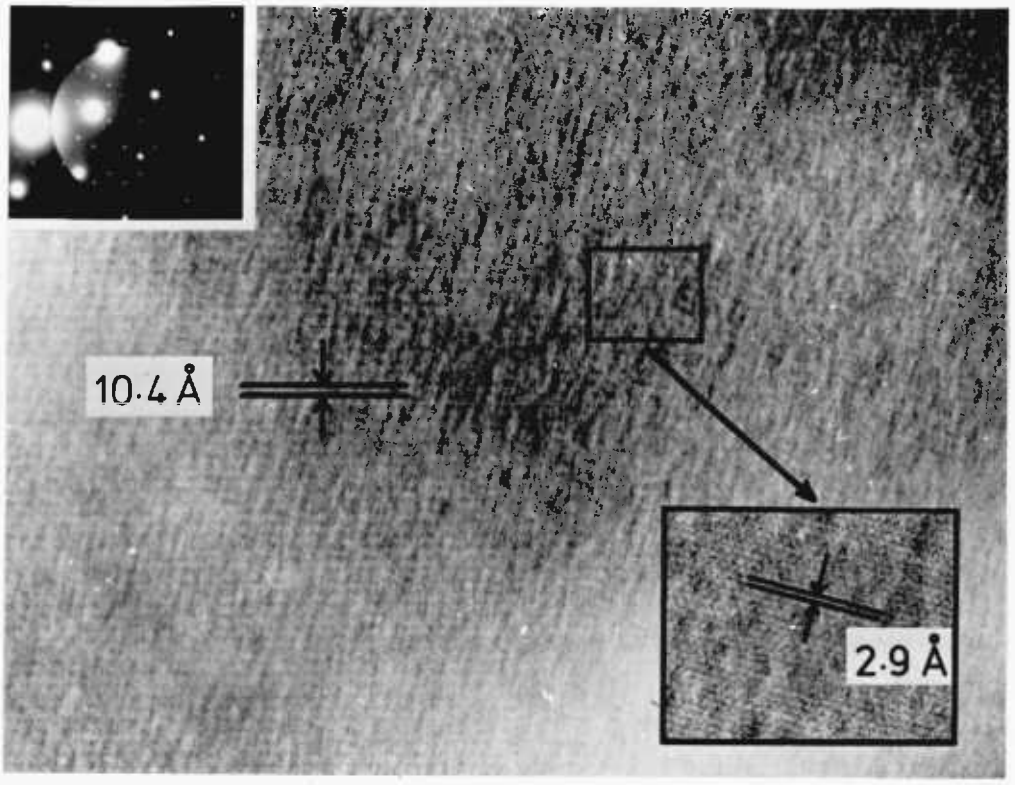


Figure 108 Phase contrast lattice image from $4H_b$ TaS_2, with incident beam normal to layers. The inset shows the diffraction conditions.

consistent with the calculated values of the distortion amplitudes, $\underline{U}_Q$ = 0.13 Å, $\underline{U}_P$ = 0.05 Å. Although it was always possible to image the 5.9 Å distortion cell planes together with the matrix lattice, the change in orientation required in order to image the fundamental 10.2 Å planes made it difficult simultaneously to observe the lattice fringes.

10.5 $4H_b$ Tantalum Disulphide

The diffraction aperture was set to be in as similar a position as possible to that used in the study of 1T TaS_2 - compare the insets of Figures 108 and 107. The fringes defining the $4H_b$ TaS_2 deformation cell, with spacing 10.4 = $2.9\sqrt{3}$ Å, are resolved when the crystal layers are perpendicular to the incident beam (Figure 108). This is consistent with the deformations, which are commensurate with the $4H_b$ TaS_2 matrix lattice, stacking in the same orientation, in marked contrast to the rhombohedral stacking of the incommensurate 1T TaS_2 deformations.

The contrast in the periodic lattice distortion fringes was considerably less in this material than in the octahedral polytype, suggesting a smaller deformation amplitude in $4H_b$ TaS_2. The low contrast made the dark field technique essential.

11 GENERAL DISCUSSION OF RESULTS

11.1 Summary of Structural Results

All the Group Va materials which have octahedral co-ordination of the metal atoms by the chalcogens, have CdI_2-like layers modulated by periodic structural distortions in some range of temperature. Most of those whose layers have trigonal prismatic co-ordination, also undergo periodic deformation of the lattice.

The overall effect of the periodic structural distortions is to produce periodic increases and reductions in bond lengths, particularly between the metal atoms within each layer. In the materials with the largest deformation amplitudes (notably the tantalum dichalcogenides) the profile of the deformations is 'saw-tooth' rather than pure sinusoidal. The effect of this is to produce clusters of atoms lying on a hexagonal mesh, as illustrated for example in Figure 92.

At higher temperatures each material is undistorted; as cooling takes place an onset temperature, T_o, is reached at which the amplitude begins to build up in certain distortion modes. There is a complication with 1T TaS_2 and 1T $TaSe_2$ in that these polytypes are stable and undistorted above about 850 K, and metastable below about 450 K. They both transform to the 2H polytype in the intermediate range of temperature, where in fact the onset temperature T_o ought to lie.

As the deformation intially builds up in all the sulphides and selenides, the direction of the distortion (i.e. phonon) wave vector $\underline{Q}$ is parallel to the matrix reciprocal axes, to $\underline{a}^*$. Diffraction results tend to suggest that just below T_o the deformation waves propagate through the crystal, although they may become static at lower temperatures. This point will

be returned to in a later section. Q is smaller in magnitude in the octahedral compounds than in the trigonal prismatic. A further difference is that in the former, Q decreases on further cooling, while in the latter Q increases. Generally speaking T_o is highest in the tellurides, and lowest in the sulphides. In addition, T_o is lower in vanadium than in tantalum dichalcogenides (octahedrally co-ordinated), and lower in niobium than tantalum dichalcogenides (trigonal prismatic).

Initially the deformation waves are incommensurate with the lattice of all the compounds (with the strict exception of the tellurides) - a very distinctive property. On further cooling there is a tendency to form a commensurate superlattice at some temperature, T_d. This is not fulfilled in niobium diselenide: indeed the sulphide of this metal does not even shows signs of the incommensurate deformation state.

The commensurate superlattice is $3\underline{a} \times 3\underline{a}$ in the trigonal prismatic polytypes, and does not involve a change in deformation wave direction at the transition, only an increase in Q of a few percent. In the octahedral compounds, the deformations are directed along the matrix axes in the incommensurate phases. However in those where Q is only slightly less than $0.3\,a^*$ (Table 25) there is a discontinuous change in the direction of $\underline{Q}$ to give a $\sqrt{13}a \times \sqrt{13}a$ superlattice. In VSe_2, Q is somewhat smaller, and shrinks to give a $4\underline{a} \times 4\underline{a}$ superlattice, the wave-vector remaining parallel to $\underline{a}^*$.

Consistency of behaviour is emphasised by $4H_b$ TaS_2, which has alternate layers with octahedral and trigonal prismatic co-ordination. Its deformation structure immediately above and below room temperature is directly comparable with the 1T polytypes, and therefore must be associated with the octahedral layers. Based on the electrical and magnetic properties

of the material (DiSalvo et al 1973) a structural transition was predicted at around 20 K, which should be similar to that occurring in the trigonal prismatic compounds. This prediction has very recently been proved correct by Tatlock (to be published). The trigonal prismatic layers of $4H_b$ TaS_2 spontaneously deform at very low temperatures in a manner directly comparable with 2H TaS_2, exactly as predicted. The mixed co-ordination of $4H_b$ TaS_2 seems chiefly to be reflected in the fact that interactions between layers alter the temperatures of onset of the deformations.

1T TaS_2 has the largest wave vector, $\underline{Q}$, of all the octahedral materials. Its behaviour appears to be unique in the Group, for it assumes an intermediate, incommensurate deformation superstructure ($1T_2$) before transforming finally to the $\sqrt{13}\,a \times \sqrt{13}\,a$ superlattice at a lower temperature.

Niobium and tantalum tellurides have been included in Table 25 for completeness. It needs to be pointed out however, that while Van Landuyt, Remaut & Amelinckx (1970) report a $\sqrt{19}\,a \times \sqrt{19}\,a$ superlattice for these compounds at room temperature after cooling heat pulsed crystals, Brown (1966) reports a somewhat different deformation superstructure. He measured a structure with only one deformation periodicity of $3\sqrt{3}\,a/2 = \sqrt{27}\,a/2$, in a direction perpendicular to $\underline{a}$. Thus $\underline{Q}$ is parallel to $\underline{a}^*$ as in all the other materials, but it exists in only one of the three symmetry equivalent orientations, so that a domain structure must result. His crystals appeared to have been prepared rather differently, so that this may explain the results, especially if one or other technique was susceptible to tellurium loss from the compound.

Values of Q for the smallest of the possible hexagonal superlattice are given in Table 26. Comparison with Table 25

Material	Coordination	Q/a* above T_d	Super-lattice	T_d	Reference
1T VSe_2	octa.	0.253	$4\underline{a} \times 4\underline{a}$	106 K	Present work
1T TaS_2	octa.	0.283	$\sqrt{13}a \times \sqrt{13}a$	190 K (340 K)	Present work & others.*
$4H_b$ TaS_2	octa. trig.pr.	0.265 0.31	$\sqrt{13}a \times \sqrt{13}a$ —	415 K —	Present work Tatlock
1T $TaSe_2$	octa.	0.278	$\sqrt{13}a \times \sqrt{13}a$	473 K	Wilson et al
1T $NbTe_2$	octa.	—	$\sqrt{19}a \times \sqrt{19}a$	—	Van Landuyt et al
1T $TaTe_2$	octa.	—	$\sqrt{19}a \times \sqrt{19}a$	—	Van Landuyt et al
2H NbS_2	trig.pr.	—	—	—	Present work
2H $NbSe_2$	trig.pr.	0.328	—	—	Present work
2H TaS_2	trig.pr.	—	$3\underline{a} \times 3\underline{a}$	75 K	Tidman et al
2H $TaSe_2$	trig.pr.	0.327	$3\underline{a} \times 3\underline{a}$	120 K	Present work

Table 25 Summary of deformation structural properties of the Group Va layer dichalcogenides.
* A similar investigation was carried out concurrently on 1T TaS_2 by Wilson et al (1975), Van Landuyt et al (1974). The three independent investigations have produced very similar results, with only slight differences in interpretation. The other workers used electron diffraction alone, and therefore only interpreted the reciprocal lattice geometry in detail.

Superlattice	Q/a*	Basis Vector
$\sqrt{3}a \times \sqrt{3}a$	0.577	$\underline{a} - \underline{b}$
$2a \times 2a$	0.50	$2\underline{a}$
$\sqrt{7}a \times \sqrt{7}a$	0.378	$2\underline{a} - \underline{b}$
$3a \times 3a$	0.333	$3\underline{a}$
$2\sqrt{3}a \times 2\sqrt{3}a$	0.289	$2\underline{a} - 2\underline{b}$
$\sqrt{13}a \times \sqrt{13}a$	0.277	$3\underline{a} - \underline{b}$
$4a \times 4a$	0.250	$4\underline{a}$
$\sqrt{19}a \times \sqrt{19}a$	0.229	$3\underline{a} - 2\underline{b}$
$\sqrt{21}a \times \sqrt{21}a$	0.218	$4\underline{a} - \underline{b}$

Table 26 Deformation wave vectors and cell basis vectors for hexagonal 2-D superlattices (cf Table 25 from experiment).

shows that those chosen by Group Va materials are in every case the superlattice with next smallest Q (octahedral) or next largest Q (trigonal prismatic co-ordination). The one exception to this would appear to be the mixed polytype, $4H_b$ TaS_2. It is conjectured that the presence of the trigonal prsimatic layers acts as an extra constraint here. Figure 109 has been drawn to illustrate the relative periodicities of the Group Va superlattices.

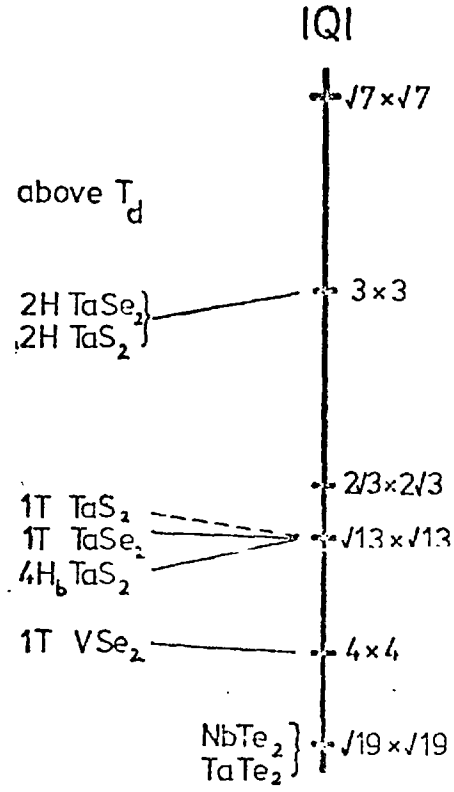


Figure 109

The two types of co-ordination are already showing marked differences in behaviour, with regard both to incommensurate and commensurate superstructures. However a further difference is found in the occurrence of the diffuse streaking: the characteristic streaks present in all the pure octahedral sulphides and selenides is completely absent in the materials with trigonal prismatic co-ordination. In the latter there is in fact some diffuse scatter, but along lines joining the

matrix reflexions, just below T_o. Deformation amplitudes are, moreover, generally larger in the octahedral materials than in the trigonal prismatic ones.

The greatest deformation amplitudes occur in the tantalum dichalcogenides; while the effect of changing the chalcogen from sulphur to selenium to tellurium is generally speaking to raise the temperatures at which the distortions occur, and to increase the amplitude.

The structural results include for many materials detailed information about the stacking of the deformation waves in successive layers. It seems likely that most incommensurate deformation waves stack rhombohedrally, especially in the octahedral materials. Transitions to commensurate superlattices are very often accompanied by a stacking change. The results suggest that, while the chalcogen layers are also distorted, this is probably a secondary effect due to the deformation of the metal layers.

The diffraction results from the study of the TaS_2(pyridine) intercalation complex have clearly shown that a stacking change of the host lattice accompanies the formation of the complex. In diffraction this complex exhibits a superlattice also, but closer study has shown this to be due to an ordering process (of the pyridine molecules) rather than to deformation of the host lattice. The periodicity of the superlattice is however rather unusual and an attempt to relate the mechanism responsible for this, to the one responsible for the deformation waves will be made in a later section (11.11.3). First however, the electronic origin of the deformation structures will be discussed in some detail.

11.2 Electronic Origin of the Structural Deformations

Conduction in the transition metal dichalcogenides, as in the metals themselves, is in the relatively narrow d-bands. Compared with the pure metals, the intermetallic distances are increased in the dichalcogenides: for instance (see Wilson & Yoffe 1969)—

Nb ... 2.86 Å ; Ta ... 2.86 Å

$NbSe_2$. 3.45 Å ; 1T TaS_2. 3.36 Å.

As a result of the reduced metal orbital overlap, the d-bands are likely to be even narrower than in the pure metal, so that the density of states at the Fermi level is high. For experimental determination of the density of states, using photoelectron spectroscopy, see Shepherd and Williams (1974). As a further consequence, carrier mobility tends to be low also in such materials.

The layer structure of these compounds leads to essentially 2-D conductivity, and the resistivity normal to the layers is an order of magnitude higher than parallel to the layers. All these conditions favour electronic instabilities and a tendency for localisation of electronic charge, so that the material becomes semiconducting with activated conduction.

There is therefore every reason to seek an electronic driving force to be responsible for the structural deformations. That this should be so is emphasised by the structural transitions occurring at the same temperatures as the electrical and magnetic anomalies. The link between the Fermi Surface and structure has been well documented for some time - see for example, Hume-Rothery (1931), Peierls (1955), Heine (1969). The theory has been successfully applied in a number of instances, an appropriate example being the long-period

superlattices in alloys (Ohshima & Watanabe (1973), Sato & Toth (1968)).

In the Group Va layer dichalcogenides the periodic superstructures must be coupled to charge-density waves in the conduction d-band (see section 3.4), and it is the presence of this coupled system which gives these compounds their very interesting properties. In discussing the charge-density wave system, it has been found particularly useful to consider the effects both in direct space (section 11.3) and in reciprocal (k-) space (11.4).

11.3 Metal Atom Clusters and Localisation of Charge

One of the most interesting results to come out of the detailed study of 1T TaS_2 is that the metal atoms group together in clusters in the distorted phases. The effect of clustering is to accentuate the periodic variations in bond length which result from purely sinusoidal deformations. Within the clusters, metal-metal distances are reduced slightly, improving orbital overlap, while in the 'gaps' between clusters there are very much increased distances (see for example Figure 92). Here the overlap of metal d-orbitals must be considerably reduced, so that there is reduced electrical conductivity in the layer as a result of the partial localisation of electronic charge in the vicinity of the clusters. This begins to explain some of the anomalous electrical measurements in 1T TaS_2, for Thompson, Gamble and Revelli (1971) report a large number of carriers yet with reduced conductivity. This is strongly suggestive of some scattering mechanism additional to normal free-carrier scattering.

With a sufficient increase in bond length between clusters, a situation could be reached in which the overlap became too

small for conductivity to occur at all, and a metal-insulator transition (Mott 1949) would have taken place. The increase in metal-metal distance (and hence the change in overlap) is closely related to $\underline{U}_Q$, the deformation amplitude. The change in metal-metal distance is in fact proportional to $\underline{U}_Q$.

In the distorted phases of $NbTe_2$ and $TaTe_2$ reported by Brown (1966) the deformation amplitude is so large that the average metal-metal distance of about 3.7 Å is decreased to 3.33 Å within the metal atom chains (equivalent to 1-D clusters) and increased to 4.51 Å between chains. At this separation the d-orbital overlap is so small that there is a finite energy gap and activated conduction in this direction through the layers (i.e. it is a 'semiconductor' in one direction, and a metal in a perpendicular direction). The two materials have been observed experimentally to exhibit 'semi-metallic' behaviour (Brixner, 1962, and Wilson & Yoffe, 1969).

A similar situation obtains in the semi-metallic distorted Group VIa compounds, β-$MoTe_2$ and WTe_2. In this case $\underline{Q}$ is larger than in the Group Va tellurides, $\frac{1}{2}\underline{a}^*$ compared with $\frac{1}{3}\underline{a}^*$. The octahedral symmetry of the undistorted material gives rise to a conduction band capable of accommodating 6 electrons. This is $\frac{1}{3}$-full with the 2 non-bonding electrons, so that the material should be metallic. There is a difference between these and the trigonal prismatic members of the Group, in which the lower symmetry environment of the metal atom splits off a full 2 electron sub-band from the other d-bands.

In WTe_2 the average metal-metal distance of about 3.55 Å is decreased to 2.90 Å in the chains, and increased to 4.37 Å between the chains. The percentage changes in bond-length are very similar to those in the Group Va tellurides. The largest deformations in any of the sulphides or selenides

occur in those of tantalum. The deformation amplitude $\underline{U}_Q$ is however rather smaller in these two compounds than in any of the four tellurides. The changes in metal-metal distance are consequently less severe: in $1T_3$ TaS_2 the average metal-metal distance of 3.36 Å is reduced to about 3.2 Å in the clusters, and increased to about 3.8 Å between clusters. While conductivity is necessarily reduced as a result of this, the effect is smaller than in the tellurides. The hexagonal symmetry of the deformation structure in the tantalum disulphide and diselenide means an approximately isotropic reduction in conductivity, which contrasts with the lower symmetry of the tellurides.

Compound	Coordination	M-M distance
2H NbS_2	trig.pr.	3.31
2H $NbSe_2$	trig.pr.	3.45
$NbTe_2$	octa.	3.7
2H TaS_2	trig.pr.	3.31
2H $TaSe_2$	trig.pr.	3.44
1T TaS_2	octa.	3.36
1T $TaSe_2$	octa.	3.48
$TaTe_2$	octa.	3.7

Table 27 Giving the average metal-metal distance within the layers of the Group Va dichalcogenides. For each metal the deformationamplitude increases towards the bottom of the table.

Allowing for the differences between the two types of co-ordination, Table 27 shows that the magnitude of the deformation amplitude (and hence the severity of the electronic/structural instability) increases with the average metal-metal distance within the layers. This is consistent with the general principles underlying metal-insulator transitions, as discussed earlier in this section, and in more detail by for instance Mott (1968) and Adler & Brooks (1967).

11.4 Deformation Waves and the Kohn Anomaly

The Kohn Anomaly was discussed in some detail in Chapter 3, as were also the conditions under which a strong Anomaly could be expected. The transition metal layer materials partially fulfil these conditions. Because they are almost 2-D conductors, their Fermi Surfaces have very little dispersion in the $\underline{c}^*$ direction, and consist of approximately cylindrical surfaces with curvature of an appreciable magnitude in one direction only. This description is only true in general terms, and the surfaces of some members of the group differ considerably in detail, but it does apply quite well for the majority of the materials.

Because of strong electron-phonon coupling under these circumstances, the anomaly in the electronic susceptibility is likely to be large for phonon wave vectors which span the Fermi Surface so that $\underline{q} = 2\underline{k}_f$. There is therefore an increased population of phonons in the modes which satisfy this condition, so that enhanced phonon scattering is observed in diffraction.

11.5 Fermi Surface Images in the Octahedral Materials

The diffuse scattering observed in the octahedral materials is therefore (section 11.4) interpreted as an image in the phonon spectrum of the parts of the Fermi Surface where the Kohn Anomaly is strong and gives rise to an enhanced population of the phonon modes. For 1T TaS_2, APW band structure calculations (Figure 9, Mattheiss 1973) have shown that the Fermi Surface in the ΓKM section of the Brillouin zone consists of surfaces enclosing occupied states, centred on the 2-fold axes at the point M. There is very little dispersion of the bands normal to the layers, and the ALH section closely resembles ΓKM.

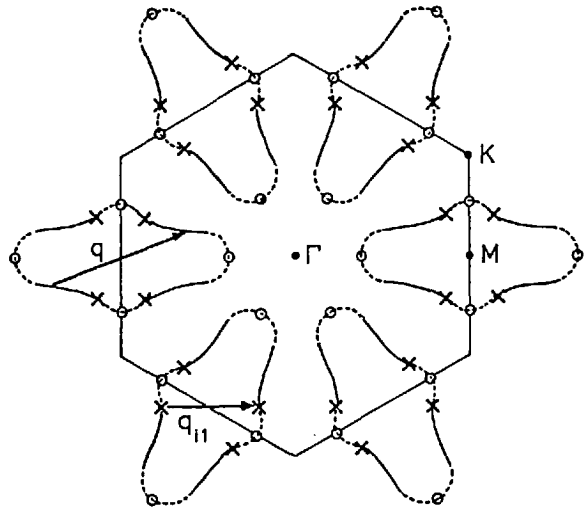


Figure 110 ΓKM section of 1T TaS_2 Fermi Surface as deduced from diffraction measurements (Chapter 7). The parts of the surface imaged in diffraction by $TA_{//}$ phonons (Figure 86) are drawn as solid lines. Parts drawn as broken lines recently confirmed by Yamada et al(1975). $\underline{q}_{i1}$ is the wave vector of the condensed mode in $1T_1$ TaS_2. Points (O) inferred from calculation (Mattheiss, 1973), and (X) from diffraction data (Chapter 6).

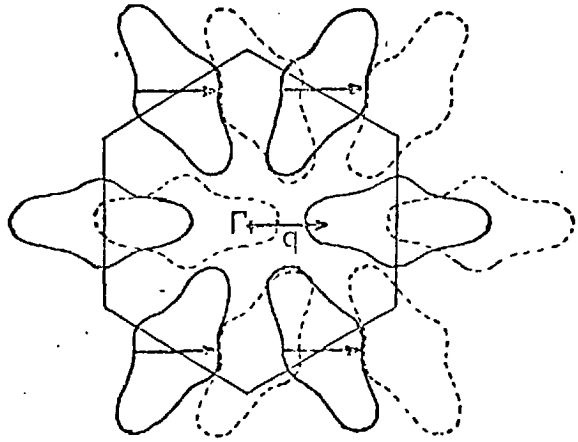


Figure 111 Showing how the Fermi Surface of Figure 110 is very well adapted for 'nesting' as a result of a perturbation of wave vector $\underline{q} = 2\underline{k}_f$.

It is possible to draw out the shape of the Fermi Surface segments from the diffraction data, since $\underline{k}_f = \frac{1}{2}\underline{q}$ (here $\underline{k}_f$ is the wave vector from the point M to the Surface). The result of the construction is presented in Figure 110 for 1T TaS_2. Wilson et al (1975) proposed a different shape for the segments, that they were elliptical in cross-section, although their derivation of this shape was not particularly clear. More recent* and accurate diffractometer measurements (Yamada, Tsang and Subba-Rao, 1975) have conclusively shown the double-bell cross-section to be the correct one (Figure 110). These workers have been able to observe practically the whole surface with their sensitive equipment, in contrast to the present studies which have enabled only the parts drawn with solid lines to be distinguished. These strongly visible regions of the Surface are in fact those with very low curvature, and consequently where theory predicts a large Kohn Anomaly (Fehlner and Loly, 1974). Figure 110 shows that the results are in good agreement with the points calculated for the high symmetry directions. The discrete reflexions in $1T_1$ TaS_2, corresponding to static distortions in modes in which the phonon frequency has been softened to zero, occur very close to, if not actually at points of inflexion of the Surface. There the curvature is zero, and theory predicts that the strongest effects should take place, for the Surface is one-dimensional in character.

More insight can be gained into why this particular direction for $\underline{Q}$ is chosen; $\underline{Q}$ is parallel to $\underline{a}^*$ and therefore parallel to ΓM rather than to ΓK in this and all the other materials studied in previous chapters. If the ability of the Fermi Surface segments to nest (fit closely together when

* The present work was published in part (Phil. Mag., 31, 255; 1975) simultaneously with the work of Wilson et al (1975), and the results of Yamada et al (1975) were published soon afterwards.

translated through $\underline{q} = 2\underline{k}_f$) is considered, it is found that four out of the six segments nest very effectively along a considerable length of the surface when the perturbation is parallel to M (Figure 111). A perturbation parallel to ΓK enables only two out of the six to nest. An elliptical Fermi Surface would clearly produce very much inferior nesting to that of the double-bell shaped Surface. Wilson et al (1975) tried to improve the nesting of their elliptical Fermi Surface by proposing a somewhat unphysical shape for the segments, with long perfectly flat sides and cylindrical ends. With this proviso, their interpretation is very similar however.

The shape of the Fermi Surface in the other octahedral materials studied can be deduced in a similar manner from the diffuse scattering observed. For 1T $TaSe_2$ (Wilson et al 1975) the Surface must be very similar in shape to the sulphide, although slightly smaller in area of cross-section (corresponding to the smaller wave vector $\underline{q}$). The Surface for $4H_b$ TaS_2 is necessarily many-sheeted, reflecting the four-layer stack. Only those sheets corresponding to the octahedral layers can be considered in this section. Diffraction data suggests that when these segments are drawn out, they must have a smaller width, but otherwise the same general shape as Surface of 1T TaS_2 (Figure 110). The diffraction image suggests that as well as being narrower still, the 1T VSe_2 Surface also differs in shape in a small but important way. The segments apparently do not have changes of sign of the curvature, and are therefore closer to being elliptical (Figure 112). This curvature difference would be consistent with vanadium selenide showing a weaker Kohn Anomaly than the other octahedral materials. Furthermore, it would be expected that as the Fermi Surface shrinks

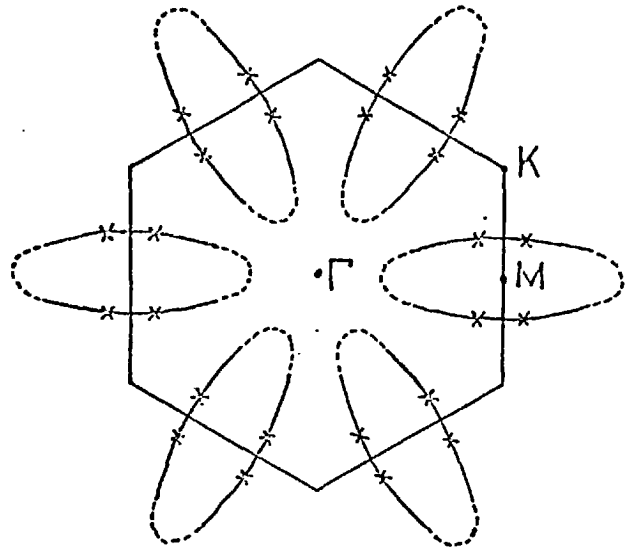


Figure 112 ΓKM section of 1T VSe_2 Fermi Surface as deduced from electron diffraction (Chapter 8). The parts of the surface directly imaged are drawn solid. Points (X) are from the diffraction data for the condensed mode.

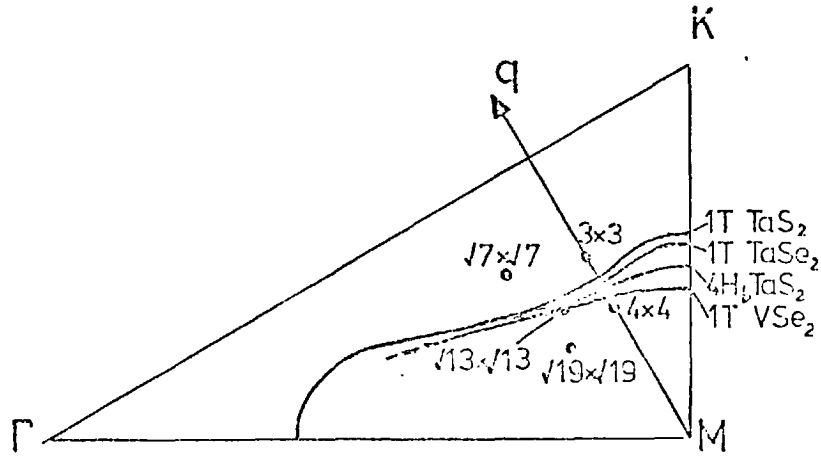


Figure 113 Hexant of Brillouin zone summarising the geometry of the Fermi Surfaces of the octahedral materials, as deduced from diffraction. Superlattice periodicities have also been marked.

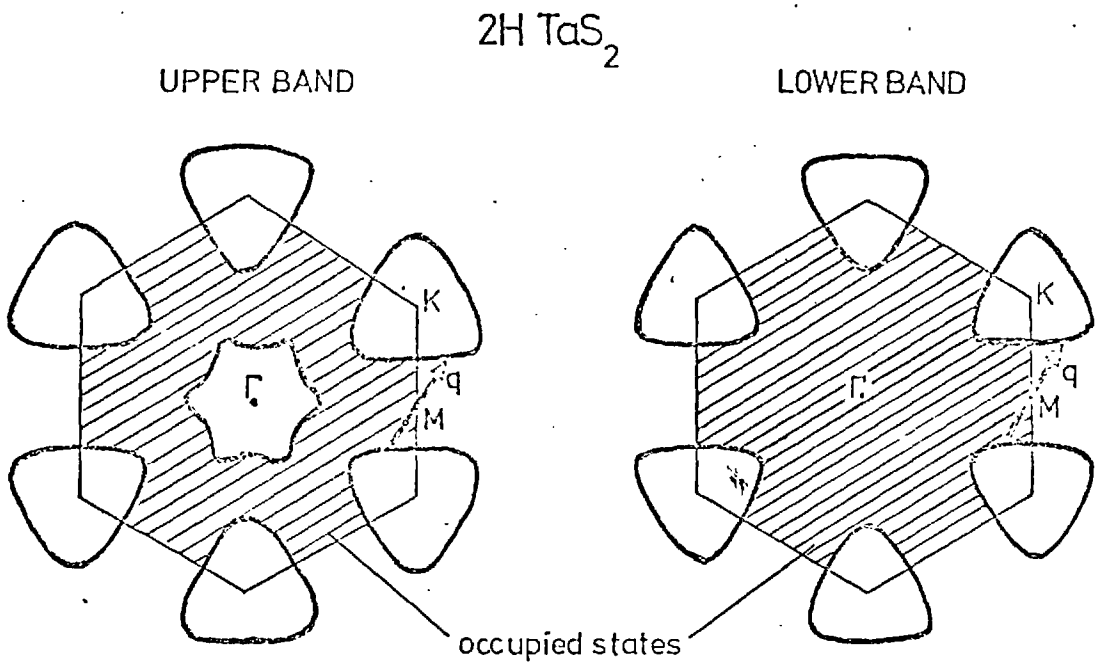


Figure 114 ΓKM section of the upper and lower band Fermi Surfaces for 2H TaS_2, as deduced from band structure calculation (Figure 9, Mattheiss, 1973).

back towards the M point it would progressively assume a shape closer to the ellipse. It must however be pointed out, following this discussion of curvature changes on the Surface, that the sign changes and the points of inflexion are observed in the distorted forms of the tantalum dichalcogenides. It is not clear whether these are present in the undistorted forms above T_o, or whether they arise as a direct result of the deformations. The proposed shapes for the Fermi Surface segments are summarised in Figure 113.

11.6 Fermi Surface Images in the Trigonal Prismatic Materials

APW band structure calculations (Mattheiss, 1973) have predicted a Fermi Surface for the trigonal prismatic layer dichalcogenides, which differ in a number of important aspects from those of the 1T compounds. First, the 2-layer repeat in the 2H materials must mean a two-sheeted Fermi Surface. The upper and lower bands (Figure 9) produce slightly different sized segments of Fermi Surface due to layer-layer interactions, in the ΓKM section. The Surface for 2H TaS_2 is shown in Figure 114, constructed from the APW data, and it is practically the same for 2H $TaSe_2$, NbS_2, $NbSe_2$, although with significant differences in spanning vector. Secondly and very importantly, it can be seen that the segments enclose unoccupied states, and that they are centred either at Γ (6-fold symmetry) or at K (3-fold symmetry). The exact shape of the segments centred at Γ is very difficult to determine accurately from the calculations.

Thirdly, there are no large regions of almost planar surface, unlike the segments of the octahedral compounds) and this may well explain the absence of the characteristic diffuse scattering in the 2H compounds. A proposal for the spanning wave vector (satisfying $\underline{q} = 2\underline{k}_f$) in Figure 114, which would agree well with

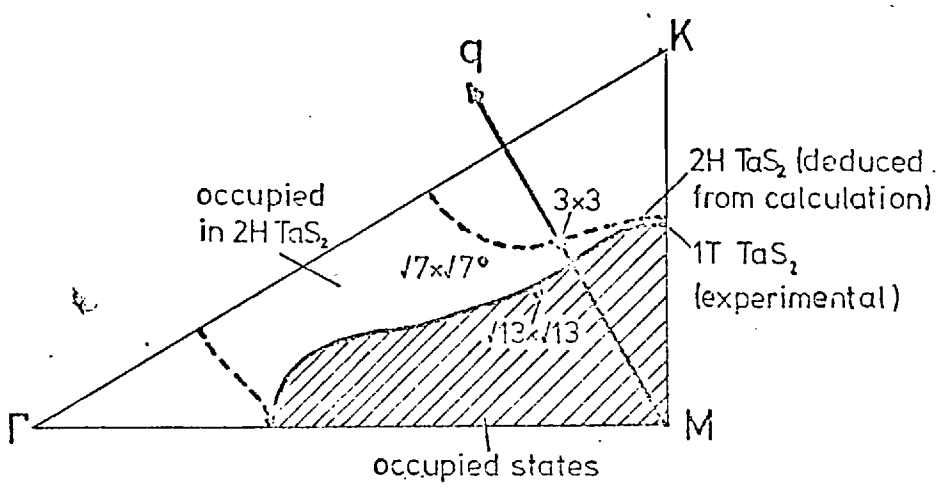


Figure 115 Comparing the Surfaces of octahedral and trigonal prismatic polytypes of TaS_2. Possible superlattice periodicities have been included.

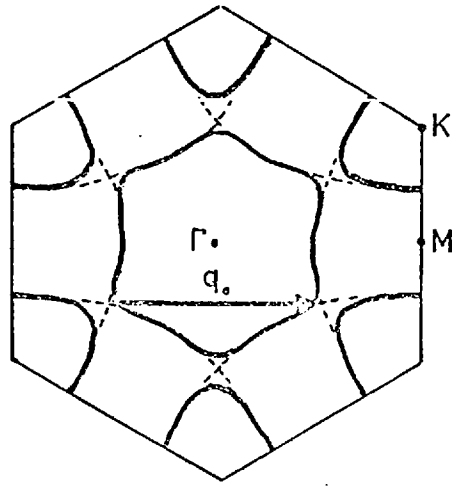


Figure 116 Alternative construction for deformation wave vector in 2H $NbSe_2$ (from Rice & Scott, 1975).

the measured deformation periodicity, is included, although other possibilities for $\underline{q}$ are certainly not ruled out at this stage. This wave vector does in fact span similar parts of the Surface to those in the octahedral compounds, but with the one apparent difference that the Surface away towards the ΓK line, rather than towards ΓM (Figure 115).

This form of Fermi Surface appears less well suited to nesting, and this together with the fact that different sheets of the Surface now compete, may explain why the distortion amplitudes are on the whole smaller in the trigonal prismatic polytypes. In fact an alternate mechanism for the stabilisation of the charge-density wave has been proposed (Rice and Scott, 1975) on the assumption of a 'saddle point' in the Surface at $\pm \underline{k}_f$. The vector they propose connects saddle points rather as shown in Figure 116 gives a divergent contribution to the electronic susceptibility $\chi(\underline{q})$ at $\underline{q} = \underline{q}_o$, which is close to $\frac{1}{2}\underline{a}^*$. This is the vector which Hughes and Liang (1975) and Wilson et al (1975) suggest may give rise to the $2\underline{a}$ x $2\underline{a}$ superlattice observed in some 2H material.

At present the lack of precision in the determination of the Fermi Surface geometry in the trigonal prismatic polytypes does not permit a quantitative choice between the vectors $\underline{q}_o = \frac{1}{2}\underline{a}^*$ and $\underline{q}_o = \frac{1}{3}\underline{a}^*$. It is interesting that Rice and Scott's model does not destroy large areas of Surface, although nesting would not do so either since it is very limited in these materials; and certainly this is consistent with improved metallic properties below T_o in the 2H polytypes.

11.7 Inelastic Neutron Scattering Results

Inelastic neutron scattering experiments are in progress at a number of laboratories. Even using a high-flux reactor,

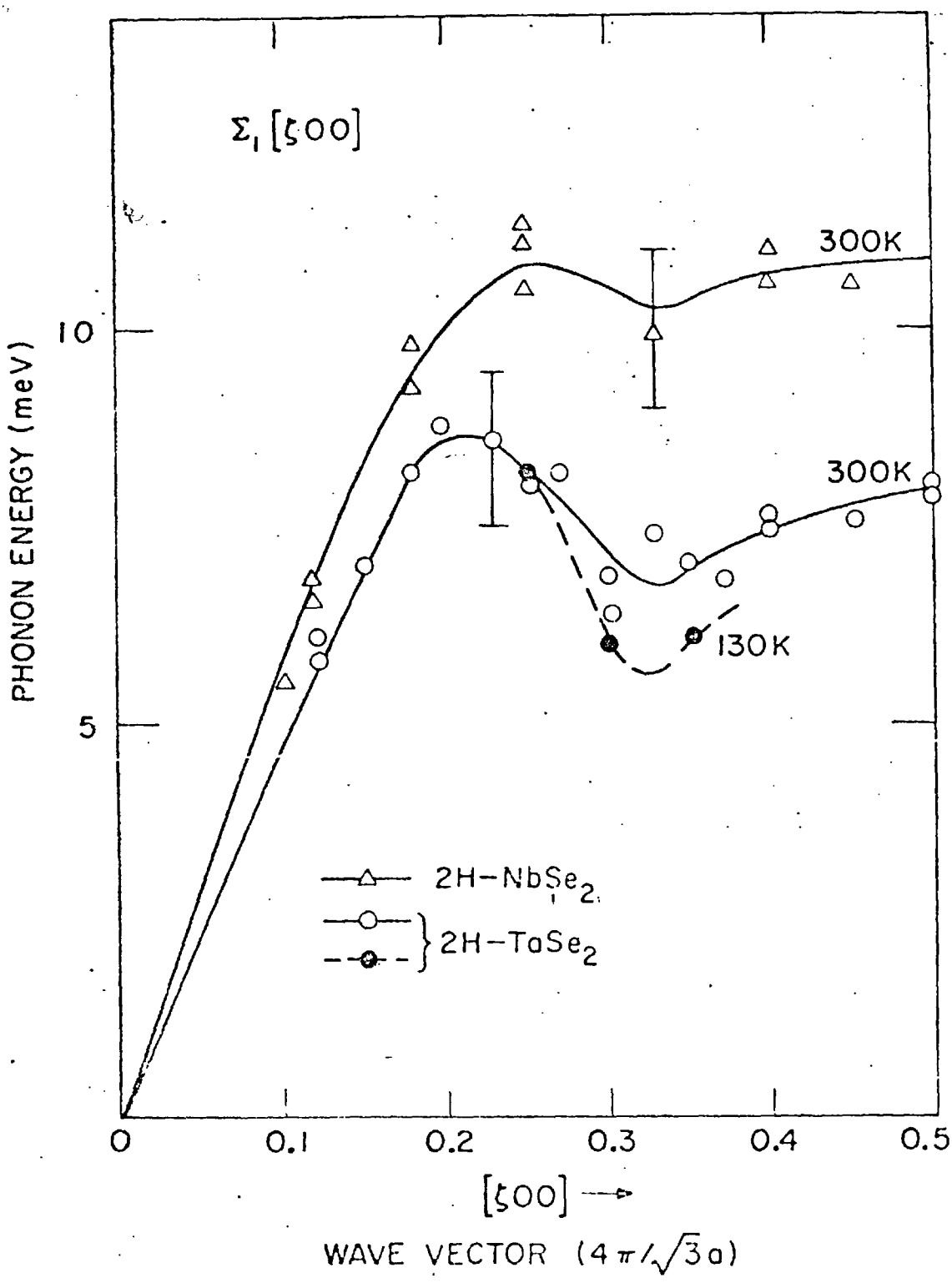


Figure 117 Direct observation of the Kohn Anomaly in the phonon spectra from trigonal prismatic layer materials (Moncton et al, 1975).

the count rate with these materials is very low, because it is extremely difficult to grow crystals which even approach the ideal large size required for such experiments. Some of the first results are reproduced in Figure 117 (Moncton, Axe and Di Salvo, 1975). These show very clearly the existence of the Kohn Anomaly in the LA branch of the phonon spectrum in two of the trigonal prismatic compunds. The results also show how the Anomaly progressively becomesstronger as the temperature is lowered in 2H $TaSe_2$. These first results are very significant, for they provide the best confirmation possible for the preceding interpretation of the periodic structural distortions in terms of an enhanced Kohn Anomaly.

In the temperature range considered by Moncton et al. (1975), the phonon mode has not been softened completely to zero, so that at 130 K the mode is still not static. It will prove interesting indeed to discover,as a result of further experiments,whether the mode becomes static at lower temperatures, i.e. when the deformation waves become commensurate with the 2H $TaSe_2$ lattice.

X-ray and electron diffraction suggest, from the sharpness of the reflexions, that the deformations are static in 1T TaS_2. It will therefore be very interesting to see whether this is confirmed by inelastic neutron scattering, and also to find out whether the modes 'unlock' from the lattice and propagate through the crystal at higher temperatures. The fact that the modes appear more likely to be static for the incommensurate distortions in the octahedral materials and dynamic in the trigonal prismatic serves to underline once again the differences between the two co-ordinations.

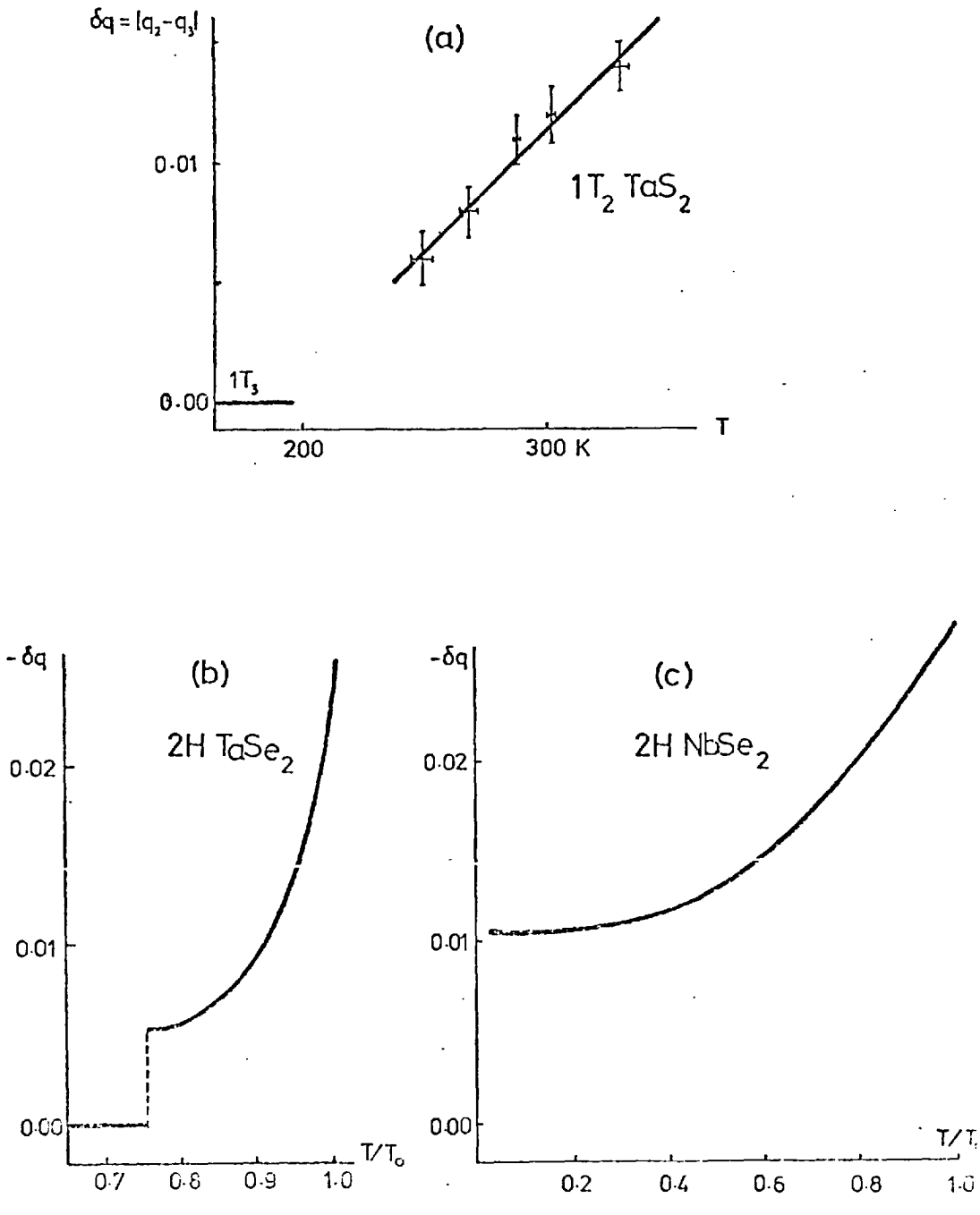


Figure 118 Variation in magnitude of incommensurate deformation wave vectors in $1T_2$ TaS_2, 2H $TaSe_2$ and 2H $NbSe_2$. (b) and (c) are from Moncton et al.

11.8 Temperature Dependence of Charge-Density Wave Vector

It was pointed out in an earlier section (11.1) that the 1T polytypes tend to transform to a commensurate superlattice phase with smaller wave vector, while the 2H polytypes tend to transform to a superlattice with a slightly larger wave vector, as the temperature of the crystal is reduced. This distinction between the two coordinations also holds for variations of wave vector when the temperature is lowered for the incommensurate phase alone.

In $1T_2$ TaS_2, $\underline{Q}$ both decreases in magnitude and rotates towards a $\sqrt{13}$ a coincidence, as described in section 6.6. The value of $\delta Q = |\underline{Q}_2 - \underline{Q}_3|$ decreases smoothly with temperature in the range of the measurements - Figure 118 (a). It was unfortunately not possible to determine experimentally whether the transition to a commensurate wave vector was smooth or discontinuous. Heat capacity and electrical measurements (Thompson, Gamble and Revelli, 1971) imply a discontinuity. This would be in keeping with the results for 2H $TaSe_2$, where Q increases as the temperature is lowered and where there is finite discontinuity just before the transition takes place (Moncton et al 1975, Figure 118 (b)). $\delta\underline{Q}$ behaves rather similarly in 2H $NbSe_2$ (Figure 118 (c)) but the charge-density wave remains incommensurate with the lattice down to 5K, the limit of their experiments.

These changes in $\underline{Q}$ must mean that in the octahedrally coordinated materials the Fermi Surface is shrinking back towards the M point on the zone boundary (Figure 112), and in the trigonal prismatic materials towards the K point, as the temperature is lowered. This could just be a result of the Surfaces changing shape, but a far more attractive explanation

is that changes in materials with both coordinations would arise from a variation in the number of occupied states, and hence also of the number of carriers, with temperature. This is because the segments enclose occupied states in the 1T polytypes and unoccupied states in the 2H polytypes. Recent photoemission studies (Shepherd and Williams, 1974) are consistent with a small overlap between the d-like conduction band and the p-like valence band in the Group Va materials, so that the density of occupied states could exhibit the required temperature variation as a result of changes in d-p overlap.

11.9 Transitions to Commensurate Superstructures

Many of the layer dichalcogenides in Group Va undergo transitions from incommensurate to commensurate superstructures. It is interesting to try and relate these transitions to the electronic properties of thr materials, and perhaps to comment on why they occur.

The charge maxima in the 2-D charge-density wave occur at the corners of the deformation cell (0,0) for sinusoidal modulation with phase π. Charge minima therefore occur at $(\frac{1}{3},\frac{2}{3})$ and $(\frac{2}{3},\frac{1}{3})$, as shown in Figure 119 (a). The maximum surplus of charge is twice as great as the maximum deficit, but the regions of charge surplus are much smaller. The result of metal atom clustering is to produce a charge distribution rather as illustrated by Figure 119 (b). In this case the charge density is constant within the regions of increased charge: the increase being relatively small. However there are deep charge minima between the clusters. Minima again are found at $(\frac{1}{3},\frac{2}{3})$ and $(\frac{2}{3},\frac{1}{3})$. The experimental data gained from the study of 1T TaS_2 showed that the phases of the charge-density

wave are such as to give a charge distribution very like that shown in Figure 119. There was also strong evidence for substantial clustering, so that Figure 119 (b) is probably very close to the true situation.

When a transition to a commensurate superstructure takes place, the pattern of the clusters and of the changed bond-lengths becomes regular and periodic in a true sense, because atoms must occupy the same sites within each deformation supercell. Thus charge-density maxima can always be associated with the same sites in the matrix lattice, e.g. a metal atom site, instead of being sometimes located close to metal atoms and sometimes close to anions as in the incommensurate case. Electrostatically therefore the transition to a commensurate superstructure must be favoured, so that the CDW amplitude would be expected to increase at T_d. If regular clustering (i.e. with metal atoms equally spaced within each cluster) occurs in the incommensurate case, then the charge minima, which may be very deep, must sometimes be located on metal sites. This is unlikely to be favoured electrostatically, and argues against regular clustering of metal atoms above T_d, and for a situation intermediate between this, and that illustrated in Figure 119 (a).

The ideal 2-D cluster of metal atoms in one of the layer materials has hexagonal symmetry, and accounts for all the atoms in the supercell. Clusters which satisfy these two conditions contains $6n + 1$ atoms, where n is a positive integer. The first three of these ($n = 1, 2, 3$) correspond to the $\sqrt{7} \times \sqrt{7}$, $\sqrt{13} \times \sqrt{13}$ and $\sqrt{19} \times \sqrt{19}$ superlattices. Any one of these is very effective therefore at localising charge within a cluster. Furthermore, with the cluster centred on

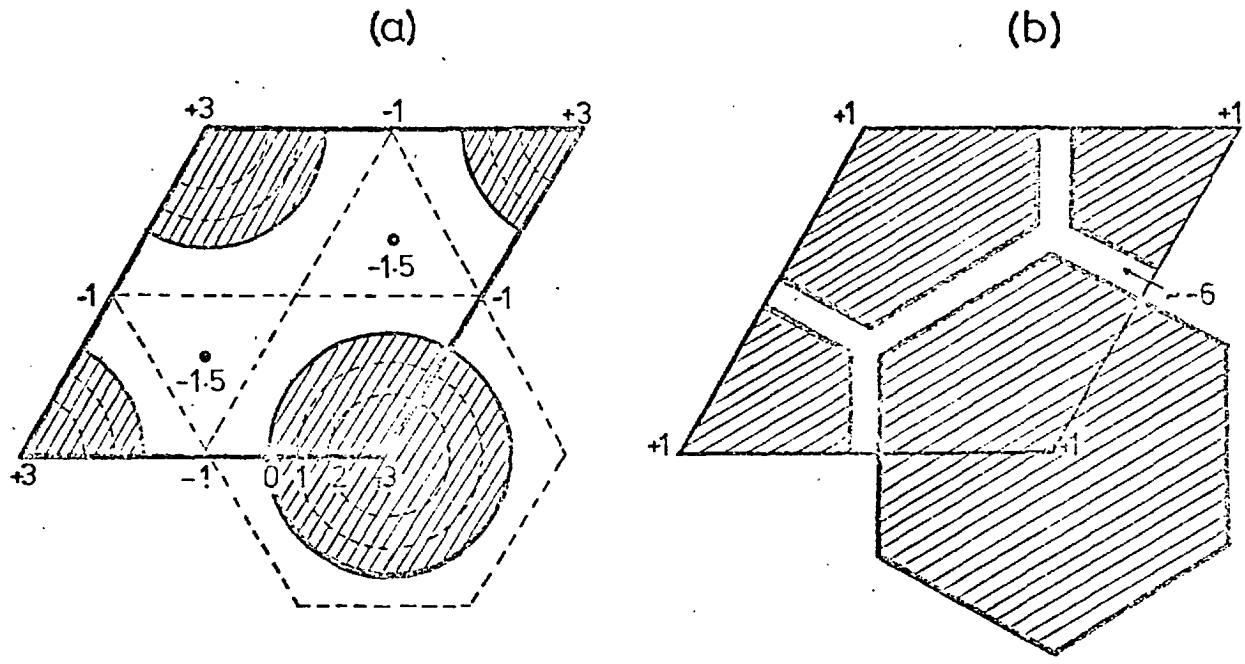


Figure 119 (a) Charge-density distribution in deformation cell resulting from sinusoidal CDWs, and (b) resulting from metal atom clustering.

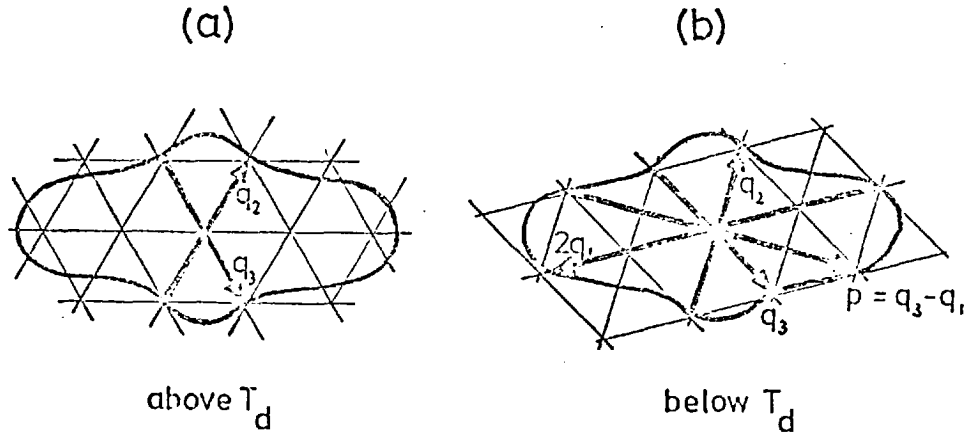


Figure 120 (a) In $1T_1$ TaS_2 only the fundamental wave vectors span the Fermi Surface; (b) in $1T_2$ and $1T_3$ apparently the higher harmonics of the distortion <u>also</u> span the Surface. This argues for the stability of the superstructures in these two phases.

a metal atom, the deep charge minima are found between metal atoms, adjacent to the anions. This reasoning is certainly consistent with the experimentally observed stability of the $\sqrt{13}a \times \sqrt{13}a$ superlattice, even after doping the host material (section 11.11.1), and may partly explain why it is adopted by so many of the compounds.

11.9.1 Materials with Octahedral Co-ordination

The Fermi Surfaces for the octahedral materials have the $\sqrt{13}a \times \sqrt{13}a$ superlattice wave vector lying close to them all (Figure 112). This vector is especially close to the Surfaces of $4H_b$ TaS_2 and 1T $TaSe_2$, so that by the time the temperature has been lowered to T_d, the magnitude of $\underline{q}$ has decreased sufficiently to rotate and switch to the commensurate periodicity directly. The case of 1T TaS_2 is sufficiently special to be taken separately in Section 11.9.4.

The switch to the ideal cluster formation possible with the $\sqrt{13}a \times \sqrt{13}a$ superlattice has the predicted effect on the electrical conductivity. Measurements (Figure 12) show almost an order of magnitude increase in the resistivity of both 1T TaS_2 and 1T $TaSe_2$ at T_d. The effect in $4H_b$ TaS_2 is less dramatic because of good conduction through the alternate trigonal prismatic layers, which are undistorted at this temperature. It is also possible to explain this increase in resistivity (Lee, Rice and Anderson, 1974) by the loss of translational invariance of the current-carrying CDW/deformation wave system, as it becomes pinned to the lattice at T_d.

Figure 112 shows that the Fermi Surface of 1T VSe_2 lies within the $\sqrt{13}a \times \sqrt{13}a$ wave vectors, so that a decrease in its cross-section with a lowering of temperature takes the Surface further away from it. A $4a \times 4a$ coincidence lies very close to the VSe_2 Surface, and the deformation wave vector is able

to contract onto this without changing direction. The $\sqrt{19}\,a \times \sqrt{19}\,a$ superlattice wave vector apparently lies too far inside the Surface for this superstructure to be adopted.

11.9.2 Energy Gaps at the Fermi Level

As it was explained in Section 3.5, the presence of deformation waves in the lattice with periodicities which span the Fermi Surface, opens up energy gaps at the spanning points on the Surface. The magnitude of the gap and its extent over the Surface depend on three factors: the distortion amplitude, the narrowness of the conduction band, and the geometry of the Surface. It is helpful to make a brief digression and consider the recently discovered 1-D conductors:

X-ray diffuse scattering studies (Comes, Lambert, Launois & Zeller, 1973; Comes, Lambert & Zeller, 1973) of the 1-D conductor KCP (i.e. $K_2Pt(CN)_4Br_{0.3}\cdot 3H_2O$) show the existence of a linear deformation wave at room temperature. Neutron scattering experiments (Renker et al, 1974) suggest that this distortion involves both a dynamic Kohn Anomaly and a static Peierls Distortion. The variation in electrical resistivity which accompanies the structural changes in KCP, from $10^{-2}\,\Omega$cm at room temperature to $10^{12}\,\Omega$ cm at 20 K (Kuse & Zeller 1971) agrees well with a transition from a metallic to a Peierls insulating state.

Whereas a gap at the Fermi Surface in the 1-D material (which constitute two points in the 1-D Brillouin zone) separates all occupied states from unoccupied, this is not necessarily true for a 2-D or 3-D material. The gap could in general be expected to extend around part only of the Surface, unless U_Q were very large, the bands very narrow and the Fermi Surface very flat. It would therefore be expected that conduction in the

distorted layer materials should be more complex, involving a certain proportion of activated conduction, according to the extent of the energy gaps. That such a situation is realistic is borne out by close study of the slopes of the resistivity curves of Figure 12, for the two compounds, 1T TaS_2 and 1T $TaSe_2$.

The increases in resistivity on passing through T_d — $10^{-3}\Omega$ cm in $1T_2$ to about 10^{-2} in $1T_3$ TaS_2, and a slightly smaller change in the selenide—are far less than in the 1-D materials, quoted above, and are inclined to suggest changes rather in the magnitude and extent of the energy gap.

The disappearance of the diffuse scattering from points all round the Fermi Surface which takes place at T_d, also implies that there is a gap in the energy over a significantly large part of the Surface in both $1T_2$ and $1T_3$.

Figure 120 (a) shows that in the incommensurate phase above T_d, only the fundamental $\underline{q} = 2\underline{k}_f$ wave vector spans the Fermi Surface. However, in the $\sqrt{13}$ a x $\sqrt{13}$ a commensurate phase - Figure 120 (b) - not only do the fundamental wave vectors span the Surface, but also some of the higher harmonics, such as $2\underline{q}_1$ and $\underline{p}_2 = \underline{q}_3 - \underline{q}_1$. It is of course not possible with present data to specify whether the vectors actually span the Surface or just lie extremely close to it. This same situation holds also in $1T_2$ TaS_2, although it is an incommensurate phase, for the differences in wave vector between this and $1T_3$ are quite small.

The discovery that certain higher harmonics also span the Fermi Surface is very thought-provoking, for it is these very harmonics which were shown to be present experimentally in 1T TaS_2 (sections 7.2.5, 7.2.6), and which lead to the clustering of metal atoms. This would therefore argue that clustering, or at least the higher harmonics necessary for clustering, of

the tantalum atoms is also favourable from the point of view of the Fermi Surface. Clearly a gap must exist at the Fermi level in the vicinity of each of these spanning wave vectors, so that the combination of them all is likely to open up a gap around a large proportion if not the whole of the Fermi Surface. This is completely consistent with the fact that these vectors span parts of the Surface which are almost flat, and where the Kohn Anomaly is likely to be enhanced. These are the parts of the Surface which are visible in the high temperature distorted phases through the diffuse scattering. A gap opened up along these areas of the Surface at the transition temperature, would very effectively explain the absence of the diffuse scattering. The phonons in these softened modes above T_d would tend to condense into the static modes at $\underline{q}_i$, $2\underline{q}_i$, $\underline{p}_i$.

Finally in this section it is noted that the above argument does not hold for $4\underline{a} \times 4\underline{a}$ or $3\underline{a} \times 3\underline{a}$ superlattices, since higher harmonic wave vectors do not span the Surface. This again is consistent with the relative difficulty of cluster formation in these two superstructures, and also serves once again to emphasise the stability of the $\sqrt{13}\,a \times \sqrt{13}\,a$ superlattice.

11.9.3 Materials with Trigonal Prismatic Coordination

In these compounds, the magnitude of the deformation wave vector increases with falling temperature. This means that the Fermi Surface moves further away from both the $\sqrt{13}\,a \times \sqrt{13}\,a$ and $\sqrt{7}\,a \times \sqrt{7}\,a$ coincidence vectors, both of which lie outside the closed surface (figure 115). The charge-density waves are nevertheless able to lock on to a coincidence superlattice which does lie within the Surface. This is the $3a \times 3a$ superlattice adopted below T_d by both 2H TaS_2 and 2H $TaSe_2$.

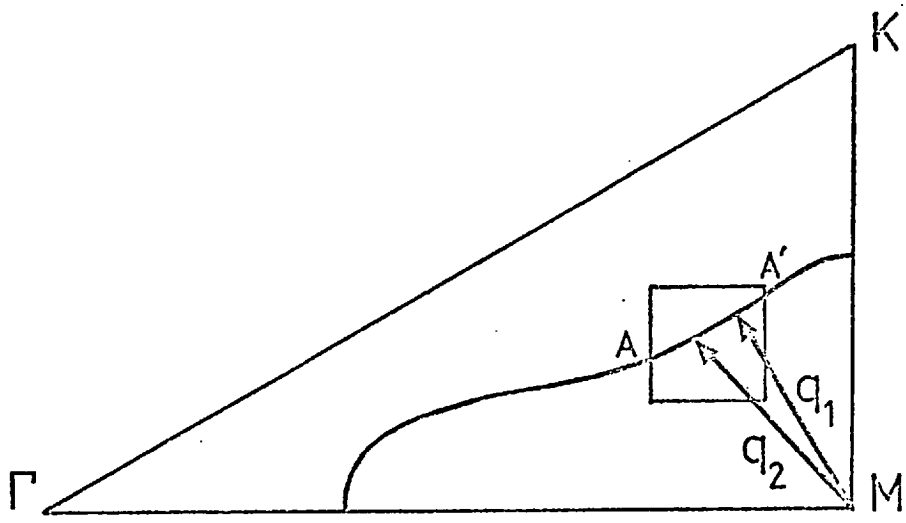
The $3\underline{a}$ x $3\underline{a}$ superlattice is however far from ideal electrostatically, for both charge minima are located at metal atoms when the charge maximum is located at a metal atoms site. Above T_d, because the superstructure is incommensurate, it is possible to produce clusters rather as in $1T_1$ TaS_2 (Figure 91). Below T_d the situation changes because clusters with hexagonal symmetry cannot be produced with the commensurate periodicity. Higher harmonics of the deformation cell have been observed experimentally in 2H $TaSe_2$ above T_d (Moncton, Axe and DiSalvo, 1975). These, by analogy with 1T TaS_2, suggest the possibility of cluster formation. In view of the above, it will be very interesting to discover from the experiments those authors have in progress what happens to the higher harmonics below T_d.

The significant difference in ease of cluster formation between the $3\underline{a}$ x $3\underline{a}$ and the $\sqrt{13}$a x $\sqrt{13}$a supercells means that the tendency to localise charge in the former is reduced as the temperature is lowered through T_d, while it is increased in the latter. This could well help to explain why the resistivity of 2H $TaSe_2$ and 2H TaS_2 decreases below T_d, in contrast to the increase in the octahedral materials, Figure 12.

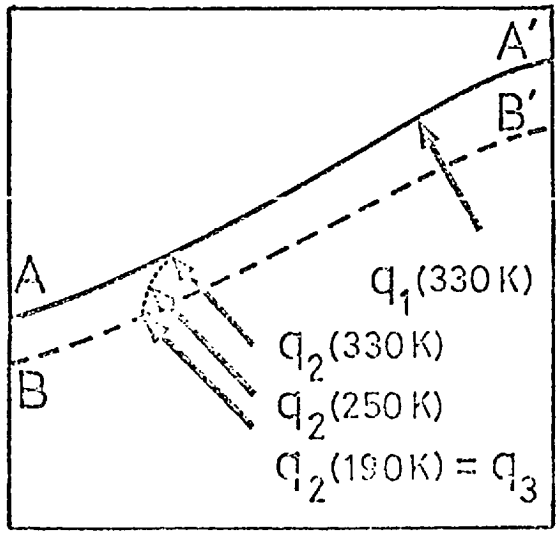
Although Q increases as the temperature is lowered in 2H $NbSe_2$, a commensurate superlattice is not adopted (Figure 118 c). It is tempting to link this with the fact that $NbSe_2$ superconducts at a relatively high temperature, because commensurate pinning of the coupled electron-phonon mode is absent (section 3.7).

11.9.4 1T Tantalum Disulphide

What makes this compound apparently unique is the transition from one incommensurate state to a second incommensurate state



(a)



(b)

Figure 121 Part of one segment of 1T TaS_2 Fermi Surface at 330 K (a). In (b) more detail is given of the variation of the deformation wave vector in the three distorted phases.

at a temperature above T_d. In particular this additional transformation distinguishes it from the selenide, which transforms directly to the $\sqrt{13}a \times \sqrt{13}a$ superlattice. The energetic favouring of the intermediate $1T_2$ phase, must derive from the material's band structure: it is difficult to conceive of an alternative explanation.

Measurements of the wave vector in the highest temperature distorted phases show that the substitution of sulphur for selenium in 1T $TaSe_2$ increases the breadth of the Fermi Surface segments in the ΓKM section. It is proposed that because of this, the $\sqrt{13}a \times \sqrt{13}a$ wave vector must lie too far inside the Surface for a direct transition to occur in the sulphide. Figure 118 gives a similar value for δq in $1T_2$ TaS_2 as in 2H $TaSe_2$ above its T_d, showing that it is consistent with this other material to adopt an incommensurate superstructure under these circumstances. For other reasons (electrostatic, strain energies increasing with rising deformation amplitude) the material has to abandon the superstructure of the $1T_1$ phase, and must adopt a second incommensurate structure, but one with $\underline{q}_2$ spanning the Fermi Surface as close as possible to $\underline{q}_3$. As the Surface shrinks with lowering temperature, $\underline{q}_2$ is able to approach progressively closer to $\underline{q}_3$, until finally δq is sufficiently small for the transition to take place to $1T_3$ TaS_2, Figure 121.

Since $\underline{U}_q$ remains in the same direction during the $1T_1$ - $1T_2$ transition so that the change in wave vector implies a change in the correlation between displacements on individual atoms, rather than a change in their direction, it is not difficult to understand why the transition has little hysteresis (Figure 11). There is far more hysteresis in the $1T_2$ - $1T_3$ transition, which involves quite radical changes: a locking of the CDW periodicity on to the lattice, and the changes in the stacking sequence of

the deformations. Finally it is noted from Section 7.5 that the measured value of $\underline{U}_q$ increases by about 30 % from $1T_1$ to $1T_2$ TaS_2: it is tempting to compare this with a very similar increase in resistivity at the transition (Figure 11).

11.10 Displacements of Anions & Stacking of Charge-Density Waves

The results presented for $1T_2$ TaS_2 in section 7.4 suggested that the sulphur atoms are drawn in towards the metal layers where the Ta - Ta separation increases, and pushed away as the Ta atoms come closer together in the clusters. This model was deduced from the phase of the deformations waves on the chalcogen sublattice, relative to the metal sublattice. This model compares very favourably with the structure proposed for the distorted tellurides of Groups Va and VIa (Figure 7, Brown 1966). The charge-density wave model implies that the deformation of the chalcogen sublattice is a secondary effect, arising because of the need to minimise strain energy following the formation of the deformation waves in the metal layers.

Because the distortions vary the thickness of layers, successive layers have to be translated in order to minimise the volume of the crystal. In fact the thickness variations match well when the translation vector is from the α site to the β site in the deformation cell. This therefore provides a structural reason for the rhombohedral packing in the 1T polytypes above T_d. The trigonal prismatic layers separate the distorted octahedral layers in $4H_b$ TaS_2 so that this argument no longer holds, and the deformations stack without the rhombohedral sequence. There may be a link between this and the experimental observation of the shorter coherence length (section 8.2) of the deformations in this material above T_d. The distortions in the trigonal prismatic materials must stack

with little or no phase correlation between adjacent layers, since the modes still propagate through the lattice, certainly above T_d.

Although periodic variations in layer thickness are also expected for the octahedral commensurate phases below T_d, rhombohedral stacking of the deformation waves would prevent the charge density maxima from being localised at ideal metal atom sites in every layer. When the α site of the $\sqrt{13}\,a \times \sqrt{13}\,a$ supercell (or the $4\underline{a} \times 4\underline{a}$ supercell) is located at a Ta atom, the β and γ sites correspond to interstitial positions adjacent to sulphur atoms. Adjacent layers can only be identical, with charge maxima at tantalum sites, if there is a stacking change in the coupled CDW/periodic deformation system.

There are 13 tantalum atoms in the 2-D layer supercell, each in principle able to act as the origin of the CDW. With hexagonal symmetry however, the number of different sites is reduced to <u>three</u>. The corresponding stacking vectors are $\underline{c}$ (giving $\alpha\alpha\alpha$ stacking), $\underline{c} + \underline{a}$, and $\underline{c} + 2\underline{a}$. The last two both give triclinic unit supercells and 13 layer stacking sequences. Diffraction evidence tends to favour the cell with the stacking vector $\underline{c} + \underline{a}$ for $1T_3$ TaS_2. Considerable stacking disorder and twinning (with stacking vector $\underline{c} - \underline{a}$) would be expected, and experimental evidence supports this.

As a consequence of the change from minimum volume stacking, a slight increase in the crystal c-axis might be expected also, because of the variations in layer thickness. A discontinuous <u>increase</u> of 0.02 Å in c is indeed detected at the $1T_2$ - $1T_3$ transition (Thompson, Gamble & Revelli, 1971).

11.11 <u>Supporting Evidence from Doping & Intercalation Experiments</u>

If the coupled CDW/periodic deformation wave system does indeed arise from a Fermi Surface instability, as it has been proposed, then the observed effects should be sensitive to

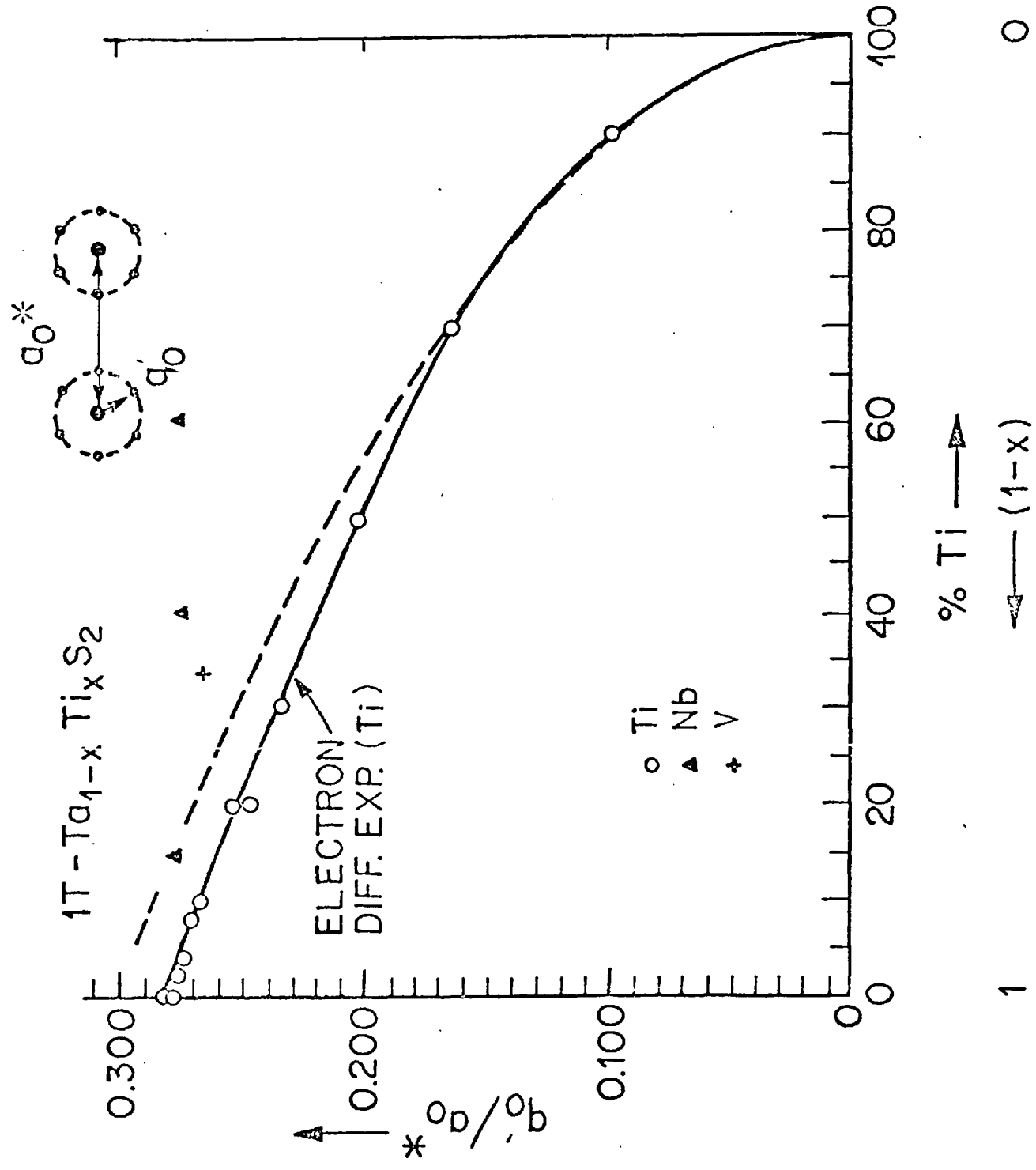


Figure 122 Variation of Fermi Surface-spanning wave vector with varying concentrations of substituent metal (Wilson et al 1975). Note that q only varies when the dopant is from another Group.

changes in the Surface as the electron concentration is varied. The variation with temperature has already been discussed effectively in Section 11.8. The electron concentration can also be changed by doping with a metal from another Group (i.e. to form a substitutional alloy), or by intercalation with an electron donor or acceptor. If such experiments give the predicted behaviour, then they constitute very strong supporting evidence for the model.

11.11.1 Doping Experiments

In a very convincing series of experiments, in which 1T TaS_2 and 1T $TaSe_2$ were doped with increasing proportions of titanium (Group IVa), Wilson et al (1975) have shown that the CDW vector above T_d shrinks as x, the concentration of the substituent, increases. This is directly related to a decrease in the average electron/atom ratio because Ti has one less electron per atom than Ta. Negligible local distortion of the cation sites occurs because all the Group IVa and Va ions are of similar radius. These authors also show (Figure 122) that approximately, $q \propto (e/a)^{\frac{1}{2}}$. This result is completely consistent with the Fermi Surface shrinking in towards the M point on the zone boundary as the number of carriers is reduced. It would also show that the area of the Surface is proportional to the number of carriers. To emphasise the significance of their results, the authors also doped the sulphide and selenide with other Group Va metal (Nb and V), and showed that this time $\vec{q}$ did <u>not</u> change, Figure 122.

The reduction of Fermi Surface area by substitutional doping of 1T TaS_2 ought to make the locking of the deformation onto the $\sqrt{13}a \times \sqrt{13}a$ superlattice occur more readily and at higher temperatures, i.e. in a similar way that T_d is higher in 1T $TaSe_2$

($\underline{q}$ = 0.278 $\underline{a}^*$) than in 1T_1 TaS_2 ($\underline{q}$ = 0.283 $\underline{a}^*$). It might furthermore be expected that when the concentration of the substituent metal reaches a certain value, the transition to the $\sqrt{13}$ a x $\sqrt{13}$ a superlattice would be suppressed.

Experimental results do generally speaking bear out these predictions, but with one very important proviso which will be given due consideration later. A small proportion of Ti, between about $\frac{1}{2}$% and 15 %, suppresses the 1T_2 phase in TaS_2 so that a transition occurs directly from 1T_1 to 1T_3 (Wilson et al 1975). Thus T_d has been raised so that 1T TaS_2 now behaves similarly to the selenide. Electrical measurements (Thompson, Pisharody & Koehler, 1972) confirm that a single transition occurs at a temperature intermediate between that of 1T_1 → 1T_2 TaS_2 and 1T_2 → 1T_3 TaS_2 transitions, when the concentration of Ti is about 10 %.

Full consideration must however be given to the following proviso: in all the doping experiments with both Group Va andIVa metals, there was ample evidence of disorder scattering. Transitions became broad and sluggish, and the satellite reflexions above T_d became broad and diffuse (Wilson et al, 1975). Thus, T_d was in fact <u>lowered</u> in 1T $TaSe_2$, and the upper transition in 1T TaS_2 was lowered also. No transitions at all occurred for more than about 15 % Ti (Thompson, Pisharody & Koehler, 1972; Wilson et al 1975), and although it would be tempting to explain this in terms of a Fermi Surface now too small, the more likely reason is that disorder has over-ridden any other consideration in suppressing the transitions. The high concentration of impurity atoms would scatter the charge-density wave very effectively causing large losses in phase correlation (McMillan, 1974; Lee, Rice & Anderson 1974). Wilson et al reported that even prolonged annealing failed to remove the disorder.

11.11.2 Intercalation Experiments

The doping experiments outlined in the previous section have demonstrated how the Fermi Surface shrinks with decreasing electron concentration. The reverse effect, expanding the Surface by increasing the concentration of carriers in the conduction band, is conveniently carried out by intercalation with a charge donor. The alkali metals produce very little change in the crystal c-axis when occupying the interlamellar space. They are therefore less likely to change the dispersion of the energy bands of the host lattice than organic molecules, many of which more than double the interlayer separation. Moreover, because the intercalated species does not enter the layers themselves, the disorder scattering experienced in the $Ti_xTa_{1-x}S_2$ alloys should not occur in the same way.

Intercalation of 1T TaS_2 with sodium, potassium or europium (capable of double ionisation) results in a change in the satellite reflexions (Clark, 1975). In addition to a series of reflexions corresponding to a superlattice of alkali metal ions in the Van der Waals gap, there are satellite reflexions of the periodic distortion type. One set of these forms a $3\underline{a}$ x $3\underline{a}$ superlattice, and is consistent with an expansion of the Fermi Surface to accommodate the electrons donated by the alkali metal. The wave vector spanning the Surface has thus increased from $0.283\ \underline{a}^*$ to $0.333\ \underline{a}^*$. Clark found that the results were generally independent of the cation chosen, and that the pattern of streaking at 150 K was very similar to that from the organic intercalation complex of $4H_b$ TaS_2 with ethylene diamine (Wilson et al, 1975). This is further evidence that these effects are linked to the Ta conduction band, rather than to the intercalated species.

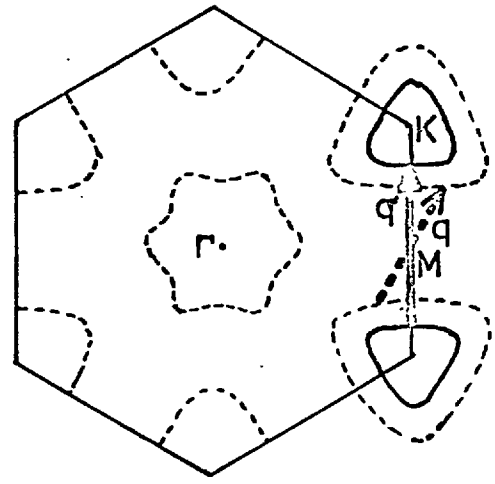


Figure 123 A possibility for the perturbation wave vector for the pyridine superlattice in intercalated 2H TaS_2, which would couple with CDWs in the host material conduction band.

With a link firmly established between intercalation and charge-density wave formation, it is interesting to consider again the intercalation complex studied in Chapter 5, i.e. $TaS_2(pyridine)_{\frac{1}{2}}$. Assuming a transfer of electron from the sp^2 hybrid orbital on the nitrogen in the pyridine ring, to the TaS_2 conduction d-band, then it might be expected that the segments of the Fermi Surface (centred at the K points on the zone boundary) would shrink. The wave vector, $\underline{q} = \frac{1}{3}\underline{a}^*$, would no longer span the Fermi Surface, so that this could explain the removal of the 80 K transition after 2H TaS_2 is intercalated with pyridine (Thompson, Gamble & Koehler, 1972).

The periodicity of the pyridine superlattice was found to be $2\frac{1}{6}\underline{a}$. This corresponds to $q = 0.40\ a^*$, parallel to the MK direction in reciprocal space. This wave vector would span an expanded electron Ferni Surface as shown in Figure 123. Although this seems the most likely candidate for $\underline{q}$, other possibilities cannot be excluded at this stage. It was pointed out in Chapter 5 that the $2\frac{1}{6}$periodicity does not lead to good alignment of pyridine molecules with ideal sites in the interlamellar space. It may be therefore that this configuration of the pyridines is partially stabilised by coupling with a charge-density wave in the TaS_2 matrix. If this is the case, then it is interesting to note that this is an example of the localisation of electronic charge in the Ta layer being stabilised not by displacements of the matrix ions, but by short range order of an intercalated species.

11.12 Pressure Measurements and Superconductivity

Grant, Griffiths, Pitt & Yoffe (1974) have shown that increased hydrostatic pressure lowers the $1T_1 \longrightarrow 1T_2$ TaS_2

transition temperature. This they interpret in terms of a 'stiffening' of the lattice, thereby reducing the amplitude of the deformation waves and inhibiting the transition.

When the pressure is increased in 2H $NbSe_2$, the superconducting transition temperature is raised, whilst in 2H NbS_2 it remains constant (Molinie, Jerome & Grant, 1974). The authors suggest a link with the CDW/deformation system which is present at these low temperatures in the selenide but not in the sulphide (Sections 9.2 and 9.3). The rise in T_c is accompanied by a fall in the temperature at which the Hall Coefficient changes sign (Huntley and Frindt, 1974), and at which periodic structural deformations are observed. The increase in pressure would again tend to suppress the distortions (or at least reduce their amplitude) by stiffening the lattice. The rise in T_c therefore suggests that the presence of the lattice deformations tends to inhibit superconductivity - this may be compared with similar conclusions reached for other materials by for example, Smith, Shelton & Lawson,(1973). From this, charge-density wave formation and superconductivity would appear to be linked, but in some senses to be competing mechanisms.

Further experimental evidence for the similarity between the CDW and the superconducting states comes from doping 2H $NbSe_2$ with iron and manganese in very small proportions (Morris, 1975). Increasing the concentration of either magnetic impurity results in a reduction of the CDW onset temperature, T_o, and in an exactly similar depression of the superconducting T_c. He argues that there must therefore be correlation between electron spins in the CDW in $NbSe_2$ which is broken by exchange interaction with impurity spin, in a manner analogous to that in a superconducting state.

Spin correlation has played little part in the discussion of charge-density waves in the layer dichalcogenides, largely because spin effects are not observable in the type of diffraction experiments on which the interpretation was based. The results of Morris for $NbSe_2$ show that it may well be an important consideration, and that the true situation is that of a mixed charge/spin density wave (section 3.4). The results of spin-dependent neutron diffraction experiments are therefore awaited with interest.

12 FINAL CONCLUSIONS AND FUTURE WORK

The results of the investigation are of considerable interest from a number of different viewpoints. Firstly the crystallographic models of the distorted structures, which have been proposed on the basis of diffraction data, are very interesting for their own sakes. Probably the most unusual concept which has been introduced, is the static, incommensurate deformation wave: the 'frozen phonon'. An incommensurate distortion of the magnitude observed in some of the materials deserves special attention. This is above all true when it is remembered that the incommensurate periodicity is maintained throughout the entire crystal, as deduced from X-ray measurements. Commensurate superlattices are observed in a wide variety of materials (for instance, the pyridine superlattice discussed in Chapter 5); incommensurate superstructures are far less common. Incommensurate periodicities imply the need for a large stabilising energy term to counteract the drive to reduce strain energy, which would otherwise cause the periodicities to lock onto a coincidence with the matrix lattice. Here then is a reason why incommensurate superstructures are relatively rare.

The theory required in order to describe the incommensurate case is necessarily complicated. The chief reason for this lies in the fact that when a periodic function modulates a periodic lattice, it produces a non-periodic structure, unless the two periodicities are commensurate. As noted in Chapter 2, which deals with scattering theory, it is possible under certain restricted conditions to approximate to a true superlattice. It is moreover an important result that calculations for the commensurate $1T_3$ phase of tantalum disulphide are compatible with those for the

incommensurate $1T_2$ phase within the range of valid approximation (section 7.7). The size however of the deformation amplitude in the tantalum dichalcogenides requires for most purposes the full analysis for an incommensurate structure. The analysis turns out to be considerably more involved than previous discussion by other authors (referred to in section 2.4) had implied. The reason for the added complication is the multiplicity of deformation waves simultaneously distorting the lattice. In addition the presence of higher order Fourier components of appreciable magnitude made it necessary to widen the analysis to include non-sinusoidal periodic distortions.

When the theory was applied to solving the deformation structure of tantalum disulphide, it was found that the model which best fitted the experimental data was one in which the metal atoms were grouped together in clusters. This result compares favourably with the clustering which is known to occur in a number of other transition metal compounds.

The transitions which were observed in diffraction, all took place at temperatures which agreed extremely well with the results of electrical and magnetic measurements. This agreement with anomalous behaviour in the electronic properties of the materials formed a useful starting point for trying to understand the reason for the spontaneous deformation of their lattices. The transitions were especially dramatic when observed continuously by electron diffraction in 1T TaS_2. Indeed, this particular compound must rank as the most interesting of the layer dichalcogenides. Perhaps more than anything else however, it must be the incommensurate — incommensurate transition (from $1T_1$ to $1T_2$) which singles this material out from the others. The rotation of the deformation wave vector in $1T_2$ TaS_2 proved

fascinating to watch (section 6.6), and also proved to be very important when it was interpreted as a vector spanning the Fermi Surface. Characteristically, 1T tantalum disulphide both had the most difficult structure to solve and interpret, and thereby gave finally the most information!

A positive attempt was made throughout the discussion sections to interpret the structural deformations in both direct space and reciprocal space. A good example of this approach can be found in the discussion of the stability and persistence of the $\sqrt{13}a \times \sqrt{13}a$ superlattice (section 11.9), for this can be understood both in terms of ease of cluster formation, and with regard to the extent of energy gaps around the Fermi Surface.

The Kohn Anomaly is enhanced in the layer dichalcogenides because of the approximately 2-D nature of the energy band structure. They therefore provide a good practical example of this effect - far better than most of the earlier materials studied. The results for the layer materials also complement very effectively the recent studies (referred to in section 11.9.2) on 1-D conductors. The more complex superstructures in the 2-D materials reflect the extra degree of freedom over 1-D.

The direct observation of the coupled charge-density wave/ periodic structural distortion system, provides an excellent experimental confirmation (also one of the first) of Overhauser's original prediction of their existence, although at the time he gave reasons why he doubted they would be so readily observable. The experimental discovery of charge-density waves complements that of spin-density waves in, for example, chromium. The charge-density wave model is consistent with the anomalous electrical and magnetic measurements which prompted to a large degree this present work.

It was gratifying also to discover that the shape of the Fermi Surface deduced from diffraction agreed well with the results of energy band structure calculations. Regrettably, however, this ability to image the Surface in diffraction is almost certainly restricted to a very select group of materials. It can never therefore be thought of as a competitor to conventional techniques, such as the de Haas - van Alphen effect.

The charge-density wave model predicts changes in the diffraction pattern as a result of increasing or decreasing the electron concentration in the conduction band, since these changes imply that the Fermi Surface enlarges or shrinks. The intercalation and doping experiments which were referred to in section 11.11 have in fact borne out this prediction. However, perhaps some of the best confirmation of the model has come from the recent neutron scattering results (11.7). These have shown beyond any doubt the progressive softening of the phonon modes due to the enhanced Kohn Anomaly.

The main emphasis in this work has been on the distorted structures, because they have proved so interesting both crystallographically and electronically. The results obtained for the intercalation complex studied are however also important. It is, first of all, most remarkable that a complex of alternate layers of MX_2 matrix and pyridine should have as regular a structure as it has. This is especially so when it is remembered that the interlayer separation doubles on intercalation. The stacking change which takes place is also significant and together with the stable structure argues for charge transfer from the pyridine to the host lattice. Perhaps the most interesting question raised with regard to this complex is whether there is a coupling with charge-density waves in the conduction d-electrons (section 11.11.3) which is responsible for the unusual

superlattice periodicity. The study did not lead to any firm conclusions about the orientationsand positions of the pyridine molecules in the interlamellar space, other than to favour perpendicular orientation. There is clearly a need for further systematic diffraction measurements to settle these questions. Since X-rays are not very sensitive to scattering from organic matter in the presence of a tantalum sulphide matrix, it is felt that neutron diffraction would be a more suitable technique to employ for this. Ideally this should be complemented by a parallel study of related intercalation complexes, especially of those where the intercalated species is a substituted pyridine.

To return to the distorted Group Va materials, the quantitative diffractometer measurements for $1T_2$ TaS_2 need to be extended to include the $1T_1$ and $1T_3$ phases, so that the transitions can be studied in detail. It would also be useful to be able to compare these results with similar measurements on 1T $TaSe_2$. Neutron diffraction, or possibly focused monochromatic X-ray diffraction, will probably prove to be the most effective technique for obtaining detailed information about the smaller amplitude deformation superstructures in the trigonal prismatic materials and in 1T VSe_2.

As a consequence of the superstructures being incommensurate, electron diffraction has proved capable of giving semi-quantitative information on structure from intensity estimates, at least for some of the distorted phases. The possibilities for multiple scattering are greatly reduced when the periodicities are incommensurate, so that a kinematical approximation has been partially valid. As soon as the deformations become coincident with a lattice periodicity, this situation can no longer hold.

Probably some of the most interesting work which could follow on from this study, would be in the field of inelastic

neutron scattering measurements of phonon dispersion curves over a wide range of temperature, especially in $1T_1$ TaS_2. It should be possible to monitor the progress of the Kohn Anomaly, so that the outstanding questions about the relationship of the diffuse scattering to the discrete satellites can be settled.

There is also considerable scope for more experiments on alkali metal intercalation complexes with layer materials which spontaneously distort. This is a simpler system structurally than the organic complexes, so that it should help with their interpretation, as well as continuing to provide evidence for links between the intercalation process and charge-density wave superstructures. Measurements of electron densities-of-states from photoemission and the changes which occur during intercalation should also prove revealing, provided that it does not prove too difficult to maintain the necessary ultrahigh vacuum with these rather unstable complexes in the system. Complexes such as $Na_x(1T\ TaS_2)$ which apparently combine ordering and deformation superlattices could well prove finally to be the most interesting materials of all.

The inter-relation of charge-density wave modes and superconductivity will almost certainly receive further theoretical effort. It will be especially interesting to discover how such ideas will apply in the case of niobium selenide, which is a good superconductor and which undergoes incommensurate distortion only.

All such experiments will rely heavily on the availability of good, single crystals, as have the experiments to date. The development of crystal growth techniques must therefore be a high priority in any future programme.

In conclusion, one of the most satisfying aspects of the work

has been the way that straightforward measurements on relatively simple equipment (such as the oscillation X-ray camera) have given a wealth of detailed information about a complex type of structure, and furthermore about the electronic structure of the material, and in particular its Fermi Surface.

ACKNOWLEDGEMENTS

First and foremost I should like to express my sincere thanks to my supervisor, Dr George S Parry, and Dr Peter M Williams for their invaluable advice and guidance and their continual inspiration throughout the course of this study.

Most of the work was undertaken in the Department of Chemical Engineering and Chemical Technology, Imperial College, and I should therefore like to thank the Head of Department and his staff for the facilities which have been made available to me. In this context a special word of thanks is due to Mrs Barbara Robinson for her help in connection with the electron microscopy. I should also express my gratitude to Dr Gordon Parkinson (Oxford University) and Dr Gordon Tatlock (Sussex University) for their assistance with low temperature electron diffraction.

I should like to thank Dr A D Yoffe and other staff of the Cavendish Laboratory, Cambridge, for valuable discussions in earlier stages of the work, and also of course the members of the Group at Imperial College for the their constant encouragement.

Some of the materials were kindly provided by Dr F Levy (École Polytechnique Fédérale de Lausanne), Dr F R Gamble (Exxon Research and Engineering), Dr P Molinié (Nantes University) and Dr A D Yoffe (Cambridge).

Finally I must acknowledge my gratitude to the Science Research Council for their financial support.

REFERENCES

Acrivos J V, Liang W Y, Wilson J and Yoffe A D, 1971, J. Phys. C, 4, L18.

Acrivos J V and Salem J R, 1974, Phil. Mag., 30, 603.

Adler D, 1968, Rev. Mod. Phys., 40, (4), 714.

Adler D and Brooks H, 1967, Phys. Rev., 155, (3), 826.

Afanas'ev A M and Kagan Y, 1963, Sov. Phys. JETP, 16, (4), 1030.

Allpress J G and Sanders J V, 1973, J. Appl. Cryst., 6, 105.

Bardeen J, Cooper L N and Schrieffer J R, 1957, Phys. Rev., 108, (5), 1175.

Barisic S, 1972, Phys. Rev. B, 5, (3), 932, and Ann. Phys., 7, 23.

Beal A R and Liang W Y, 1973, Phil. Mag., 27, (6), 1397.

Benda A, 1974, Phys. Rev. B, 10, (4), 1409.

Bjerkelund E and Kjekshus A, 1967, Acta Chem Scand., 21, 513.

Bohm H, 1975, Acta Cryst. A, 31, 622.

Bowen H, Donohue J, Jenkin D, Kennard O, Wheatley P and Whiffen D, 1958, Tables of Interatomic Distances, (London Chem. Soc., Burlington House).

Brillouin L, 1946, Wave Propagation in Periodic Structures (Dover).

Brixner L H, 1962, J. Inorg. Nucl. Chem., 24, 257.

Brockhouse B N, Rao K R and Woods A D B, 1961, Phys. Rev. Lett., 7, (9), 93.

Brown B E, 1966, Acta Cryst. 20, 264 and 268.

Brown B E and Beerntsen D J, 1965, Acta Cryst., 18, 31.

Carter C B and Williams P M, 1972, Phil. Mag., 26, (2), 393.

Chan S-K and Heine V, 1973, J. Phys. F, 3, 795.

Clark B, unpublished work.

Comes R, Lambert M, Launois H and Zeller H R, 1973, Phys. Rev. B, 8, (20), 571.

Comes R, Lambert M, and Zeller H R, 1973, Phys. Stat. Sol. (b), 58, 587.

DiSalvo F J, 1971, Ph.D. thesis, Stanford University.

DiSalvo F J, Bagley B G, Voorhoeve J M and Waszczak J V, 1973, J. Phys. Chem. Solids, 34, 1357.

DiSalvo F J, Maines R G and Waszczak J V, 1974, Sol. St. Commun., 14, 497.

Ehrenfreund E, Gossard A C and Gamble F R, 1972, Phys. Rev. B, 3, (5), 1703.

Fehlner W and Loly P D, 1974, Sol. St. Commun., 14, 653.

Frohlich H, 1954, Proc. Roy. Soc. A, 223, 296.

Gamble F R, DiSalvo F J, Klemm R A and Geballe T H, 1970, Science, 168, 568.

Gamble F R, Osiecki J H, Cais M, Pisharody R, DiSalvo F J and Gamble T H, 1971, Science, 174, 493.

Gamble F R, Osiecki J H and DiSalvo F J, 1971, J. Chem. Phys., 55, 7.

Goodenough J B, 1967, Mat. Res. Bull., 2, 165.

Grant A J, Griffiths, T M, Pitt G D and Yoffe A D, 1974, J. Phys. C, 7, L249.

Greenaway D L and Nitsche R, 1965, J. Phys. Chem. Solids, 26, 1445.

Halperin B I and Rice T M, 1968, Sol. St. Phys., 21, 115.

Hashimoto S and Ogawa S, 1970, J. Phys.Soc. Jap., 29, 710.

Heine V, 1969, The Physics of Metals: I Electrons, Chapter 1 (ed. J Ziman, C.U.P.).

Herring C, 1966, Magnetism, Vol. IV (Eds. Rado and Suhl, Academic Press).

Hicks W T, 1964, J. Electrochem. Soc., 111, 1058.

Hughes H P and Liang W Y, 1975, J.Phys. C, 7, L 162.

Huisman R, De Jonge R, Haas C and Jellinek F, 1971, J Sol. St. Chem., 3, 56.

Hume-Rothery W. 1931, The Metallic State (O.U.P. New York).

Huntley D J and Frindt F R, 1974, Can. J. Phys., 52, 861.

Iijima S, 1971, J Appl. Phys., 42, 5891.

James R W, 1948, The Optical Principles of the Diffraction of X-rays (London: Bell).

James P B and Lavik M T, 1963, Acta Cryst., 16, 1183.

Jellinek F, 1962, J. Less-Common Metals, 4, 9.

Jellinek F, Brauer G and Muller H, 1960, Nature, 4710, 376.

Kittel C, 1971, Introduction to Solid State Physics, 4th Edition, (Wiley).

Kohn W, 1959, Phys. Rev. Lett., 2, 393.

Korekawa M, 1967, Theorie der Satellitenreflexe (Munich).

Lee H W S, Garcia M, McKinzie H and Wold A, 1970, J. Sol. St. Chem., 1, 190.

Lee P A, Rice T M and Anderson P W, 1974, Sol. St. Commun. 14, 703.

Lomer W M, 1962, Proc. Phys. Soc., 80, 489.

Lomer W M, 1967, Phase Stability in Metals and Alloys (eds. Rudman, Stringer & Jaffe, London: McGraw-Hill).

Mattheiss L F, 1973, Phys. Rev. B, 8, 3719.

McMillan W L, 1975, Phys. Rev. B, 12, (4), 1187 and 1197.

Molinie P, Jerome D and Grant A J, 1974, Phil. Mag., 30, (5), 1091.

Moncton D E, Axe J D and DiSalvo F J, 1975, Phys. Rev. Lett.,

Morris R C, 1975, Phys. Rev. Lett., 34, (18), 1164.

Mott N F, 1949, Proc. Phys. Soc. A, 62, 416.

Mott N F, 1968, Rev. Mod. Phys., 40, (4), 677.

Mott N F and Jones H, 1936, Theory of the Properties of Metals and Alloys (Oxford).

Nilsson G and Rolandson S, 1974, Phys. Rev. B, 9, (8), 3278.

Ohshima K and Watanabe D, 1973, Acta Cryst. A, 29, 520.

Omloo W and Jellinek F, 1970, J. Less-Common Metals, 20, 121.

Overhauser A W, 1968, Phys. Rev., 167, (3), 691.

Overhauser A W, 1971, Phys. Rev. B, 3, (10), 3173.

Peierls R E, 1955, Quantum Theory of Solids (Oxford: Clarendon Press).

Renker B, Pintschovius L, Glaser W, Rietschel H, Comes R, Liebert L and Drexel, 1974, Phys. Rev. Lett., 32, (15), 836.

Rice T M and Scott G K, 1975, Phys. Rev. Lett., 35, (2), 120.

Rice T M and Strassler S, 1973, Sol. St. Commun., 13, 125.

Rudorff W and Sick H H, 1959, Angew. Chem., 71, 127.

Røst E and Gjertsen L, 1964, Z. Anorg. allg. Chem., 328, 299.

Sato H and Toth R S, 1968, Bull. Soc. for Min. Cryst., 91, 557.

Schafer H, 1964, Chemical Transport Reactions (Academic Press).

Shepherd F R and Williams P M, 1974, J. Phys. C, 7, (23), 4427.

Silbernagel B G (unpublished work).

Smith T F Shelton R N and Lawson A C, 1973, J Phys. F, 3, 2157.

Somoano R B, Hadek V and Rembaum A, 1973, J. Chem. Phys., 58, (2), 697.

Tatlock, G, 1976 (submitted for publication).

Thompson A H, 1974, Nature, 251, 492.

Thompson A H, Gamble F R and Koehler R F, 1972, Phys. Rev. B, 5, (8), 2811.

Thompson A H, Gamble F R and Revelli J F, 1971, Sol. St. Commun., 9, 981.

Thompson A H, Pisharody K R and Koehler R F, 1972, Phys. Rev. Lett., 29, (3), 163.

Tidman J P, Singh O, Curzon A E and Frindt R F, 1974, Phil. Mag., 30, (5), 1191.

Valic M I, Abdolall K and Williams D L, 1974, Proc. 18th Ampere Conference, Nottingham).

Van Landuyt J, Remaut G and Amelinckx S, 1970, Phys. Stat. Sol., 41, 271.

Van Landuyt J. Van Tendeloo G and Amelinckx S. 1974. Phys. Stat. Sol. (a), 26, 359 and 585.

Van Maaren M H and Schaeffer G M, 1966, Phys. Lett., 20, 131.

Wildervanck J C and Jellinek F, 1964, Z. Anorg. allg. Chem., 328, 309.

Williams P M and Robinson B A, 1973, Nature, Physical Science, 245, (144), 79.

Wilson A H, 1953, Theory of Metals, (C.U.P.).

Wilson J A,DiSalvo F J and Mahajan S, 1975, Adv. Phys., 24, 117.

Wilson J A and Yoffe A D, 1969, Adv. Phys., 18, 193.

Woll E J and Kohn W, 1962, Phys. Rev., 126, (5), 1693.

Yamada Y, Tsang J C and Subba-Rao G V, 1975, Phys. Rev. Lett., 34, (22), 1389.

Yoffe A D, 1973, Festkorperprobleme XIII, 1 (Ed. Queisser, Viweg, Braunschweig).

Zeller H R, 1973, Festkorperprobleme XIII, 31 (Ed Queisser, Viweg, Braunschweig).

Ziman J M, 1959, Electrons and Phonons (Oxford: Clarendon Press).

Ziman J M, 1972, Principles of the Theory of Solids (2nd edition, C.U.P.).

PUBLICATIONS

Williams P M, Parry G S and Scruby C B, 1974, Phil. Mag., 29, (3), 601.

Parry G S, Scruby C B and Williams P M, 1974, Phil. Mag., 29, (3), 695.

Scruby C B, Williams P M and Parry G S, 1975, Phil. Mag., 31, (2), 255.

Scruby C B, Williams P M, Parry G S, Parkinson G M, Tatlock G, 1976, Proc. EMAG 75, Bristol, (Ed. Venables J A), p.377.

Scruby C B, 1976, Proc. EMAG 75, Bristol, (Ed. Venables J A), p.271.

Williams P M, Scruby C B and Tatlock G J, 1975, Sol. St. Commun., 17, 1197.

APPENDIX 1

(a) Diffraction from 1-D Commensurate Clusters

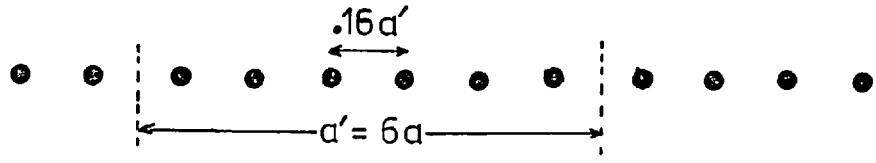
Suppose that the undistorted lattice periodicity is a, and that the supercell periodicity is a' = 6a. Suppose further that the deformation produces clusters of atoms in 1-D, so that the interatomic separation within each cluster is:

$$0.96a = 0.16\,a'$$

Then the fractional coordinates, x_i, of the six atoms within the unit supercell are given by:

$$\pm 0.08,\ \pm 0.24,\ \pm 0.40.$$

where the origin has been chosen thus:



Hence the geometrical part of the structure factor is given by:

$$\frac{F}{f} = \sum_i \exp(2\pi i h x_i)$$

$$= 2[\cos(0.16\pi h) + \cos(0.48\pi h) + \cos(0.8\pi h)]$$

Values of the structure factor for $h \leq 14$ are calculated as:

h	1	2	3	4	5	6	7
$\frac{F}{f}$	0.26	-0.29	0.37	-0.53	1.00	-5.46	-2.09

8	9	10	11	12	13	14
1.10	-0.92	1.00	-1.43	4.01	4.01	-2.06

These figures are plotted out in Fig. 26, section 2.6.4

(b) Diffraction from 1-D Incommensurate Clusters

Suppose that there is a'saw-tooth' deformation wave of periodicity Λ in a 1-D crystal of periodicity a. Then defining $Q = 1/\Lambda$, the displacement from an ideal sites at $r = \ell$ is given by:

$$\delta r(\ell) = U_Q \sum_{n=1}^{\infty} (-1)^n \left\{ \frac{\sin(2\pi Q.\ell)}{n} \right\}$$

where U_Q is the amplitude of the fundamental component, and a Fourier series expansion has been carried out for the sawtooth modulation function (see section 2.6.3).

The maximum displacements in the sawtooth wave are given by

$$\pm \tfrac{1}{2}\pi U_Q.$$

Substituting $x = 2\pi K U_Q$, the scattering at $K = M \pm Q$ is given therefore by (compare equations in section 2.4.1):

$$F(M \pm Q) = V(K)\prod_n \left\{ \sum_{N_n} J_{\mp N_n} \frac{(-1)^n x}{n} \right\}$$

subject to the following constraint -

$$\pm Q = \sum_n N_n (nQ)$$

The only solutions for double scattering (i.e. with <u>two</u> terms in the summation) are with: $N_n = +1, N_{n-1} = -1$; or $N_n = -1$, $N_{n-1} = +1$, where all other $N_n = 0$. When these terms are added to the terms for single scattering, the following is obtained:

$$\begin{aligned} F(M \pm Q) = V(K)\Big\{ & J_{\mp 1}(x)J_0(\tfrac{1}{2}x)\ldots J_0\left(\frac{(-1)^n x}{n}\right)\ldots \\ & + J_{\pm 1}(x)J_{\mp 1}(\tfrac{1}{2}x)J_0(\tfrac{1}{3}x) \ldots . \\ & + J_0(x)J_{\pm 1}(\tfrac{1}{2}x)J_{\mp 1}(\tfrac{1}{3}x)J_0(\tfrac{1}{4}x)\ldots \\ & + \ldots\ldots\ldots\ldots \text{ etc } \Big\} \end{aligned}$$

i.e.

$$F(M \pm Q) = V(K)\left\{\prod_n J_0\left(\frac{x}{n}\right)\right\}\left\{ \frac{J_1(x)}{J_0(x)} + \frac{J_1(x)J_1(\tfrac{1}{2}x)}{J_0(x)J_0(\tfrac{1}{2}x)} + \ldots\ldots\ldots \right\}$$

All the negative signs have cancelled out except in the first term, which unlike the remaining terms in only a single quotient. The $(n+1)$th term is given by:

$$t_{n+1} = \frac{J_1\left(\frac{x}{n}\right)\, J_1\left(\frac{x}{n+1}\right)}{J_0\left(\frac{x}{n}\right)\, J_0\left(\frac{x}{n+1}\right)}$$

For sufficiently large n, for instance greater than some n', the zero and first order Bessel Function may be approximated:

$$J_0\left(\frac{x}{n}\right) = 1; \quad J_1\left(\frac{x}{n}\right) = \tfrac{1}{2}\left(\frac{x}{n}\right)$$

It may however be necessary to calculate the first n' - 1 terms exactly before being able to use this approximation.

$$\therefore \quad t_{n+1} = \frac{x}{2n} \times \frac{x}{2(n+1)}$$

$$= \frac{x^2}{4} \times \frac{1}{n(n+1)}$$

Therefore for $n > n'$ the terms tend to a series given by the summation: $\frac{1}{4}x^2 \quad \frac{1}{n(n+1)}$

The sum of this is finite, and given by (with a selection of values for n'):

For $n' = 1$, the series sums to $\frac{1}{4}x^2$.

.. $n' = 2$ .. .. $\frac{x^2}{8}$

.. $n' = 3$ .. .. $\frac{x^2}{12}$

In particular it should be noted that the sum of the series is double the magnitude of the first term. If the first term is in fact calculated exactly and the remaining terms summed in the above manner, we obtain for t_{n+1} :

$$t_{n+1} = \frac{J_1(x)\ J_1(\frac{1}{2}x)}{J_o(x)\ J_o(\frac{1}{2}x)} + \frac{x^2}{8}$$

The expression of $F(M \pm Q)$ on the previous page involves a product of an infinite number of zero order Bessel Functions. We can evaluate the first two, i.e. $J_o(x)$ and $J_o(\frac{1}{2}x)$, exactly, and then approximate the rest (assuming small argument) as follows:

$$J_o(\frac{x}{n}) \simeq 1 - \tfrac{1}{4}(\frac{x}{n})^2$$

$$\prod_{n=3}^{\infty} J_o(\frac{x}{n}) \simeq 1 - \tfrac{1}{4}\sum_{n=3}^{\infty}(\frac{x}{n})^2$$

$$\simeq 1 - 0.1\,x^2$$

We are thus able to evaluate the infinite number of terms in the expressions for the structure factors, and obtain:

$$F(M \pm Q) = V(K)\left\{J_o(x)J_o(\tfrac{1}{2}x)(1 - 0.1\,x^2)\right\}\left\{\frac{J_1(x)}{J_o(x)} + \frac{J_1(x)J_1(\frac{1}{2}x)}{J_o(x)J_o(\frac{1}{2}x)} + \frac{x^2}{8}\right\}$$

Only the first term changes its sign from M + Q to M - Q, i.e.

$$F(M \pm Q) = \pm F(\text{fundamental}) + F(\text{higher harmonics})$$

This shows very cearly how <u>all</u> the contributions from higher harmonics accentuate the asymmetry in magnitude of the satellites

at M + Q and M - Q. The structure factor can also be calculated for the matrix reflexions. This is somewhat simpler, and only involves the infinite product of zero order Bessel Functions, for which an approximation has already been given. i.e.

$$\begin{aligned} F(M) &= V(K)\prod_n J_o(\tfrac{x}{n}) \\ &= V(K)\, J_o(x)\, J_o(\tfrac{1}{2}x)(1 - 0.1\, x^2) \end{aligned}$$

We are now in a position to use these results to calculate structure factors for an incommensurate 'sawtooth' deformation wave with $\Lambda = (6 + \epsilon)\, a$, where $\epsilon \ll 1$. This superstructure is <u>almost</u> commensurate with $Q \triangleq \frac{a^*}{6}$.

We choose U_Q so as to give the same overall displacements as were used in the model for the commensurate deformation superlattice, thus:

$$\begin{aligned} 2(\tfrac{1}{2}\pi U_Q) &= 0.04\, a \\ \therefore \quad x &= 2\pi K U_Q \\ &= 0.08\, h, \text{ where } \quad h = Ka. \end{aligned}$$

The results of this calculation give for the geometrical part of the structure factors of the matrix reflexions (h = 1,2) and their first order satellites:

Reflexion	h = 1	h = 2
M - Q	0.15	0.20
M	0.91	0.67
M + Q	0.34	0.56

These values are plotted out in Figure 27 (Section 2.6.5).

APPENDIX 2

Fortran Programme to determine phonon combinations at a matrix reflexion (M), a first order satellite (M + Q), a second order satellite(M + P), respectively. In each case the version of the programme appropriate for the reflexion is followed by a listing of the combinations.

```
PROGRAM PHONONS    73/73   OPT=2                                FTN 4.1+P373

      PROG=A1 PHONONS(INPUT,OUTPUT,,,TAPE7,TAPE5=INPUT,TAPE6=OUTPUT)
C     MULTI-PHONON PROCESSES GIVING SCATTERING AT M
      DO 5, N1 = 1,7
      N1 = N1 - 4
      DO 50 N2 = 1,7
      N2 = N2 - 4
      DO 50 N3 = 1,7
      N3 = N3 - 4
      I3=N6-N3
      J3=I3*I3(N1)+I3*I3(N2)+I3*I3(N3)
      DO 50 N4 = 1,5
      N4 = N4 - 3
      I4=I3+N4+N4
      J4=J3+I3*I3(N4)*2
      DO 50 N5 = 1,5
      N5 = N5 - 3
      I5=I4-N5
      J5=J4+I3*I3(N5)*2
      IF(J5-3)51,51,50
   51 DO 41 N6 = 1,5
      N6 = N6 - 3
      I6=I5-N6
      J6=J5+I3*I3(N6)*2
      IF(J6-3)41,41,40
   41 DO 31 N7 = 1,5
      N7 = N7 - 3
      J7=J6+I3*I3(N7)*2
      IF(J7-3)31,31,30
   31 DO 21 N8 = 1,5
      N8 = N8 - 3
      I8=I6+N8+N8
      J8=J7+I3*I3(N8)*2
      IF(J8-3)21,21,20
   21 DO 10 N9 = 1,5
      N9 = N9 - 3
      IF(I8-N9-N9)4,5,4
    5 IF(3*N1+2*N2+N3-3*N4+3*N5+4*N7-2*N8-2*N9)10,6,10
    6 J8=J8-I3*I3(N9)*2
      IF(J8-3)7,7,8
    7 PRINT(6,11)N1,N2,N3,N4,N5,N6,N7,N8,N9
      PRINT(7,11)N1,N2,N3,N4,N5,N6,N7,N8,N9
   10 CONTINUE
    9 CONTINUE
    8 CONTINUE
   40 CONTINUE
   50 CONTINUE
   60 STOP
  100 FORMAT(9I8)
      END
```

```
      PROGRAM PROMOMS(INPUT,OUTPUT,TAPE5,TAPE5=INPUT,TAPE6=OUTPUT)
C     MULTI-PROMOM PROCESSES GIVING SCATTERING AT M + 01
      DO 51 N1 = 1,7
      N1 = N1 - 4
      DO 51 N2 = 1,7
      N2 = N2 - 4
      DO 51 N3 = 1,7
      N3 = N3 - 4
      IA=N2-N3
      JJ=IA*IAMS(N1)+IAMS(N2)+IAMS(N3)
      DO 51 N4 = 1,5
      N4 = N4 - 3
      I4=I3+N4+N4
      J4=JJ+IAMS(N4)*2
      DO 51 N5 = 1,5
      N5 = N5 - 3
      I5=I4-N5
      J5=J4+IAMS(N5)*2
      IF(J5-1)51,51,50
   51 DO 41 N6 = 1,5
      N6 = N6 - 3
      I6=I5-N6
      J6=J5+IAMS(N6)*2
      IF(J6-1)41,40,40
   41 DO 31 N7 = 1,5
      N7 = N7 - 3
      J7=I6+IAMS(N7)*2
      IF(J7-1)31,30,30
   31 DO 21 N8 = 1,5
      N8 = N8 - 3
      I8=I6+N8+N8
      J8=J7+IAMS(N8)*2
      IF(J8-3)21,20,20
   21 DO 11 N9 = 1,5
      N9 = N9 - 3
      IF(I8-N9**2)11,5,11
    5 IF(J8*(J8-1)-2*(2*N5+3*N6+4*N7-2*N5-2*N8+2))10,6,10
    6 J9=J8+IAMS(N9)*2
      IF(J9-3)7,10,10
    7 WRITE(6,100)N1,N2,N3,N4,N5,N6,N7,N8,N9
      WRITE(6,100) N1,N2,N3,N4,N5,N6,N7,N8,N9
   10 CONTINUE
   11 CONTINUE
   21 CONTINUE
   31 CONTINUE
   41 CONTINUE
   51 CONTINUE
      STOP
  100 FORMAT(3I6)
      END
```

```
      PROGRAM PHONONS(INPUT,OUTPUT,TAPE8,TAPE9=INPUT,TAPE6=OUTPUT)
C     C  C.A.-PHONON  PROGRAM  GIVING  SCATTERING  T  +  D1
      DIMENSION N1(7),N2(7),N3(7),N4(7),N5(7),N6(7),N7(7),N8(7),N9(7)
      DIMENSION IA(7),JA(7),KA(7),LA(7),MA(7),NA(7),OA(7),PA(7),QA(7)
      N1=1
      N2=N1-4
      N3=N2+3
      N4=N3-4
      N5=N4+3
      N6=N5-4
      N7=N6+3
      IA(1)=N1-N7
      JA(1)=IA(1)+IA(N1)+IA(N2)+IA(N7)
      N1=N1+1
      N2=N2+1
      N3=N3+1
      N4=N4+1
      N5=N5+1
      N6=N6+1
      N7=N7+1
      IA(2)=N1-N7
      JA(2)=JA(1)+IA(N1)*2
      N1=N1+1
      N2=N2+1
      N3=N3+1
      N4=N4+1
      N5=N5+1
      N6=N6+1
      N7=N7+1
      IA(3)=N1-N7
      JA(3)=JA(2)+IA(N1)*2
      IF(JA(3)-3)51,50,50
   51 N1=N1+1
      N2=N2+1
      N3=N3+1
      N4=N4+1
      N5=N5+1
      N6=N6+1
      N7=N7+1
      IA(4)=N1-N7
      JA(4)=JA(3)+IA(N1)*2
      IF(JA(4)-3)41,40,40
   41 N1=N1+1
      N2=N2+1
      N3=N3+1
      N4=N4+1
      N5=N5+1
      N6=N6+1
      N7=N7+1
      IA(5)=N1-N7
      JA(5)=JA(4)+IA(N1)*2
      IF(JA(5)-3)31,30,30
   31 N1=N1+1
      N2=N2+1
      N3=N3+1
      N4=N4+1
      N5=N5+1
      N6=N6+1
      N7=N7+1
      IA(6)=N1-N7
      JA(6)=JA(5)+IA(N1)*2
      IF(JA(6)-3)21,20,20
   21 N1=N1+1
      N2=N2+1
      N3=N3+1
      N4=N4+1
      N5=N5+1
      N6=N6+1
      N7=N7+1
      IA(7)=N1-N7
      JA(7)=JA(6)+IA(N1)*2
      IF(JA(7)-3)11,10,10
    5 IF(2*N1-N2-N3-3*N4+3*N5+N6+4*N7-2*N8-2*N9)10,6,10
    6 JA=JA(7)+IA(N1)*2
      IF(JA-3)7,10,10
    7 WRITE(6,100)N1,N2,N3,N4,N5,N6,N7,N8,N9
      WRITE(6,100) N1,N2,N3,N4,N5,N6,N7,N8,N9
   10 CONTINUE
   11 CONTINUE
   20 CONTINUE
   30 CONTINUE
   40 CONTINUE
   50 CONTINUE
  100 FORMAT(9I3)
      END
```

APPENDIX 3

Main Fortran Programme for calculating structure factors.

```
      48    CONTINUE
      50    CONTINUE
            READ(10,2,6)HM,EK,EL
      95    FORMAT(1H0,15HMATRIX REFLEXION  ,3F4.0)
            K1=1
            K2=1
            K=7
     164    DO 11 K = K1,K2
            SU(K)=0.
            IF(K-7)11,12,13
     11     DO 170 I = 1,6M
            DO 170 J = 1,6
            A(I,J) = A7(I,J)
     180    CONTINUE
     170    CONTINUE
            WRITE (6,207)
     207    FORMAT(1H0,36H  MATRIX  K VECTOR   ETA     ALPSFLS)
            GO TO 151
     12     M1 = 151
            DO 171 I = 1,6M
            DO 161 J = 1,6
            A(I,J) = A8(I,J)
     161    CONTINUE
     171    CONTINUE
            IK=K-1
            GO TO (31,32,33,34,35,36) IK
     31     WRITE(6,331)
     331    FORMAT(1H0,11HSM( 1 0. 1))
            GO TO 12
     32     WRITE(6,332)
     332    FORMAT(1H0,11HSM( 1-1.-1))
            GO TO 12
     33     WRITE(6,333)
     333    FORMAT(1H0,11HCM( 1-1  1))
            GO TO 12
     34     WRITE(6,334)
     334    FORMAT(1H0,11HCM(-1 0.-1))
            GO TO 12
     35     WRITE(6,335)
     335    FORMAT(1H0,11HSM(-1 1. 1))
            GO TO 12
     36     WRITE(6,336)
     336    FORMAT(1H0,11HSM( 0 1.-1))
            GO TO 12
     13     M1 = 157
            DO 172 I = 1,6M
            DO 162 J = 1,6
            A(I,J) = A9(I,J)
     162    CONTINUE
     172    CONTINUE
            IK=K-7
            GO TO (41,42,43,44,45,46) IK
     41     WRITE(6,441)
     441    FORMAT(1H0,11HSM( 1-2. 0))
            GO TO 12
     42     WRITE(6,442)
     442    FORMAT(1H0,11HSM(-1-1. 0))
            GO TO 12
     43     WRITE(6,443)
     443    FORMAT(1H0,11HCM(-1 1  0))
            GO TO 12
     44     WRITE(6,444)
     444    FORMAT(1H0,11HSM(-1 0. 1))
            GO TO 12
     45     WRITE(6,445)
     445    FORMAT(1H0,11HSM( 1 1. 0))
            GO TO 12
     46     WRITE(6,446)
     446    FORMAT(1H0,11HSM( 0-1. 0))
     120    DO 181 I = 1,6M
            CALL MULT(7,A(I,K),XX)
            NN = IFIX(A(1,M)) + 1
            IF(XX)14,14,15
     14     IF(XX.NE.0.)IF(XX.NE.4) GO TO 15
            SU(K) = -SU(K)
            GO TO 16
     15     SU(K) = XX(NN)
     181    CONTINUE
            PROD = SUM(1)
            DO 25 I = 2,6
     25     PROD = PROD*SUM(I)
     180    CONTINUE
     181    SU(K) = SU(K) + PROD
      C
      C     SUBROUTINE TO CALCULATE EQUATION FOR ETA(TA)
            SUMKL=SU(K)/2.0
            ETA=SUMKL/1.5 +1.0
            IF=ET


            EQUATE(IFT)=ELLIPT(IFT)
            FX(IFT) = FX(IFT) + (FX(IFT+1) - FX(IFT))*EQUATE(IFT)
            CF(K) = SU(K)*EQ
      C
      C     WRITE VALUES OF CALCULATED OBJECTIVE FACTORS, ETC..
            WRITE(6,211) CF(K),SU(K),ETA,SUM(K)
     211    FORMAT(1H0,4F9.4)
     110    CONTINUE
            K=K+1
            K1=K1+1
            K2=K2+1
            IF(K.LE.9)GO TO 160
     11     CONTINUE
            STOP
```